Effect of Hydrogen on the Corrosion Performance of Zirconium Alloys

A thesis submitted to The University of Manchester for the degree of Doctor of Philosophy in the Faculty of Engineering and Physical Science

2012

Jianfei Wei

School of Materials

List of Contents

Total words: 54793.

List of Tables

List of Figures

Effect of Hydrogen on the Corrosion Performance of Zirconium Alloys

A thesis submitted to The University of Manchester for the degree of Doctor of Philosophy in the Faculty of Engineering and Physical Science

2012

Jianfei Wei
School of Materials, The University of Manchester

This study is part of the multidisciplinary research program funded by the EPSRC aimed at further understanding the mechanisms behind the oxidation, transition and breakaway of zirconium alloys. The current study concentrates on the effect of artificially introduced hydride rich rim region upon the corrosion performance of zirconium alloys.

The methodology of cathodic hydrogen charging of zirconium specimen has been described. The intention is to create a hydride rich rim similar to observation made in end-of-life fuel claddings from nuclear reactor. The overall hydrogen levels in the samples were determined via inert gas fusion and the local hydride volume fractions via laboratory x-ray diffraction. The residual stress state in the rim was investigated by synchrotron x-ray diffraction. The rim was determined to have local hydrogen levels about 11,000 wt.ppm and predominantly δ-hydrides. Hydrided samples and their references were tested in autoclaves simulating primary water environment. Reference samples exhibited typical corrosion kinetics with a change from pre- to post-1st transition. The duration before 1st transition varies with alloy chemistry and heat treatment conditions. Hydrided samples generally experienced accelerated corrosion while the extent to which the material was affected depends on alloy chemistry. Parabolic rather than cubic oxide growth with a very slow early corrosion rate was recorded in hydrided alloys. Both hydrided and reference samples of three Zr-Sn-Nb alloys, ZIRLO^{TM}, low tin ZIRLO and X2 with tin concentration ranging from 0.14 to 0.92 wt.% became the gravity of further characterisations since they exhibited improved corrosion performance with decreasing tin content. The microstructure of the oxide was investigated via cross-sectional Scanning Electron Microscope (SEM). The residual stress state in tetragonal and monoclinic phases as well as tetragonal phase fraction were studied via synchrotron x-ray diffraction, showing high in-plane compressive stresses in the oxide of different levels depending on the phase and alloy. The presence of a hydride rim lowered the residual stress. White oxide in hydrided samples displays lower residual stress level, smaller tetragonal phase fraction and higher degree of oxide grain misorientation when compared to black oxide regions of reference and hydrided samples. It was also found that the hydride rim region undergoes local depletion of hydrides in alloy with low Sn content during the early stage of aqueous corrosion. Finally a model was given to describe the different roles played by individual oxide and hydride phases during the oxidation of zirconium alloys.

Declaration

No portion of the work referred to in the thesis has been submitted in support of an application for another degree or qualification of this or any other university or other institute of learning

Copyright Statement

1. The author of this thesis (including any appendices and/or schedules to this thesis) owns certain copyright or related rights in it (the “Copyright”) and s/he has given The University of Manchester certain rights to use such Copyright, including for administrative purposes.

2. Copies of this thesis, either in full or in extracts and whether in hard or electronic copy, may be made only in accordance with the Copyright, Designs and Patents Act 1988 (as amended) and regulations issued under it or, where appropriate, in accordance with licensing agreements which the University has from time to time. This page must form part of any such copies made.

3. The ownership of certain Copyright, patents, designs, trade marks and other intellectual property (the “Intellectual Property”) and any reproductions of copyright works in the thesis, for example graphs and tables (“Reproductions”), which may be described in this thesis, may not be owned by the author and may be owned by third parties. Such Intellectual Property and Reproductions cannot and must not be made available for use without

the prior written permission of the owner(s) of the relevant Intellectual Property and/or Reproductions.

4. Further information on the conditions under which disclosure, publication and commercialisation of this thesis, the Copyright and any Intellectual Property and/or Reproductions described in it may take place is available in the University IP Policy (see

   http://www.campus.manchester.ac.uk/medialibrary/policies/intellectual-property.pdf), in any relevant Thesis restriction declarations deposited in the University Library, The University Library's regulations (see http://www.manchester.ac.uk/library/aboutus/regulations) and in The University's policy on presentation of Theses.

Acknowledgement

I would like to express my sincere gratitude to my supervisor Prof. Michael Preuss for his guidance as my advisor over the years it took me to reach this stage. This project would not have been accomplished without his expert advice and knowledge. I am also most grateful for his unfailing patience and understanding during my study and especially the sometimes-difficult circumstances. The past years in Manchester have become one of the most important and formative experiences in my life.

I'm grateful to many people, especially Dr. Martine Blat-Yrieix and Dr. Antoine Ambard of EDF R&D; Dr. Lars Hallstadius and Dr. Mats Dahlbäck of Westinghouse; Prof. Bob Cottis, Prof. Stuart Lyon, Dr. Philipp Frankel and Mr. Kenneth Gyves of the University of Manchester for generously sharing their time, expertise and resources to better my study. I thank them for their hospitality, experience and wisdom. Over my years of experiments at School of Materials, The University of Manchester, Dr. Christopher Wilkins, Dr. Ali Gholinia, Ms. Judith Shackleton, Mr. Gary Harrison, Mr. Mark Harris, Mr. Gary Pickles and Mr. Thomas Neild have all endured my endless waves of questions. I thank them for their supports in even the most unexpected circumstances, many experiments would have failed without them. I would also like to acknowledge my friends Mr. Efthymios Polatidis, Mr. Fabio Di Gioacchino, Dr. Thomas Simm and Ms. Rebeca Sandala. Their humour and optimism eased the pressure off me during difficult times, and have inspired many interesting discussions related to this research.

Last, but not lease, I would like to thank my wife Hui for her love and encouragements. Her unconditional support kept me going and in the end made all my work possible. My parents, Guo and Shiying have my deepest gratitude. They inspired my first interest in science during childhood. Over the years, their love, dedication and support laid the groundwork of my dissertation.

This project is supported in part by Engineering and Physical Science Research Council (EPSRC) and MoD in the UK for funding the research as part of the Materials for Energy call (research code: EP/E036171/1). This project would not have been possible without the strong support of our industrial project partners (in alphabetical order) EDF, National Nuclear Laboratory, Rolls-Royce, Serco and Westinghouse, who have provided substantial in-kind and financial support and our academic project partners from the University of Oxford and the Open University.

1 Introduction

1.1 Background

Zirconium alloys are widely used in nuclear reactors as fuel rod cladding and structural materials. Their superior corrosion resistance, adequate mechanical properties and low thermal neutron cross-section make zirconium alloys particularly suitable for such applications. However, corrosion and particularly breakaway corrosion of zirconium alloys limit the lifespan of fuel rods and their potential for higher fuel efficiency. Studying the mechanism behind zirconium corrosion is hence of engineering importance.

1.2 The current study

The research project presented in this thesis is part of the EPSRC MUZIC project, which is a multidisciplinary project undertaken by a consortium of universities including the University of Manchester, the University of Oxford and Open University. The overall goal of this project is to further understand the mechanism behind corrosion and breakaway corrosion in zirconium alloys, which is to be achieved via multi-technique approaches such as Transmission Electron Microscopy (TEM), High Resolution Transmission Electron Microscopy (HR-TEM), Scanning Electron Microscopy (SEM), 3D-atom probe, 3D-Focused Ion Beam (FIB) sectioning, synchrotron X-ray diffraction, Raman Spectroscopy, Nanoindentation and in-situ electrochemical impedance spectroscopy. The combination of those techniques provides information on different aspects of zirconium corrosion from a length scale of several centimetres to a length scale of the atomic range.

Research activities within this thesis concentrate on evaluating the effect of a hydride rim upon the corrosion performance, which is considered to be critical to breakaway corrosion. In order to conduct this research, a large amount of work was invested on obtaining specimens with artificially introduced hydride rim prior autoclave corrosion and recording corrosion kinetics of hydrided and reference samples from a variety of alloys. Particular interests were focused on ZIRLO^{TM}, low tin ZIRLO and X2 materials since they demonstrated relationships between tin content and corrosion performance. This thesis describes the cathodic hydrogen charging technique and autoclave corrosion of the reference and hydrided materials. The hydrided materials and corroded materials were characterised using SEM, TEM, laboratory X-ray diffraction and synchrotron X-ray diffraction.

1.3 Rationale for submitting the thesis in an alternative format and structure of this PhD thesis

A significant amount of autoclave corrosion data as well as characterizations of the oxide via synchrotron radiation, SEM, TEM and laboratory X-ray has been gathered. The amount of data is already sufficient for publication of journal papers. It was decided that such publications will help gather invaluable feedbacks from outside of the research group. The writing process of publications can also act as milestones of the current research; it helps the construction of working hypothesis during the ongoing research activities. The published work will also further benefit future researchers in the same field of work.

Following this introduction, a literature review chapter has been constructed based on previous research in the field, especially the corrosion kinetics and proposed

mechanisms for transition. This is followed by the formation of hydrides during corrosion of zirconium and its detrimental effect. The next chapter discusses the principles of cathodic hydrogen charging while detailed description and discussion of the technique are presented in proposed publication No.1. This is followed by proposed publication No.2, which discusses the autoclave corrosion experiments. Publication No.3 and No.4 focus on the characterization of oxide grown on reference and hydrogen charged ZIRLO^{TM}, low tin ZIRLO and X2. They also each propose models describing the mechanism behind zirconium corrosion, transition and breakaway. A summary of the model is given following publication No.4. Finally a conclusion is given and several aspects for future research are proposed.

The co-authors for the 4 proposed publications are R. J. Comstock and Lars Hallstadius of Westinghouse Electric Co., who kindly provided the raw materials for the entire MUZIC project; M. Blat and A. Ambard of EDF - R&D, who characterized the chemical compositions of the raw materials, and were entrusted with the cathodic hydrogen charging procedure and operation of the autoclaves; P. Frankel and K. Govender of the Materials Performance Centre, School of Materials, The University of Manchester, who trained the author in the use of synchrotron x-ray diffraction and TEM as well as demonstrating extensive experience and knowledge on the nature of the technique and subsequent analysis; E. Polatidis of School of Materials, The University of Manchester, who took turns with the author to make the most of the limited beam time at EDDI and the last and the most, Prof. Michael Preuss, Prof. Bob Cottis and Prof. Stuart Lyon of the Materials Performance Centre, School of Materials, The University of Manchester, my supervisors, who are in

charge of the entire project. The author could not have achieved any of the following without the support and guidance of the above: characterisation of the hydrogen charged material before autoclave corrosion, autoclave corrosion tests on hydrided and reference materials, characterization of the generated oxide via SEM, TEM, laboratory X-ray diffraction and texture measurements, synchrotron x-ray diffraction and proposal of a complete model for mechanisms behind transition and breakaway of zirconium corrosion.

The work of these authors is acknowledged here and inside the proposed publications respectively.

2 Literature Review

2.1 Overview

As the 40th element in the periodic table, zirconium has an atomic weight of 91.22. Pure zirconium has a density of 6.52 g/cm^3 and two allotropic modifications, the hexagonal close packed (hcp) alpha phase which is stable up to 862°C and the body centred cubic (bcc) beta modification which is stable from 862°C up to the melting point at 1845±15°C [1]. Zirconium possesses a combination of unique physical, chemical and nuclear properties, which makes it particularly suitable for use in thermal reactors. The material requirements for cladding material in water cooled reactors can be stated as follows [2-5]:

1. Mechanical strength and stability under severe stresses resulting from high thermal gradients.
2. Leakage reliability in high-temperature, high-pressure, corrosive, dynamic and radioactive systems.
3. Resistance to mechanical damage by radiation.
4. Limited formation of high activity products when exposed to nuclear reaction.
5. Adaptability to simple remote maintenance and repair plus an over all addition of a low neutron absorption cross section.

Due to its exceptional corrosion resistance, relative high strength at the service temperature of thermal reactors and a very low neutron absorption cross section of 0.18 barn [6], zirconium and zirconium alloys have been widely employed in the

heat-production core of nuclear reactors since the early 1950s. The main purposes for the use of zirconium are as follows [3, 7, 8]:

1. Provide permanent internal structure.
2. As an alloying element, increase the bulk or modify the properties of the fuel.
3. As a clad, protect the fuel and prevent contamination of coolant.

2.2 Zirconium and zirconium alloys

An extensive range of alloys has been developed to meet the requirements of different types of reactors. The low solubility of many alloying elements makes most zirconium alloys generally very dilute alloys. Alloying elements of zirconium can be conveniently catalogued in to five groups [9, 10]:

1. Alpha-stabilizers (raise the α - β transition temperature): Al, O, Sn, N, B.
2. Beta-stabilizers (decrease the α - β transition temperature): Nb, Ta, Th, U.
3. Eutectic and eutectoid: Ag, Be, Co, Cr, Cu, Fe, Mn, Mo, Ni, V, W, H.
4. Miscellaneous: C, Ge, Si.
5. Complete solid solubility: Hf, Ti.

Eutectoid elements such as molybdenum, tungsten, vanadium, chromium, manganese, iron, cobalt, nickel, and copper, with a large number of outer d electrons are expected to lower the α - β transition temperature and enlarge the beta phase region. Carbon is considered as an α stabilizer in some literatures. The effect of alloying elements on beta transition temperature is given in Figure 1 [10].

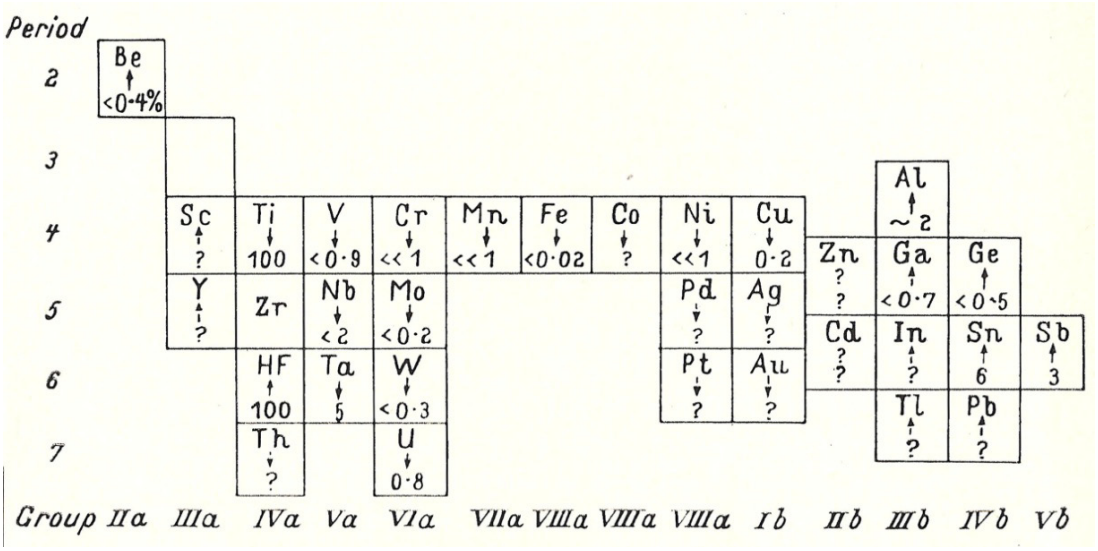

Figure 1: Solubility of alloying elements and their effects on the transformation temperature of zirconium. Arrow indicates direction of transformation shift upon alloying; dashed arrow indicates predicted shift, solid arrow indicates measured direction. Note: numbers below arrows indicate maximum solubility in alpha zirconium (atomic percent) [10].

There are two primary alloy systems, the zirconium-tin system favoured by the American and European users, and the zirconium-niobium system developed in the former USSR and Canada [7]. As the representation of the zirconium-tin system, Zircaloy family was first introduced into commercial light water reactor in the 1960s. Currently, the only Zircaloys still in service are Zircaloy-2 as fuel cladding in Boiling Water Reactors (BWRs) and Zircaloy-4 as fuel cladding, fuel components in Pressurised Water Reactors (PWRs) [11]. The tin addition was initially introduced into zirconium alloys to improve the poor corrosion performance caused by impurities such as nitrogen and carbon. This was not achieved by suppressing the largely diffusion controlled pre-1st transition oxidation kinetics, but by the synthesis of a more uniform thick oxide film that does not suffer from oxide spalling [12]. The improvement was accompanied by a generally earlier onset of the linear post-transition oxidation where diffusion no longer controlled the growth of oxide [13]. It was suggested that tin, which is soluble in zirconium, combined with other

alloying elements found in the Zircaloy family (chromium, iron and nickel), which are largely insoluble, assist the developments of a more uniform thick oxide and improve the overall corrosion performance [14]. Small intermetallic second phase particles (SPPs) accelerate corrosion of the slowly oxidising metal grains, flatten the stress distribution in the oxide, consequently cause less cracking and spalling of the oxide [14]. Modern manufacture processes of zirconium raw material have decreased the amount of impurities and therefore the requirement of tin has been reduced. Attempts have been made to lower the Sn content in the Zircaloy family to and below the ASTM range, resulting in improved corrosion performance [15-19]. Contradicting mechanisms relating tin content to both increased and decreased amount of tetragonal oxide phase have been suggested [15, 16, 19].

E110, M5 and Zr–2.5Nb are typical zirconium-niobium system alloys. While E110 and M5 are employed in PWRs for fuel cladding, Zr-2.5Nb is employed in HWRs for pressure tubes. The kinetic transition generally occurs later in zirconium-niobium system alloys than in zirconium-tin system alloys [20]. Correlations between corrosion resistance and distribution and size of SPPs similar to that in Zircaloys are also observed, where uniform distribution of fine iron-niobium SPPs are key to corrosion performance in PWRs [21]. Dilute zirconium-niobium alloys show good corrosion performance free from the effect of heat treatment since all niobium additions stay in solid solution [22]. Comparison within the group of 0.5-1.0 wt.% niobium containing alloys has demonstrated that corrosion performance improves with increasing niobium content, which is believed to be related to iron-niobium precipitations in the zirconium matrix [7].

A new alloy group combining both tin and niobium additions has been developed and selected as advanced cladding material by Westinghouse since the 1980s. The most widely used one of this group is ZIRLO^{TM}, which is generally employed in PWRs as structural and cladding materials. ZIRLO^{TM} has exhibited superior corrosion performance over Zircaloy-4 materials under typical PWR conditions [7, 11, 23-25].

For comparison, Table 1 summarises the nominal chemical composition of 6 typical zirconium alloys widely used as fuel claddings in water cooled nuclear reactors [11, 24, 26-32].

Table 1: Nominal chemical composition of typical zirconium alloys (wt. %) [11, 24, 26-32].

Element	Zircaloy-2	Zircaloy-4	ZIRLO^{TM}	Zr-2.5Nb	M5	E110
Sn	1.20-1.70	1.20-1.70	0.90-1.20	<0.01	—	—
Nb	—	—	0.98-1.0	2.40-2.80	1.00	0.97
Fe	0.07-0.20	0.18-0.24	0.11-0.1	<0.15	—	0.01
Cr	0.05-0.15	0.07-0.13	<0.05	<0.02	—	—
Ni	0.03-0.08	—	—	—	—	—
O	0.11-0.14	0.11-0.14	0.09-0.15	0.09-0.13	0.10	0.05

2.3 Corrosion of zirconium alloys

2.3.1 Background

Generally, zirconium is considered to have excellent resistance against acids and alkalis. It is superior to titanium and tantalum in alkalis. Even in acid zirconium shows excellent resistance with only exceptions to hydrofluoric acid, concentrated sulphuric and phosphoric acids [33]. Considering the corrosion resistance noted above, one would expect zirconium to perform similarly in aqueous environments (water and steams). However, important exceptions are worthy to be mentioned. It appears that pressurized water at elevated temperature (360°C for example) can be a highly corrosive medium, and inconsistent corrosion behaviours of zirconium alloys have been observed from complete disintegration in days to a few mg/dm^2 of weight gain in a year, depending on the alloying elements [33].

It was the demand from the nuclear industry which drove zirconium and its alloys beyond laboratories and minor usages such as photographers' flashbulbs and getter for electronic tubes. Applications in the chemical industry are still limited as zirconium alloys have yet to achieve any economic advantage over other corrosion-resistant alloys. The interest of this literature review concentrates on the aqueous corrosion of zirconium alloys in PWR environment where the formation of surface oxide film is the dominate mechanism.

2.3.2 Corrosion kinetics

The reaction of zirconium with water follows the equation below:

$$Zr + 2H_2O \rightarrow ZrO_2 + 2H_2 \qquad (1)$$

Note that almost all of the hydrogen atoms generated during this reaction are released back into the environment in the form of hydrogen gas, while all the oxygen is sustained in solid form as a thin film of oxide adherent to the surface of the material. It is hence convenient to use the oxidation weight gain as a direct gauge representing the thickness of the oxide film (15mg/dm^2 of oxidation weight gain ≈ 1 μm of oxide grown ≈ 0.66 μm of zirconium consumed [25, 34]). The corrosion kinetics can be divided into three stages:

Stage 1. The initial stage of the kinetics can be described as a pre-1st transition period with an approximately cubic rate law instead of the widely predicated parabolic rate law for a diffusion controlled process [3, 9, 35-45]. During this period, a thin, tightly adherent film of oxide with black appearance grows on the surface of the corrosion test piece. The oxide film has an almost uniform thickness across the surface of the corrosion test piece and gradually thickens in accordance with the near cubic rate law. The near cubic pre-1st transition corrosion kinetics can be described in the expression of the form:

$$\Delta W = K_p t^n \qquad (2)$$

where ΔW is the sample weight gain in unit of mg/dm^2, t is the autoclave exposure time in unit of days, n is the corrosion kinetics exponent and K_p is the rate constant that changes with temperature (360°C in this study) and alloy chemistry. Hauffe et al. explained that parabolic rate law is expected for a corrosion process controlled by either the bulk diffusion of oxygen through a perfect oxide [40] or by the crystallite boundary diffusion, which is

more rapid than bulk diffusion [46, 47]. This is only true if the size and shape of the oxide grains remain constant as the corrosion progressed. A reduction in grain boundary area, such as epitaxial growth of the oxide grains, would slow down a process dominated by crystallite boundary diffusion and bring about near cubic rate growth. The columnar oxide grain structure observed via electron microscopy (Figure 2 [48]) supports this argument by demonstrating the preferential growth direction during oxidation. A histogram summarising actual measured exponents of the near cubic rate law is presented in Figure 3 [48], where the variations between individual measurements have been attributed to the variation during the development of the columnar grain structure.

Stage 2. At the end of the cubic rate law period, a sudden transition involving sharp increase in corrosion rate occurs and is followed by near cubic rate growth again. This phenomenon is termed as 1^{st} transition and further followed by series of successive cycles of transition. An actual weight gain diagram showing this cyclic nature is displayed in Figure 4 [24]. Note that although the post-1^{st} transition corrosion follows the near cubic rate law of the initial cycle, data suggests that time to transition decreases with each cycle [3, 9, 24, 37, 39-41, 49-53]. The initiation of 1^{st} transition is accompanied by the appearance of small grey areas on the black oxide surface. As 1^{st} transition progresses, the grey regions then grow bigger, spread across the surface and eventually form a uniform layer of grey oxide covering the entire surface of the corrosion test piece. The observed

stratification in the oxide films (Figure 6 [25]) has been linked to this cyclic nature of the corrosion kinetics [24, 37, 43, 49, 54, 55].

Stage 3. As can be clearly seen from Figure 5 [34], after further prolonged exposure, corrosion accelerates to an approximately linear rate. The onset of such period is termed as breakaway. The linear rate law can be described by an expression of the form:

$$\Delta W = K_L t + C \tag{3}$$

where ΔW is the sample weight gain in unit of mg/dm^2, t is the autoclave exposure time in unit of days, K_L is the linear rate constant in unit of mg/dm^2/day and C is the intercept of the weight gain at zero exposure time.

Investigation on the oxide featured by Godlewski et al. [56] indicates that the oxide is a mixture of monoclinic and tetragonal ZrO_2 phase. While the monoclinic phase is generally the stable phase between room temperature and 360°C, the tetragonal phase is believed to be stabilized by localized stresses, grain size or dissolved alloying elements. The grain morphology of the oxide is a mixture of equiaxed grains and columnar grains. Equiaxed grains are high in tetragonal content while columnar grains are high in monoclinic content [25, 57] when studied by TEM. When the oxide is formed in Lithiated water, degradation of corrosion resistance is observed. It is proposed that lithium hydroxide avoids the formation of an inner barrier layer by preventing the columnar structure from developing. It is believed that equiaxed oxide grains formed during corrosion are less protective [57]. Considering that oxide tends to develop cracks and porosity during growth [58, 59], the accumulation of tetragonal oxide near the metal/oxide interface and the mixture of equiaxed and columnar grains [24, 37] have been linked to the transition

in the corrosion kinetics. Un-oxidised Second Phase Particles (SPPs) in the parent metal matrix are usually incorporated into the oxide layer, and remain metallic for a certain period before they undergo oxidation. This is also associated with the breakaway of corrosion kinetics [60]. The increased rate of oxidation after breakaway as well as the previous cyclic nature of post-1st transition can be observed in Figure 5 [34].

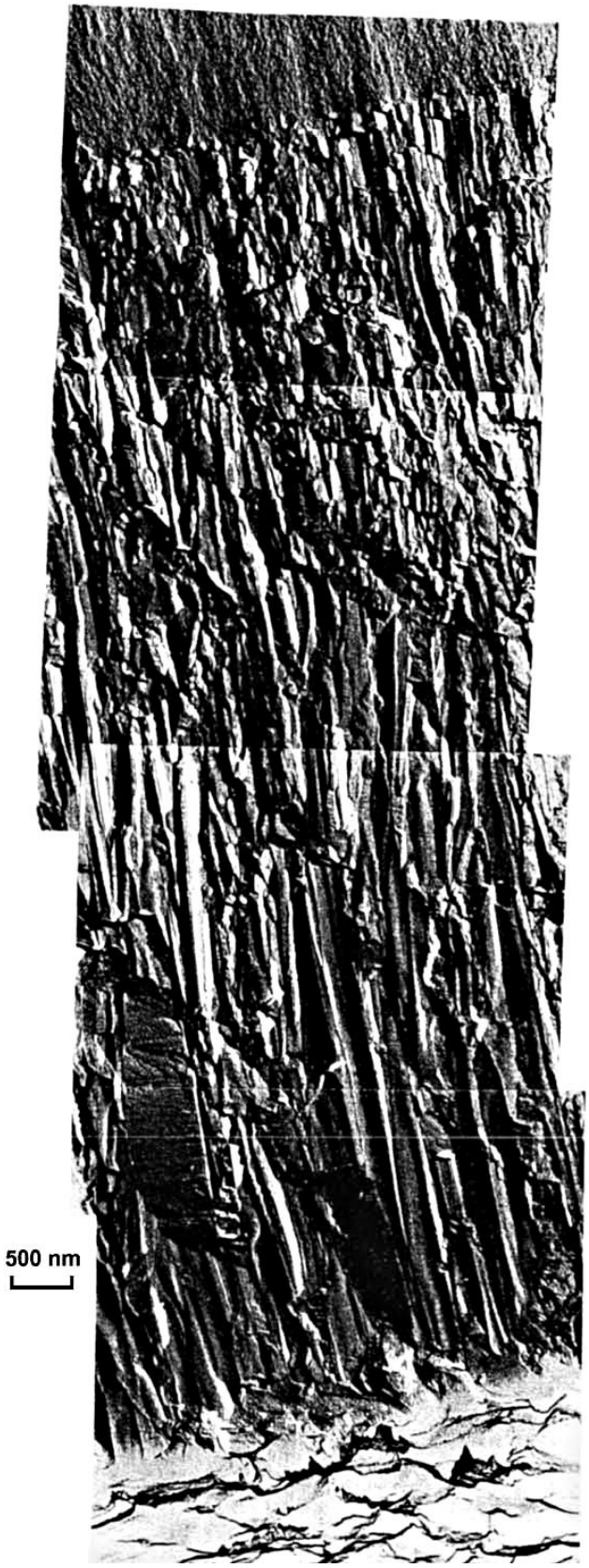

Figure 2: Columnar oxide crystallite growth on Zr after 24hr in 600°C air [48]. Oxide-metal interface is at bottom. Micrograph is from a two stage (Formvar/carbon) replica of the oxide fractured (after dissolution of the Zr matrix) by gluing the oxide to a glass microscope slide, scribing the back surface of the slide, and fracturing the composite of slide and oxide.

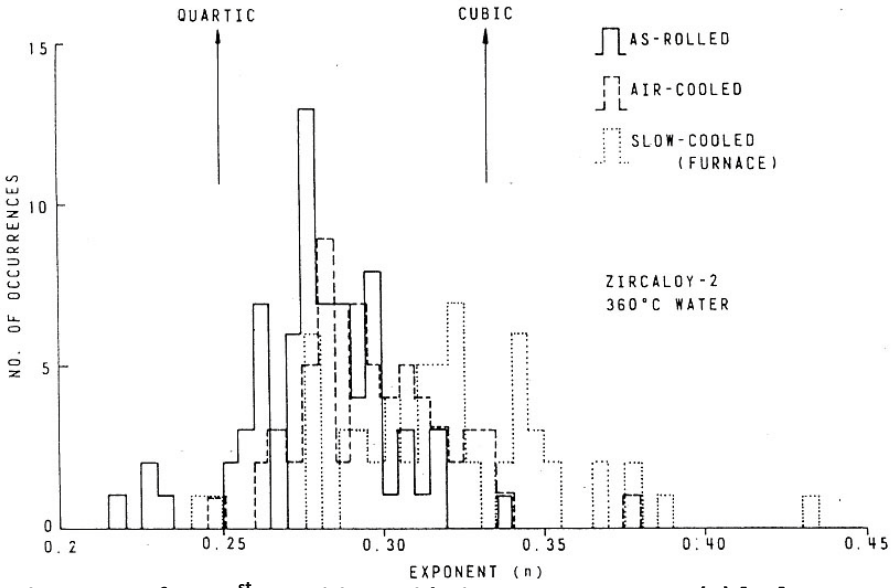

Figure 3: Histogram of pre-1st transition oxidation rate exponents (n) [48].

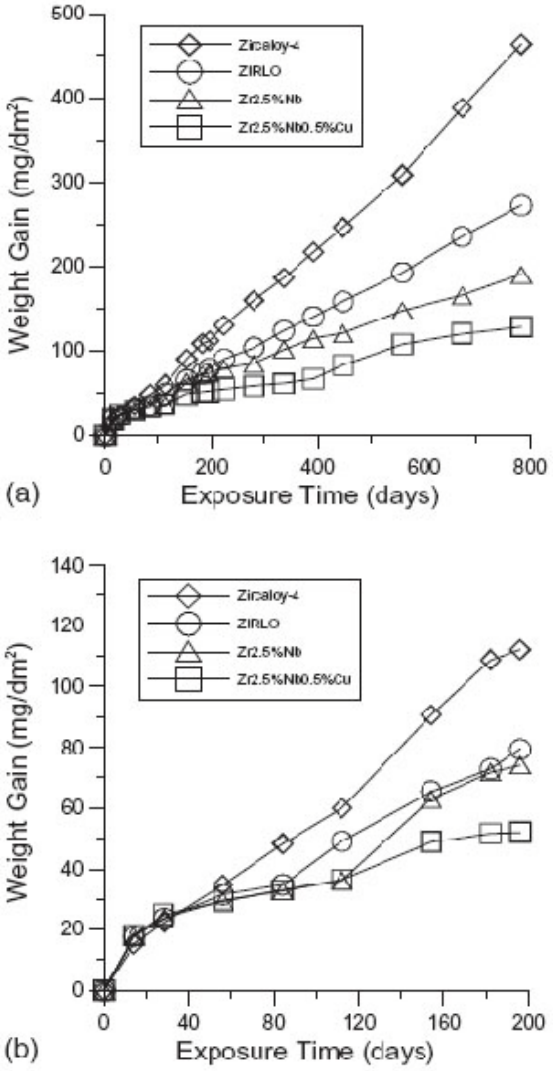

Figure 4: Corrosion weight gain profile of Zircaloy-4, ZIRLO™, Zr-2.5%Nb and Zr-2.5%Nb-0.5%Cu in pure water at 360°C (a) after 784 days and (b) showing initial 200 days [24].

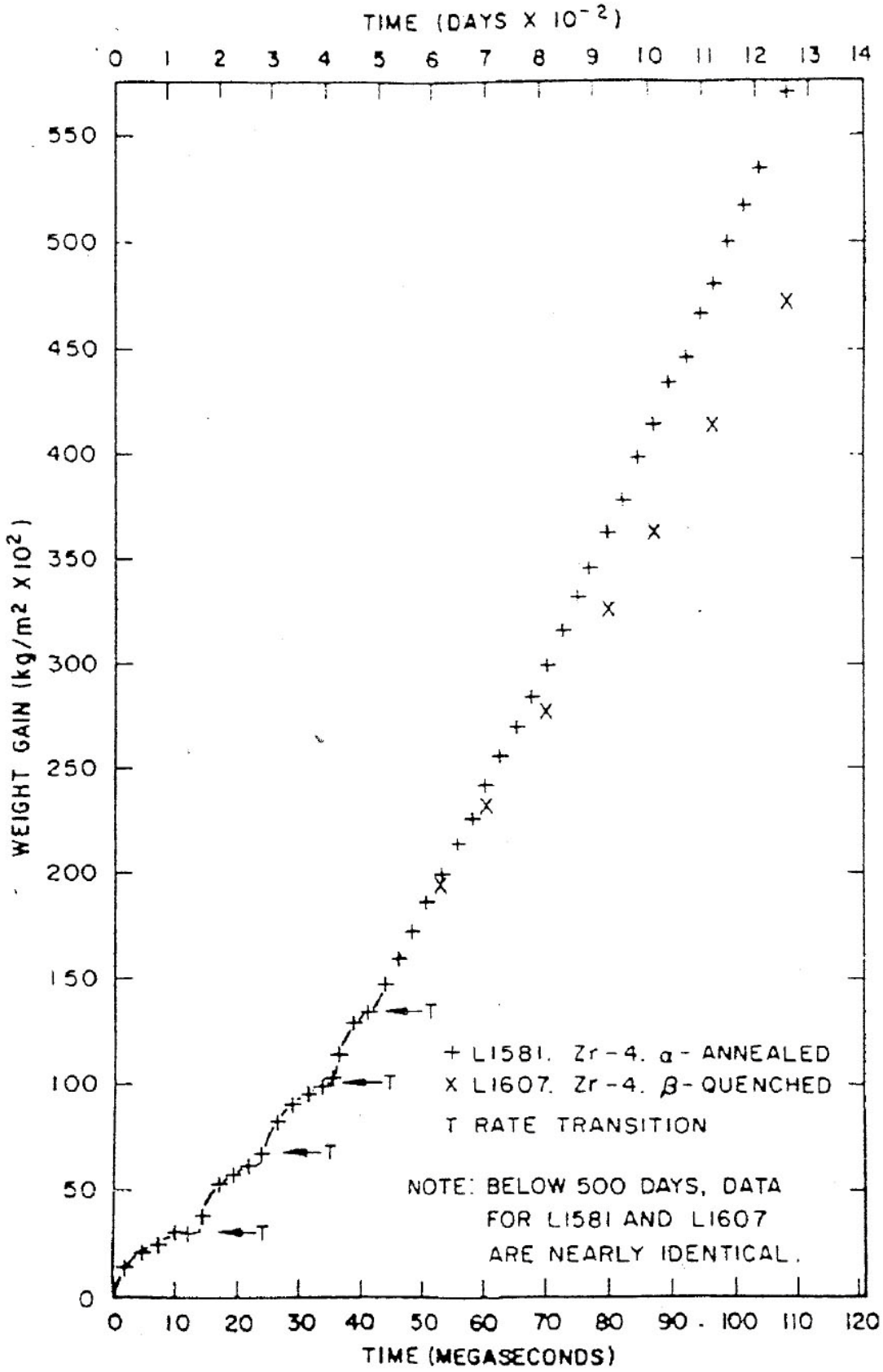

Figure 5: Cyclic nature and breakaway of post-transition corrosion of Zircaloy-4 in 360°C water [34].

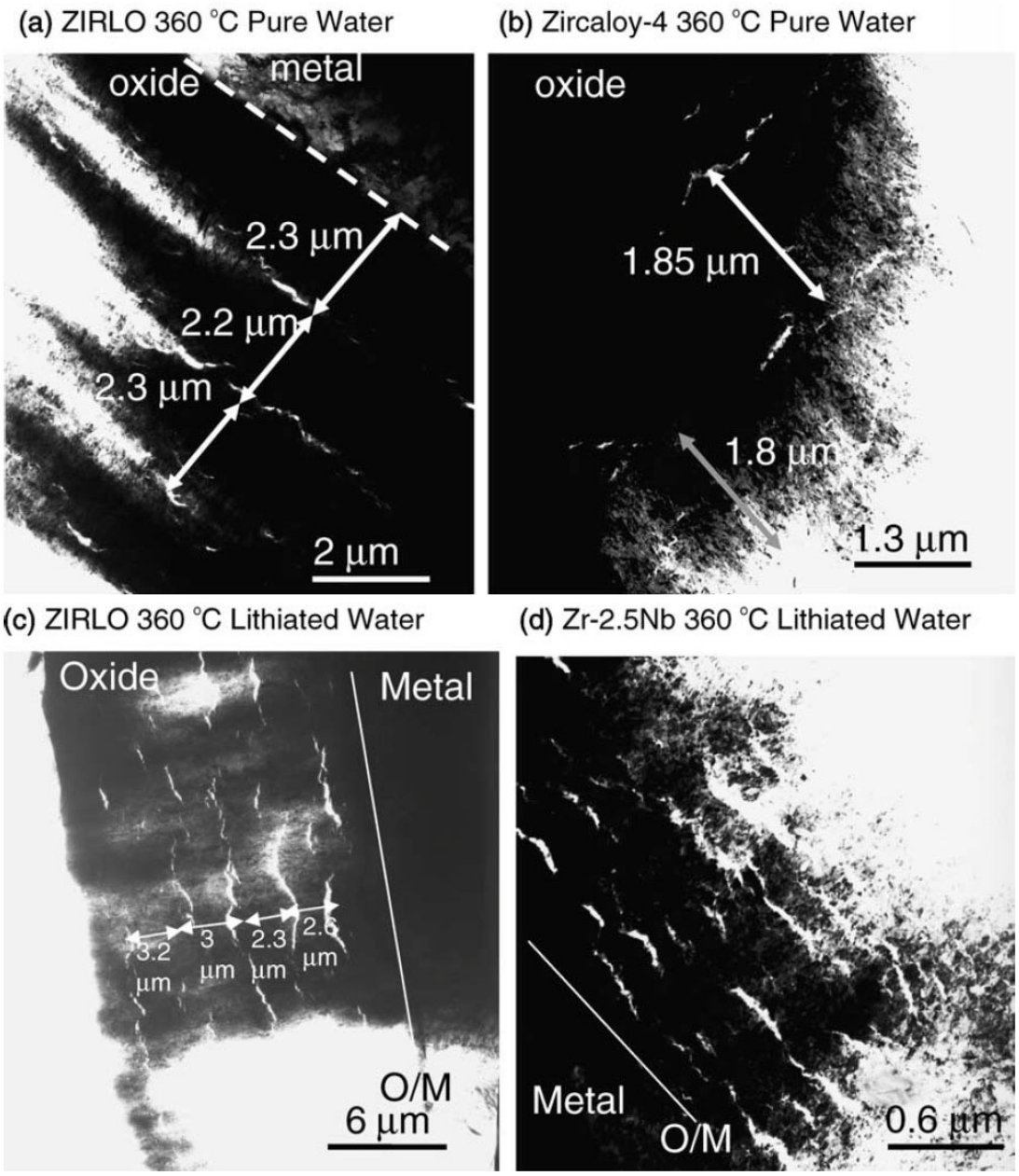

Figure 6: Low magnification bright-field electron micrographs in (a) ZIRLO, (b) Zircaloy-4 alloy oxides formed in 360°C pure water environment for 784 days, and (c) ZIRLO, (d) Zr-2.5Nb in 360°C pure Lithiated water environment for 369 and 3 days, respectively [25].

2.3.2.1 Effect of temperature upon linear corrosion kinetics

Plotting the weight gain of post-breakaway corrosion kinetics as a function of the exposure time using Equation 3 produces a straight line with K_L as the slope. The temperature dependence of the linear rate constant K_L has been demonstrated to follow the Arrhenius-type expression of the form [34]:

$$K_L = Bexp[-Q_L/RT] \tag{4}$$

where B is an empirical constant in unit of mg/dm^2/day, Q_L is the activation energy for the linear region of oxidation in unit of J/mol, R= 8.314 J/(mol K) and T is the absolute temperature in unit of K. A linear relationship between ln(K_L) and 1/T is established. Combining Equation 3 and Equation 4 brings about the expression below relating the linear region oxidation weight gain with both exposure time and oxidation temperature:

$$\Delta W = \{Bexp[-Q_L/RT]\}t + C \tag{5}$$

The above expression is further fitted with data collected on autoclave corrosion studies and the empirical expression for linear corrosion kinetics is given by Hillner [34]:

$$\Delta W = \{1.12 \times 10^8 exp[-12529/T]\}t \tag{6}$$

where all the terms have been defined previously. The empirical constant B and activation energy Q_L are in agreement with the reported value for the diffusion of oxygen in zirconia [61]. Maroto et al. further demonstrated that the linear corrosion kinetics can be fitted with the kinetics of the diffusion of oxygen vacancies through bulk oxide [62].

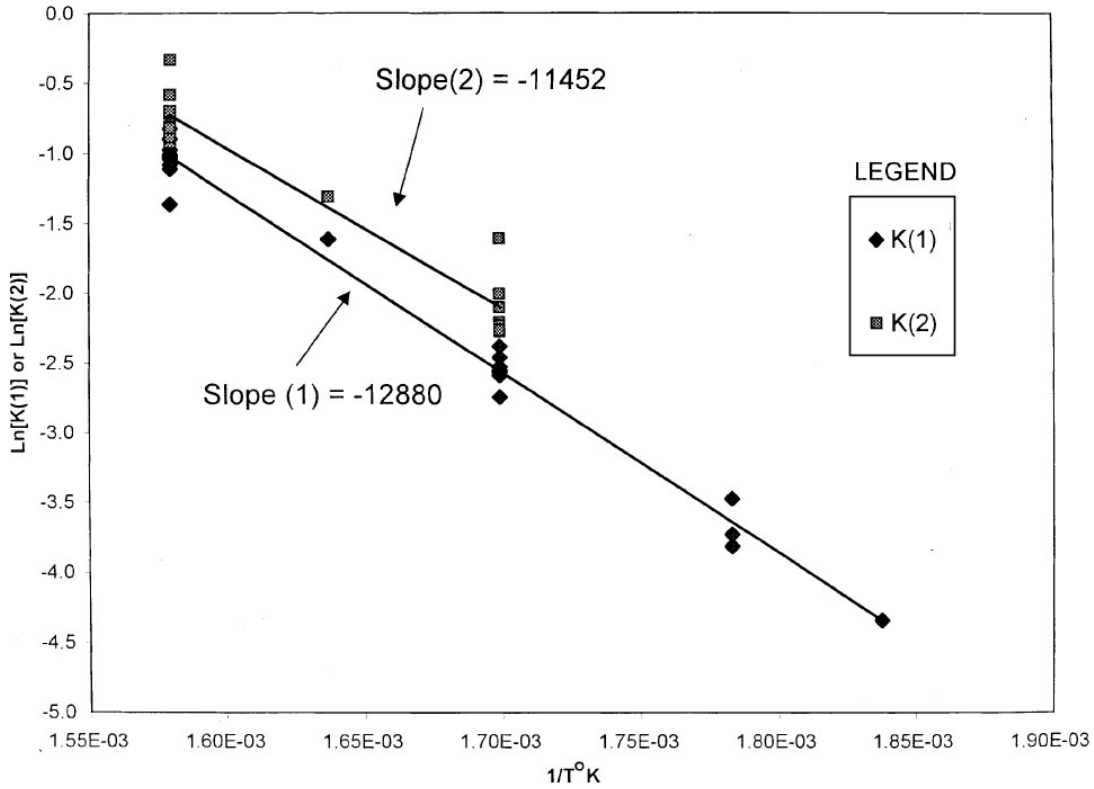

Figure 7: The natural logarithm of the linear rate constants as a function of the inverse absolute temperature (K). Weight gain data collected on autoclave oxidised Zircaloy-4 materials [34].

2.3.2.2 Effect of impurities

Impurity contents in metals have a remarkable effect on the corrosion resistance of zirconium in aqueous environment at elevated temperature. The most concerning impurities can be picked up during processing and service. In attempts to study the late stage of corrosion and break away corrosion within a reasonable time span, several important impurity elements have been investigated systematically. The results are reviewed here.

1. Nitrogen affects the performance of zirconium pronouncedly even in a tiny amount. For instance, fewer than 40 wt.ppm of nitrogen can lead to breakaway within a short time, and transition time decreases with increasing nitrogen content. At slightly higher nitrogen content, specimens

even disintegrate completely. Consequently an empirical limit of 50 wt.ppm of nitrogen is proposed, regardless of the production problems to maintain such limit. This deleterious effect was counteracted by the addition of tin, which in turn facilitated the zirconium-tin system alloy's development. The nitrogen effect on corrosion of zirconium is presented in Figure 8 [63]

2. Carbon can adversely accelerate the corrosion of zirconium due to preferential corrosion of carbides. Microscopy studies have revealed complete oxidation of carbide in a high-carbon alloy whereas the matrix stays relatively unattacked. Using cold work to break up and disperse the carbides can considerably increase the corrosion resistance of carbon-contaminated zirconium [64]. Tin additions are beneficial to reduce the effect of carbon on corrosion rate, but it is still preferable not to have carbon contamination.

   The corrosion rate increases with carbon content and breakaway occurs in comparatively short time once carbon exceeds 0.1 at.%. Consequently maximum of 400 wt.ppm of carbon is proposed for applications which require good corrosion resistance. The carbon effect on corrosion of zirconium is shown in Figure 9 [64].

3. Titanium has a range of content from 0.1 to 4 at.% in which minimum corrosion resistance is observed. Either below or above this range, zirconium-titanium alloys exhibit good corrosion performance. Adding 0.2 wt.% (<0.1 at.%) of titanium into Zr-1 wt.%Nb leads to a corrosion weight gain ≈1200 mg/dm^2 after one day of autoclave exposure at 360°C [65], while

the typical weight gain for this alloy is around 60 mg/dm^2 after 180 days of autoclave exposure [66]. Both titanium itself and its carbides are quite corrosion resistant. Consequently a maximum 80 wt.ppm of titanium is suggested [9].

4. Aluminium exhibits pronounced harmful effects with concentrations higher than 0.1 at%. Hence a maximum 0.01 at.% is proposed. Tin counteracts its effects [9, 67].
5. Hydrogen was originally considered to be a non-harmful content based on early short-time exposures. It was later identified that 100 wt.ppm of hydrogen causes appreciably faster corrosion than 50 wt.ppm [9].
6. Oxygen presence of 0.5 wt.% only slightly affects corrosion resistance but 1 wt.% (far exceeding actual quantities present in ductile metal) is reported to have severe effects. It is also worth mentioning that in PWRs, a critical oxygen concentration in the coolant results in dramatic reduction of hydrogen pick up, whereas smaller amount of oxygen has only minor effect on the reduction of the hydrogen uptake [68].
7. Some other impurities are harmful only when present in sufficient amount: calcium 0.0025 at%; magnesium 0.0020 at.%; chlorine 0.0015% and silicon 0.0020%. Hafnium, copper and tungsten are innocuous, while iron, chromium and nickel are beneficial [33].

It is important to note that while the effect on corrosion performance of certain elements in zirconium is known, there is little knowledge of the root cause for such effects.

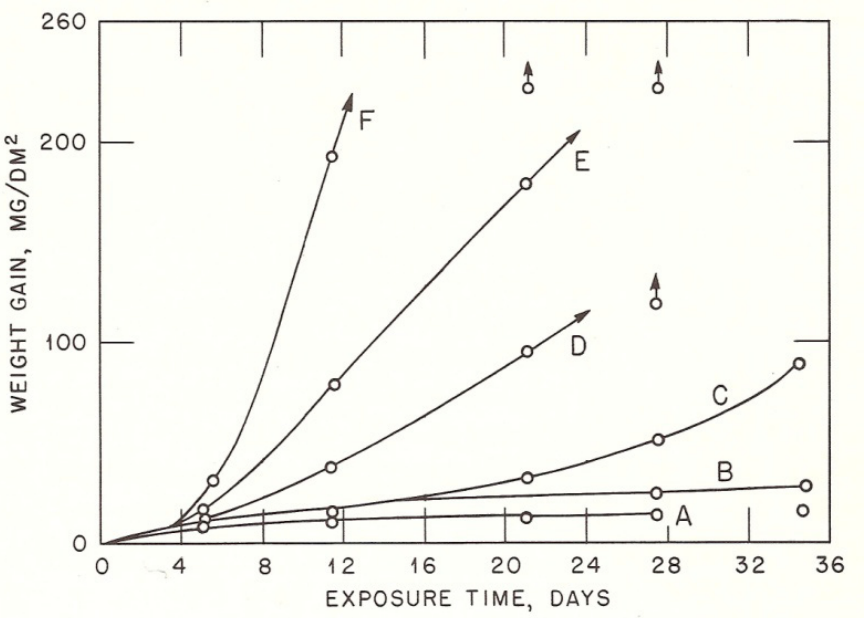

	Nominal	Analyzed		Nominal	Analyzed
A	30	30	D	70	40
B	40	30	E	80	90
C	50	30	F	140	130

Figure 8: Effect of nitrogen content upon the corrosion resistance of crystal-bar zirconium. Samples were made by powder-metallurgy techniques; 316°C water. The nitrogen content in parts per million is tabulated above in wt.ppm [63].

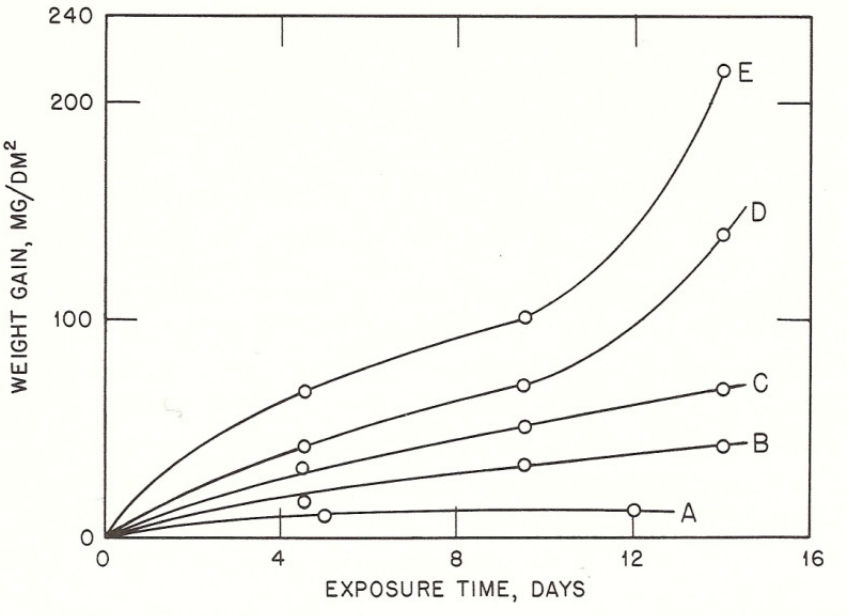

	Nominal	Analyzed		Nominal	Analyzed
A	300	300	D	1300	900
B	700	400	E	1500	1000
C	1100	600			

Figure 9: Effect of carbon content upon the corrosion resistance of crystal-bar zirconium. Samples were made by power-metallurgy techniques; 316°C water. The carbon content in parts per million is tabulated above in wt.ppm [63].

2.3.3 Oxide phases of zirconium

Phase equilibria diagram for the zirconium-oxygen system is given in Figure 10 while the structure data of the involved phases is presented in Table 2 [69]. Zirconia has three stable polymorphs at atmospheric pressure: the monoclinic phase at room temperature, the tetragonal phase at intermediate temperature and face-centred cubic phase at high temperature.

Table 2: The zirconium-oxygen system structure data [69].

Phase	Composition: at.% of Oxygen	Symmetry	Space group
α-Zr	0 ~ 35	hexagonal	P63/mmc
β-Zr	0 ~ 10.5	Body-Centred Cubic	Im $\bar{3}$ m
α-ZrO_{2-x}	61 ~ 66.6	Monoclinic	Fm $\bar{3}$ m
β-ZrO_{2-x}	66.5 ~ 66.6	Tetragonal	$P4_2/nmc$
γ-ZrO_{2-x}	66.6	Face-Centred Cubic	$P2_1/c$

Monoclinic zirconia is the predominant oxide phase generated during the oxidation in PWRs' environment while tetragonal zirconia is much less in phase fraction and has the tendency of accumulating near the oxide/metal interface, i.e. the oxidation progression front [24, 52, 55, 70-72]. The fully reversible tetragonal-to-monoclinic phase transformation is considered to be martensitic in nature and is associated with a 3~5% volume expansion [73-75]. Generally speaking, the tetragonal phase that forms becomes unstable in typical PWR environment and has the tendency of transforming into monoclinic zirconia. However, as demonstrated in Figure 11 [76], the transformation temperature is greatly affected by the presence of compressive stress. The δ-ZrO_2 phase in Figure 11 is a high-pressure phase of orthorhombic symmetry. With increasing temperature, the orthorhombic phase transforms to

tetragonal. A highly compressive stress state generated during corrosion (volume expansion from zirconium to zirconia, Pilling-Bedworth ratio = 1.56 [35, 77]) is expected in the oxide. The compressive stress therefore stabilises the metastable tetragonal zirconia [50, 55, 78, 79], and should also result in a balancing tensile stress in the metal phase [52, 55, 80]. Note that compressive stress alone might not be sufficient to stabilise the tetragonal zirconia to room temperature. Other potential contributors to the stabilisation include tetragonal crystal size and impurities in the oxide [81-84]. It has been suggested that equiaxed tetragonal grains larger than the thread hold size of 30 nm depend on the stabilisation provided by the compressive stress [15].

Under specific conditions such as added W or an O deficiency, the high temperature cubic zirconia structure has been found to exist in metastable state at room temperature. These contributing factors required to stabilise the cubic phase are not presented in PWRs or corrosion autoclaves. Small volume fraction of the cubic phase has been detected via X-ray diffraction technique during high temperature oxidation experiments (up to 3000K in reducing atmosphere [85]). Generally speaking, the metastable phase transforms either directly or through a gradual transformation sequence into the stable monoclinic phase [69, 86].

The tetragonal oxide phase tends to accumulate near the oxide/metal interface, as reported by researchers using laboratory X-ray diffraction, Raman spectroscopy and HRTEM [52, 55, 70-72]. Further investigation via high energy synchrotron X-ray diffraction even recorded a periodic intensity variation of a tetragonal reflection as a function of the location of measurement inside the oxide layer. The variation of

intensity acts as an indirect index for the amount of tetragonal phase present in the oxide. The appearance of higher tetragonal amount corresponds to the stratification inside the oxide film [24].

Rather than supporting the accumulation of tetragonal phase near the oxide/metal interface, Godlewski et al. observed with Raman spectroscopy that tetragonal phase is distributed through the entire thickness of the oxide film before 1st transition, whereas after the 1st transition it is only found in the inner region of the oxide [56]. Further investigation by Godlewski et al. indicated that tetragonal fraction not only decreases at the 1st transition, but also increases again until 2nd transition and decreases repetitively [52]. Other studies either supported this abrupt decrease of tetragonal amount at/near transition/transitions [87] or proposed a smoother decrease with no sudden evolution associated with the transition [15, 88, 89].

Tetragonal oxide grains are usually associated with equiaxed grains which are generally smaller than monoclinic grains which are associated with columnar grains [25]. Observation by Wadman et al. [90] indicated that the outmost layer of oxide film, effectively the oldest part of the oxide, is a mixture of equiaxed monoclinic grains, equiaxed tetragonal grains, columnar monoclinic grains and very few amount of columnar tetragonal grains. Porosities were located at the end of such columnar grains, and associated with the tetragonal to monoclinic phase transformation [90-92]. The tetragonal to monoclinic phase transformation of zirconium dioxide is believed to be diffusionless and martensitic in nature, accompanied by 3-5 % volume expansion [73]. Electron diffraction revealed an

orientational relationship between the two oxide phases: $\{\bar{1}11\}$ and $\{111\}$ reflections of monoclinic phase // $\{111\}$ reflection of the tetragonal phase [16]. To date, the exact role of tetragonal phase during corrosion still remains elusive since contradictive observations have been made relating higher tetragonal phase fraction with either deteriorated [15, 16, 24, 81, 93] or improved corrosion resistance [94, 95]. Most investigations of the tetragonal phase have been carried out by creating cross-sectional samples and therefore creating a free surface. Since at least some of the tetragonal phase is expected to be stress stabilised, the question remains if any of such grains are still present when a free surface is generated.

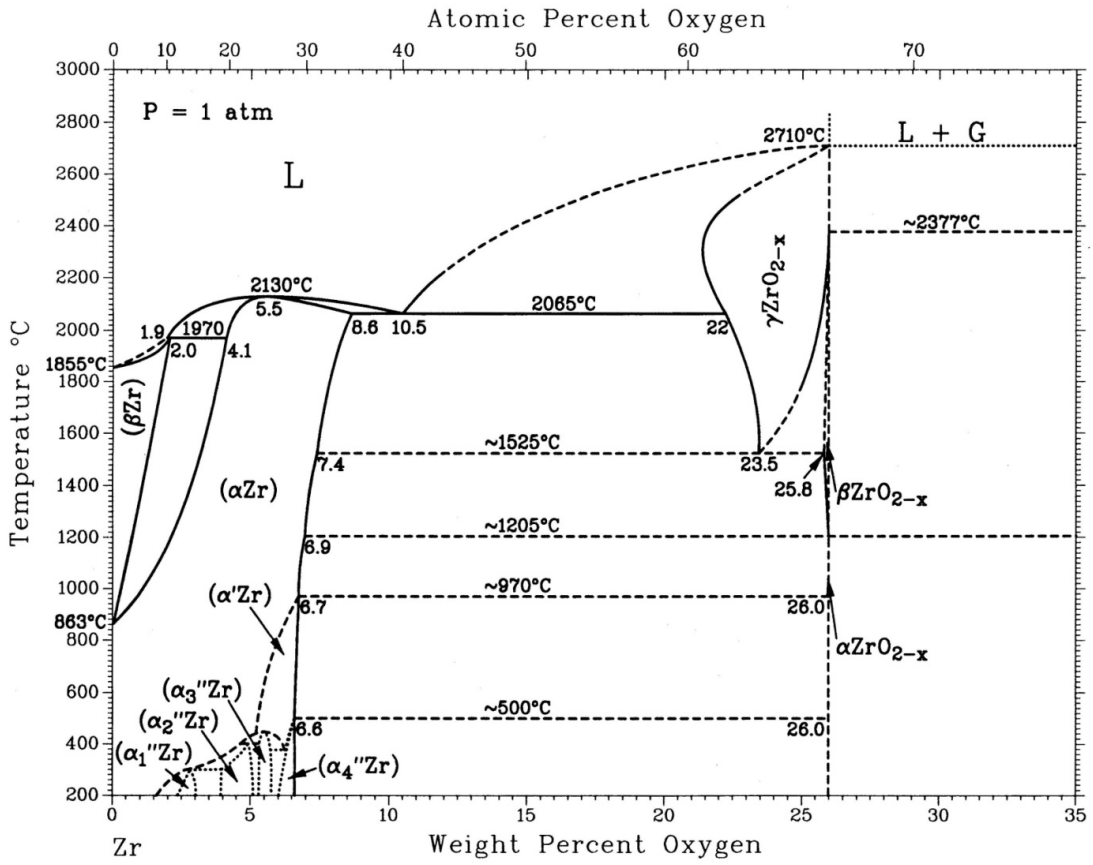

Figure 10: The zirconium-oxygen system phase diagram [69].

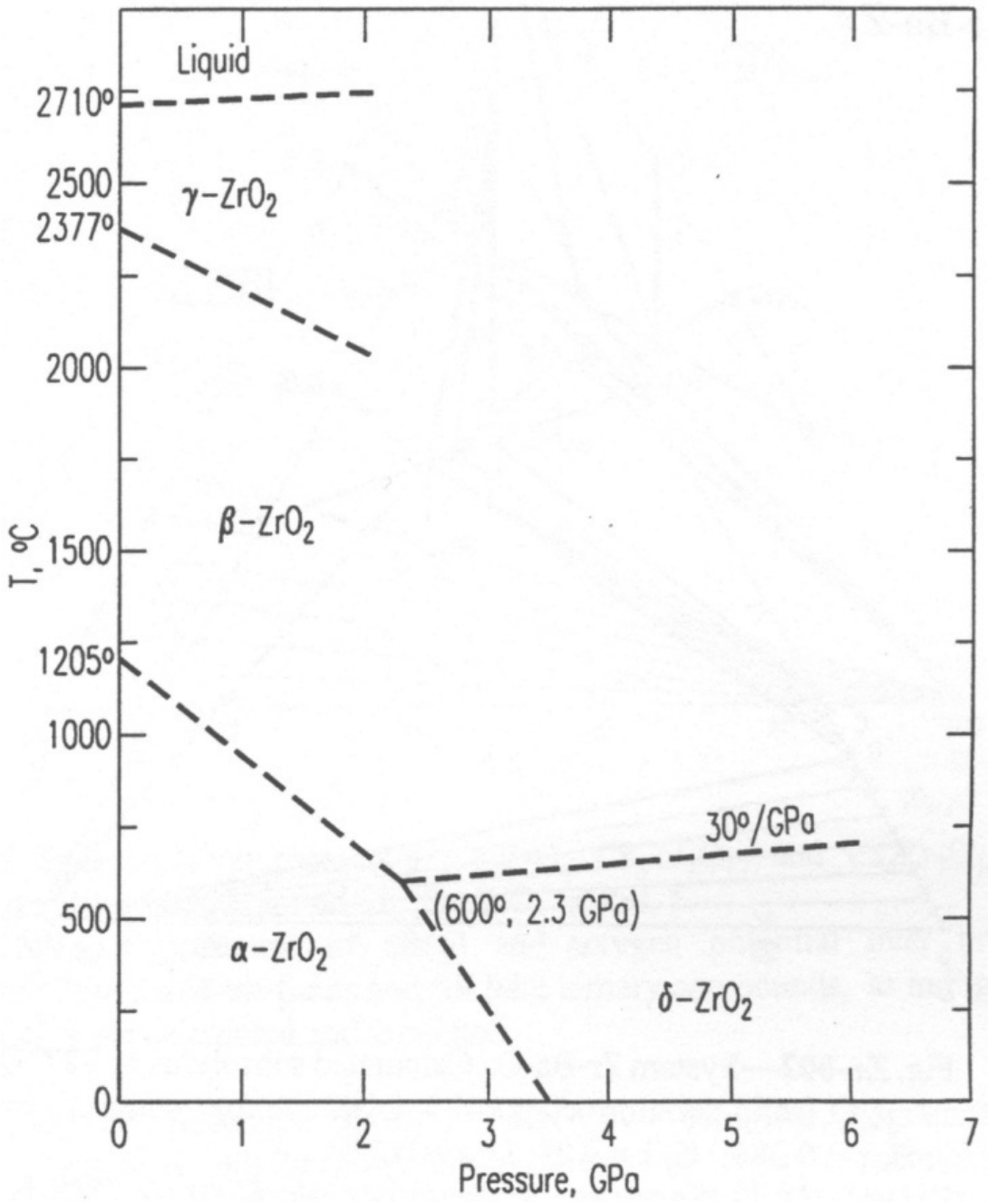

Figure 11: Pressure-temperature equilibrium phase diagram of zirconium dioxide [76].

2.3.4 Corrosion mechanisms

2.3.4.1 Pre-transition corrosion mechanism

Based upon the similarity between the oxidation of zirconium in oxygen and in water, it has been proposed that the oxide grows by the inward diffusion of oxygen ions through a vacancy mechanism, and that zirconium oxide has an anion-defect type lattice, Figure 12 [96]. Acting as the rate-controlling process, the vacancy mechanism is activated by the exchange of oxygen ions with vacancies. Vacancies and electrons move from the metal/oxide interface to the oxide/media surface, where one oxygen-ion vacancy, two electrons and one water molecule react to form one oxygen ion and two hydrogen ions. The oxygen ion then diffuses inwards. This vacancy diffusion mechanism will continue until a certain critical oxide thickness is reached corresponding to the transition and/or eventually breakaway [96]. The mechanism determining the transition and/or breakaway remains unclear, while hypothesis exists: micro-cracks might form due to either the lattice-mismatch between metal and oxide or the transformation between tetragonal and monoclinic modifications of zirconium dioxide (ZrO_2), which then increase the corrosion rate by acting as diffusion short cuts [97].

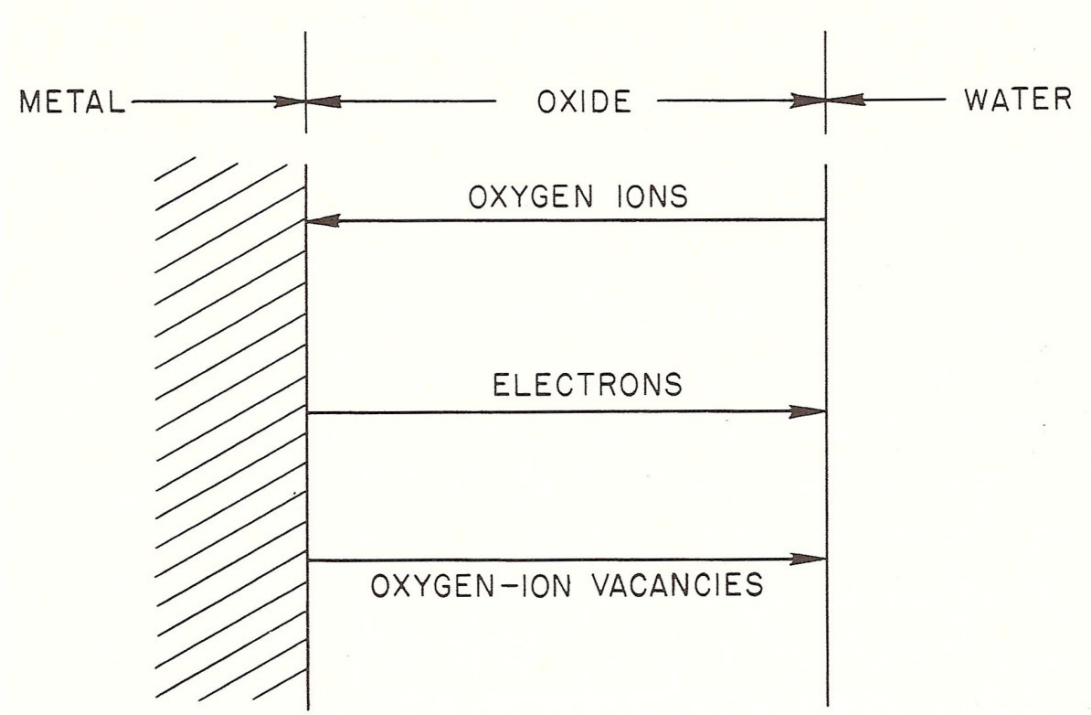

Figure 12: Schematic representation of diffusion of oxygen ions, electrons and oxygen-ion vacancies in the zirconium dioxide lattice during corrosion. In addition, hydrogen also diffuses through the oxide as ion or through discontinuities as molecule [96].

Consider situation (a) in Figure 13 [9]: one oxygen-ion vacancy is linked to two neighbouring zirconium ions whose valences have been altered to +3, hence any foreign ions that add electrons to the lattice tend to decrease the concentration of oxygen-ion vacancies. Any pentavalent and hexavalent substitutional cations, any monovalent substitutional anions, or any interstitial cations will decrease the concentration of vacancies. On the other hand, monovalent, divalent, and trivalent substitutional cations and trivalent anions will increase the concentration [98]. The diffusion rate of oxygen-ions and the corrosion rate are controlled by both the concentration and mobility of the vacancies. As shown in Figure 13 (b), by introducing nitrogen anions, additional vacancies are generated. Such vacancies are less mobile as they must be linked to nitrogen anions, but still, the over-all effect will increase the diffusion rate.

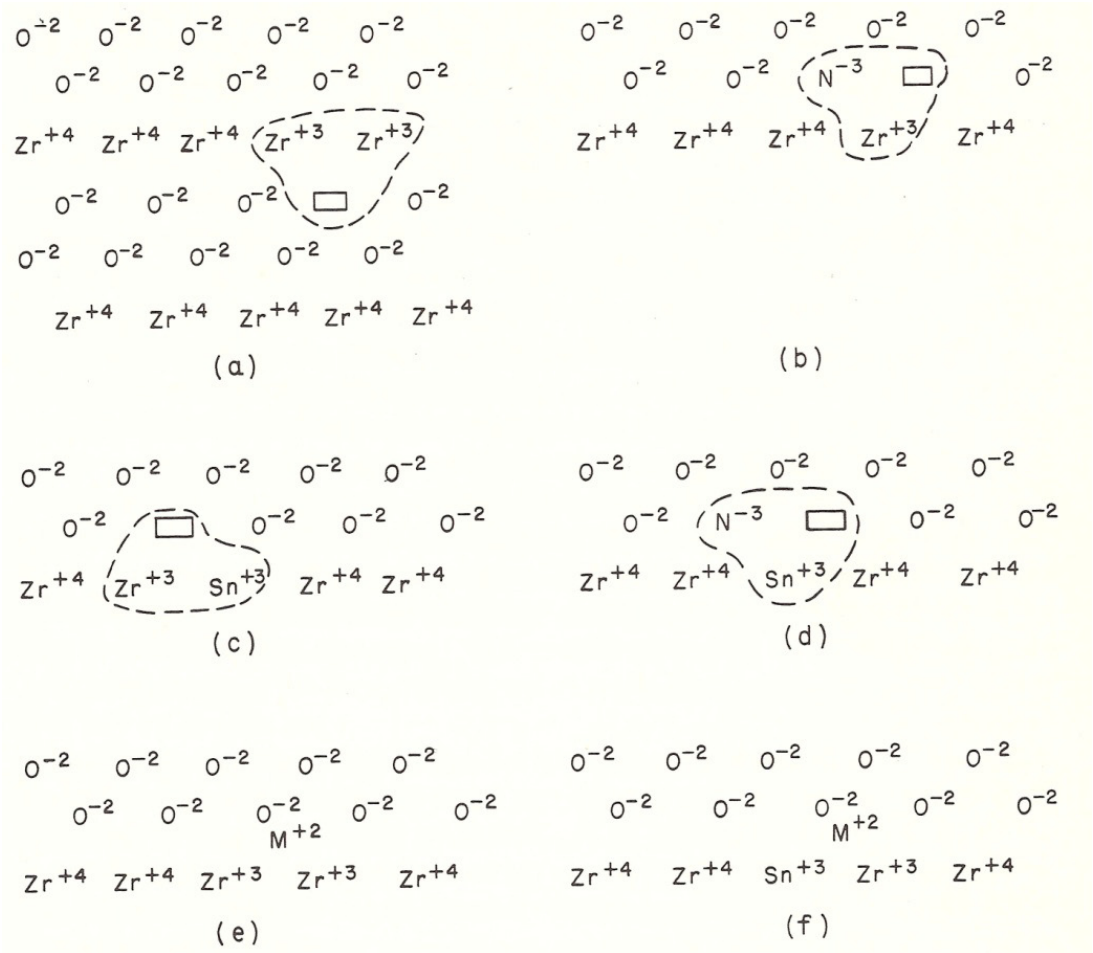

Figure 13: Schematic representation of anion type vacancies in zirconium dioxide, (a) normal anion vacancy with redistribution of charge, (b) anion vacancy produced by the presence of nitrogen anion in lattice, (c) anion vacancy produced by the presence of tin cation in lattice, (d) anion vacancy due to nitrogen anion trapped by tin cation, (e) concentration of anion vacancies decreased by interstitial cation and (f) concentration of anion vacancies decreased due to tin cation and interstitial cation [9].

The effect of tin addition is demonstrated in Figure 13 (c) and (d), an extra anion vacancy is introduced neighboring a tin cation. Note that the energy of group Zr^{+3}, Sn^{+3} and O^{-2} is lower than that of the group Zr^{+3}, Zr^{+3} and O^{-2} of Figure 13 (a), and the ionic radius of Zr^{+4} and Sn^{+4} is nearly the same [96]. The mobility of anion vacancies will be reduced as Zr^{+3} is virtually immobile. Meanwhile, anion N^{-3} tends to stay ambient to Sn^{+3} and O^{-2}. In both conditions, the mobility of the vacancy and the corrosion rate are reduced. Figure 13 (e) and (f) describe the effect of

interstitial cations on vacancies, and their interaction with tin cations. The concentration of vacancies in both cases is reduced.

It has been previously discussed that a parabolic rate law is expected for a corrosion process either controlled by the bulk diffusion of oxygen through a perfect oxide [40] or by the crystallite boundary diffusion, which is more rapid than bulk diffusion [46, 47]. Decades of researches have demonstrated that a nearer to cubic rate law is expected for pre-1st transition stage of the corrosion [3, 9, 38-45]. This leads to the subsequent suggestion that pre-transition oxide is not a perfect diffusion barrier. Dawson et al. [99] reported that oxidation of Zircaloy-2 in oxygen and water vapour does follow the parabolic kinetics, though only for the initial hundred nm of oxide thickness. Oxidation then follows the cubic rate law until transition occurs. The following mechanisms have been suggested:

1. A compressive stress state in the oxide is generated due to the high Pilling-Bedworth ratio of 1.56 [35, 77]. The compressive stress increases with the progression of oxidation, making the diffusion of oxygen more difficulty by compressing the oxide lattice [100-102]. This effect will influence the diffusion of oxygen through bulk of the oxide rather than diffusion through the crystallite boundary.
2. Since the crystallite boundary diffusion is more rapid than bulk diffusion of oxygen, a reduction of the crystalline boundary area will facilitate the cubic rate law. As demonstrated previously in Figure 2 and schematically in Figure 14 [23], at the initial stage of oxidation, the thin oxide layer is composed of small roughly equiaxed crystallites. A preferential growth of the oxide along

the oxidation progression direction leads to a columnar oxide crystallite structure and a reduction of crystalline boundary area. The driving force for this structure evolution is also the large compressive stress generated during corrosion. Since the thickness of such oxide layer is very small compared with the thickness of the actual corrosion test piece, a biaxial stress state is expected [55].

3. Random formation of cracks at or near the oxide/metal interface has also been reported to reduce the oxygen diffusion rate [99, 103].

It must be mentioned that other observations on materials oxidised in conditions other than PWR services environment (i.e. 800°C in air or steam or low pressure oxygen) have demonstrated parabolic rate law. Those conditions are outside the scope of this PhD study.

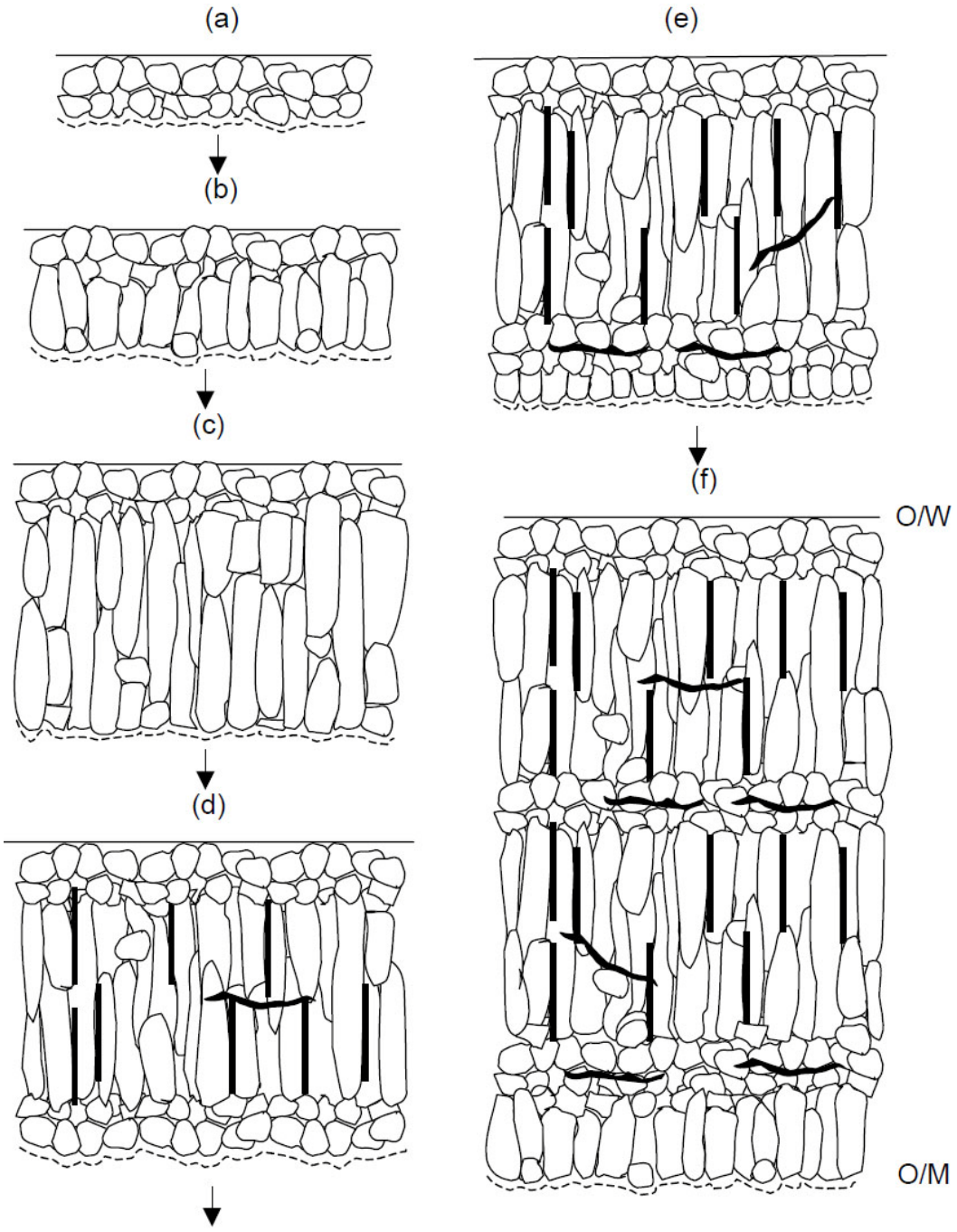

Figure 14: Schematic description of the proposed mechanism for advancement of the oxide layer based on the experimental observations. Successive cartoons indicate successive snapshots of the advancement of the oxide layer and of the microstructure of the oxide as a function of overall oxide thickness and distance from the oxide-metal interface [23].

2.3.4.2 Breakdown of the protective oxide layer

Oxide thickens during the progression of the pre-1st transition stage, and the corrosion rate slows down, which has been associated with the gradual thickening of the protective oxide. However, as reviewed by B. Cox [3], numerous studies over

the decades indicated that it is not possible to grow oxide films thicker than 2 ~ 3 μm on zirconium alloys without a change in the kinetics which leads to either the successive cyclic kinetics stage and eventually an approximately linear kinetics stage, or directly into the approximately linear kinetic stage. It has been demonstrated that this change of kinetics, a.k.a. transition, takes place in at least three forms when in different corrosion/oxidation environments:

1. Para-linear transition of oxidation rate in high temperature air. This form of transition exhibits no increase of oxidation rate throughout the whole process. The kinetics simply steadily evolves from roughly parabolic or cubic to linear [54]. The lack of increase in oxidation rate is demonstrated by oxidation of zirconium in air at different temperature in Figure 15 [48].
2. Gentle transition of oxidation rate in oxygen or low-pressure steam. The evolution of kinetics from a cubic to an accelerated near linear rate law takes place across a time interval comparable to the entire pre-transition stage or the length of individual successive cycles. An example of oxidation of zirconium in steam is given in Figure 16 [104].
3. Sudden transition of corrosion rate in pressurised aqueous solution at 300 ~ 360°C. The duration of this transition is considerably shorter than the duration of the two previous forms. The sharp increase of corrosion rate, the successive cycles of mimic pre-transition kinetics and eventual breakaway into near linear rate law have been demonstrated previously in Figure 4 and Figure 5.

The third mode of kinetics evolution takes place in an environment which is representative of the service environment of PWRs' primary circuit. Therefore similar oxide microstructure is expected. Micrographs of oxide grown on M5 claddings of PWR are shown in Figure 17 [49], exhibiting the layered structure.

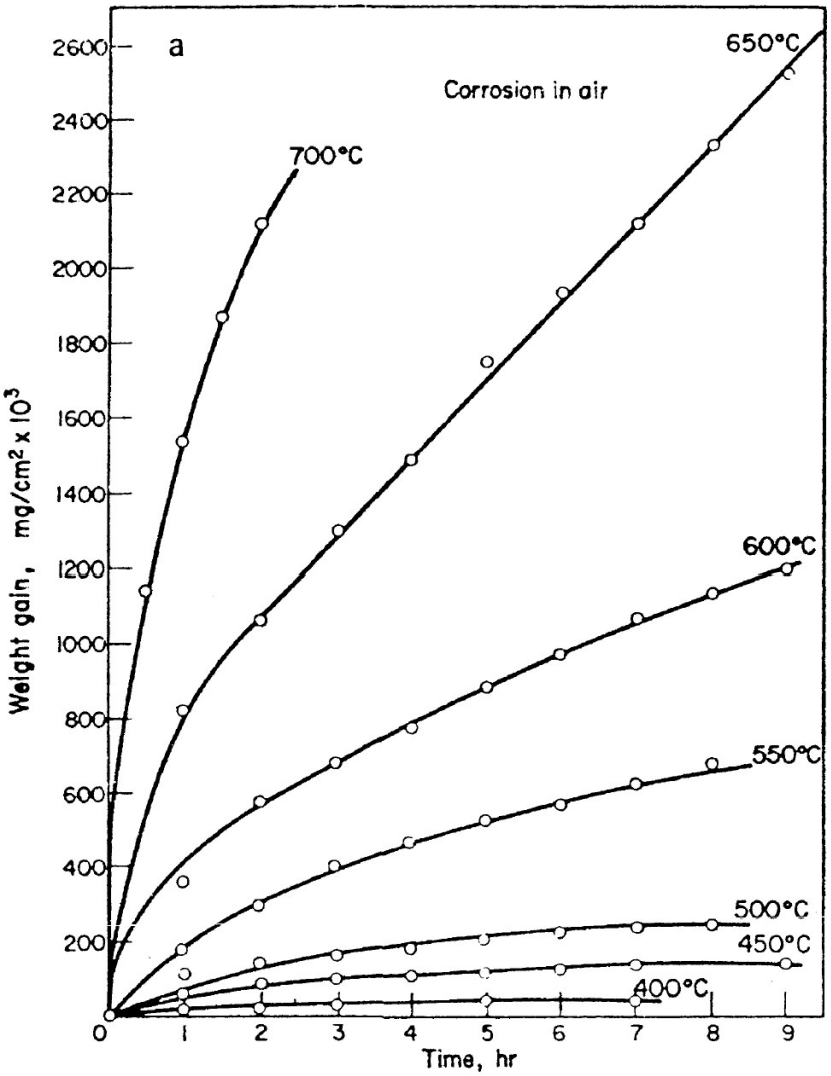

Figure 15: Para-linear oxidation kinetics for Zr in air at high temperatures [48].

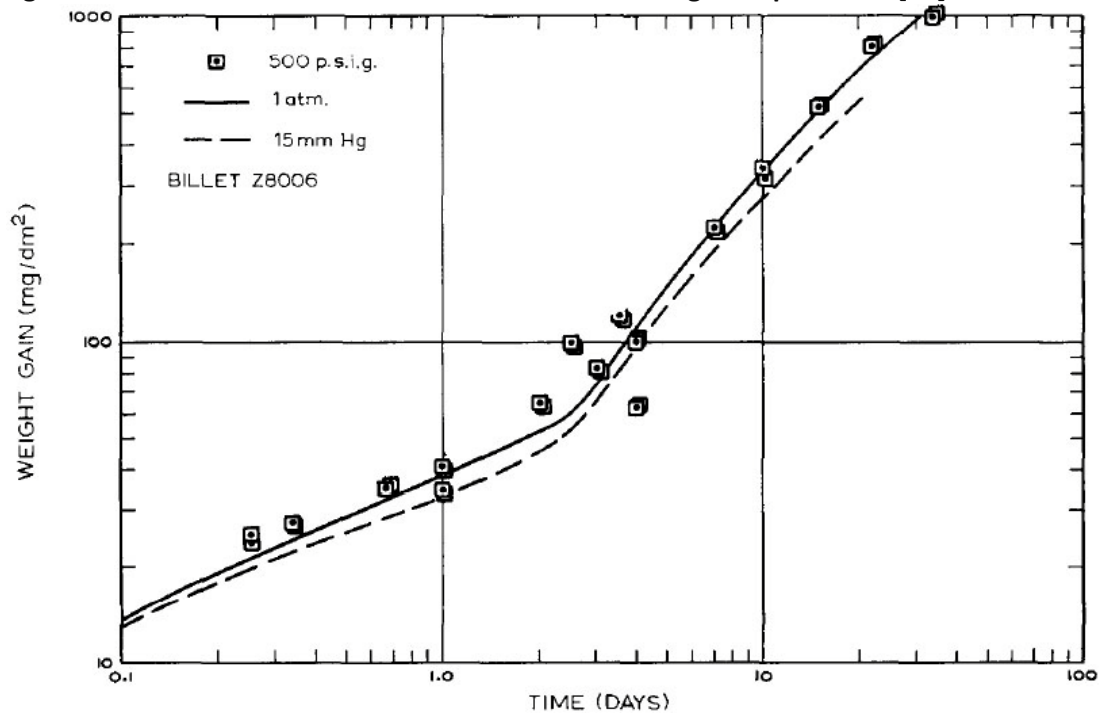

Figure 16: Oxidation of Zircaloy-2 in steam at 500°C and different pressure [104].

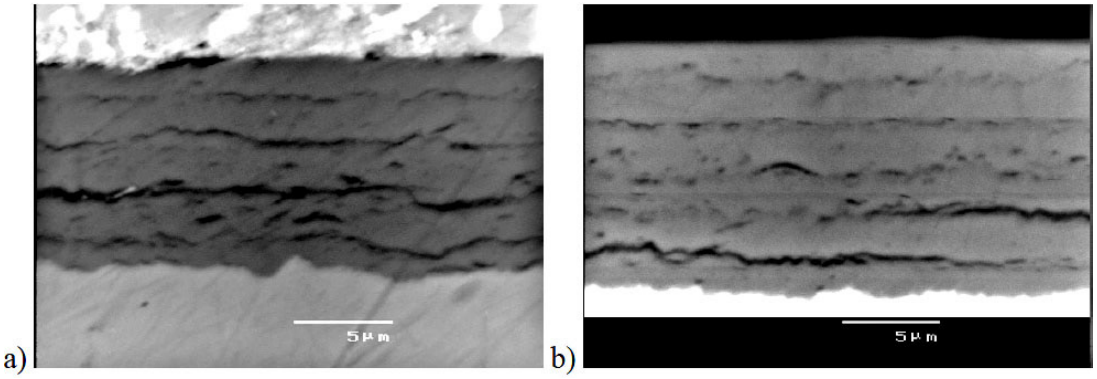

Figure 17: SEM micrographs, on cross sections, in backscattered electron mode, of M5 oxide layers formed in PWR after a) 5 and b) 6 cycles at span 4, 1780-1980 mm elevation from fuel rod bottom [49].

The principle of kinetics transition is the break down of the thin layer of protective material which acts as a diffusion barrier. Note that the diffusion barrier does not need to be a perfect structure, certain number of flaws are expected to exist. It takes more than a few defects to cause the transition, for example: cracks and porosities act as corrosion short cuts by allowing the transport of molecules. Over the decades of research on zirconium corrosion, a number of mechanisms have been proposed for the breakdown of the protective oxide layer. Several of the most recognised hypothetical mechanisms are presented below. Note that more than one, if not all, of the proposed mechanisms might be active:

1. As discussed in the previous chapter, the progression of oxidation brings about the formation of a highly compressive residual stress field in the oxide, due to the 56 vol.% volume expansion of zirconium dioxide formation [35, 77]. The compressive stress stabilises the metastable tetragonal oxide phase [50, 55, 78, 79]. The tetragonal phase has been reported to form and accumulate at the corrosion progression front, the metal/oxide interface [24, 52, 55, 70-72]. The compressive stress in the oxide is firstly balanced by the tensile stress in the zirconium metal substrate beneath. ‘New’ oxide is then

formed at the interface under compression, adding tensile stress component to metal beneath and previously formed oxide above. Also, the metal substrate eventually creeps upon prolonged corrosion exposures, resulting in the relaxation of both tensile stress in the metal and compressive stress in the oxide [52, 55, 80].

Combining the relaxation of the stress and continuous formation of 'new' oxide at the interface, a stress gradient is subsequently generated, with the highest compressive stress at the oxide/metal interface and decrease towards the outer part of the oxide [54, 55, 79, 80]. An eventual tensile stress state is expected to be reached firstly by the outmost layer of oxide. An example of actual measured compressive stress gradient inside the oxide is presented in Figure 18 [55], although in this particular case, the outmost layer of oxide has not reached the proposed tensile state.

Cracks are expected to initiate in the oxide under tension and propagate perpendicular to the metal/oxide interface. Note that propagation of the cracks will only proceed to the depth where the stress in oxide changes from tension to compression. A thin barrier layer with good integrity will be left [105]. The reported gradual increase of compressive stresses in the oxide before transition and sharp drop after the transition are in agreement with this mechanical breakdown mechanism [52, 55].

This mechanism proposes that the successive cycles of corrosion rate are the result of cracks perpendicular to oxide surface acting as corrosion short cuts, bypassing the rest of the oxide [106]. However cracks are usually observed parallel rather than perpendicular to the oxide surface.

Perpendicular cracks are often attributed as artifacts due to sample preparation.

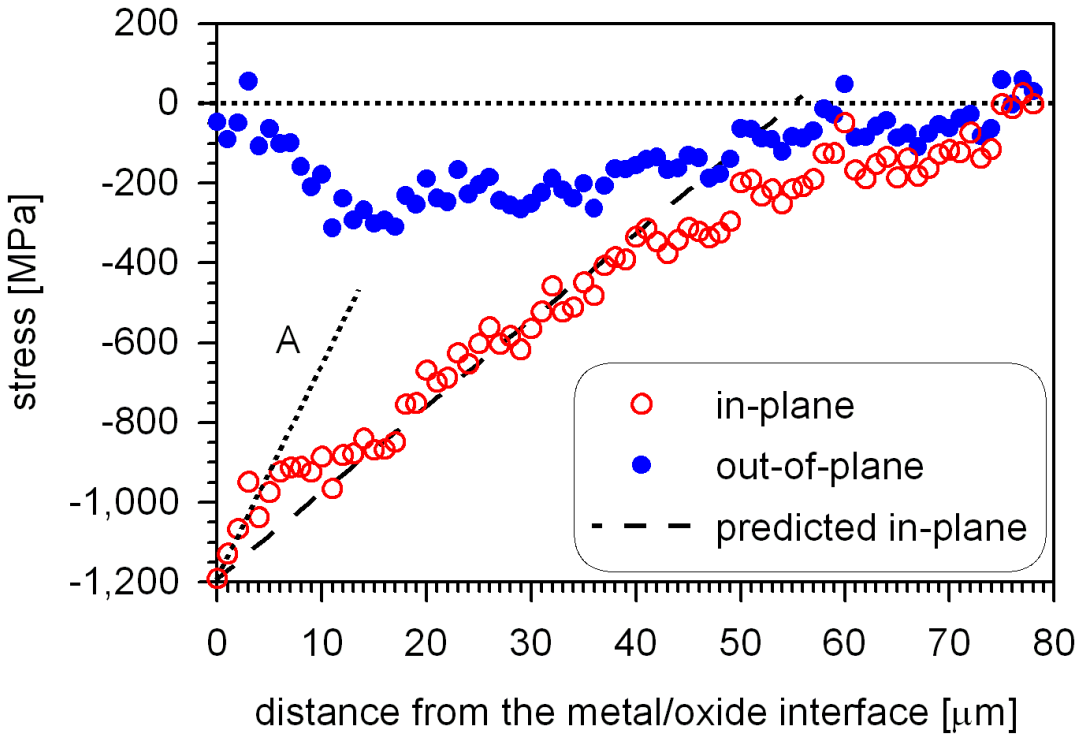

Figure 18: In-plan residual stresses as a function of distance from the metal/oxide interface for Optimized-ZIRLO tested for 600 days at 415°C. Measured by synchrotron X-ray diffraction at ID11, ESRF [55].

2. It is suggested that the strong compressive stress in the oxide could lead to the formation of cracks parallel to the oxide/metal interface. When local stress concentration exceeds the level the oxide can mechanically sustain, de-bonding of weak regions of the interface and buckling of oxide are initiated [107]. Note that parallel cracks do not act as corrosion short cuts unless they have been connected by perpendicular cracks. Convincing evidence has not been provided to support such three dimensional network of cracks.
3. Superficial crack formation and propagation could also be initiated by environmental degradation of the oxide. The stress stabilised tetragonal

oxide phase has been reported to undergo surface reaction with OH- as schematically demonstrated in Figure 19 [108]. Chemically stabilised tetragonal oxide phase, on the other hand, has been reported to undergo degradation from tetragonal to monoclinic phase in contact with moisture [109]. The resulting porosity could develop further through the entire oxide, eventually reaching the oxide/metal interface [110], [111]. At the moment, direct evidence supporting this mechanism has not been reported.

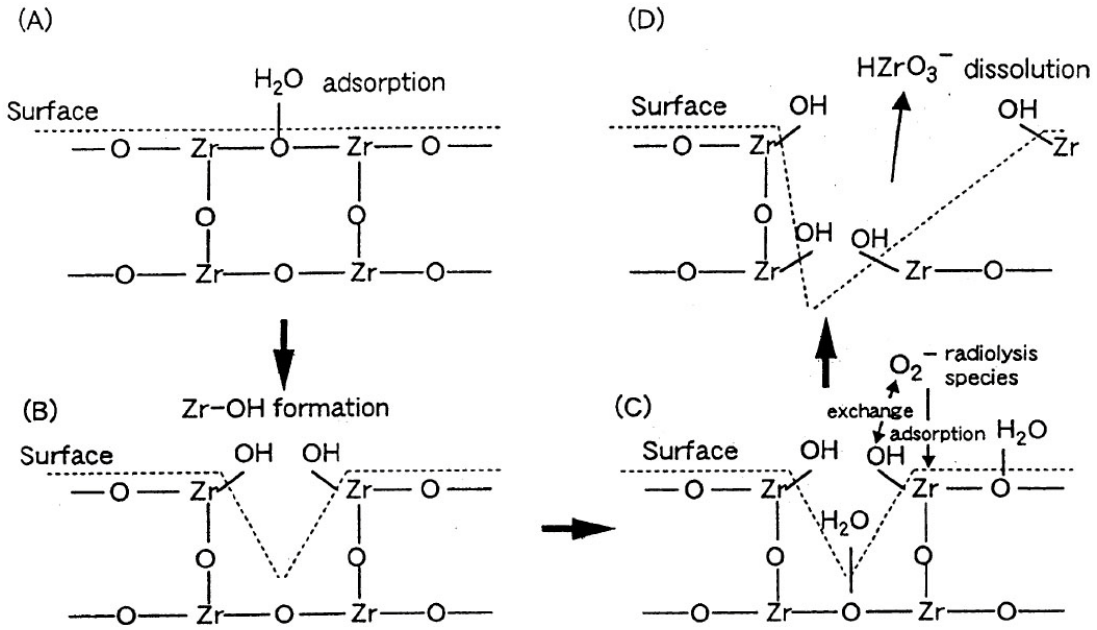

Figure 19: Model of dissolution process of zirconium oxide into water [108].

4. The dissolution of zirconium oxide in LiOH solutions has been well documented [105, 112]. Early studies suggested that the tetragonal phase suffers preferential dissolution in LiOH [113]. However a later study demonstrated that the attack of zirconium dioxide is balanced between the two modifications. Preferential attack is concentrated on crystallite boundaries causing porosity [114]. The suggested preferential dissolution of tetragonal phase is merely a miss-interpretation of the degradation in water described in previous paragraph [3]. Compared with these experimental

environments, the primary water has a much lower concentration of LiOH solution and hence an even lower solubility of zirconium dioxide is expected [113].

5. Tetragonal oxide grains are usually associated with equiaxed grains while monoclinic grains are associated with columnar grains [25]. TEM investigations indicated the oxide film is a mixture of equiaxed tetragonal grains and columnar monoclinic grains [90]. Small cracks and porosities are located on the outer end [90-92] and inner ends of such columnar grains, penetrating very close to the metal/oxide interface [115]. The transformation of initially stress stabilised tetragonal oxide to monoclinic oxide is associated with 3 ~ 5 % volume expansion [73, 116], which brings about the formation of such cracks near the oxide/metal interface since tetragonal oxide phase has been reported to accumulate there [24, 52, 55, 70-72, 105]. Porosity is also expected due to the resulting shear during the transformation [105]. It is important to mention that TEM investigations of such oxide nanostructure have often been questioned since the observed crystallite boundary cracks and porosities are potentially artifacts, either directly created by sample preparation or formed afterwards since the thin foil samples no longer sustain the required residual stress to stabilise the tetragonal phase. This argument is partially supported by the fact that much fewer amount of tetragonal phase is observed via TEM studies than via Raman spectroscopy [71, 105]. Synchrotron radiation diffraction measurements conducted by A. Yilmazbayhan et al. [24] observed a repetitive variation of tetragonal phase fractions across the thickness of the

oxide, supporting the association of tetragonal to monoclinic phase transformation with kinetics transitions. The diffraction method is considered non-destructive and more reliable. However, in both cases (Raman and synchrotron X-ray), a free surface means that the stress state is not fully maintained.

2.4 Effects of hydrogen on the aqueous corrosion behaviour of zirconium alloys

2.4.1 Origin of hydrogen

Zirconium alloys are widely employed as pressure tubes and cladding tubes in primary water circuit of the PWRs. During services of a reactor, hydrogen comes from two principal sources [117-119]: the addition of LiOH for maintaining primary water's pH between 10.0 and 10.7, and the corrosion reaction of zirconium with primary water, which has been previously described in Equation 1. External hydrogen sources also include radiolysis of the coolant water and dissolved hydrogen gas [117]. The majority of the hydrogen recombines to form hydrogen gas. Table 3 [9] gives the heat of solution over a range of temperature. The heat of solution is the difference between partial molar free energy of hydrogen in α-zirconium phase and in hydrogen gas phase. It is clear that hydrogen is more stable in solid solution in zirconium matrix than it is as hydrogen gas over the services temperature range of reactor. Hence a small fraction of hydrogen may be trapped inside the zirconium matrix. Hydrides will be precipitated when local hydrogen concentration reaches the solubility limit (120 wt.ppm at reactor services temperature [120, 121]).

The temperature dependence of hydrogen solid solution in zirconium is shown in Figure 20 [9]. Hydrides will firstly precipitate in regions of lower temperature. In the case of zirconium claddings, the inner surface of the clad is heated by the fuel, while the outer surface is in direct contact with the primary water coolant. Thus the resulting temperature gradient brings about the preferential precipitation of hydrides near the outer surface of a cladding tube, which is effectively the oxide/metal interface, corrosion progression front. Figure 21 [49] is the microstructural representation of hydride distribution in cladding tubes samples after different length of exposure in nuclear reactor. Both hydride rich rim region and circumferential oriented hydride strings in the bulk of the clad are visible.

Table 3: Heat of solution of hydrogen in α-zirconium phase [9].

Temp °C	cal/g -atom	Temp °C	cal/g -atom
700	+247	300	-5540
600	-1155	200	-7180
500	-2650	100	-8692
400	-4020	0	-10291

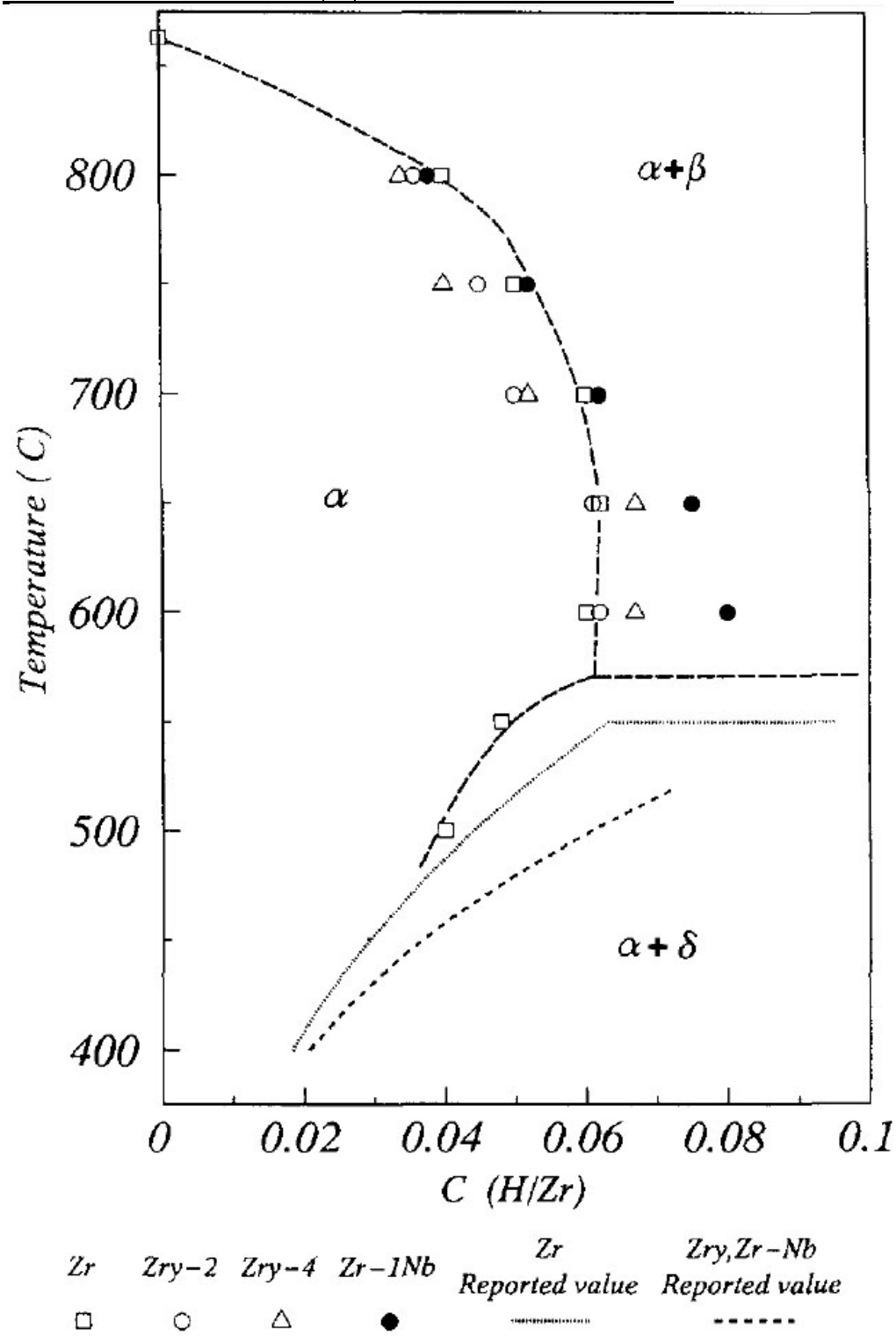

Figure 20: Temperature dependence of hydrogen solubility in different zirconium alloys [122].

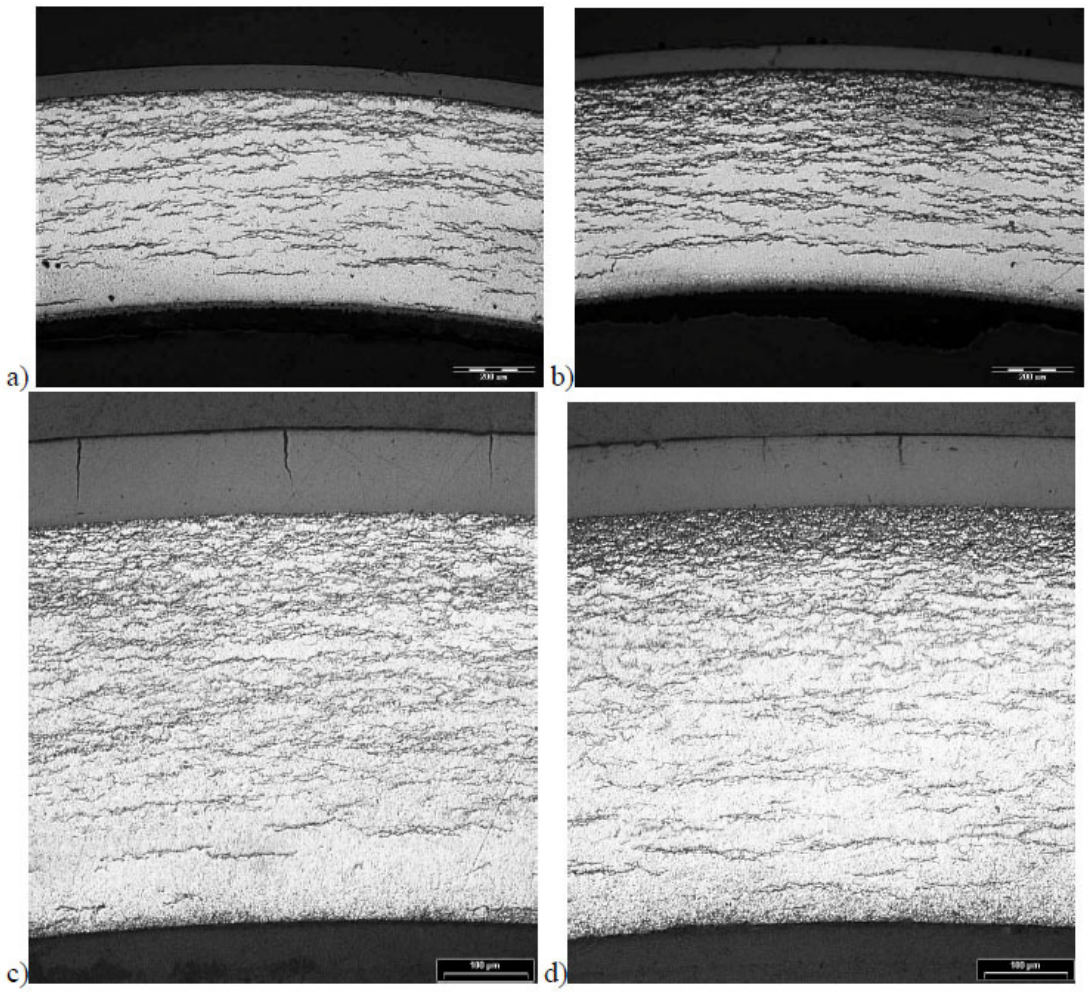

Figure 21: Optical micrographs of the hydride distribution and oxide layer on Zircaloy-4 irradiated for 6 cycles in PWR at (a) and (b) span4, 1851-2001 mm from fuel rod bottom, (c) and (d) span 6, 3000-3200 mm elevation from fuel rod bottom [49].

2.4.2 Absorption of hydrogen

In the case of an oxide free surface, zirconium metal can rapidly absorb hydrogen [123]. A perfect oxide layer on the surface no matter the thickness will act as an almost impermeable barrier against hydrogen migration [124]. As demonstrated in Table 4 [123], the diffusivity of hydrogen in zirconium metal is 10^{10} greater compared with that in zirconium oxide. Thus it is inevitable that any hypotheses about hydrogen absorption during aqueous corrosion are linked to the nature of the oxide layer grown on the zirconium alloy surface. However, the mechanism via which hydrogen atoms penetrate this layer is still not understood. The

measurement of diffusion coefficients for hydrogen in zirconia is considered to be generally flawed [125] since it is evidential that migration of hydrogen to and escape down pores inside the oxide becomes the primary process. Even though, those values represent a significant difference.

Table 4: Diffusivity data of hydrogen in zirconium based alloys and their oxide at 400°C [123].

Material		*D (cm^2 s^{-1})*	*Method*	*Expression / Ref.*
Zr and Zircaloy	Polycrystalline α Zircaloy-2	4.1×10^{-6}	Hot extraction	(1) Sawatzky
	Polycrystalline Zr	2.8×10^{-6}	Tracer-based	Khatamian et al.
Oxide scales	Polycrystalline 1 μm oxide layer on pure Zr	1.9×10^{-16}	Tracer-based	(2) Khatamian et al.
	Polycrystalline 1 μm oxide layer on Zr-2.5% Nb	2×10^{-13}	Tracer-based	(3) Khatamian et al.

The macroscopic description of the zirconium corrosion kinetics has been given in previous chapter, and is briefly summarised here. The total process can be divided into two distinct periods: The first one is the initial pre-1st transition period relating to the formation of protective or passive corrosion products at the surface (the impermeable barrier layer). The second one is the post-transition period, composed of successive cycles mimicking the pre-transition kinetics. During the post-transition period, the impermeable barrier is re-constructed and lost repetitively, which has been associated with the observed stratification in the oxide films [24, 37, 43, 49, 54, 55]. Therefore it can be clearly seen that, for hydrogen absorption to be able to progress together with aqueous corrosion, hydrogen must be able to penetrate the zirconium oxide layers by either diffusion or migration.

The cathodic half cell reaction of corrosion is given below:

$$2e^- + \boxed{O} + H_2O \rightarrow O^{2-} + 2H \quad (7)$$

where e^- is electron, $\boxed{O}$ is oxygen vacancy in zirconia lattice and H is hydrogen atom. The hydrogen atom then travels into the zirconium matrix in three steps [126]:

1. One adsorbed water molecule reacts with an anion vacancy at the surface, leaving two protons and one oxygen anion (or one proton and hydroxyl).
2. Electrons migrate from the oxide/metal surface to discharge the protons.
3. Some of the hydrogen re-combines to form hydrogen molecules and escapes into the environment while the rest migrates through the oxide layers into the metal [127].

A perfect layer of oxide acts as perfect impermeable barrier against corrosion medium and hydrogen transportation. However, a significant number of defects are deemed to exist in the oxide layer and decrease the extent of impermeability of the protective oxide layer. Andrieu et al. [128] postulated for thin oxide layers formed on zirconium alloys, unoxidised SPPs in the dense oxide layer act as diffusion short circuit pathways, equivalent to connecting metal/oxide interface to the corrosion medium. As oxidation proceeds, the SPPs become oxidized and the hydrogen transportation is slowed down ($\approx 1/\text{oxide thickness}$). A second type of defects, which is small crack in the oxide, is believed to allow the transportation of molecular species and increase the transport rate [127].

2.4.3 Hydrogen pickup mechanism in Zircaloy family alloys

A schematic description of the hydrogen pick up process in Zircaloys is given by Rudling and Wikmark in Figure 22 [129]. This description uses the interpreted form Reaction Resistance (RR), which is the inverse rate constant, to describe the process. In each individual step of corrosion and hydriding, the rate limiting parameters will have the highest RR and hence govern the overall reaction rate. This description considers the hydrogen pick up in Zircaloy takes place in two different routes: hydrogen either transports through the barrier layer directly at thin oxide layer situation, or takes advantage of the SPPs as transportation short cuts at relatively thick oxide situation. It can be also concluded that direct transport of hydrogen through barrier dominates the hydrogen pick up in early stage of corrosion when $RR_{H,\ barrier\ layer}$ is still insignificant. With the progression of pre-transition corrosion, $RR_{H,\ inti.\ barrier\ layer}$ dramatically increases with the oxide layer thickness and transport mechanism shifts to the SPPs route, which is represented by $RR_{H,\ SPPs}$.

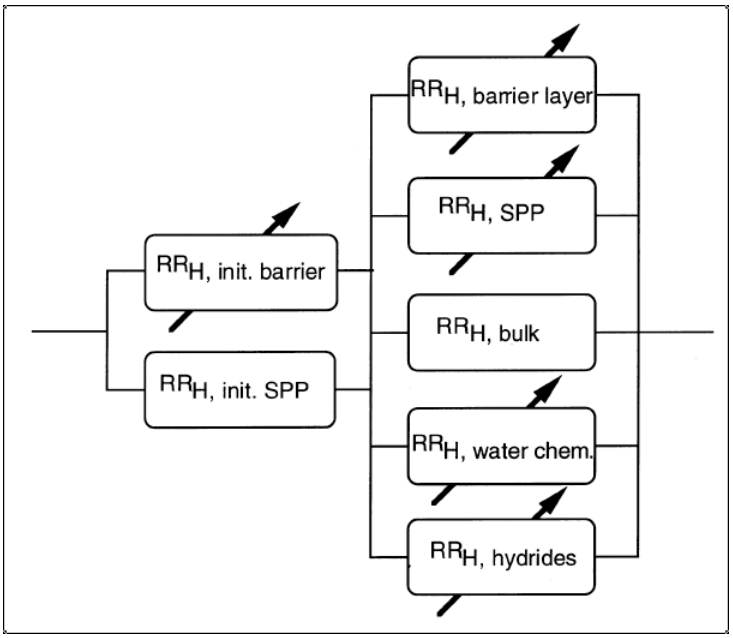

Figure 22: Schematic picture of the hydriding mechanisms, where RR_H refers to the reaction resistance of hydrogen pick up, init refers to initial condition [129].

SIMs imaging by Bossis et al. [130] demonstrated that in Zircaloy-4 samples there is a good correlation between the localisation of hydrogen in the oxide and the presence of SPPs, which is strongly supporting the role of SPPs in hydrogen uptake in Zircaloy-4, Figure 23 [130].

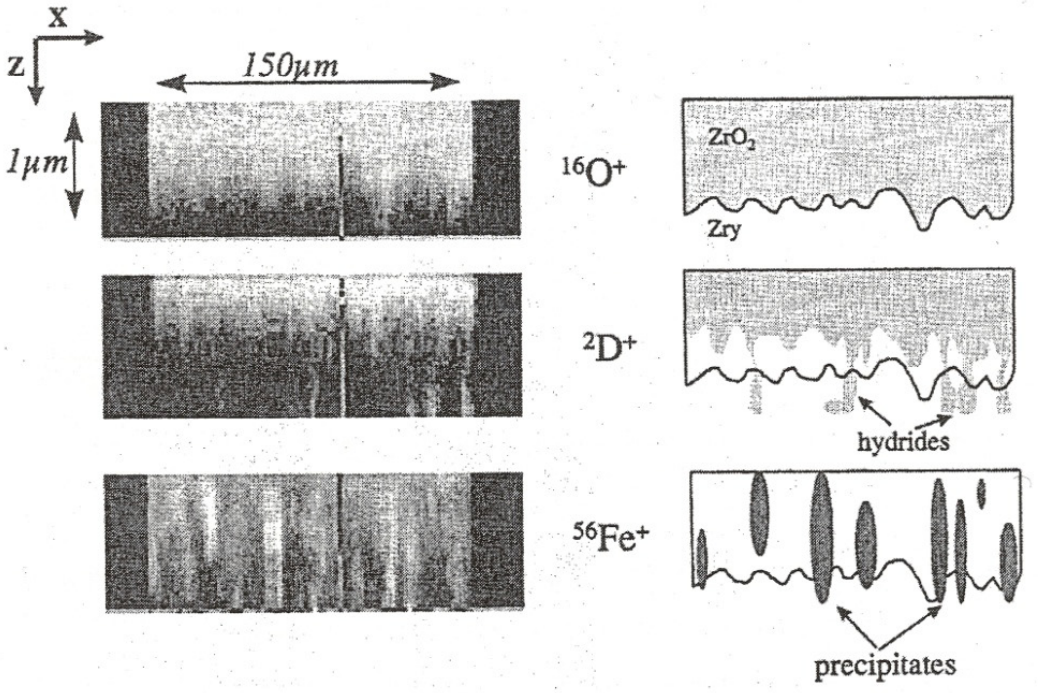

Figure 23: SIMs cross section of a 3D reconstitution, distribution and associated schematic representation of oxygen, deuterium and iron in the oxide of a Zircaloy-4 sample, oxidised 48 hr at 673K in heavy water [130].

2.4.4 Hydrogen pickup mechanism in Zr-Nb family alloys

Ramasubramanian et al. studied the hydrogen pickup in Zr2.5Nb alloy with FTIR and SIMs [131] before further suggesting that the sharp decrease of hydrogen profile as a function of depth in the oxide is not the result of a diffusion profile, but the result of different density of crystallite boundary pathways in the oxide. A schematically description is given in Figure 24 [131]. The hypothesis considers hydrogen species near the surface of the oxide as hydroxyls and absorbed water molecules. Crystallite boundaries then act as hydrated pathways for hydroxyls and adsorbed

water molecule. Protons firstly enter the oxide via the randomly occurred pathway openings at the oxide/environment interface; then travel through the pathways and enter the metal at the end of the pathways. This hypothesis also assumes that there is one barrier layer at the end of the pathways, which is one thin oxide layer with positive charge due to ionised anion vacancies at the metal/oxide interface. The barrier energy is lowered by the negative corrosion potential and such barrier layer should have constant thickness in the post-transition corrosion stage.

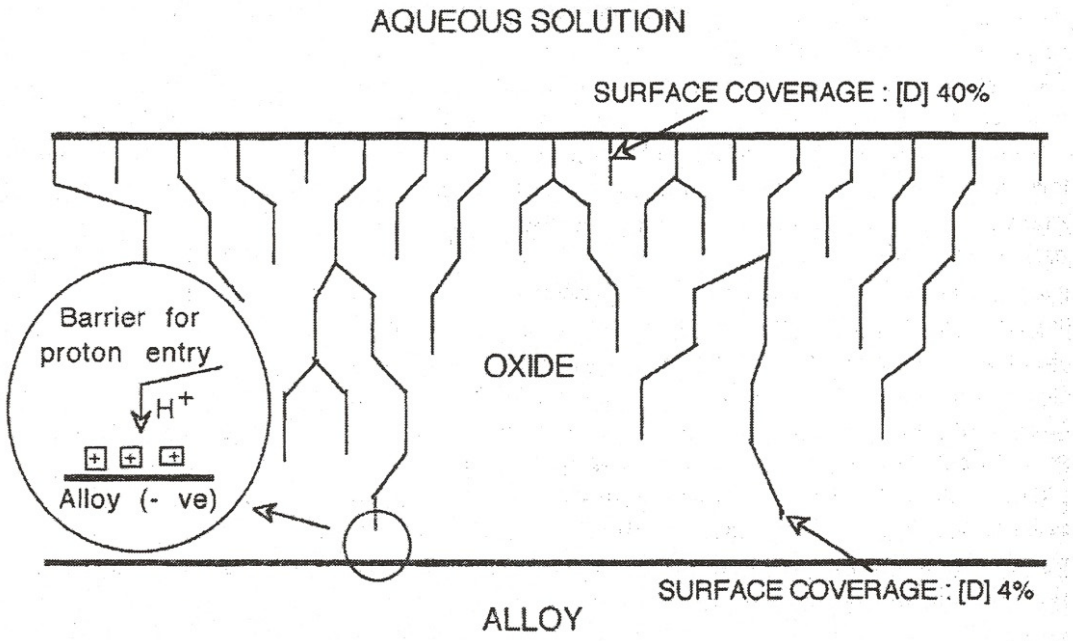

Figure 24: A schematic diagram illustrating the interconnected hydrated pathways in a 1 µm thick oxide film on Zr2.5Nb alloy, grown in 1MPa steam at 400°C for 24 hours, surface coverage data is from SIMS depth profiles for deuterium in oxide [131].

2.4.5 Impacting parameters of hydrogen pickup during corrosion

The parameters that impact hydrogen pickup during corrosion are:

1. Corrosion rate inherently affects the absorption of hydrogen since corrosion is one of the sources of hydrogen and the nature of oxide layer evolves with it [132]. The thickness of the barrier oxide layer represented by $RR_{H,\ barrier\ layer}$ plays an important role. In previous paragraphs two different entry

routes for hydrogen have been proposed, either through SPPs short cut or directly through the barrier. The later one is entirely impossible unless the barrier oxide layer is extremely thin, since the solubility and diffusion rate of hydrogen in zirconia is negligible [123].

2. Rudling and Wikmark [129] suggested that the higher hydrogen pickup in PWRs than in BWRs is due to higher oxygen potentials in BWR coolant, which increases the reaction resistance $RR_{H,\ water\ chem}$ under BWR conditions.
3. The size distribution of SPPs also has an impact on the hydrogen pickup in terms of corrosion rate. It is proposed that the barrier oxide layer is thicker for a higher density of SPPs above certain critical size, (25-50 nm in BWRs) [133]. A relative denser region in the oxide layers designated as 'veins' forms from all SPPs above this critical size. However, with increasing SPPs size, there will be relatively fewer veins and hence easier for cracks to propagate inside the oxide layer towards the oxide/metal interface, resulting in less effective thickness of protective barrier oxide layer. In contrast, materials with smaller SPPs (still above the critical size) will form oxide layers with many veins, capable of preventing cracks from propagating, resulting in a thicker effective barrier oxide layer. Therefore a hypothetical SPPs size distribution for optimum corrosion rate exists for the formation of a barrier layer [134].
4. Another impacting parameter is the chemical composition of the SPPs. Nickel bearing SPPs are considered to be inferior to chromium bearing SPPs, resulting in a smaller reaction resistance. The recorded higher hydrogen

pickup in Zircaloy-2 (with both nickel and chromium bearing SPPs) than in Zircaloy-4 (with only chromium bearing SPPs) favours this argument [105].

2.4.6 Hydride phases in zirconium

2.4.6.1 Zirconium-hydrogen system phase diagram

Figure 25 [135] displays the phase diagram of the zirconium-hydrogen system. The solubility of hydrogen varies significantly with temperature from less than 0.3 at.% at 300 °C to almost 50 at.% at 700°C, eutectoid alpha-zirconium and hydride at 560±10°C and the eutectoid composition is 42±3 at.% of hydrogen. Hydrides are stable only above the eutectoid temperature but can be retained to below 560°C as a metastable phase, i.e. the γ phase with 55 to 65 at.% hydrogen.

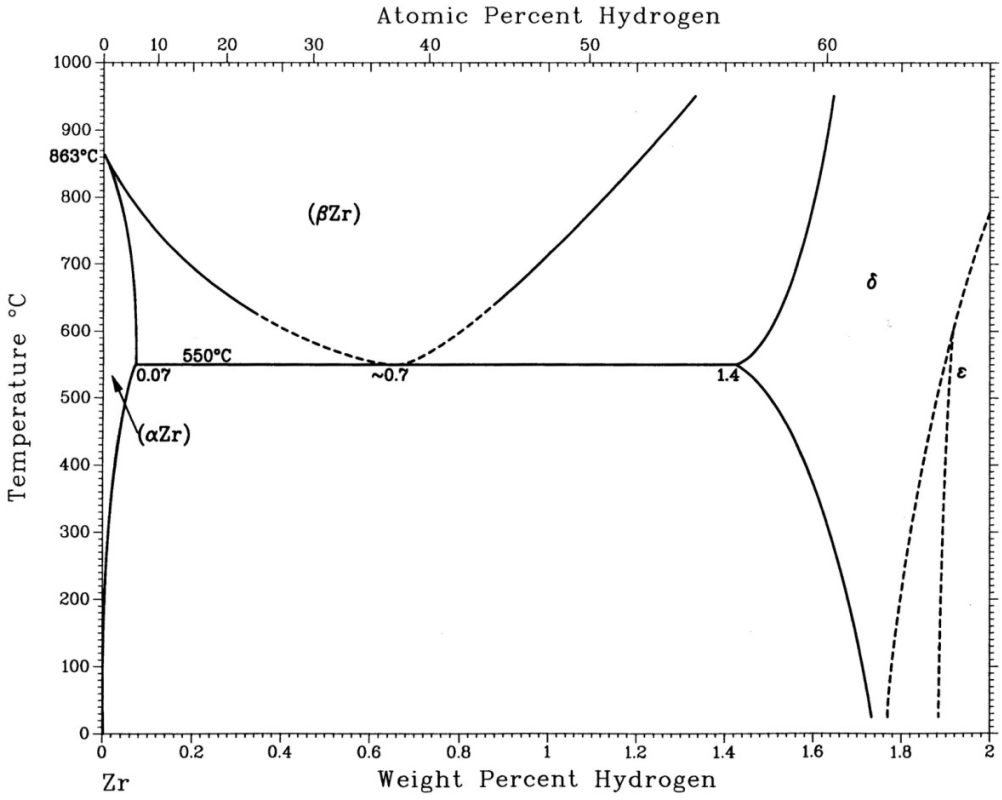

Figure 25: The zirconium-hydrogen system phase diagram [135].

There are three common modifications of zirconium hydride phase, the γ phase, the δ phase and the ε phase, all presented in Table 5 [136-138],:

1. Face centred tetragonal (fct) γ phase with a_0=4.596 Å, c_0=4.969 Å and composition around ZrH, with Hydrogen atoms on the tetrahedral sites of the (110) plane.

2. The face centred cubic (fcc) δ phase with a_0=4.781 Å, which has a composition range around $ZrH_{1.6}$. The Hydrogen atoms are randomly distributed among 8 possible tetrahedral sites.

3. Face centred tetragonal (fct) ε phase with a_0=3.520 Å, c_0=4.440 Å and a wide range of composition from $ZrH_{1.65}$ to $ZrH_{1.965}$.

Table 5: Lattice parameters of various phases presented in hydrided Zircaloy-4 [137].

Phase	PDF Nos.	ZrH_x where x≈	Structure	a_0 (nm)	C_0 (nm)
α-Zr (matrix)	00-005-0665	0	Hexagonal	0.3232	0.5147
γ-Hydride	00-034-0690	1	Tetragonal	0.4596	0.4969
δ-Hydride	00-034-0649	1.66	Cubic	0.4781	-
ε-Hydride	00-017-0314	2	Tetragonal	0.352	0.445

Only two of the modifications are shown in the phase diagram in Figure 25 for γ is usually considered to be metastable. The δ hydride phase is the most common of the three. X-ray diffraction investigation by Yamanaka et al. [138] showed that the lattice parameter increases slightly with increasing hydrogen content, as shown in where the Table 6 [136] together with some of the mechanical and physical properties. An empirical equation [138] is also given:

$$a(nm) = 0.4706 + 4.382 \times 10^{-3} \times C_H(\frac{H}{Zr}) \quad (8)$$

where a is the lattice parameter and $C_H(\frac{H}{Zr})$ is the stoichiometry of the δ hydride phase.

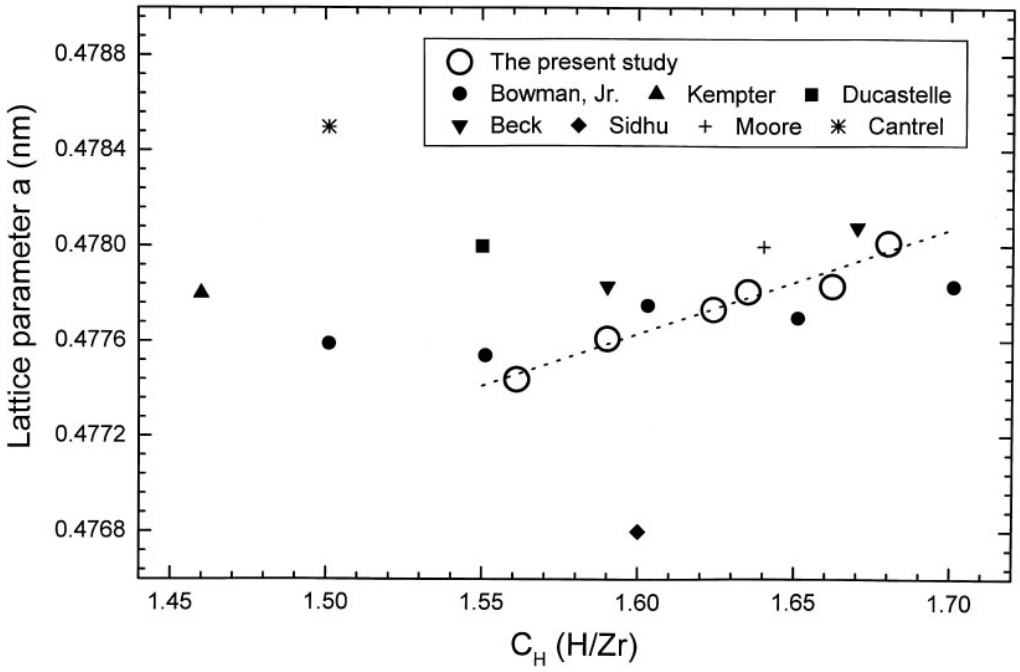

Figure 26: Change in the lattice parameter a of δ ZrH_{2-x} with the hydrogen content C_H [138].

The γ-hydride phase has been long regarded as a metastable phase. Only recently, in-situ cooling experiments using neutron diffraction have shown that the δ-hydride phase can appear first, followed by a slow transformation into γ-hydride phase (Figure 27 [139]). This transformation occurs at temperature bellow 180°C on a time scale of days or even weeks. The reaction can be described by the formula below:

$$\alpha - Zr + \delta - ZrH_{1.6} \rightarrow \gamma - ZrH \qquad (9)$$

Table 6: Physical and mechanical properties of zirconium and typical hydride phases [136].

	Hydrogen content	Lattice parameter		Density	Mechanical properties		Thermal properties	
	C_Q (Q/Zr)	a (nm)	c (nm)	ρ (kg/m^3)	E (GPa)	ν	θ_D (K)	α (K^{-1})
αZr	0	0.3232	0.5147	6.507×10^3	95.49	0.334	274.4	1.710×10^{-5}
δZrH_{2-x}	1.47	0.4771	–	5.671×10^3	137.8	0.317	335.9	2.481×10^{-5}
	1.54	0.4774	–	5.664×10^3	137.8	0.316	335.8	2.580×10^{-5}
	1.64	0.4778	–	5.655×10^3	133.3	0.325	329.6	2.702×10^{-5}
	1.66	0.4779	–	5.653×10^3	131.7	0.322	327.8	2.737×10^{-5}
δZrD_{2-x}	1.55	0.4768	–	5.686×10^3	158.2	0.250	366.0	2.033×10^{-5}
	1.57	0.4771	–	5.677×10^3	157.2	0.268	363.1	2.381×10^{-5}
	1.66	0.4771	–	5.682×10^3	150.7	0.265	355.6	2.674×10^{-5}

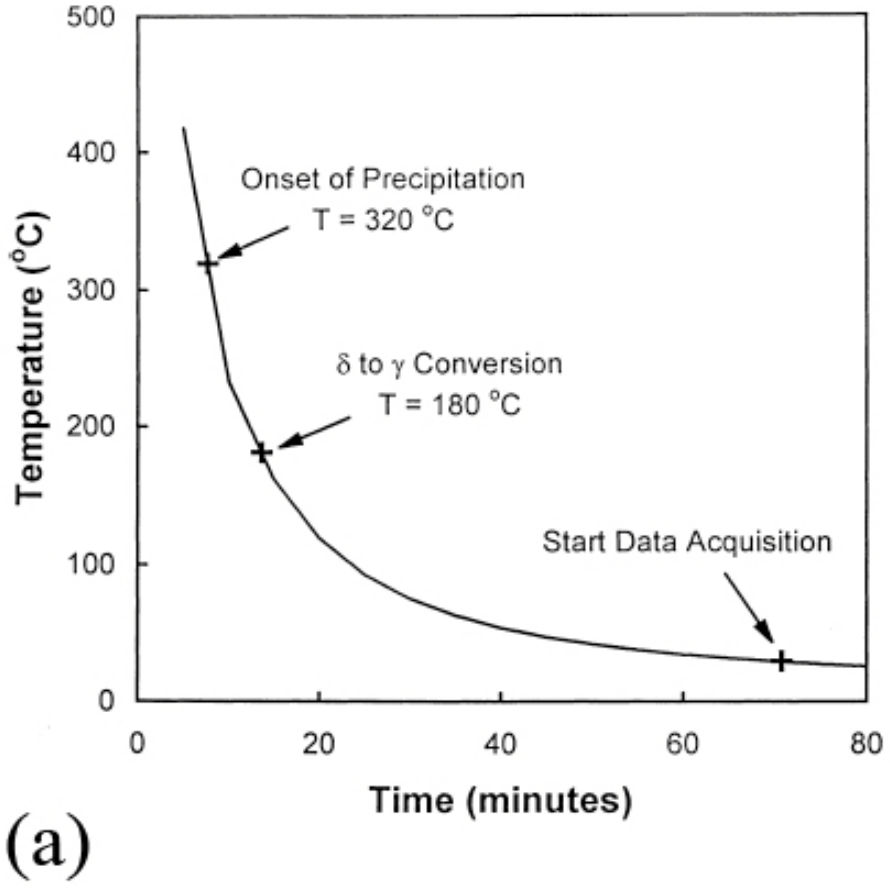

(a)

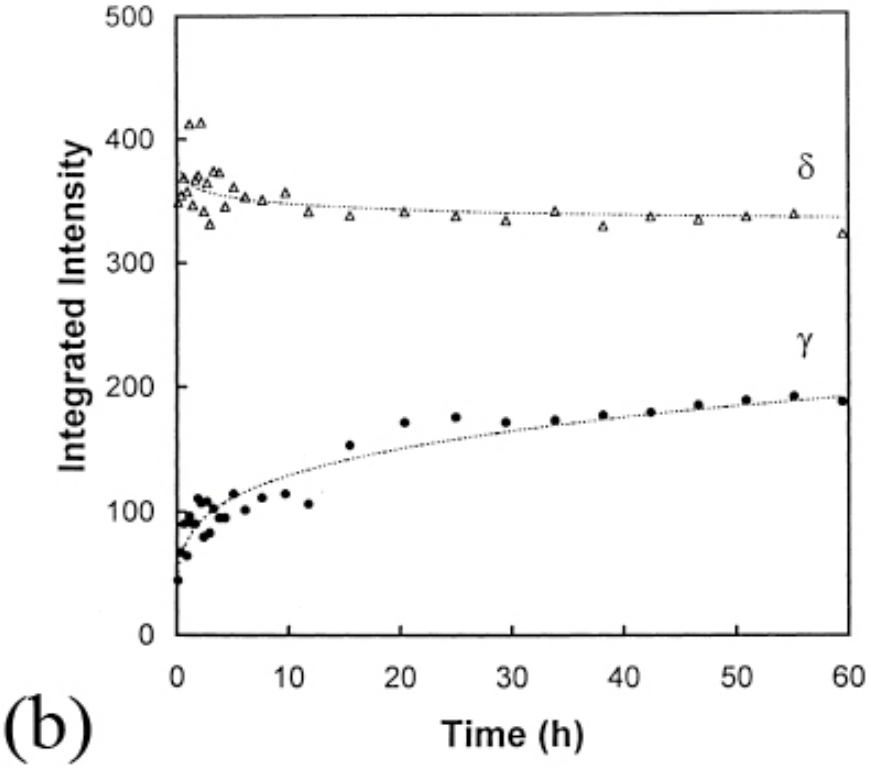

(b)

Figure 27: Transformation of δ-$ZrH_{1.6}$ to γ-ZrH at low temperature, (a) cooling curve for specimen in neutron diffraction experiment, (b) kinetics of δ to γ transformation in Zr-2.5Nb at 17°C after being cooled form 450°C [139].

2.4.6.2 Nucleation and growth of hydrides

The transformation from zirconium metal to zirconium hydride phase is associated with 17% volume expansion [137, 140, 141], hence it is expected that hydride grains will be under considerable compressive stress where the neighbouring metal grains will be under tension. This local distortion is accommodated by the generation of dislocation loops around the hydride grain, as it can be seen in Figure 28 [142]. Solid solution of hydrogen in α-zirconium lattice on the tetrahedral sites of the hcp unit cell also causes distortion to the lattice, making positions such as grain boundaries, twin boundaries, habit planes in matrix and between twins the preferred precipitation site for hydrides [143]. The following lattice planes have been suggested as probable hydride habit planes: prismatic plane $\{10\bar{1}0\}$ [144], twinning plane $\{10\bar{1}2\}$, $\{11\bar{2}1\}$ and $\{11\bar{2}2\}$ [145], pyramidal plane $\{10\bar{1}1\}$ [145] and the most commonly reported plane $\{10\bar{1}7\}$ [146, 147]. After nucleation, both Cox [148] and Weatherly [149] have reported the local hydrogen concentration in dislocation loops due to lattice distortion, which allows the nucleation of a second hydride platelet adjacent to the first one and further generation of more dislocation loops. When observed in lower magnification, the continuous successive nucleation of small hydride platelet adjacent to each other constructs the image of a long continuous hydride structure, often referred as strings (i.e. Figure 21).

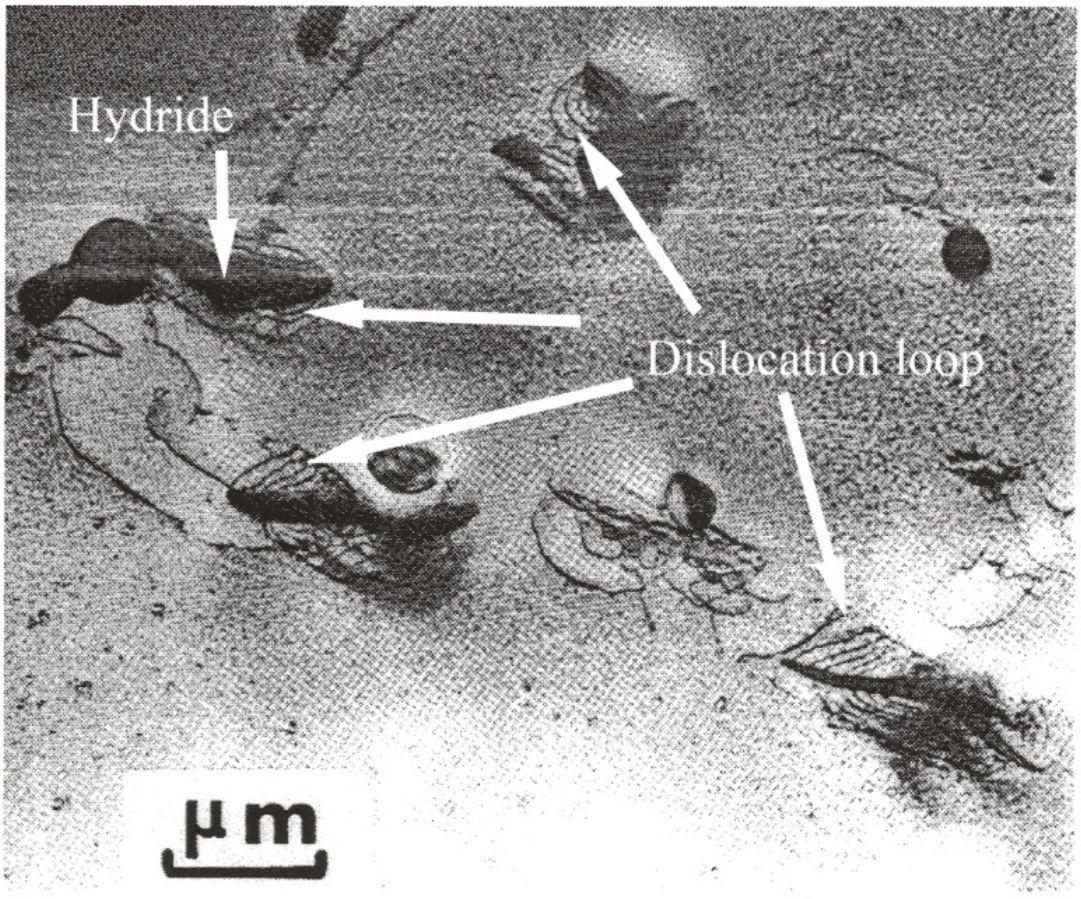

Figure 28: Hydrides nucleation at intermetallic particles in Zircaloy-2, with dislocation loops around the hydride grains [142].

2.4.7 Effects of hydride presence on the corrosion behaviour of zirconium alloys

As quoted by B. Cox [3], the hydrogen absorption during corrosion in aqueous environments is one of the earliest observations made during the study of zirconium alloy corrosion. The exact contribution of hydrides upon the corrosion behaviour of zirconium alloys have been studied for decades. However early studies have suggested that the presence of hydrides has little effect on the corrosion performance of zirconium alloys [150, 151]. This argument was gradually proven at least approximately in the following decades. Numerous investigations were conducted on different zirconium alloys in steam, air, oxygen and pressurised aqueous environment. The accumulated results provide firm evidence of the detrimental effect imposed by hydrides on the corrosion of zirconium alloys [3, 9, 49, 51, 80, 152-155]. Yet even at this stage the exact extent of such effect and its mechanism remains elusive. Pressurised water corrosion experiments at 360°C conducted by Kido et al. [155] suggested an increase of corrosion rate on samples with relatively low concentration of hydrogen. However the accelerated corrosion actually took place firstly in edge regions of their samples where the localised hydrogen concentration was much higher. M. Blat et al. [80, 156] artificially charged zirconium samples with hydrogen prior to corrosion using cathodic and gaseous hydrogen charging techniques. Recorded corrosion kinetics on samples with different contents of hydrogen suggested that the effect of hydrides is directly proportional to hydrogen concentrations, as demonstrated in Figure 29 [156]. This effect is in good agreement with observations done by Khatamian [154] and

Oskarsson [81]. Note that the corrosion progression front is a mixture of zirconium metal and zirconium hydride, characterisation of this region is extremely difficult. Microstructure examinations indicated that oxide layers grown on pre-hydrided samples generally have higher density of cracks with shorter crack length [156]. As mentioned in previous chapter, such cracks have deleterious effect upon the integrity of the barrier oxide layer. It is hence suggested that the precipitation of hydrides enhances the initiation of cracks by altering the local stress distribution, therefore accelerates corrosion by facilitating access of oxidising species to the oxide/hydride interface through the barrier layer.

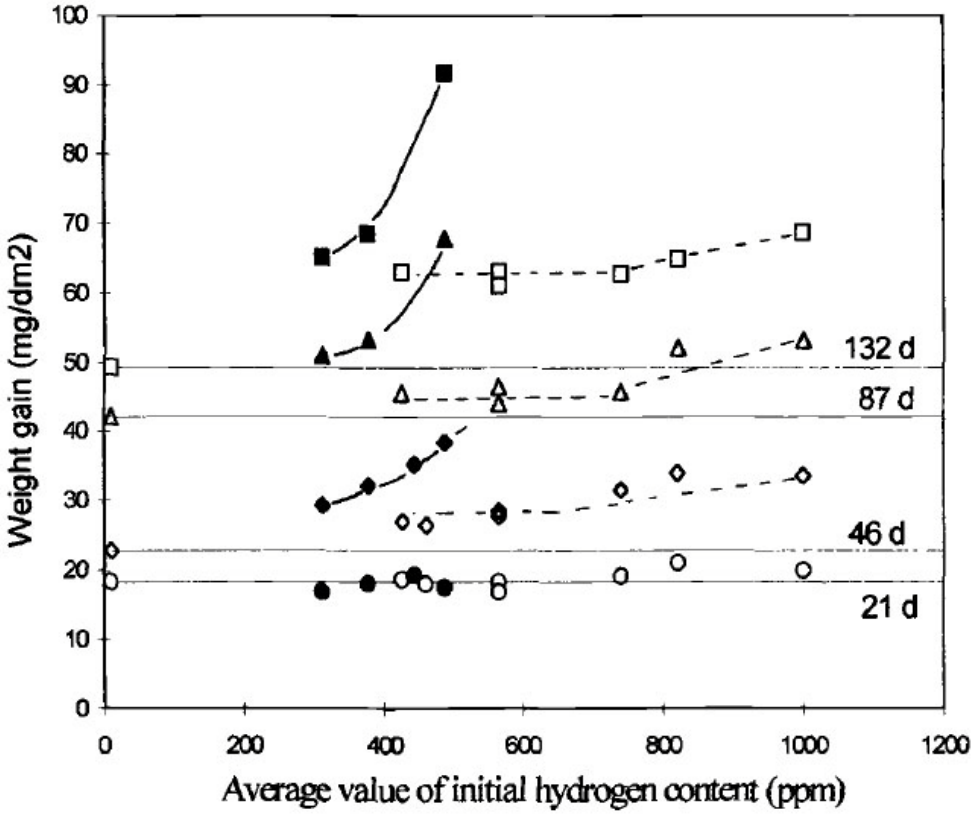

full symbols : cathodic charging
open symbols : gaseous charging

O : 21 d (500 h) ; ◊ : 46 d (1100 h) ; Δ : 87 d (2100 h) ; □ : 132 d (3200 h)

Figure 29: Effect of average initial hydrogen content on the corrosion rate in primary light water (2 ppm Li, 1000 ppm B, 360°C) [156].

3 Experimental

Experimental techniques are discussed respectively in the proposed publications. To avoid repetition, this chapter will only provide additional information which is not fully discussed in later chapters.

3.1 Materials

The alloys involved in this study are Westinghouse alloys ZIRLO^{TM}, low tin ZIRLO, X2, Westinghouse and Rolls-Royce variance of Zircaloy-4. The chemical compositions of the alloys were determined at the EDF Research and Development facility in Moret-Sur-Loing, France and can be found in later chapters. The alloys were provided in 4 heat treatment conditions: cold worked, stress relieve annealed (SR), partially recrystallised (pRX) and recrystallised (RX), and 2 geometries: tube (Φ=9.5mm, wall thickness t=0.6) and sheet (t=0.5-5.0 mm). Under Ar protection in quartz capsule (Figure 30), cold worked alloys received 1hr of stress relieve anneal at 500°C before ranked as SR material.

Figure 30: Sheet ZIRLO^{TM} samples in a quartz capsule awaiting stress relieve anneal.

Materials were further cut into smaller pieces, 30 mm long in the case of tube and 20×30mm in the case of sheet, with the longer direction being the former rolling direction. Samples were then pickled in a solution of 10 vol.% hydrofluoric acid, 45 vol.% nitric acid and 45 vol.% distilled water for 3 minutes to remove inorganic

contamination from the fabrication process. Particularly in the case of Nb containing alloys, fine Nb rich particles, which were unsolvable, adhered to the surface of the pickled sample. All pickled samples received 10 minutes of ultrasonic bath in acetone and ethanol respectively to remove such carry-over. A mirror-like surface was created by the pickling, as shown in Figure 31. SEM examinations in Figure 32 compare the surface quality of as received material with that of pickled one. The smooth surface of pickled sample is ready for future cathodic hydrogen charging and autoclave corrosion experiments.

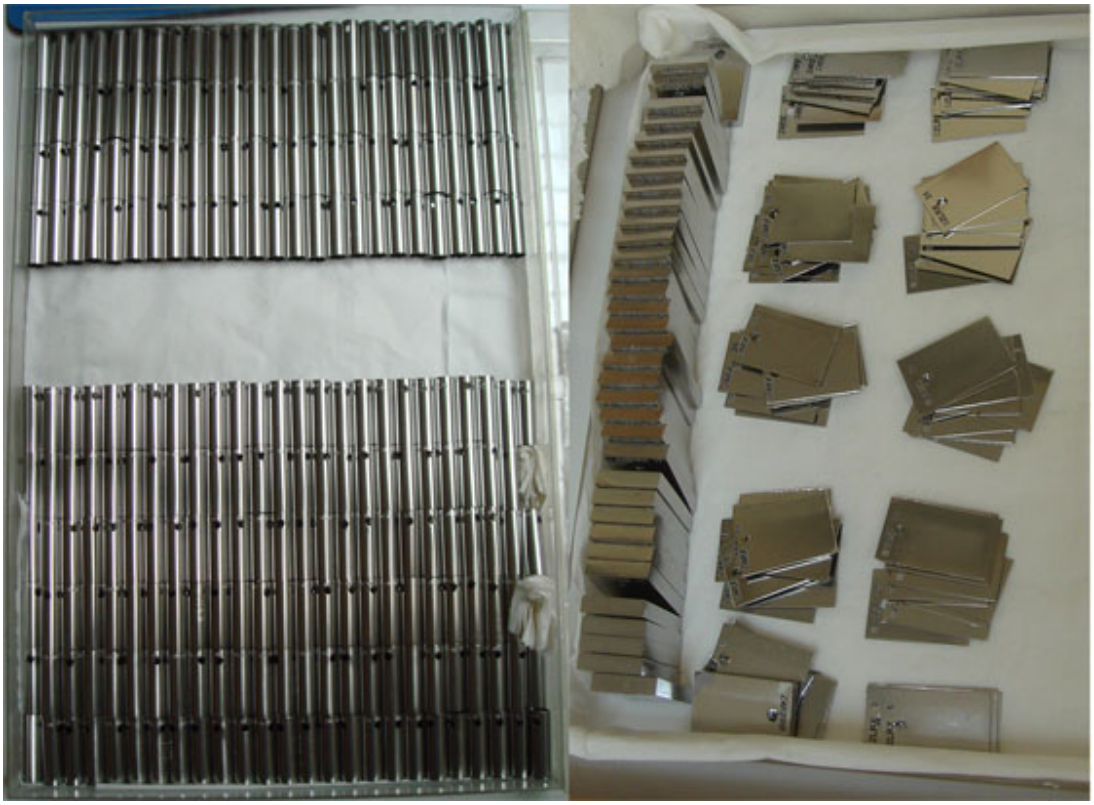

Figure 31: Tubes and sheets after pickling.

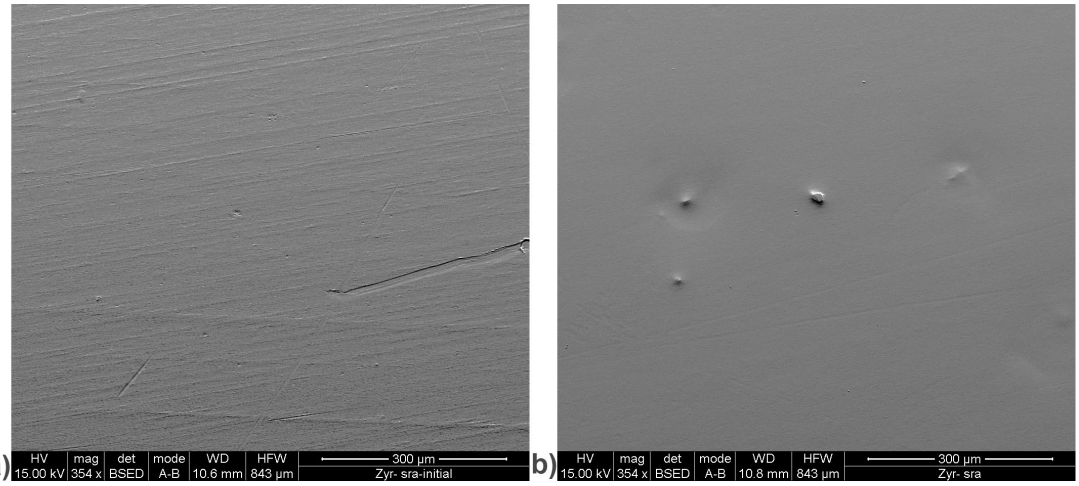

Figure 32: Surface examination of Zircaloy-4 A SR samples, (a) before pickling and (b) after pickling.

The freshly pickled samples were each given a unique ID, which has been kept un-altered through out the project. Table 7 is the summary of the IDs for both non-hydrided and hydrided samples.

Table 7: ID of the samples, letter i stands for the number.

Alloy	Non-hydrided			Hydrided	
	ID	MUZIC A short term	MUZIC B long term	ID	MUZIC C
X2 - SR	X2SRi	1-20	21-48	HX2SRi	1-20
X2 - RX	X2RXi	1-20	21-48	HX2RXi	1-20
Low tin ZIRLO - SR	OZLSRi	1-20	21-48	HOZLSRi	1-20
Low tin ZIRLO - pRX	OZLpRi	1-20	21-48	HOZLpRi	1-20
Low tin ZIRLO - RX	OZLRXi	1-20	21-48	HOZLRXi	1-20
ZIRLO™ - SR	ZLSRi	1-20	21-48	HZLSRi	1-20
ZIRLO™ - RX	ZLRXi	1-20	21-48	HZLRXi	1-20
sheet ZIRLO™ - SR	SZLSRi	1-20	21-48		
sheet ZIRLO™ - RX	SZLRXi	1-20	21-48		
Zircaloy 4 A - SR	Z4SRi	1-20	21-48	/	
Zircaloy 4 A - RX	Z4RXi	1-20	21-48		
Zircaloy 4 B - RX	Z4RXRRi	1-20	21-48		

3.2 SEM examination

Imaging of the oxide after corrosion experiment generally requires cross-sectional samples. Before cutting, a Ni layer approximately 50µm thick was coated on all

corrosion tested samples to protect the oxide. Detailed description of Ni coating is provided in a later chapter. Samples were then mounted in bakelite and ground on silicon carbide abrasive papers in sequence of 400, 600, 800, 1200, and 2500 grit. Each grinding stages took approximately 5 minutes. Polishing was performed using diamond paste, spending 5 minutes on 6 µm, 5 minutes on 1 µm and 10 minutes on 0.25 µm. The final polishing was conducted on a BUEHLER VibroMet^{TM}2 Vibratory Polisher using ϕ=0.05 µm polishing alumina suspension. Specimens spent 4 hours under 120 Hz, 20 % amplitude and 0.5 N load. Based on our experience, the best solution for characterisation of the zirconium matrix by optical microscopy is: 5 vol.% of hydrofluoric acid, 10 vol.% of nitric acid, 10 vol.% of sulphuric acid and 75 vol.% of distilled water. An example is given in Figure 33.

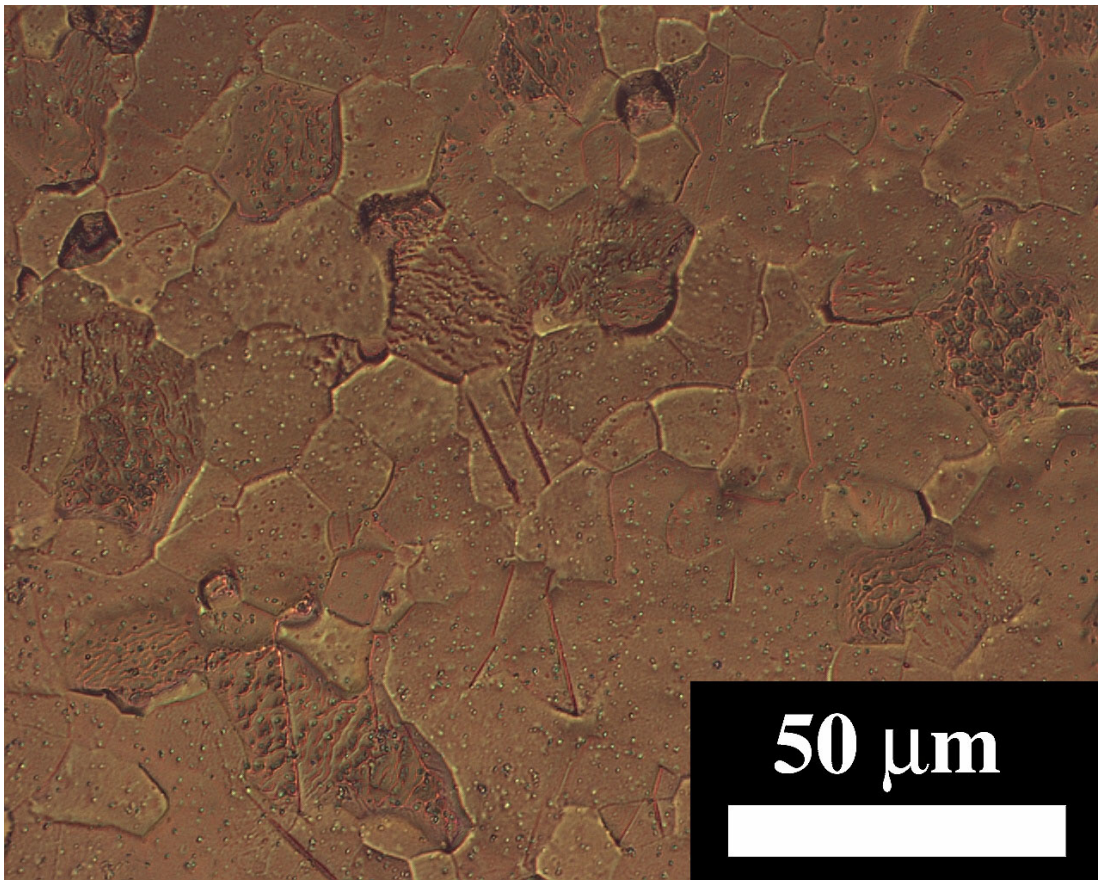

Figure 33: Optical microscopy of Zircaloy 4 B - RX, illuminated with normal light, x500 magnification.

Oxide examination requires higher resolution since the integrity of the oxide is evaluated by the density of the cracks. A solution of 5 vol.% hydrofluoric acid, 45 vol.% nitric acid and 50 vol.% distilled water at room temperature was used purely for etching away the metal debris trapped in the cracks. The etched surface was further plasma purged and carbon coated using a Gatan Model 682 PECS^{TM} precision etching & coating system. The plasma purge was conducted in a vacuum chamber at 8kV and 60° tilt. Immediately after that, a carbon layer around 5 nm thick was deposited. The carbon layer protects the cross sectional surface and greatly reduces the charging by electrons in SEM. Imaging of the cross sectional samples was performed using a Philips XL30 FEG-SEM. Exhibited in Figure 34 are the cross-sectional SEM images of a Zircaloy-2 beta quenched sample oxidised in steam at 415°C. This oxidised test piece was kindly provided by R. J. Comstock of the Westinghouse Electric Co., Pittsburgh, USA and Lars Hallstadius of the Westinghouse Electric Co., Sweden. It is clear that cracks and oxide have better contrast in Back Scatted Electron mode (BSE), which provides atomic and orientation contrast, than in Secondary Electron mode (SE), which provides topography information. The undulated metal/oxide interface in Figure 34 is actually a 3-D structure as further demonstrated in Figure 35. The metal substrate was chemically etched away, leaving the interface untouched.

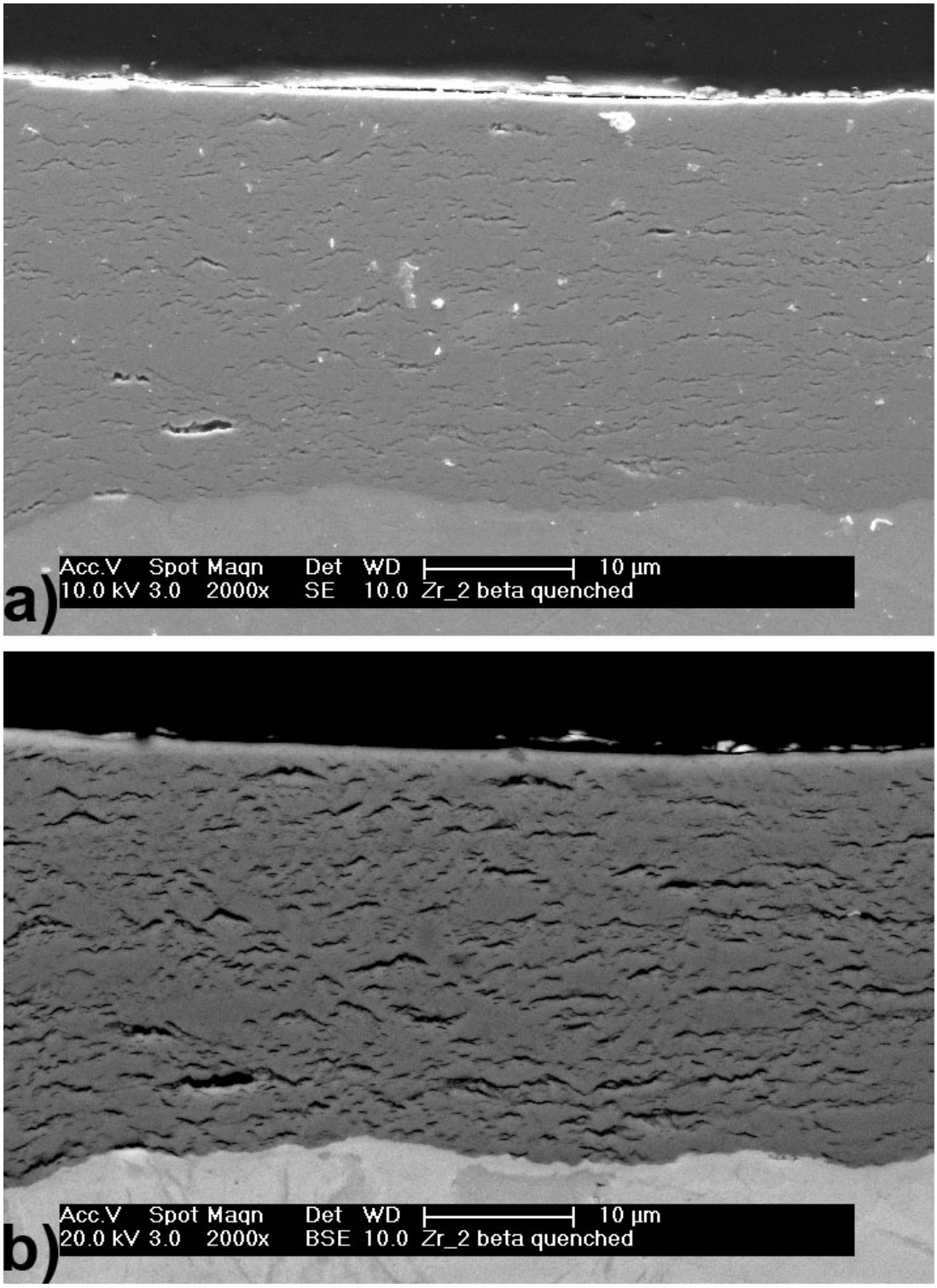

Figure 34: Zircaloy-2 beta quenched samples previously oxidised for 660 days at 415°C in steam, (a) secondary electron image and (b) back scatted electron image.

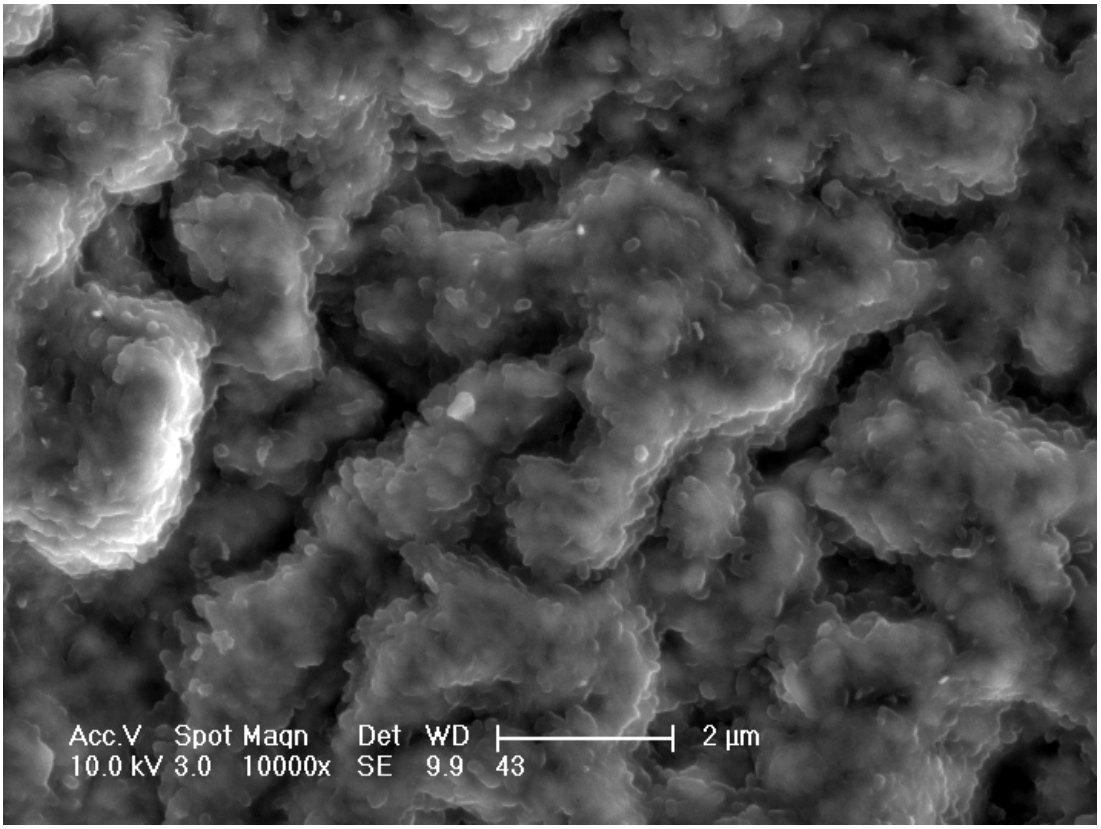

Figure 35: Secondary Electron image of metal-free Zircaloy-4 RX samples air oxidised for 144 hrs at 415°C. Image was taken when looking perpendicular to the metal/oxide interface, the metal substrate was removed via chemical etching.

3.3 Focused Ion Beam (FIB) and Transmission Electron Microscopy (TEM)

FIB is a common technique for TEM sample preparation especially when the precise location of a TEM sample is of importance. For instance, the current study employs the in-situ lift-out (INLO) technique to extract specimen from the bulk hydrides of cathodically hydrided materials. Other advantages of FIB sample preparation include the potential of creating thin film sample with near parallel surfaces, large electron-transparent area, high throughput and reliability [157].

A FEI Nova 600 NanoLab dual-beam instrument, which integrates FIB and SEM, was employed for this study. The INLO procedure for TEM specimen extraction from zirconium/hydride mixture is described below:

- Deposition of protective layer: 1 µm thick of Pt was deposited on top of the target site.
- Trenching and rough milling: large trenches are milled at maximum beam current, creating a foil 10-15 µm long and 1-2 µm thick, thus defining the shape and orientation of the foil (intercepting the hydride platelet in this particular case). A U-shaped cut was made at the end of this stage to partially free the foil.
- Transfer: Using an AutoProbe^{TM} 200 nanomanipulator of the Omniprobe, Inc., the foil was transferred onto a TEM half-gride.
- Thinning and fine milling: the thickness of the foil was progressively decreased by fine milling on both of the alternating sides.
    - 960 seconds at 30 kV, 500 pA.
    - 840 seconds at 30 kV, 280 pA.
    - 1500 seconds at 30 kV, 93 pA.
    - 420 seconds at 8 kV, 120 pA.
    - 420 seconds at 5 kV, 98 pA.
    - 120 seconds at 2 kV, 210 pA.

  The sample stage repetitively tilted between 52° and 54° to ensure uniform thickness of the sample.

A final thickness less than 100 nm was achieved. The TEM foil was then investigated using a Philips CM200 TEM operating at 200kV. With selected area aperture, a selected area diffraction pattern (SADP) of the hydride grain of interest was captured. For crystalline materials, the SADP pattern exhibits strongest intensity at

specific angles where the Bragg-diffraction condition is satisfied. This diffraction pattern is a representation of crystalline structure and sample orientation. Phase identification was conducted by comparing the captured diffraction pattern to reference crystal structures, which in this study confirmed the hydride grains in hydrogen charged samples have an f.c.c. crystal structure. By physically moving the objective aperture to select diffracted electron beams of the f.c.c. crystal, Dark Field (DF) images highlighting one of the hydride grains were captured in displaced-aperture DF mode.

3.4 The synchrotron X-ray diffraction technique

Synchrotron X-ray diffraction was employed as the main characterisation technique for the oxide layer. The angles for coherent scattering of the X-ray from a crystallite lattice are described in the Bragg's expression below:

$$n\lambda = 2d \sin\theta \tag{10}$$

where n is the integer, λ is the wavelength of incident beam, d is the spacing between crystal lattice planes and θ is the angle between the incident beam and diffracted beam. A Bragg peak is produced if the diffracted X-ray from certain lattice planes interfered constructively, as shown in Figure 36. In the case of monochromatic radiation where all photons are refined in a fixed wavelength, the lattice spacing and lattice parameters are the function of Bragg peaks' position.

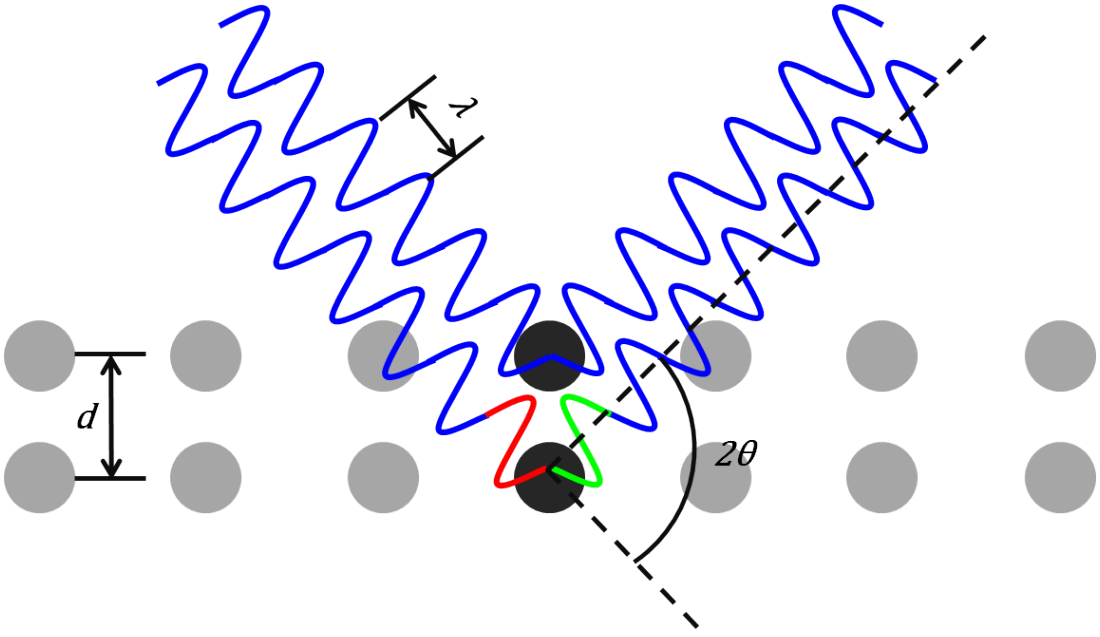

Figure 36: Constructive interference under Bragg's condition.

The EDDI beamline of BESSY II (Berlin) is, however, an energy dispersive beamline dedicated to material science. EDDI was designed by BESSY and HMI and built by the Budker Institute in Novesibirsk. Although the designed energy spectrum ranges

from 15 to 150 keV, the evaluable diffraction spectrum for typical energy dispersive diffraction experiments lies between 20 to 80 keV. The beamline makes direct use of the white synchrotron beam provided by the wiggler, as shown in Figure 37 [158]. In this case of polychromatic radiation with a fixed 2θ, the above expression is modified by introducing Planck's relation below:

$$E = \frac{hc}{\lambda} \tag{11}$$

where E is the energy of a photon, λ is the wavelength, c is the speed of light in vacuum and h is the Planck constant. The lattice spacing is now represented by the energy level of the diffracted photons instead of 2θ angles.

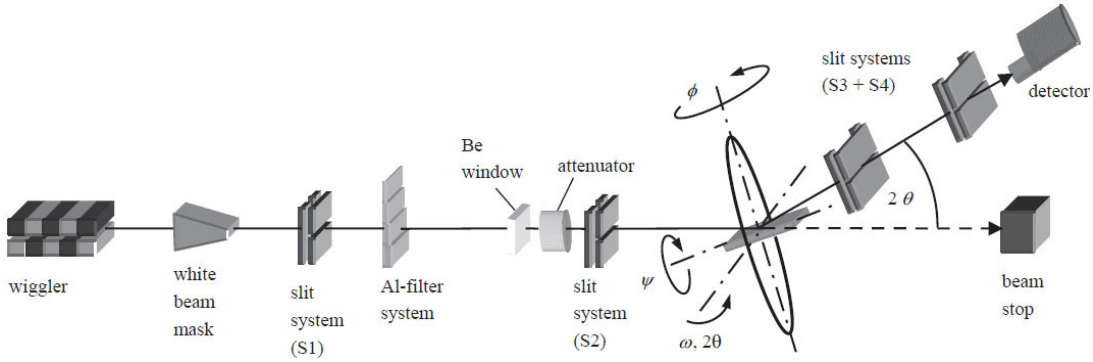

Figure 37: Schematic layout of the EDDI beamline components [158].

In the case of the present work, an incident beam of 500 x 500 µm was employed. The diffracted beam was defined by sets of slits to 30 µm. Samples were mounted on a motorised stage with 5 degree of freedom and capable of movement in sub-micron accuracy, Figure 38. With a calibrated laser and integrated CCD system, it was possible to pinpoint the synchrotron beam on the exact location of interest, in our case, different regions of the oxide layer (black, grey and white regions). Counting time for the measurement was decided to be 60s balancing the signal to noise ratio and the relatively limited beam time. To make the best use of the

limited beam time, 2 customised sample stages were designed and manufactured at School of Materials, The University of Manchester. Up to 7 tubes or 6 sheets could be mounted and measured at a time, each having its rolling direction parallel to the beam direction.

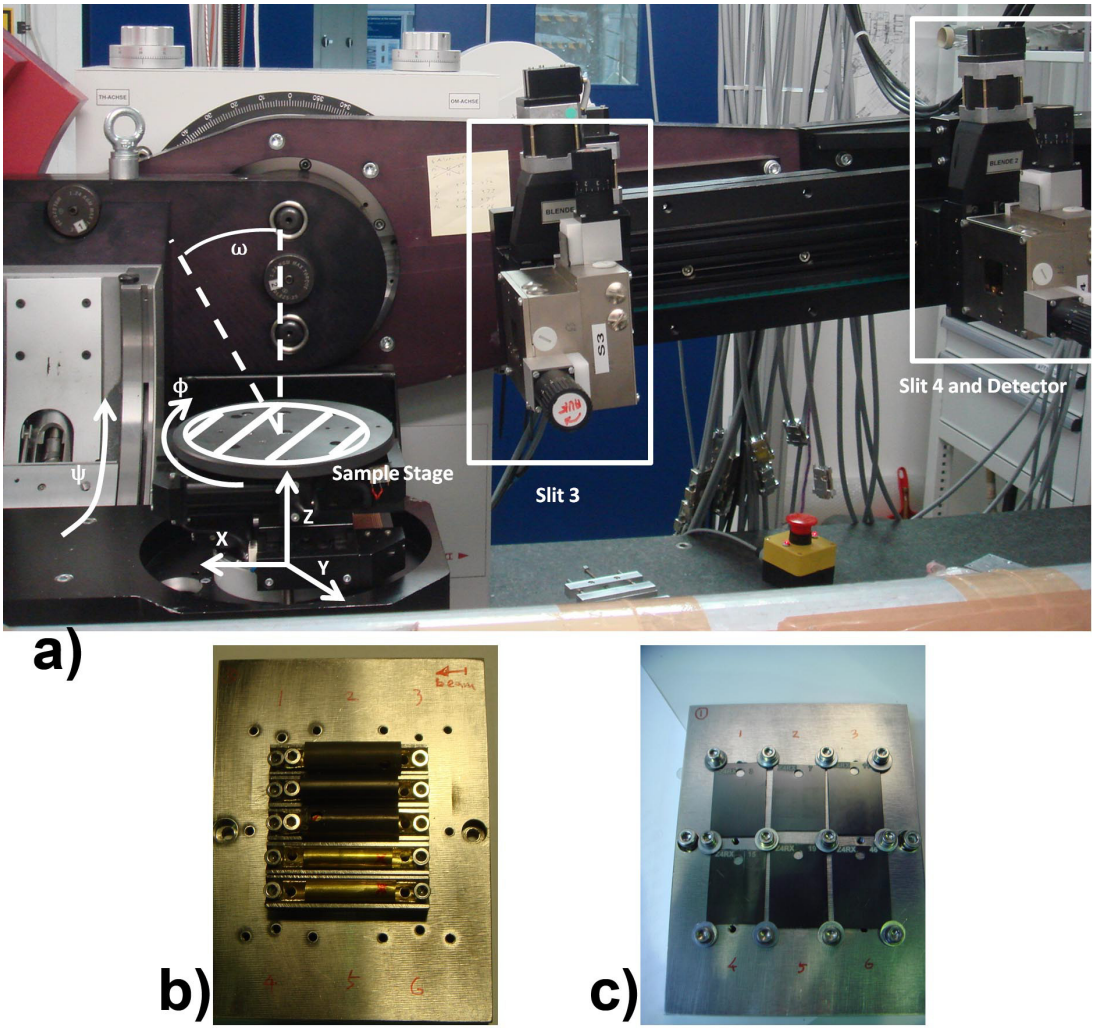

Figure 38: (a) EDDI-diffractometer with 5-axes positioner and removable slit systems, (b) and (c) customised stages for MUZIC tubes and sheets.

The diffractometer, beamline hatch and the detector system are controlled by the computer software package *spec* [159] of the Certified Scientific Software. A liquid nitrogen cooled LEGe detector from CANBERRA is used for data acquisition. The specified detector resolution by CANBERRA is 160 eV at 10 keV energy and 420 eV at 100 keV [158]. The acquired spectrum is analysed using a MATHEMATICA™ script

developed in-house by EDDI's beamline scientists. The diffraction peaks are fitted using a Pseudo-Voigt function, providing information such as peak intensity, peak position and Full Widths at Half Maximum (FWHM).

The strategy of the current study is to obtain residual stress information regarding the oxide via the $sin^2\psi$ approach. The concept of the employed $sin^2\psi$ method and data analysis has been described in publication 1, 3 and 4 respectively. To avoid repetition, only a brief description is presented here.

The principle of the $sin^2\psi$ method is the tilting of a sample in a plane perpendicular to the incident beam and measurement of $d_{\varphi\psi}$ at different ψ angles, which is described in the expression below [160]. Note that biaxial stress-state is assumed for this method (i.e. thin oxide film or hydride rich layer grown on the surface).

$$\varepsilon_{\varphi\psi} = \frac{d_{\varphi\psi} - d_0}{d_0} = \frac{1}{2} S_2 \sigma_\varphi sin^2\psi + S_1(\sigma_{11} + \sigma_{22}) \quad (12)$$

where $\varepsilon_{\varphi\psi}$is the strain generated by residual stress in polycrystallite, $S_1 = -\frac{\nu}{E}$, $S_2 = \frac{1+\nu}{E}$, $d_{\varphi\psi}$ is the d spacing at different ψ angles, $d_0$is the stress free d spacing, σ_{11} and σ_{22} are the principal stresses.

It can be further deduced that the residual stress in the material: $\sigma_\varphi = \left(\frac{E}{1+\nu}\right)\left(\frac{\partial d_{\varphi\psi}}{\partial sin^2\psi}\right)\frac{1}{d_0}$. Note that at ψ = 0°, $d_{\varphi 0} = d_0[1 + S_1(\sigma_{11} + \sigma_{22})] = d_0\left[1 - \frac{\nu(\sigma_{11}+\sigma_{22})}{E}\right]$. Since ν is much smaller than E, $d_{\varphi 0}$ is considered to be equal to the stress free d spacing d_0. This is especially convenient in the case of tetragonal zirconium oxide. Tetragonal phase is unstable at room temperature and zero stress state, making the measurement of d_0 impossible.

Another advantage of the $sin^2\psi$ method is that it is non-destructive, so that the sample can be retained for future study. The current study utilised this by re-inserting measured specimens back to autoclave corrosion experiments. The same specimens were measured again after additional exposures. Previous researchers attempted alternative measurement techniques to determine residual stresses of material. F. Garzarolli et al. [161] steam oxidised Zircaloy-4 sheets at 400°C. Samples were then ground from one side to remove the oxide. The curvature of the thin remaining metal resulting from the compressive stresses in the oxide was used to evaluate the average stress in the oxide. Similar practice was conducted in [162] and improved by Y.–S. Kim et al. who performed in-situ measurements during oxidation of only one side of the sample [163]. The curvature measurement only provides macro-stress information over the entire sample, and generally involves partial or complete destruction of the sample. The Raman technique is capable of recording residual stress state in different oxide phases as well as providing phase fraction information with high spatial resolution [164]. Raman also suffers from surface sensitivity issue since only the top few nanometres of the material are investigated. It is possible to obtain depth profile of both phase fraction and residual stress information by preparing cross-sectional samples. However, whether and to what extent the creation of a cross-sectional surface interferes with the results remains unclear. X-ray diffraction method uses lattice spacing as strain gauges. By altering the incident angle and beam energy, the variable penetration depth can be adjusted according to the thickness of the oxide. Previous applications usually combined laboratory X-ray with $sin^2\psi$ method to provide residual stress information regarding the oxide. The nature of laboratory X-ray diffraction makes it

difficult to apply the same method on small quantity of tetragonal phase. It also suffers from relatively big error due to peak broadening and low resolution due to the size of the beam [165-168]. The high flux and brilliance of the synchrotron X-ray allow data acquisition with a much higher strain resolution and better quality when compared with laboratory X-ray. By combining $sin^2\psi$ method and monochromatic radiation, residual stress measurements were conducted without the requirement for strain-free lattice parameters [169, 170]. Note these studies did not take into account the depth variation of stress in the oxide. M. Preuss et al. [55] employed monochromatic radiation in transmission mode to investigate both tetragonal and monoclinic phase fraction, texture and residual stress information of the oxide with high spatial resolution as well as depth profiling. Unlike the $sin^2\psi$ method, in this case strain-free lattice spacings are required for the investigated reflections. Note that the extraction of transmission samples involved creation of 2 fresh surfaces. Hence this methodology suffers from the same issue as Raman does. The selection of diffraction peaks for further analysis as well as the elastic constants for different phases has been described respectively in proposed publication 1, 3 and 4.

3.5 Pole figure measurement

The morphology of the oxide grain is indirectly represented by the strength of the oxide texture. By measuring pole figures on the exact same samples investigated on the EDDI beamline, attempts were made to correlate oxide grain misorientation with the corrosion performance. A BRUKER D8 Discover diffractometer was employed to record pole figures on corroded tubes. The diffractometer is equipped with third generation Göbel Mirrors providing high flux X-ray for thin film

applications. A Co X-ray source was selected, operating at 35KV and 40mA in point focus mode (λ=1.789Å). With PolyCap^{TM} on the primary side, a circular X-ray beam with ϕ=0.5mm was defined. A customised laser device and multi-position sample holder were designed and manufactured for this diffractometer. Using a fluorescence calibration stage, the laser spot was adjusted to indicate the position and area which coincide with the X-ray beam. Due to the relatively small spot size, it is possible to conduct measurements on both grey and black regions of the oxidised samples. This procedure is similar to that has been applied during synchrotron measurements at EDDI, BESSY II. A 0.02 mm thick high purity Fe filter was installed on the primary side to suppress the background. No filter was used on secondary side during measurements. Measurements were conducted in coupled $\theta/2\theta$ mode with 3 seconds counting time. The range of polar angles was from 0° to 85° at 5° increment, azimuth angles from 0° to 360° at 10° increment. Measurements were focused on $(\bar{1}11)$ reflection of the monoclinic oxide phase because this peak could be measured with the highest certainty. The estimated penetration depth in the current setup was 8 µm, exceeding the oxide thickness of any involved samples. The diffractometer was calibrated daily using a corundum reference standard. The recorded spectrums were analysed using computer software package MULTEX^{TM} developed by Bruker AXS GmbH, which generates pole figures also calculates maximum normalised intensities.

4 Proposed Publications

4.1 Introduction

As discussed in a previous chapter, the aqueous corrosion of zirconium metal phase is the main source of hydrogen. In order to understand the mechanism behind effects of hydrogen upon the corrosion behaviour of zirconium alloys, the ideal approach would be studying materials which have undergone prolonged corrosion and naturally formed a hydride rich region near the oxide/metal interface. This requires a temperature gradient in the sample which can not be easily provided during autoclave testing. The extensive degree of oxidation required by hydride rim formation would also generate a thick oxide layer on the sample surface, acting as an obstruction for investigations. A feasible solution is to employ artificial hydrogen charging via cathodic hydrogen charging technique prior to autoclave corrosion experiments. The aim is to obtain unoxidised samples with hydrogen content above the hydrogen solubility limit, which is about 120 wt.ppm at 360°C [120, 121],. The distribution and the structure of the hydrides are required to be representative of room temperature observations on sample experienced prolonged autoclave corrosion test or actual end-of-life clad from nuclear reactor.

Proposed publication No.1 gives a detailed description of the cathodic hydrogen charging technique as well as analysis and discussion regarding the hydride rim. Based on the results, successfully hydrided test pieces were selected for use in subsequent autoclave corrosion experiments. All accepted test pieces have an overall hydrogen level of about 600 to 700 wt.ppm, corresponds to about 11,000 to 12,000 wt.ppm of local hydrogen concentration at the outmost region of the tubes.

The surface quality of the hydrided tubes was checked via SEM examinations on randomly selected samples from each alloy and heat treatment conditions. Seven alloys and heat treatment conditions were accepted as suitable for further experiments. They were stress relief annealed and recrystallised X2; stress relief annealed, partially recrystallised and recrystallised low tin ZIRLO; stress relief annealed and recrystallised ZIRLO^{TM}. Test pieces of 50cm length were cut into smaller specimens of 30mm length. 180 hydrided specimens were prepared. The control group used non-hydrogen charged specimens as reference. 612 reference specimens were prepared. The amount of specimens was decided on these grounds: to provide sufficient amount of data for corrosion kinetics evaluation, to counteract potential sample lost during prolonged autoclave experiments and to provide readily oxidised specimens for future investigations.

Detailed descriptions of the autoclave experiments as well as preliminary analysis are presented in proposed publication No.2. Autoclave corrosion experiments were performed at the EDF Research and Development facility in Moret-Sur-Loing, France. At this stage, individual specimens were each given a unique identification code, which was kept unaltered during this PhD study. This specimen ID is linked to a data base which collects information such as alloy type, heat treatment, cathodic hydrogen charging results, allocated position inside the autoclave, autoclave exposure history, recorded weight gain data at each autoclave stop and history of characterizations conducted on specific specimen.

In total, four autoclaves were used. MUZIC A autoclave aimed at providing samples and corrosion kinetics data up to the 1st transition for reference materials. MUZIC B

autoclave aimed at providing samples and corrosion kinetics data after several transitions and breakaway for reference materials. MUZIC C autoclave aimed at providing samples and corrosion kinetics representative of the early and/or immediate breakaway behaviour of hydrided materials. Finally MUZIC D autoclave aimed at providing data and samples from initial corrosion stage of both reference and hydrided materials.

To date, autoclave corrosion experiments are still continuing in MUZIC B autoclave. Two distinctive trends are observed: reference samples experience 1st transition earlier with increasing tin content; corrosion of hydrided samples is more susceptible to acceleration with increasing tin content. Based on the results presented in publication No.2, three alloys in recrystallised condition were selected for more detailed characterisations in publication No.3. The same alloys were studied again in publication No.4, comparing the effect of hydride rim upon the corrosion performance. We are currently preparing publication No.1 for Materials Chemistry and Physics, No.2 for Corrosion Science, No.3 and No.4 for Acta Materialia.

Publication Number 1

Synthesis of a hydride rich rim on zirconium alloys: a cathodic hydrogen charging method

Synthesis of a hydride rich rim on zirconium alloys: a cathodic hydrogen charging method

J. Wei[1], P. Frankel[1], K. Govender[1], M. Blat[2], A. Ambard[2], R. J. Comstock[3], Lars Hallstadius[4], S. Lyon[1], R.A. Cottis[1] and Michael Preuss[1]

1: Materials Performance Centre, School of Materials, The University of Manchester, UK

2: EDF - R&D, Moret sur Loing, France

3: Westinghouse Electric Co., Pittsburgh, USA

4: Westinghouse Electric Co., Sweden

Abstract

The paper describes the methodology of cathodic hydrogen charging of zirconium alloy sheet and tube material followed by a heat treatment with the intention to create a hydride rich rim similar to observations made in end-of-life fuel claddings on in-reactor material. The overall hydrogen levels in the samples were determined via inert gas fusion while hydride volume fractions within the rim were determined using laboratory X-ray diffraction analysis. Detailed microstructure, texture and phase analysis of the hydride rich rim was undertaken by means of scanning and transmission electron microscopy as well as laboratory X-ray diffraction. The residual stress state in the rim was investigated by synchrotron X-ray diffraction. It was found that the hydrogen charging process is very sensitive to the chemistry of the cell solution. A vertically assembled charging cell can significantly reduce the

amount of trapped air bubbles, hence reducing disturbances caused by contact break up. With the given geometry of the charging cell in the present study it was possible to create a crack free and consistent hydride rich rim in tube but not sheet material. The hydrogen levels in the hydride rich rim near the surface were about 11,000 wt.ppm and it was found that the rim consists predominantly of δ hydrides with a stoichiometry close to $ZrH_{1.7}$. The stresses in the hydrides were found to be surprisingly low after heat treatment. Crystallographic texture measurements of the hydrides and the metal confirmed that the typical $(0002)_{\alpha-Zr} \parallel (111)_{\delta-Zr}$ crystallographic relationship is created by the anodic charging process. The observations of the artificially created hydride rich rim are discussed in the context of end-of-life clad observations from the literature.

Introduction

During reactor service of zirconium alloys, the predominant source of hydrogen atoms is the corrosion reaction between water and zirconium. Other sources of hydrogen include radiolysis of coolant water and LiOH addition for pH control [1-3]. While the majority of the hydrogen atoms created during the corrosion process remains in the cooling medium, the zirconium matrix picks up a small fraction of hydrogen. The hydrogen pick up has to be considered in fuel rod performance since hydrogen has a limited solubility in the zirconium lattice under normal operating temperatures leading to hydride formation. At 360°C, which is close to typical service temperature and a typical temperature used during autoclave testing, the solubility limit is 120 wt.ppm [4, 5]. An important aspect of hydrides in zirconium is that hydrogen diffuses down temperature gradients and up stress gradients [6].

Hydrides in zirconium are expected to generate significant residual stresses due to the associated 17% volume expansion with the hydride formation [7]. They also tend to reorientate when the material is exposed to a thermal cycle under tensile stresses [8-11]. Since the encapsulated fuel and water coolant create a through thickness temperature gradient in the clad, hydrides tend to accumulate at the outer surface of cladding tubes. Hydrides in zirconium cladding are of concern since they have a detrimental effect on mechanical performance [12-14], and can cause fuel rod swelling and distortion due to their low density compared to the metal [15-18]. It has been also proposed that the formation of a hydride rim results in breakaway corrosion [6, 19-26], although a mechanistic explanation of such deterioration remains elusive.

The formation of a hydride rich rim requires prolonged exposure in either reactor core or a heat flux rig that allows undertaking corrosion testing in the presence of a temperature gradient, which makes any mechanistic corrosion studies in the presence of a severe hydride rim difficult. An alternative approach is to first artificially introduce hydrogen into zirconium metal and synthesis the formation of a hydride rich rim by cathodic hydrogen charging before exposing the material to autoclave testing.

The present work describes in detail the process of cathodic charging and includes a detailed analysis of the hydride rich rim created in this way. A total of four commercial alloys and one model alloy in up to 3 different heat treatment conditions were hydrogen charged in order to identify any effects of the alloy chemistry on the ability to hydrogen charge zirconium alloys. The hydrided material

was subsequently investigated by SEM, TEM, laboratory X-ray and synchrotron X-ray diffraction to determine the structure, phase fraction, crystallographic texture and stresses in the hydrides. The observations were compared with available data from the public domain on hydride rims created by in-reactor testing.

Experimental

Materials Preparation

The alloys studied here are Zircaloy-4 (Nb-free Zr alloys), ZIRLO^{TM}, low tin ZIRLO and X2 (Nb-containing Zr alloys). Table 1 summarises the key alloying elements of these alloys as well as their initial hydrogen concentration. Chemical compositions were determined at the EDF Research and Development facility in Moret-Sur-Loing, France. All material had been provided by Westinghouse. A total of three heat treatment conditions, stress relieve annealed (SR), partially recrystallised (pRX) and recrystallised (RX) were employed. Note that the partially recrystallised low tin ZIRLO alloy is also known as Optimised-ZIRLO^{TM}, which is a commercial alloy distributed by Westinghouse. X2 is an experimental alloy.

Two types of sample geometry were selected. Tube samples of 500 mm in length (9.5 mm in diameter) and sheet samples of 85 mm in length (24 mm in width). The wall thickness of the tube samples was 0.6 mm. The ZIRLO^{TM} sheet samples were 0.5 mm thick while Zircaloy-4 sheet samples had a thickness of 0.7 mm. All samples were pickled in a solution of 10 vol.% hydrofluoric acid, 45 vol.% nitric acid and 45 vol.% distilled water for 3 minutes to remove inorganic contamination from the fabrication process. The resulting clean surface was considered to be beneficial for

subsequent hydrogen charging by providing better contact surface for the charging circuit.

Cathodic hydrogen charging and the determination of overall hydrogen level

Cathodic hydrogen charging was conducted in a 0.1 mole/L KOH solution with a fixed current density of 10 mA/cm^2. The choice of charging solution was based on preliminary experiments conducted by the EDF R&D which suggested that KOH solution is gentler than conventional acidic solutions and leads to homogeneous and more controllable results. The schematics of the cathodic hydrogen charging cell as well as the set up of the charging circuit can be found in Figure 1 (a). A special electrode design was employed in order to only cathodically hydrogen charge the outer surface of tube samples. A spring loaded Pt-mesh was insert into the tube to provide uniform contact across the full longitude direction. The inner surface of the tube was then insulated from the charging solution by insulator plugs at the two end of the tube, Figure 1 (b). A simpler mechanical connection was employed on sheet samples since both surfaces require hydrogen charging, Figure 1 (c).

A single tube sample was inserted into the centre of a cylindrical platinum counter-electrode (Figure 2) and together placed into the horizontal charging batch. The platinum counter-electrode, a.k.a. 'platinum basket', is 60 mm in diameter and 600 mm in length. It was soon discovered that air bubbles were generated during the prolonged charging process, and trapped inside the platinum basket, breaking up its contact with the charging solution. By converting the horizontal charging bath into a vertical charging cell (Figure 3), the air bubbles were quickly released from the

charging solution, no longer causing disturbances. Sheet samples were always charged in vertical charging cells, with a shorter platinum counter-electrode (60 mm in diameter and 100 mm in length). All the charging cells were insulated from the atmosphere. Generally, each cycle of cathodic charging lasted around 10 days.

After cathodic charging, hydrogen concentrations were determined by inert gas fusion analysis using a H-MAT 2500 (Ströhlein) analyser at the EDF Research and Development facility in Moret-Sur-Loing, France. The process involves smelting of a 3 mm long quarter of the tube sample or a 3 x 5 mm piece of the sheet sample. The generated gas was carried into a measurement chamber by a flow of reference gas. Thermal conductivity of the carrier gas free of hydrogen (purified Ar with residual hydrogen, oxygen and nitrogen removed via molecular sieve and Carbon monoxide via a special reagent) was compared with that of the mixture (carrier gas + hydrogen). With appropriate calibration, the mass of H in the sample was extracted and by dividing it by the total mass of the sample, it gave the overall hydrogen concentration in wt.ppm. Calibration of the Wheastone bridge (measurement chamber) was performed by introducing calibrated volumes of pure hydrogen gas into the circuit before every measurement. The calibration was checked frequently by smelting a reference sample. By adding a pellet of tin it was possible to reduce the fusion temperature and carry out smelting at 1550°C. Note that this technique only provides the overall hydrogen level in the entire sample, not local hydrogen concentrations.

In case the hydrogen levels were low after the first cycle, further 10 days charging was carried out. The maximum charging time was 40 days. Once the material had

reached a minimum level of around 500 ppm, charging was stopped and a heat treatment for 24 hours at 400°C followed by furnace cooling was carried out. The purpose of the heat treatment was to slightly redistribute hydrogen further into the bulk of the materials, as well as relaxing the residual stresses generated during hydrogen charging. A final hydrogen analysis was carried out on each sample at the top end, the middle part and the bottom end.

Characterisation of the hydrogen charged materials

Cross-sectional samples were prepared for microstructure examinations of the hydrogen charged materials. Ni-coating was applied prior to mechanical sample preparations in order to protect the hydride rich rim. Samples were coated in a solution of $NiSO_4 \cdot 6H_2O$ (240 g/L), $NiCl_2 \cdot 6H2O$ (45 g/L), H_3BO_3 (30 g/L), Saccharin (1 g/L), Sodium Lauryl Sulphate (0.2 g/L) and Coumarin (0.18 g/L) with a fixed current density of 20 mA/cm^2. Cross-sectional samples were subsequently ground and polished followed by etching the sample in a solution of 5 vol.% hydrofluoric acid, 45 vol.% nitric acid and 50 vol.% distilled water at room temperature. Freshly etched samples further received deposition of a carbon layer around 5 nm thick using a Gatan Model 682 PECS^{TM} precision etching & coating system for SEM. The carbon layer helped reducing charging effects during SEM imaging. The microstructure characterisation was carried out in a Philips XL30 field emission gun scanning electron microscope (FEG-SEM).

Laboratory X-ray diffraction was used to obtain phase identification and local hydride phase fraction information. A Philips X'Pert MPD operating at 45kV (Cu-tube) in glancing-angle set up was used. A fixed Incident beam at $\theta = 6°$ ensured

that 90 % of the signal was collected from the top 3 µm of the specimen surface. Diffraction spectra ranging from 25° to 85° were recorded and a Rietveld analysis was carried out using the commercial software package Topas^{TM}.

A BRUKER D8 Discover diffractometer operating at 35kV (Co-tube) in coupled θ/2θ mode was employed to undertake crystallographic texture measurements on the hydrides and the metal matrix in an attempt to determine the crystallographic relationship between the two phases. A spot size of d≈0.5mm was selected and the maximum penetration depth was estimated to be around 8µm. The maximum chi angle during the texture measurements was 85°. Partial pole figure were collected for (0002) reflection of the α–Zr phase and the (111) reflection of the δ-hydride phase in order to confirm the crystallographic relationship usually observed between the two phases [27].

A FEI Nova 600 NanoLab dual-beam instrument, which integrates a Focused-Ion-Beam (FIB) and FEG-SEM, was used to extract Transmission Electron Microscopy (TEM) specimens. These specimens were subsequently investigated using a Philips CM200 TEM operating at 200 kV.

Synchrotron X-ray diffraction experiments were carried out on the EDDI beam line at BESSY II, Berlin, Germany, to determine the residual stress state of the hydrides and the surrounding metal. A detailed description of the EDDI beam line can be found in [28]. Since the measurements were carried out close to the surface, it was assumed that the stress state of the hydrides and the metal matrix is biaxial with zero out-of-plane stress. This assumption then allowed to conduct residual stress measurements following the $\sin^2\Psi$ set up with incident beam and EDX detector

both fixed at 3° when Ψ = 0°. Combined with the assumption of a biaxial stress state in a Cartesian coordinate system, residual stresses in different phases of the thin hydride rich rim layer (α–Zr and δ Zr-hydride) were measured non-destructively without the requirement for stress free lattice parameters. Stress values measured in rolling and transverse directions showed no significant variations. A BESSY II in-house analysis program written in MATHEMATICA^{TM} was used for processing diffraction data. Elastic properties used for each phase are presented in Table 3 [17, 18, 29].

Results and discussion

Cathodic hydrogen charging

First charging trials failed in many cases by not exceeding 100 wt.ppm hydrogen even after extended exposure. Impurities in the KOH solution (A) were suspected to be the cause and a second batch of KOH solution, KOH (B), was produced. Using solution (B), successful hydrogen charging was achieved in all tube samples within a single 10 days session. An impurity analysis of the two solutions (Table 2) confirmed that solution (A) had indeed slightly higher impurity levels than solution (B). The average hydrogen levels for each tube alloy and condition are shown in Figure 4. The data show no clear trend between the three alloys and the different heat treatment conditions. The measurements of the top end, middle part and bottom end of each tube showed no systematic variation of hydrogen levels. However, significant variability of hydrogen levels was found between samples of the same condition, which is reflected in significant error bars seen for some conditions in Figure 4.

Hydriding conducted on the sheet samples was erratic even after switching to KOH B solution. Most of the Zircaloy-4 sheet samples received around 650 to 1000 wt.ppm of overall hydrogen levels after 30 days of charging but some samples failed to charge completely. In the case of ZIRLO^{TM} sheets most samples failed to charge even when increasing the charging time to 4 cycles.

Characterization of the hydride rich rim

In order to investigate the integrity of the hydride rich rim created by cathodic charging, SEM examinations were conducted on sheet and tube samples. Figure 5 displays an example of recrystallised Zircaloy-4 sheet with overall [H] of around 950 wt.ppm. Surface examinations of hydrogen charged sheet samples without further sample preparation revealed small cracks every few microns as well as pits sized from 5 to 10 μm, Figure 5 (a). Figure 5 (b) indicates that the cracks are about 2 to 5 μm long and tens of nm wide. The image also suggests that the cracks have grown along grain boundaries of the former metal grain, which is now occupied by clusters of hydride grains. The pits are of the same size and shape range of former metal grains, which suggests that they have dropped out spontaneously. Cross-sectional back-scattered electron mode images were taken at many different locations to investigate thickness variations of the hydride rich rim. It was found that in sheet material the hydride rich rim was thickest near the edge (at least 20 μm) and thinnest (about 5 μm) in the middle of the sample. Figure 5 (c) shows an extreme example displaying a dramatic hydride rich rim thickness variation within less than 100 μm. Note that in a backscatter image the hydride rich rim is darker than the metal matrix. The image also reveals that the cracks observed from the top of the

sheet (Figure 5 (b)) had only grown a few microns into the hydride rich rim. Examples of a hydrogen charged tube sample can be seen in Figure 6. In this case, recrystallised ZIRLO^{TM} with overall [H] of around 700 wt.ppm is displayed. Figure 6 (a) shows almost no surface cracks in the tube sample. The few and distant spaced cracks were about 1 to 2 μm in length and randomly oriented on the surface. No relationship between crack direction and grain boundary of former metal grains were observed (Figure 6 (b) and (c)). The cracks were only sub-microns deep and the majority of the hydride rich rim can be generally considered as crack free, Figure 6 (d). Further cross-sectional microstructural examinations of hydrogen charged tube material revealed that the rim region had a consistent thickness of around 15-20 μm and that the heat treatment had resulted in widely spaced strings of hydrides orientated circumferentially throughout the wall of the clad (Figure 7 (a) and (b)). While it was impossible to visualise individual hydrides in the rim, the bulk hydrides appeared to be chains of individual platelet-shaped hydride grains each 5 to 10 μm long and several hundred nm wide, Figure 7 (c) and (d).

The potential field built up around the Zr sample controls the process of cathodic hydrogen charging. The overall charging current was fixed at 10 mA/cm^2, making the process independent of sample area variations. However the local distribution of the potential field strongly depends on the geometry of the sample. As demonstrated in Figure 8, the edges of sheet samples are exposed to high potential fields and therefore are bound to receive more hydrogen charging compared with the middle of the sheet. In contrast, tube samples receive a uniform potential field and therefore will form a more uniform hydride rich rim. This schematic drawing is

in good agreement with the variation of rim thickness as described earlier although it does not explain the dramatic variation demonstrated in Figure 5 (c). The poor quality of the hydride rich rim and variable rim thickness in sheet material was of great concern for subsequent corrosion experiments. For this reason, any further investigations were stopped on this sample geometry.

The thickness of the hydride rich rim was evaluated by averaging multiple measurements across the hoop direction of one specimen (sample pool includes X2 – SR, low tin ZIRLO – RX and ZIRLO^{TM} - RX) in cross-sectional SEM analysis. Figure 9 plots averaged hydride rich rim thickness of individual tube samples against the overall hydrogen level. Not surprisingly, high overall hydrogen levels in the sample translate into a thick hydride rich rim. TEM observations revealed that the string of bulk hydrides observed by SEM consists of a number of platelet-shaped hydride grains of 600 to 800 nm in length and between 100 to 200 nm wide. Diffraction pattern analysis suggested a cubic (Fm-3m space group) crystal structure confirming the presence of δ-hydrides in the rim, Figure 10. Phase fraction analysis was carried out in the top 3 μm of the hydride rich rim using glancing angle X-ray diffraction. Measurements were carried out for a series of samples with different overall hydrogen level. A typical diffraction pattern recorded on the hydride rim can be seen in Figure 11, demonstrating the appearance of fittable (111), (200) and (220) hydride reflections. Rietveld analyses of such diffraction spectra were carried out either considering δ, γ and ε-hydrides or δ-hydrides only. Since the inclusion of the ε and γ hydride phases did not improve the Rietveld fit, the analysis suggests the presence of δ-hydrides only. The lattice parameter of the δ-hydride phase was

determined to be 4.780 Å, suggesting a stoichiometry closer to $ZrH_{1.7}$ rather than the often quoted $ZrH_{1.6}$ for δ-hydrides [18]. Figure 12 demonstrates that in addition to the rim thickness also the hydrogen concentration in the hydride rich rim varied with the overall content of hydrogen in the material. Within the measured samples, the δ-hydride phase fraction varied between about 60 vol.% to about 90 vol.%.

Incomplete pole figures for the metal matrix and the hydride phase, measured by laboratory X-ray, are presented in Figure 13. The measurements clearly confirm a crystallographic relationship with $(0002)_{\alpha-Zr} \parallel (111)_{\delta-Zr}$ that has been widely reported for bulk hydride in zirconium alloys [30-32].

The residual stresses of both δ-hydride phase and α-Zr phase inside the rim region were analysed using synchrotron X-ray diffraction as described earlier. Note, the material had been heat treated after cathodic charging, which is expected to have affected the residual stress field. For the stress analysis, the (111) δ-hydride and $(10\bar{1}1)$ α-Zr reflections were fitted using a Pseudo-Voigt function. The fitted $d_{spacing}$ are plotted against $\sin^2\Psi$ values in Figure 14, demonstrating only slight deviation from linearity that is probably a result of the hydride texture. In general, the hydrides were determined to be slightly in compression (up to -170 MPa) while the metal had the tendency of being slightly in tension (up to +150 MPa). Considering the associated 17% volume expansion from α-Zr to δ-$ZrH_{1.6}$ [16, 33, 34], a highly compressive stress field (several GPa) in the hydride phase as well as a tensile stress field in the neighbouring metal phase would have been expected. On the other hand, the difference in coefficients of thermal expansion for α-Zr and δ-$ZrH_{1.6}$ alone (Table 3) would generate a tensile stress field in the hydride phase and a

compressive stress field in the metal (600 MPa in hydride and 400 MPa in metal when cooled from 400°C assuming zero stress at high temperature, no creep relaxation and a biaxial stress field near the surface). Since the residual stress characterisation was carried out at room temperature, it seems that the expected high compressive stresses in the hydrides are at least partially compensated by the thermal mismatch between the hydrides and the metal matrix when the material is cooled down. It is also conceivable that some of the original stresses were relieved during the 24 hours heat treatment.

Comparison to end-of-life in-reactor cladding material

As described earlier, the purpose of creating a hydride rim by cathodic charging was to simulate the hydride rim of an end-of-life clad where hydrides have preferentially accumulated adjacent to the oxide/metal interface [21, 24, 35, 36]. The overall hydrogen level of clad is approximately proportional to the oxide thickness, from < 10 µm of oxide and < 100 wt.ppm of hydrogen to over 70 µm and 600 ~ 700 wt.ppm [37, 38] although those values will vary depending on hydrogen pick up rate. SEM investigations of in-reactor material [12, 36, 37, 39-42] typically show a mixture of hydrides and metal matrix as well as strings of small hydrides circumferentially oriented in the bulk of the clad. The artificially introduced hydride rim has a very abrupt interface with the metal while the rim of end-of-life clad has a much more gradual one. However, when testing the corrosion behaviour of such rim, one might expect that the difference in hydride rim/metal interface hardly poses any influence on the corrosion behaviour.

Detailed hydride rim characterizations of irradiated materials are generally difficult and only very few publications are publically available, which makes a comparison with the present data rather difficult. Using Elastic Recoil Detection Analysis (ERDA), P. Bossis et al. reported no higher than 2500 wt.ppm of local hydrogen concentration in the rim region of zirconium clad with 70 MWd/kgU and 75 μm thick of oxide [21]. This value is in contradiction with other observations and predications based on EPRI PWR Fuel Cladding Corrosion (PFCC) [43, 44], where a solid rim of hydride (around 18,000 wt.ppm) is expected for any oxide layer exceeding 60 μm. It might be speculated that ERDA largely underestimates hydrogen contents since its low analysis depth (less than 0.6 μm in this particular case) makes it highly depended on surface representation. For instance, oxidation of the cross-sectional sample might affect measurements.

Using conventional image analysis technique, A. M. Garde et al [12] investigated a series of end-of-life Zircaloy-4 clads from Calvert Cliffs Unit 1 and Arkansas Nuclear One Unit 2 reactor. For clads with a 60 - 140 μm thick oxide and 600 - 950 wt.ppm of overall [H], the rim regions were determined to have 50 ~ 90 vol.% of hydride, equivalent to 10,000 ~ 17,000 wt.ppm of [H]. This local hydrogen concentration in the rim is strongly supported by additional observations of end-of-life Zircaloy-4 clads [39] and ZIRLO^{TM} clads [36, 40]. Therefore, most data available in the open literature suggest that the hydride volume fraction created in the present study is a good representation of end-of-life clad material. No investigations of hydride phase analysis, residual stresses in the hydride rim or texture of the hydrides were found in the literature. However, considering the drivers for the observed hydride stresses

and texture might suggest that those observations would be the same in a hydride rich rim of an end-of life clad.

Summary

Cathodic hydrogen charging were performed on X2, low tin ZIRLO, ZIRLO^{TM} and Zircaloy-4 materials of three heat treatment conditions - stress relieved, partially recrystallised and recrystallised. Two types of sample geometries were employed. The main findings can be summarised as follows:

- Cathodic hydrogen charging is very sensitive to the chemistry of the charging cell solution. Impurity concentration difference of tens of wt.ppm can completely halt the progression of hydrogen charging.
- Vertically assembled charging cell can significantly reduce the amount of air bubbles trapped during this period, hence reducing disturbances caused by contact break up.
- The given cell geometry allowed reliable charging of tube material but made it practically impossible to charge sheet samples reliably due to variation in potential field distribution. The resulting variation in rim thickness could be improved by better design of the charging cell. It is not clear at this stage if better cell design for sheet material would also reduced the numerous cracks observed on the surface of hydrogen charged sheets.
- Successfully charged tube samples have a practically crack free hydride rich rim region on the outer surface of the tube, as well as strings of bulk hydrides circumferentially oriented after annealing the material for 24 hours

at 400°C. Both the rim and bulk hydrides were determined to be δ-hydrides with a crystallographic relationship of $(0002)_{\alpha-Zr} \parallel (111)_{\delta-Zr}$.

- A lattice parameter of 4.780 Å measured for the hydride suggests a stoichiometry closer to ZrH1.7 rather than the often quoted ZrH1.6 for δ-hydrides. The rim has a consistent thickness across the entire tube sample and the thickness increases with overall hydrogen level. Local hydrogen concentration within the top 3 μm of the rim is around 11,000 wt.ppm when overall hydrogen level is between 600 to 700 wt.ppm, in agreement with hydrogen concentration observed in the rim region of actual end-of-life clads.
- Synchrotron X-ray diffraction investigation demonstrated that after heat treatment, the hydride phase in the rim region is only slightly under compression while the neighbouring metal phase is slightly under tension. The stresses are considered to be the combination of remaining residual stresses from hydride formation and thermal stresses due to difference in thermal expansion coefficient.

Acknowledgement

The authors would like to thank the Engineering and Physical Science Research Council (EPSRC) and MoD in the UK for funding the research as part of the Materials for Energy call (research code: EP/E036171/1). The project would not have been possible without the strong support of our project partners (in alphabetical order) EDF, National Nuclear Laboratory, Rolls-Royce, Serco and Westinghouse, who have provided substantial in-kind and financial support.

Figures and Tables

Table 1: Chemical composition of the material studied before cathodic hydrogen charging.

Alloy	Heat treatment	Geometry	Alloying Elements				
			Fe[wt%]	Sn[wt%]	Nb[wt%]	Cr[wt%]	H [wt.ppm]
X2	SR[1], RX[2]	tube	0.08	0.14	0.90	< 0.01	17±8
Low tin ZIRLO	SR, pRX[3] and RX	tube	0.09	0.66	0.91	< 0.01	4±1
ZIRLO™	SR, RX	tube	0.09	0.92	0.91	< 0.01	10±4
ZIRLO™	SR, RX	sheet	0.09	0.94	0.92	< 0.01	27±8
Zircaloy 4	SR, RX	sheet	0.17	1.24	< 0.01	0.10	12±3

1: stress relieved condition.
2: recrystallised condition.
3: partially recrystallised condition.

Table 2: Impurity analysis results of the KOH compounds (all units are in ppm).

	KOH	K_2CO_3	Na^+	Pb^{2+}	Ca^{2+}	PO_4^{3-}	SO_4^{2-}	SiO_2	Cl^-	Al^{3+}	Cu^{2+}	Fe^{3+}	N	Ni^{2+}
A	balance	20000	5000	5	20	20	50	100	50	10	N/A	10	5	N/A
B	balance	10000	5000	5	10	5	5	50	5	20	2	5	5	5

Table 3: Material properties from [17, 18, 29].

Phase	Ref.Code	Crystal System	Space Group		Lattice Parameters (Å)		v	E (GPa)	α (K^{-1})
					a	c			
δ-$ZrH_{1.6}$	04-004-8914	fcc	Fm-3m	[17, 29]	4.780	-	0.322	132	2.737E-05
α-Zr	04-008-1477	hcp	P63/mmc	[18, 29]	3.242	5.169	0.34	96	1.710E-05

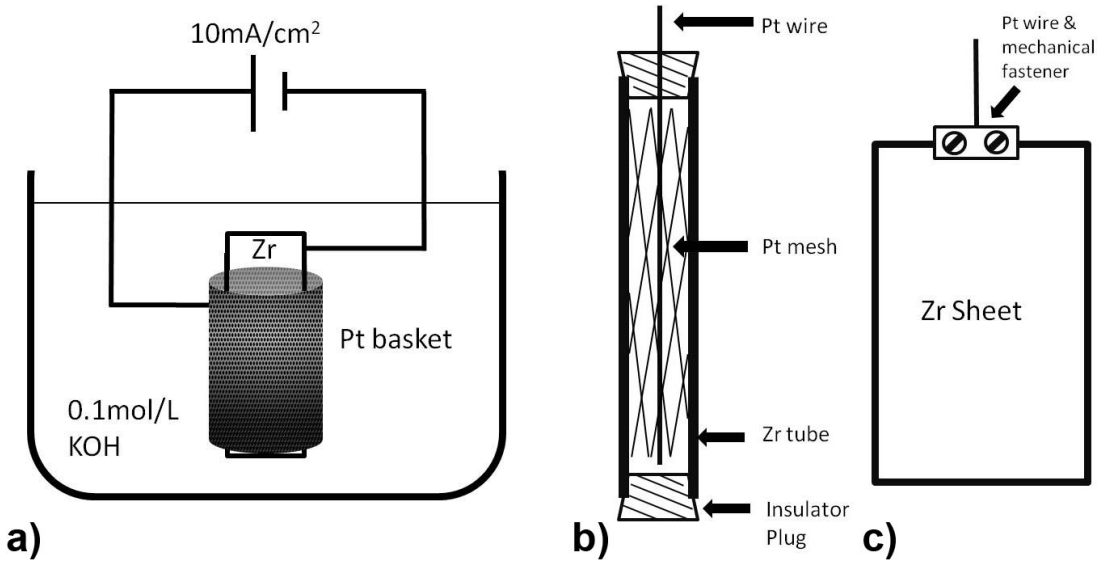

Figure 1: Schematics demonstrating (a) the cathodic hydrogen charging cell with cylindrical Pt counter electro basket, (b) design of the tube sample assembly and (c) design of the sheet sample clamp.

Figure 2: Basket shaped Pt counter electro used during hydrogen charging.

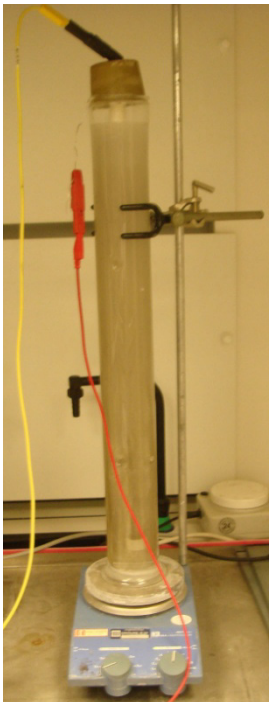

Figure 3: Vertical hydrogen charging cell for Zr cladding tubes.

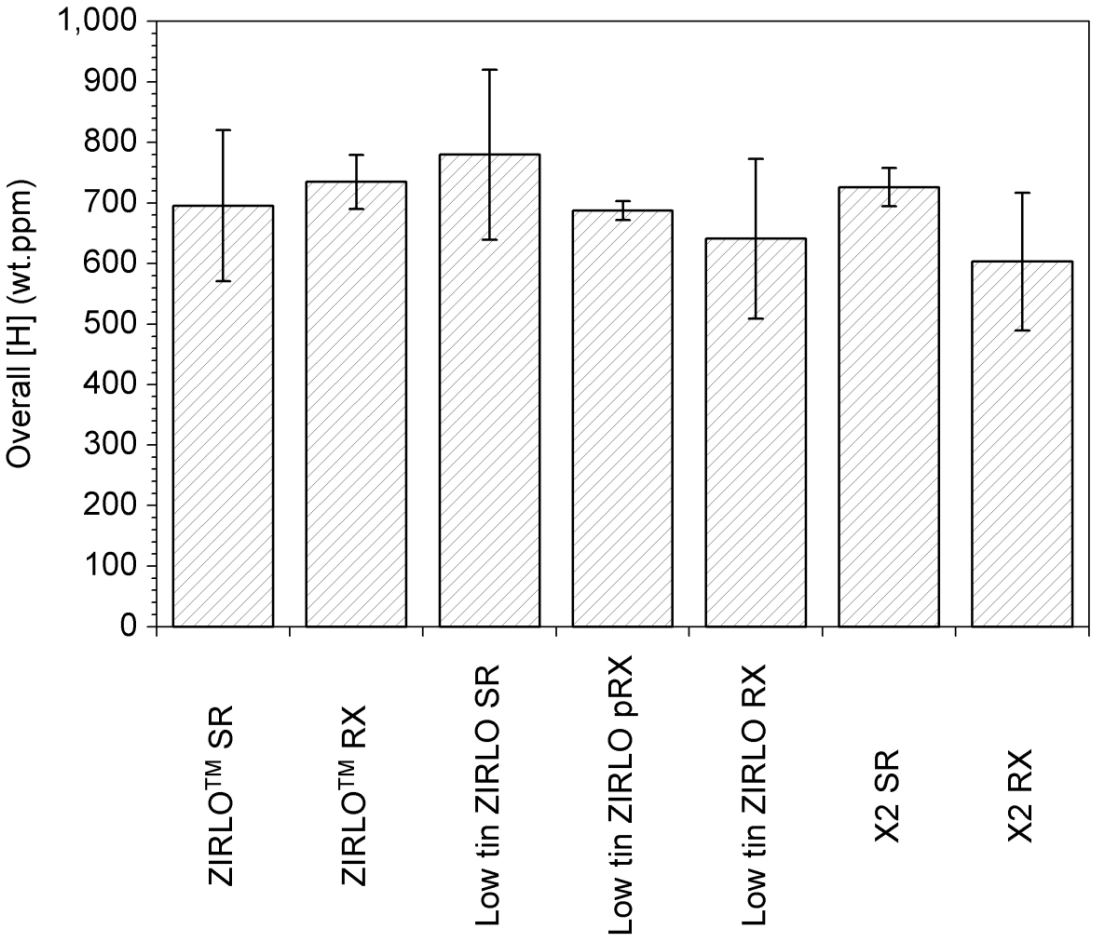

Figure 4: Results of cathodic hydrogen charging conducted on cladding tubes after 10 days of hydriding. The error bars represent the standard deviation of multiple measurements. At least 6 measurements were conducted on each sample.

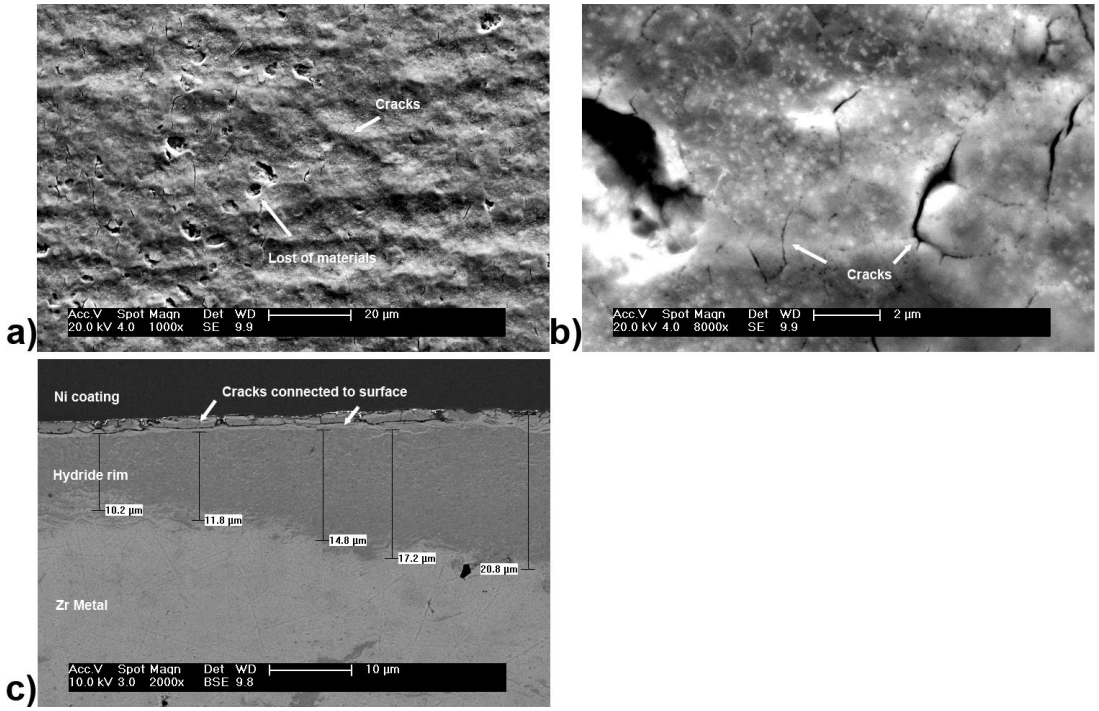

Figure 5: SEM examinations on Zircaloy-4 - RX sheets after 10 days of cathodic hydriding followed by 24 h at 400°C; overall [H] around 950 wt.ppm. (a) and (b) second electron mode SEM images representative of the surface morphology of the sheet specimens, (c) cross-sectional back-scattered electron mode SEM images representative of the hydride rim at location 5 mm from edge of the sample.

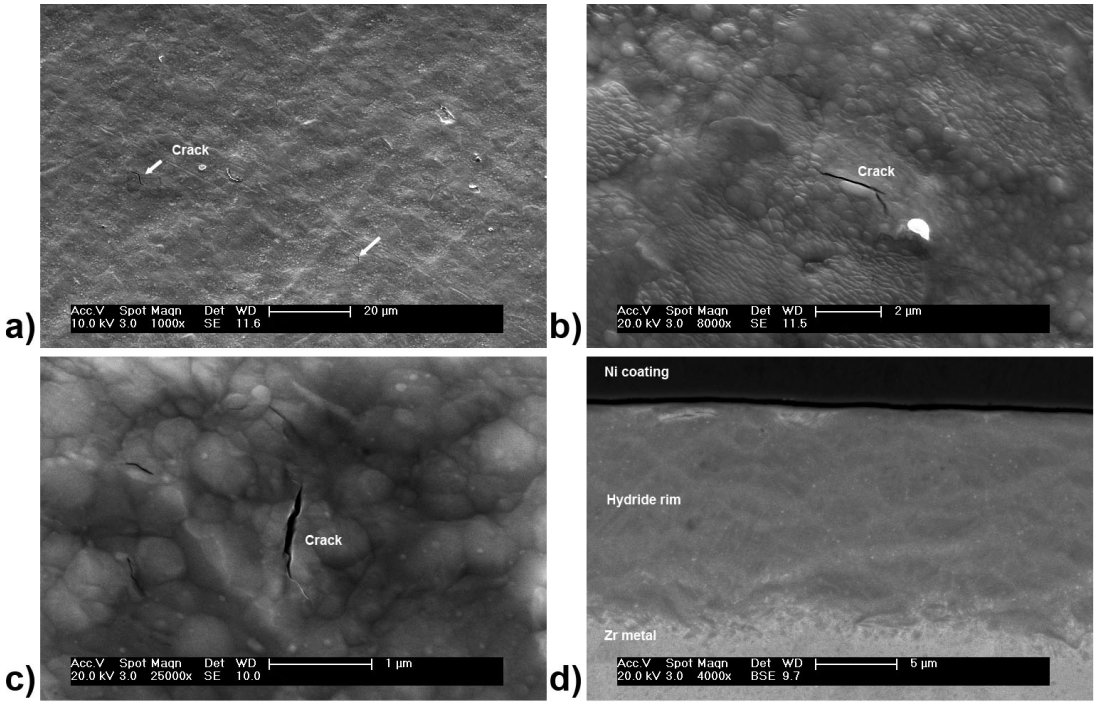

Figure 6: SEM examinations on ZIRLO^{TM} – RX tubes after 10 days of cathodic hydriding followed by 24 h at 400°C; overall [H] around 700 wt.ppm. (a), (b) and (c) second electron mode SEM images representative of the surface morphology of the tube sample and (d) cross-sectional back-scattered electron mode SEM images representative of the hydride rim.

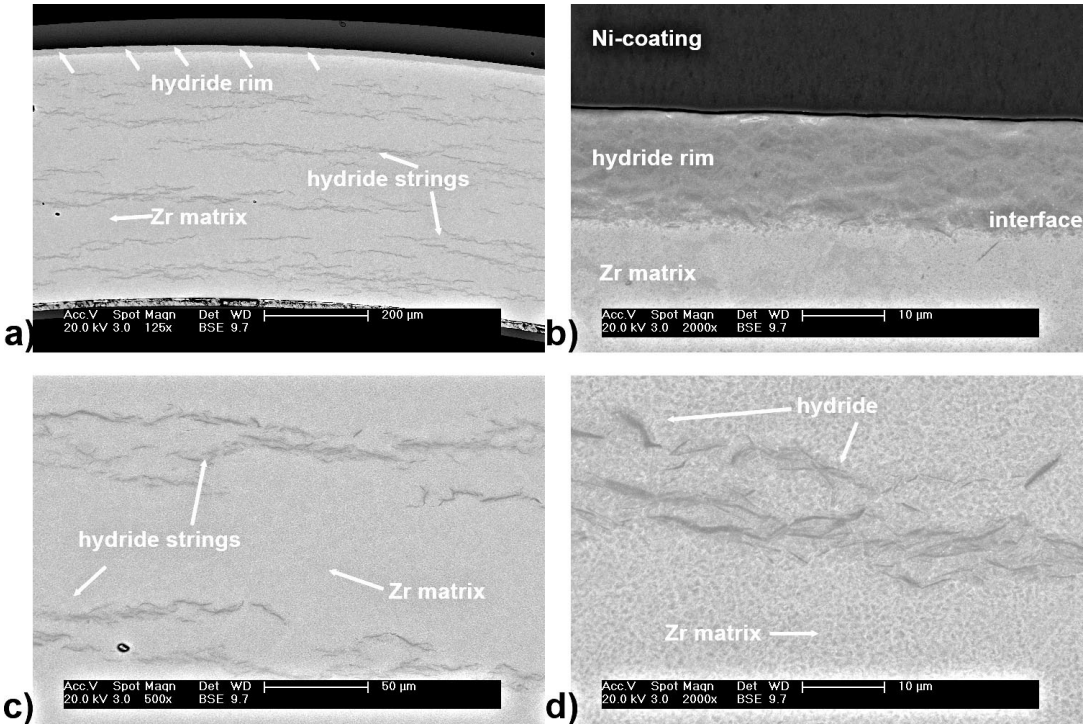

Figure 7: Hydrides distribution in a ZIRLO^{TM} – RX tube after 10 days of cathodic hydriding followed by 24 h at 400°C; overall [H] around 700 wt.ppm. Back-scattered electron mode SEM image showing a dense hydride rim at the outer surface of the clad (a) and (b), re-distributed hydrides in bulk Zr metal (c) and (d).

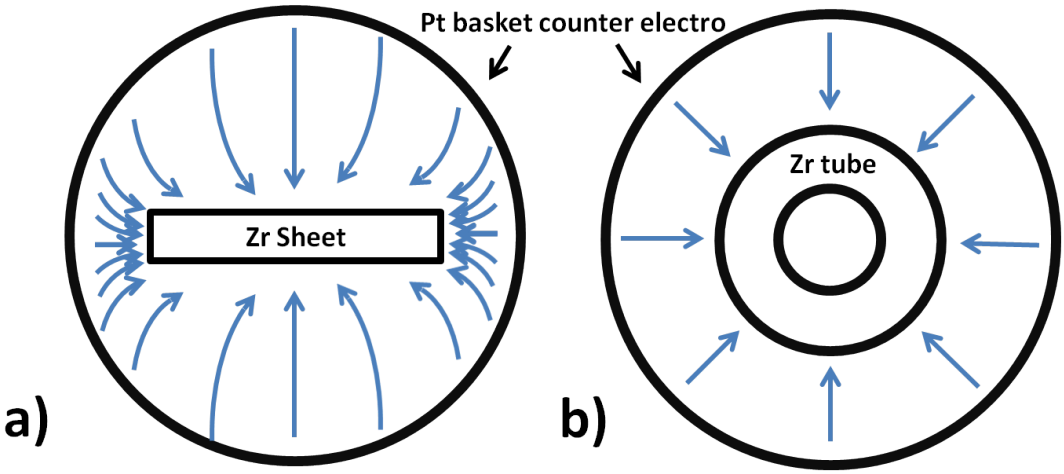

Figure 8: Schematics demonstrating the potential field distribution in an active cathodic hydrogen charging cell for (a) sheet sample inserted into a cylindrical Pt counter electro basket and (b) tube sample, both looking from above of the vertical hydrogen charging cell. The arrows indicate the direction of the potential and the density of the arrows indicates the strength of the potential field.

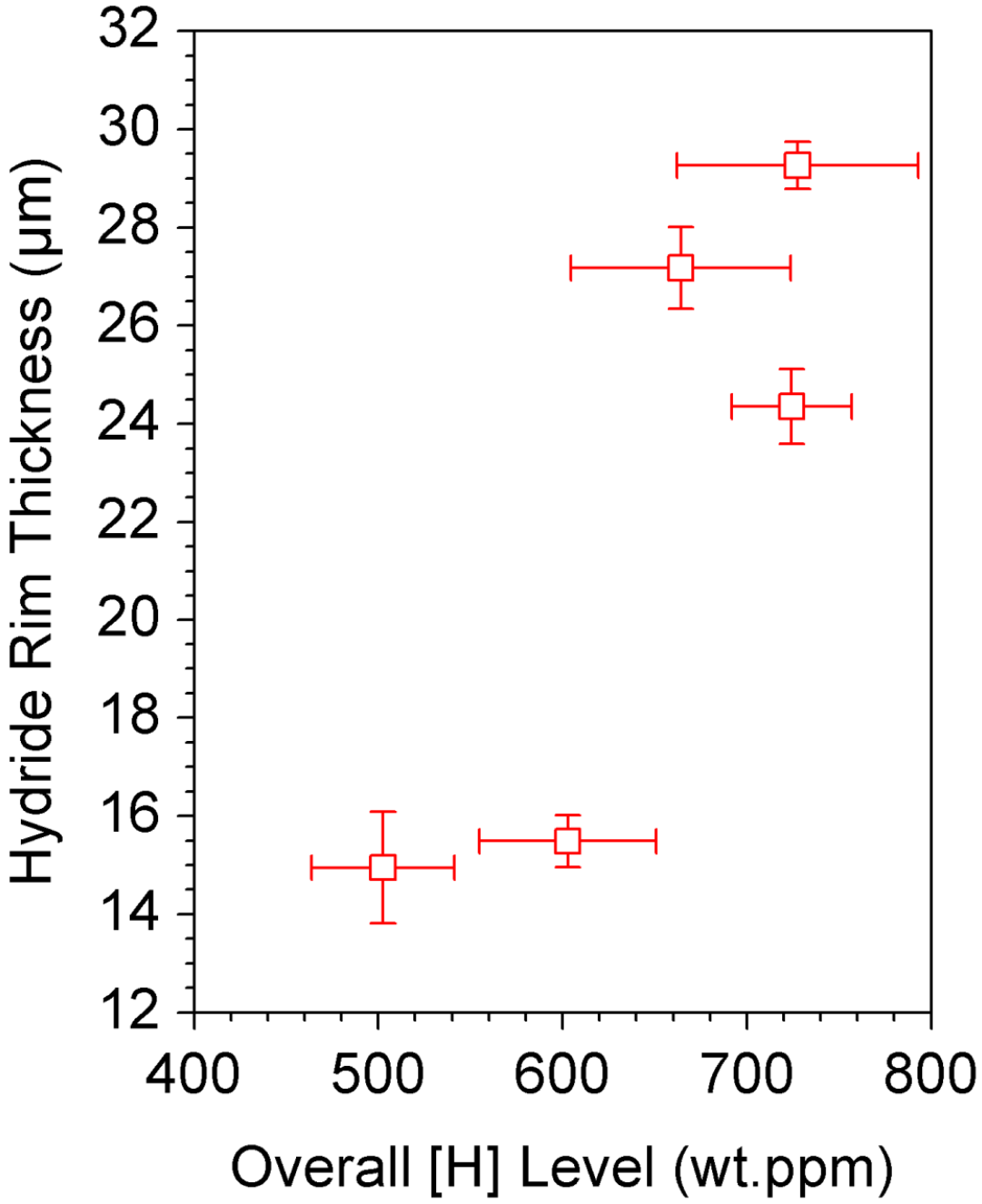

Figure 9: Thickness of the hydride rich rim plotted as a function of overall hydrogen level, the error bars represent the standard deviation of multiple measurements conducted on the same test piece. At lest 6 measurements were conducted on each test piece.

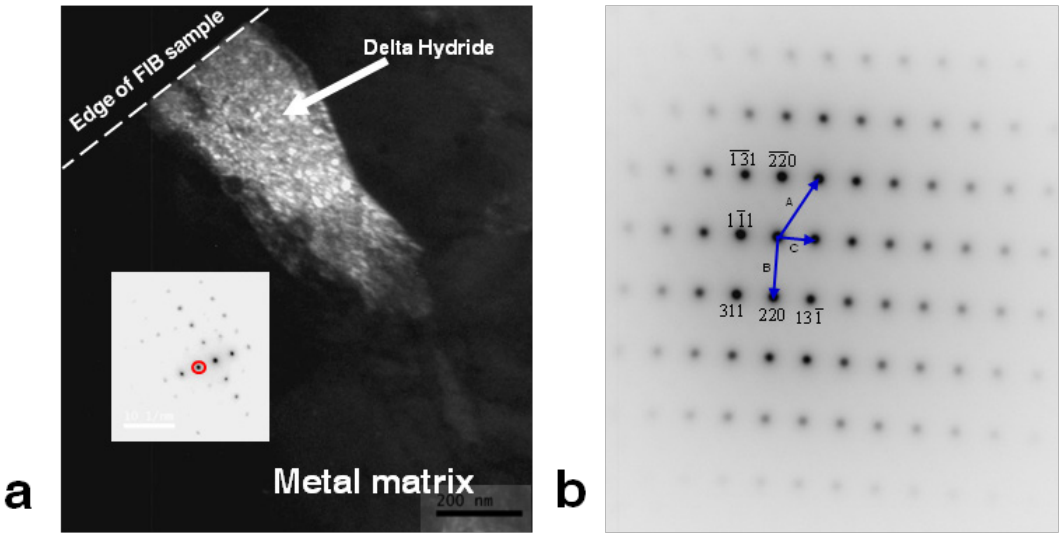

Figure 10: TEM dark field image of a δ-hydride grain observed in the hydride rim of a hydrogen charged ZIRLO™ cladding tube sample, overall [H] around 700 wt.ppm, (a) and the corresponding diffraction pattern with a $[\bar{1}12]$ zone axis confirming f.c.c δ-hydride.

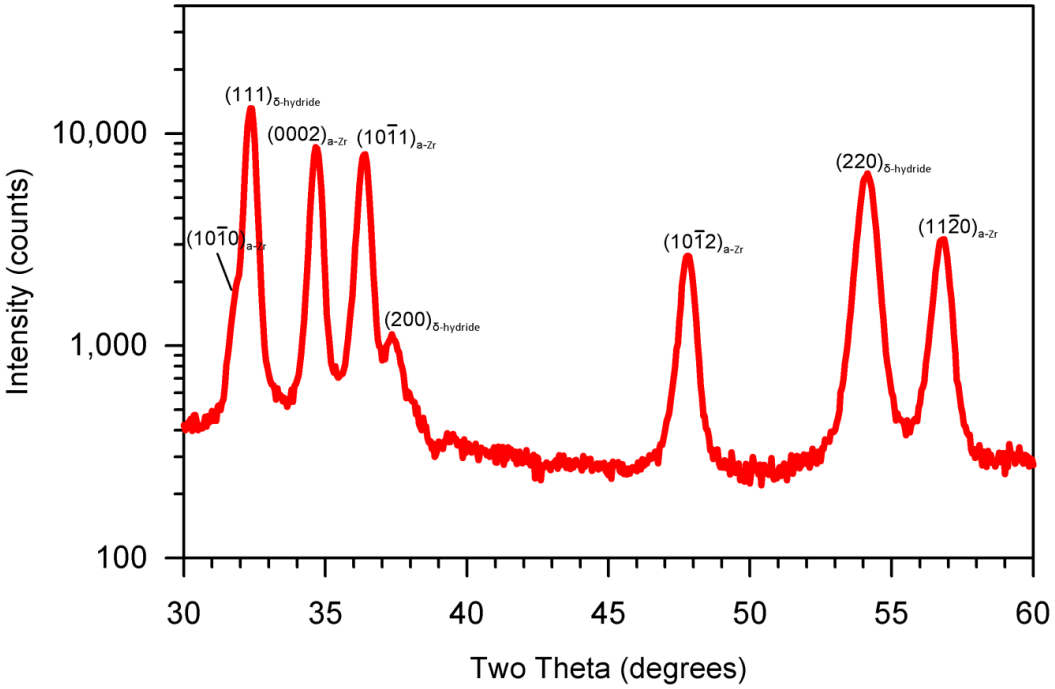

Figure 11: Example of glancing angle diffraction spectrum (6º) recorded on recrystallised ZIRLO™ cladding tube after 10 days of cathodic hydriding followed by 24 h at 400°C; overall [H] around 700 wt.ppm. Measurements conducted using a Philips X'Pert MPD operating at 45kV (Cu-tube). Spectrum recorded via laboratory X-ray diffraction technique. Labelled are the (10$\bar{1}$0), (0002), (10$\bar{1}$1), (10$\bar{1}$2) and (11$\bar{2}$0) of the α–Zr phase and (111), (200) and (220) of the δ-hydride phase.

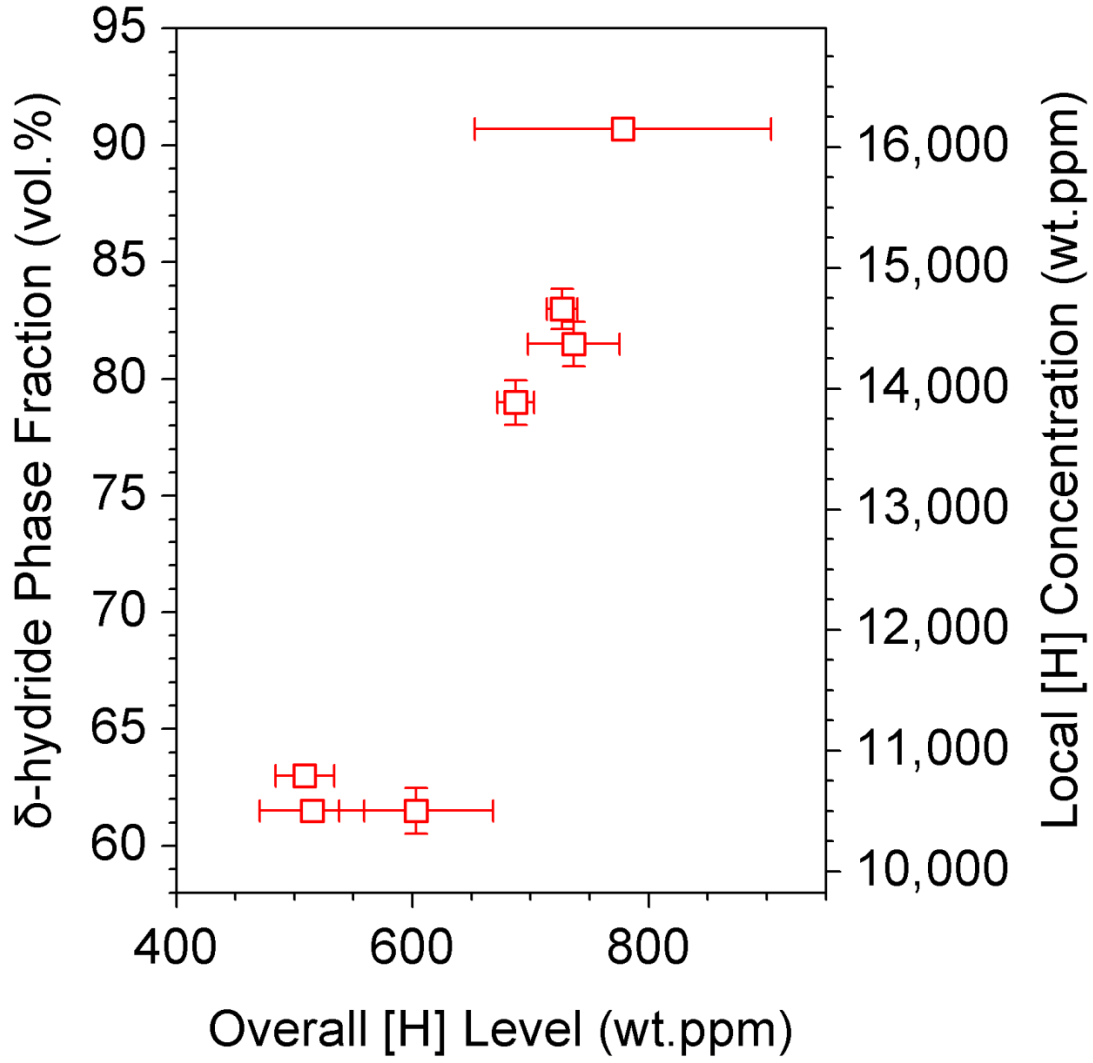

Figure 12: Hydride phase fraction measured via laboratory X-ray diffraction plotted against the overall hydrogen level of the sample, the error bars represent the standard deviation of multiple measurements conducted on the same test piece. At least 7 measurements were conducted on each test piece.

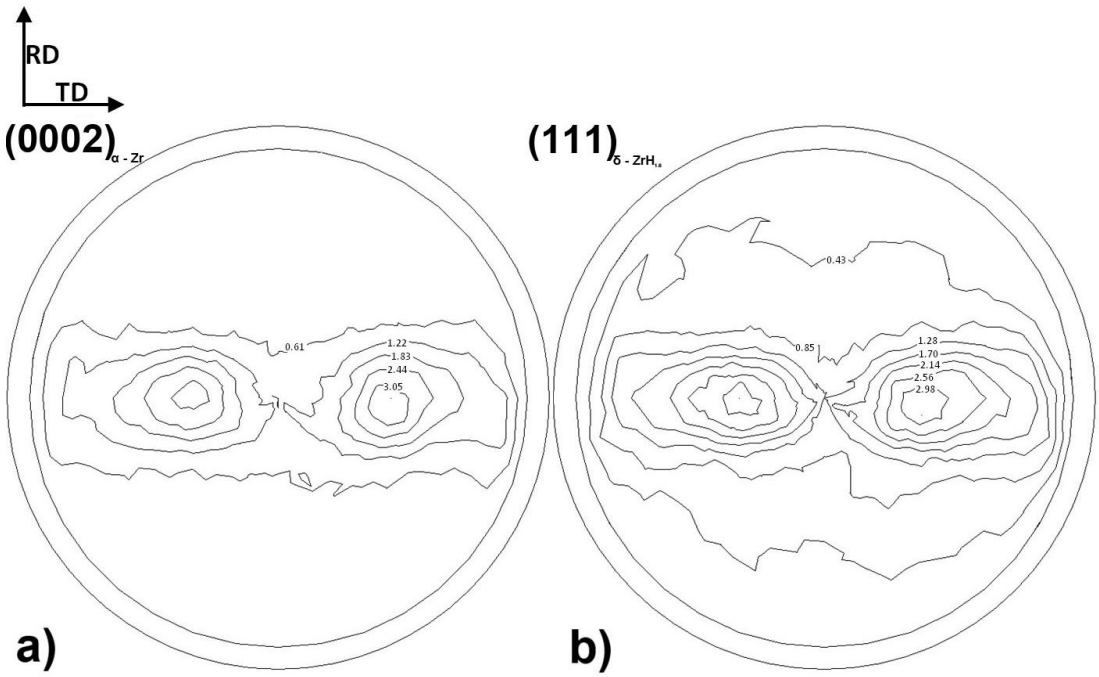

Figure 13: Typical pole figures measured by laboratory X-ray with maximum chi = 85°, showing (a) (0002) reflection of the α–Zr phase, (b) (111) reflection of the δ–hydride phase.

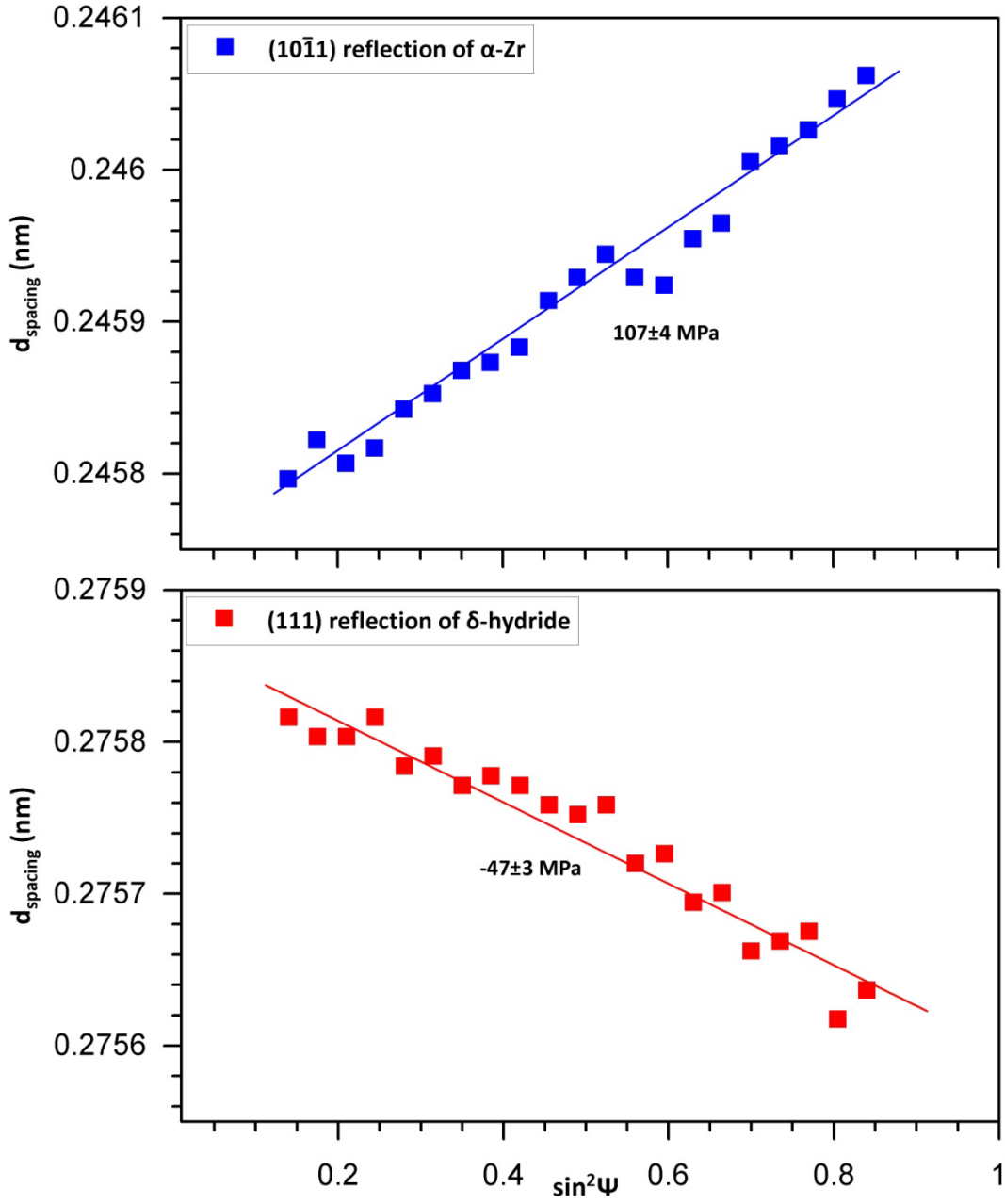

Figure 14: A typical plot of $d_{spacing}$ as a function of the $sin^2\Psi$ values measured at EDDI beamline of BESSY II demonstrating the degree of variations, (a)$(10\bar{1}0)$reflection of the α-Zr phase, (b) (111) reflection of the δ-hydride phase. Samples was a hydrogen charged ZIRLO™ cladding tube sample, overall [H] around 700 wt.ppm.

References

1. Clayton, J.C., *Out-of-Pile Nickel Alloy-Induced Accelerated Hydriding of Zircaloy Fasteners*, in *6th International Symposium on Zirconium in the Nuclear Industry*, D.G. Franklin and R.B. Adamson, Editors. 1982, ASTM International: Vancouver, British Columbia, Canada. p. 572-591.
2. Garde, A.M., G.P. Smith, and R.C. Pirek, *In-PWR Irradiation Performance of Dilute Tin-Zirconium Advanced Alloys*, in *13th International Symposium on Zirconium in the Nuclear Industry*, G.D. Moan and P. Rudling, Editors. 2002, ASTM International: Annecy, France. p. 490-506.
3. Kammenzind, B.F., et al., *Hydrogen pickup and redistribution in alpha-annealed Zircaloy-4*, in *11th International Symposium on Zirconium in the Nuclear Industry*, E.R. Bradley and G.P. Sabol, Editors. 1996, ASTM International: Garmisch-Partenkirchen, Germany. p. 338-370.
4. Kearns, J.J., *Terminal solubility and partitioning of hydrogen in the alpha phase of zirconium, Zircaloy-2 and Zircaloy-4.* Journal of Nuclear Materials, 1967. **22**(3): p. 292-303.
5. Mcminn, A., E.C. Darby, and J.S. Schofield, *The Terminal Solid Solubility of Hydrogen in Zirconium Alloys*, in *12th International Symposium on Zirconium in the Nuclear Industry*, G.P. Sabol and G.D. Moan, Editors. 2000, ASTM International: Toronto, Canada. p. 173-196.
6. Lustman, B. and F.K. Jr, *The Metallurgy of zirconium*. 1st ed. National Nuclear Energy series, Div. 7, v. 4. 1955, New York: McGraw-Hill. 776.
7. Guo, X.H., et al., *An elastoplastic phase-field model for the evolution of hydride precipitation in zirconium. Part I: Smooth specimen.* Journal of Nuclear Materials, 2008. **378**(1): p. 110-119.
8. Ma, X.Q., et al., *The phase field model for hydrogen diffusion and γ-hydride precipitation in zirconium under non-uniformly applied stress.* Mechanics of Materials, 2006. **38**(1-2): p. 3-10.
9. Maki, H. and M. Sato, *THERMAL DIFFUSION OF HYDROGEN IN ZIRCALOY-2 CONTAINING HYDROGEN BEYOND TERMINAL SOLID SOLUBILITY.* Journal of Nuclear Science and Technology, 1975. **12**(10): p. 637-649.
10. Varias, A.G. and A.R. Massih, *Simulation of hydrogen embrittlement in zirconium alloys under stress and temperature gradients.* Journal of Nuclear Materials, 2000. **279**(2-3): p. 273-285.
11. Kammenzind, B.F., et al., *The Long Range Migration Of Hydrogen Through Zircaloy In Response To Tensile And Compressive Stress Gradients*, in *12th International Symposium on Zirconium in the Nuclear Industry*, G.P. Sabol and G.D. Moan, Editors. 2000, ASTM International: Toronto, Canada. p. 196-233.
12. Garde, A.M., G.P. Smith, and R.C. Pirek, *Effects of Hydride Precipitate Localization and Neutron Fluence on the Ductility of Irradiated Zircaloy-4*, in *11th International Symposium on Zirconium in the Nuclear Industry*, E.R. Bradley and G.P. Sabol, Editors. 1996, ASTM International: Garmisch-Partenkirchen, Germany. p. 407 - 429.
13. Grigoriev, V., B. Josefsson, and B. Rosborg, *Fracture Toughness of Zircaloy Cladding Tubes*, in *11th International Symposium on Zirconium in the Nuclear Industry*, E.R. Bradley and G.P. Sabol, Editors. 1996, ASTM International: Garmisch-Partenkirchen, Germany. p. 319-337.
14. Kreyns, P.H., et al., *Embrittlement of Reactor Core Materials*, in *11th International Symposium on Zirconium in the Nuclear Industry*, E.R. Bradley and G.P. Sabol, Editors. 1996, ASTM International: Garmisch-Partenkirchen, Germany. p. 319-337.

15. Kearns, J.J. and C.R. Woods, *Effect of texture, grain size, and cold work on the precipitation of oriented hydrides in Zircaloy tubing and plate.* Journal of Nuclear Materials, 1966. **20**(3): p. 241-261.
16. Daum, R.S., Y.S. Chu, and A.T. Motta, *Identification and quantification of hydride phases in Zircaloy-4 cladding using synchrotron X-ray diffraction.* Journal of Nuclear Materials, 2009. **392**(3): p. 453-463.
17. Yamanaka, S., et al., *Characteristics of zirconium hydride and deuteride.* Journal of Alloys and Compounds, 2002. **330-332**: p. 99-104.
18. Yamanaka, S., et al., *Thermal and mechanical properties of zirconium hydride.* Journal of Alloys and Compounds, 1999. **293-295**: p. 23-29.
19. Blat, M. and D. Noel, *Detrimental Role of Hydrogen on the Corrosion Rate of Zirconium Alloys*, in *11th International Symposium on Zirconium in the Nuclear Industry*, E.R. Bradley and G.P. Sabol, Editors. 1996, ASTM International: Garmisch-Partenkirchen, Germany. p. 319-337.
20. Blat-Yrieix, M., et al., *Toward a Better Understanding of Dimensional Changes in Zircaloy-4: What is the Impact Induced by Hydrides and Oxide Layer?* Journal of ASTM International (JAI), 2008. **5**(9): p. 16.
21. Bossis, P., et al., *Comparison of the High Burn-Up Corrosion on M5 and Low Tin Zircaloy-4*, in *14th International Symposium on Zirconium in the Nuclear Industry*, P. Rudling and B. Kammenzind, Editors. 2005, ASTM International: Stockholm, Sweden. p. 494-525.
22. Cox, B., *Some thoughts on the mechanisms of in-reactor corrosion of zirconium alloys.* Journal of Nuclear Materials, 2005. **336**(2-3): p. 331-368.
23. Cox, B. and T. Johnson, *Observation of a Second Transition Point During the Oxidation of Zirconium Alloys*, in *Corrosion*. 1962. p. 33.
24. Garde, A.M., *Enhancement of Aqueous Corrosion of Zircaloy-4 Due to Hydride Precipitation at the Metal-Oxide Interface*, in *9th International Symposium on Zirconium in the Nuclear Industry*, C.M. Eucken and A.M. Garde, Editors. 1991, ASTM International: Kobe, Japan. p. 566-592.
25. Khatamian, D., *Role of hydrides on the oxidation and deuterium pickup of Zr-2.5Nb in D2O at 573 K.* Journal of Alloys and Compounds, 2005. **404-406**: p. 297-302.
26. Kido, T., *A Study on Enhanced Uniform Corrosion of Zircaloy-4 cladding during High Burnup Operation in PWRs*, in *6th Internanional Symposium on Environmental Degradation of Materials in Nuclear Power Systems - Water Reactors*, R.E. Gold and E.P. Simonen, Editors. 1993, The minerals, Metals & Materials Society: San Diego, California, USA. p. 449-456.
27. Une, K. and S. Ishimoto, *Crystallographic measurement of the β to α phase transformation and δ-hydride precipitation in a laser-welded Zircaloy-2 tube by electron backscattering diffraction.* Journal of Nuclear Materials, 2009. **389**(3): p. 436-442.
28. Genzel, C., et al., *The materials science synchrotron beamline EDDI for energy-dispersive diffraction analysis.* Nuclear Instruments and Methods in Physics Research Section A: Accelerators, Spectrometers, Detectors and Associated Equipment, 2007. **578**(1): p. 23-33.
29. Northwood, D.O., I.M. London, and L.E. Bähen, *Elastic constants of zirconium alloys.* Journal of Nuclear Materials, 1975. **55**(3): p. 299-310.
30. Une, K. and S. Ishimoto, *EBSP measurements of hydrogenated Zircaloy-2 claddings with stress-relieved and recrystallized annealing conditions.* Journal of Nuclear Materials, 2006. **357**(1-3): p. 147-155.

31. Une, K., et al., *Crystallography of Zirconium Hydrides in Recrystallized Zircaloy-2 Fuel Cladding by Electron Backscatter Diffraction.* Journal of Nuclear Science and Technology, 2004. **41**(37): p. 731-740.
32. Kiran Kumar, N.A.P. and J.A. Szpunar, *EBSD studies on microstructure and crystallographic orientation of δ-hydrides in Zircaloy-4, Zr–1% Nb and Zr–2.5% Nb.* Materials Science and Engineering: A, 2011. **528**(21): p. 6366-6374.
33. Carpenter, G.J.C., *The dilatational misfit of zirconium hydrides precipitated in zirconium.* Journal of Nuclear Materials, 1973. **48**(3): p. 264-266.
34. Santisteban, J.R., et al., *Hydride precipitation and stresses in zircaloy-4 observed by synchrotron X-ray diffraction.* Acta Materialia, 2010. **58**(20): p. 6609-6618.
35. Bourgoin, J., et al., *Corrosion Behavior Analysis of Cladding Alloy in EDF's PWR. Evaluation of the Hydriding Effect*, in *EUROCORR'96*. 1996: Nice, France.
36. Holston, A.-M.A., et al., *A Combined Approach to Predict the Sensitivity of Fuel Cladding to Hydrogen-Induced Failures during Power Ramps*, in *2010 LWR Fuel Performance/TopFuel/WRFPM*. 2010: Hyatt Regency Grand Cypress, Orlando, Florida, USA. p. 167-183.
37. FUKETA, T., et al., *Behavior of High Burnup LWR Fuels during Design-basis Accidents; Key Observations and an Outline of the Coming Program*, in *2010 LWR Fuel Performance/TopFuel/WRFPM*. 2010: Hyatt Regency Grand Cypress, Orlando, Florida, USA. p. 244-254.
38. Tägtstrom, P., et al., *Effects of Hydrogen Pickup and Second-Phase Particle Dissolution on the In-Reactor Corrosion Performance of BWR Claddings*, in *13th International Symposium on Zirconium in the Nuclear Industry*, G.D. Moan and P. Rudling, Editors. 2002, ASTM International: Annecy, France. p. 96-118.
39. Garde, A.M., W.H. Slagle, and a.D. Mitchell, *Hydrogen Pick-Up Fraction for ZIRLO™ Cladding Corrosion and Resulting Impact on the Cladding Integrity*, in *2009 LWR Fuel Performance/TopFuel/WRFPM*. 2009: Paris, France. p. Paper 2136.
40. Holston, A.-M.A., V. Grigoriev, and G. Lysell, *Studies of hydrogen assisted failures initiating at the cladding outer surface of high burn-up fuel using a modified Ring Tensile Technique*, in *2007 International LWR Fuel Performance Meeting/TopFuel/WRFPM*. 2007: San Francisco, California, USA. p. 202-213.
41. Lee, C.B., et al., *Post-irradiation Examination of High Burnup UO_2 Fuel*, in *2004 International Meeting on LWR Fuel Performance/TopFuel/WRFPM*. 2004: Hyatt Regency Grand Cypress, Orlando, Florida, USA. p. 167-183.
42. MIYASHITA, T., et al., *CORROSION AND HYDROGEN PICK-UP BEHAVIORS OF CLADDING AND STRUCTURAL COMPONENTS IN BWR HIGH BURNUP 9X9 LEAD USE ASSEMBLIES*, in *2007 International LWR Fuel Performance Meeting/TopFuel/WRFPM*. 2007: San Francisco, California, USA. p. 401-408.
43. Cheng, B., P.M. Gilmore, and H.H. Klepfer, *PWR Zircaloy Fuel Cladding Corrosion Performance, Mechanisms, and Modeling*, in *11th International Symposium on Zirconium in the Nuclear Industry*, E.R. Bradley and G.P. Sabol, Editors. 1996, ASTM International: Garmisch-Partenkirchen, Germany. p. 137-160.
44. White, A.J., A. Sawatzky, and C.H. Woo, *A Computer Model for Hydride-Blister Growth in Zirconium Alloys*. 1985, AECL-8386, Whiteshell Nuclear Research Establishment, Pinawa, Manitoba, ROE 1LO.

End of Publication 1

Publication Number 2

An autoclave study of zirconium alloys with and without a hydride rich rim

An autoclave study of zirconium alloys with and without a hydride rim

J. Wei[1], P. Frankel[1], M. Blat[2], A. Ambard[2], R. J. Comstock[3], Lars Hallstadius[4], S. Lyon[1], R.A. Cottis[1] and Michael Preuss[1]

1: Materials Performance Centre, School of Materials, The University of Manchester, UK

2: EDF - R&D, Moret sur Loing, France

3: Westinghouse Electric Co., Pittsburgh, USA

4: Westinghouse Electric Co., Sweden

Abstract

Autoclave corrosion experiments were conducted on a number of zirconium alloys in different heat treatment conditions. The alloys tested in the present work were X2, low tin ZIRLO, ZIRLO™ and Zircaloy-4. Typical corrosion kinetics with a change from pre- to post-1st transition was observed with ZIRLO™ and Zircaloy-4 displaying the shortest time to 1st transition after 120~140 days of autoclave exposure, followed by low tin ZIRLO materials after 140~260 days. X2 materials showed no sign of transition even after 360 days although one sample tested to 540 days had gone though transition. Material in stress relived condition (SR) generally experienced 1st transition earlier than the same alloy in recrystallised condition. Pre-1st transition samples had a universally black oxide layer, which eventually developed grey patches when transition occurred. Practically all non-hydrogen

charged alloys showed a strong trend towards cubic oxide growth rates. Cathodic hydrogen charging was conducted to simulate end of life condition of cladding tubes, forming a hydride rich rim region at the outer surface of the cladding tubes. Hydrogen charged materials generally experienced accelerated corrosion of different degree with the exception of X2 and partially recrystallised low tin ZIRLO showing no sign of acceleration. It therefore seems that Sn has not only a detrimental effect on non-hydrogen charged material but also in the case a hydride rich rim is created. It was noted that most materials with a hydride rich rim exhibit very slow early corrosion rate and parabolic rather than cubic oxide growth.

Introduction

Zirconium based alloys are the material of choice for fuel cladding, channels and grids that make the structural components of fuel assemblies in water cooled nuclear power plants since the early 1950s. The two properties of zirconium alloys, that largely influence their selection, are their excellent high-temperature water-corrosion resistance and very low thermal neutron absorption cross-section. The initial kinetics of zirconium corrosion in high temperature pressurised water environment can be described as a pre-1st transition period with an approximately cubic growth rate rather than the parabolic law as predicated for diffusion controlled process [1-13]. This is followed by successive cycles of sudden transitions, which involve sharp increase in oxidation kinetics followed by a corrosion rate similar to pre-1st transition kinetics. The cyclic transition kinetics are repeated until an accelerated, roughly linear breakaway corrosion takes place [3, 5-8, 11, 14-19]. Considerable efforts have been made to understand the mechanisms behind such

transition and breakaway in the oxidation kinetics since elimination or delay of such behaviours will greatly improve the overall corrosion performance of zirconium alloys. However, to date, our understanding of these two phenomena is still very limited. A number of mechanisms have been proposed for the breakdown of the pre-transition oxide, and it has been suspected that more than one, if not all, of the mechanisms will be active in any given corrosion conditions [5]. Among them, one of the prominent mechanisms is the tetragonal to monoclinic phase transformation in the oxide due to a stress gradient inside the oxide thin film that might lead to cracking of the oxide, as reported by Preuss et al. [20] and various other researchers such as [21, 22]. In general, a Pilling-Bedworth ratio of 1.56 from zirconium to zirconia [1, 23] brings about a build up of compressive stress inside the oxide layer with the highest stress level measured at the oxide/metal interface and decreasing towards the outer surface of the oxide. It has been suggested that the highly compressive stress at the interface stabilises the tetragonal phase of the first oxide that forms at the interface [17, 19, 20, 24-26], as well as causing creep in the metal substrate beneath [21]. Subsequently, as the corrosion front progresses inwards, the stress of the left behind oxide relaxes, destabilising the tetragonal phase, which results in a martensitic phase transformation from tetragonal to monoclinic oxide associated with a 5% volume expansion [27]. It is believed that this significant volume expansion leads to formations of cracks in the oxide that will ultimately result in the transition of the corrosion kinetics [5, 28, 29].

During prolonged reactor services, zirconium cladding picks up hydrogen from the following sources: hydrogen atoms generated during the corrosion reaction

between water and zirconium, radiolysis of coolant water and LiOH addition for pH-control [30-32]. Hydrides will be precipitated when local hydrogen concentration reaches the solubility limit, which is 120 wt.ppm at 360°C [33, 34]. Combined with the temperature dependence of hydrogen solid solution limit in zirconium [35], a preferential precipitation of hydrides is bound to occur firstly at regions of lower temperature, which is the outer surface of a clad (oxide/metal interface, corrosion progression front). Such accumulation of hydrides has been correlated with breakaway corrosion once a high volume fraction of hydrides has been reached in the rim, although the route cause for accelerated corrosion is still unclear. [5, 11, 14, 16, 21, 36-40]. Microstructure observations of oxides, grown on an artificially formed hydride rich rim, have shown high levels of porosity [36, 40]. It has been suggested that the complex stress field at the metal/oxide interface will result in fracture of the brittle hydride, disturbing the coherency at the metal/oxide interface and therefore reducing the so-called barrier oxide layer [16]. Another potential argument for accelerated corrosion in the presence of a hydride rich rim is the volume expansion during hydride formation (17% [41-43]), which reduces the Pilling-Bedworth ratio to 1.29 when oxidising zirconium hydride. It has been argued that this could result in lower compressive stresses in the oxide [44]. However, previous work has shown that the reduction of Sn delays the transition to high burnup corrosion acceleration in terms of fluence in Zr-Sn-Nb-FeCrV alloys [45] and it is difficult to see how the two arguments above will be affected by alloy chemistry.

The purpose of the present paper is to provide detailed experimental data recorded during extensive autoclave corrosion testing in simulated primary water chemistry of 3 different Nb containing alloys with varying Sn content and two Zircaloy-4 variants (Nb-free Zr alloy). In some cases, material was available as clad tubes while in other cases it was available as sheet. A further variant was the final heat treatment of the material either producing a stress relieved, partially recrystallised or fully recrystallised condition. While these experiments focused on early corrosion kinetics and time-to-first-transition, the tube material was also cathodically hydrogen charged prior to autoclave testing in an attempt to simulate end-of-life condition of actual reactor claddings in order to identify material sensitivity to breakaway corrosion.

Experimental

Materials Preparation

Two types of sample geometry were involved in this study. Tube samples were 30 mm long and 9.5 mm in diameter while sheet samples were 30 x 20 mm^2. Note that the long side of the sheet samples was in the rolling direction. The wall thickness of all tube material is 0.6 mm, while the thickness of the sheet samples is either 0.5 mm in the case of ZIRLO^{TM} material, 0.7 mm in the case of Zircaloy-4 (A) and 5.0 mm in the case of Zircaloy-4 (B). All samples were pickled in a solution of 10 vol.% hydrofluoric acid, 45 vol.% nitric acid and 45 vol.% distilled water for 3 minutes to remove inorganic contamination from the fabrication process. Chemical compositions and the as received hydrogen concentration of the material were determined at the EDF Research and Development facility in Moret-Sur-Loing,

France and are presented in Table 1. The alloys were provided in either two or three heat treatment conditions: stress relieve annealed (SR), partially recrystallised (pRX, only for low tin ZIRLO) and recrystallised (RX). Note that the partially recrystallised condition of the low tin ZIRLO alloy is also known as Optimised-ZIRLO^{TM}, which is a commercial alloy distributed by Westinghouse. Westinghouse provided all material apart from the 5 mm thick Zirclaoy-4 (B) sheet, which was provided by Rolls-Royce plc. The rational behind the choice of alloys was to compare a Nb containing (ZIRLO^{TM} sheet) with a non-Nb containing (Zircaloy-4 sheet) alloy and to study the effect of Sn in Nb containing alloys (tin content decreases from ZIRLO^{TM} to Low tin ZIRLO to X2). Note that X2 is an experimental alloy while all other alloys are commercial alloys.

Cathodic hydrogen charging

Cathodic hydrogen charging was conducted on pickled tube samples in a 0.1 mole/L KOH solution with a fixed current density of 10 mA/cm^2. This process resulted in the formation of a hydride rich rim with fairly consistent thickness on the outer surfaces of tube samples. The 10-day charging process was followed by a 24-hour homogenisation heat treatment at 400°C in Ar to redistribute some of the hydrogen further into the bulk of the test piece. Averaged hydrogen levels of individual test pieces were determined by inert gas fusion analysis using a H-MAT 2500 (Ströhlein) analyser. This method only accounts for overall hydrogen concentration and provides no information regarding the distribution of hydrogen. Using a Philips X'Pert MPD operating at 45kV (Cu-tube) in glancing-angle set up (θ = 6°), it was revealed that samples with an overall hydrogen level between 600 to 700 wt.ppm

have the top few microns of material composed of around 60% of δ-hydride [46]. This corresponds to about 11,000 wt.ppm of localised hydrogen concentration. In comparison, it has been predicted that a solid hydride rim is formed once the oxide has grown to a thickness of 60 μm. These predictions have also been confirmed by hot cell observations [47]. Note that a fixed Incident beam at θ = 6° ensures 90 % of the signal is collected from the top 3 μm of the specimen surface. Since the duration of the autoclave corrosion experiments of the hydrogen charged samples was relatively short, only material from within this range was consumed. More details regarding the cathodic charging procedure and the microstructure analysis of the hydride rim can be found in [46].

Autoclave corrosion

Corrosion experiments were conducted in static isothermal autoclaves operating at 360°C in primary water chemistry ([LiOH] = 2 wt.ppm, [H_3BO_4] = 1000 wt.ppm), with a saturation pressure of around 18 MPa. The autoclave was deaerated each time during heat up at 125°C. To enable tracking of oxidation weight gain as a function of autoclave corrosion exposure, as well as generating samples that have experienced different duration of autoclave exposures, sets of 4 samples were introduced into the autoclave periodically (every 20 days in the case of non-hydrided samples, every 10 days in the case of hydrided samples). Samples were rinsed in de-ionized water, dehydrated with ethanol and compressed air and weighted prior to loading into the autoclave. Weighted samples were first loaded in a stainless steel basket before inserted together into the autoclave, Figure 1. A graphical representation of the detailed loading plan as well as an autoclave test scheme is presented in Figure

2, highlighting insertion time of each set, and the spread of individual samples from each set across different layers of the basket. The positions of individual samples were not altered throughout the autoclave corrosion tests. The loading plan was introduced as a counter measure to potential temperature heterogeneity inside the autoclave. However, in most cases no significant differences in corrosion kinetics were observed for samples of the same condition and set. Periodic weighting of all the exposed samples was conducted between individual exposures, after which the samples were re-installed to their original position inside the autoclave. Both pre- and post-corrosion weight measurements were conducted on a METTLER TOLEDO XS205 DualRange Analytical Balance. The calibration of the balance was inspected after every 10 measurements. Note that weight measurements were normally conducted within hours after opening the autoclave. Samples were dipped into ethanol and dried by compressed air before conducting the weight measurements.

The corrosion exposures on non-hydrided (reference) materials aimed to provide samples and corrosion kinetics data from the early stage of corrosion up to (and around) the 1^{st} transition, while exposures on hydrided materials aimed to provide samples and corrosion kinetics data from the onset of corrosion as well as potential early or immediate accelerated corrosion similar to breakaway behaviour. The non-hydrided and hydrided samples were kept separate in two autoclaves.

Result and Discussion

Corrosion kinetics of non-hydrided reference material

Figures 3 is the summary of the averaged pre-1st transition corrosion weight gain plotted as a function of autoclave exposure time for all 12 non-hydrided materials. The pre-1st transition corrosion kinetics can be described by

$$\Delta W = K_p t^n \quad (1)$$

where ΔW is the sample weight gain in unit of mg/dm^2, t is the autoclave exposure time in unit of days, n is the corrosion kinetics exponent and K_p is the rate constant that is directly proportional to diffusivity of ionic species, which changes with temperature (360°C in this study) and alloys chemistry. Using the computer software package Origin™, linear regression analysis was applied to extract the kinetic parameters. The fitted corrosion kinetics exponents, rate constants and R-squared values can be found in Table 2 together with the required exposure time and weight gain to reach first transition. Each fit was based on corrosion kinetics repetitively collected on 20 individual samples. The data show that the corrosion kinetics tend to follow cubic rather than parabolic law, which has been often reported by other researchers (for instance [5]). No correlations between exponent, $K_p$values and time to first transition were identified. Neither was it possible to find any correlations between n and alloy chemistry. However, most alloys in the stress relieved condition showed slightly more cubic growth kinetics as well as greater $K_p$values than their equivalent alloy in the recrystallised condition.

Weight gain curves of individual alloys and conditions are shown in Figure 4 to 9. Note that weight gain data of each individual measurement instead of averaged ones are plotted in Figure 4 to 9, illustrating the level of scatter. Photographs of actual samples are also included displaying the surface features of the pre-/post-1st transition oxide. A more detailed example of the change of oxide surface appearance before, during and after transition is given for sheet ZIRLO^{TM} – SR in Figure 10. It is clear that the onset of 1st transition was accompanied by the appearance of small grey spots on the black oxide surface. The grey spots then grew bigger, spread across the surface and eventually formed a uniform layer of grey oxide covering the entire surface of the sample. Note that Figure 10 (g) was taken on a specimen with a further 440 days of exposure after reaching 1st transition. Since sheet ZIRLO^{TM} – SR material reached its 1st transition in 100 days, the sample shown in Figure 10 (g) is expected to have experienced at least 5 transitions. The oxide appearance at this stage was significantly brighter than after 40 days of the first transition.

With up to 300 days of autoclave exposure recorded, non-hydrided X2 materials showed identical kinetics in both SR and RX conditions as demonstrated in Figure 4. No trace of 1st transition was observed and a black oxide was seen as early as after 20 days of corrosion and for all samples to 300 days of corrosion, Figure 4 (A), (C) and (D). A second batch of autoclave exposures, aimed at recording long term corrosion kinetics, was conducted on X2 material. A second series of tests confirmed that X2 showed no sign of 1st transition up to 360 days of exposure and ~45 mg/dm^2 weight gain, but clearly a dark and light patchy surface (Figure 4 (B)

and (E)) after 540 days of exposure and ~80 mg/dm^2 weight gain. It is hence suggested that X2 materials (both SR and RX conditions) will initiate 1st transition between 360 - 540 days of exposure. Weight gain data collected during the second batch of autoclave exposures is not included since only 2 data points exist.

Similar pre-1st transition corrosion kinetics was recorded for non-hydrided low tin ZIRLO (Figure 5). During transition, all samples displayed the expected patchy oxide surface of black and grey areas (Figure 5 (B), (D) and (F)). The longest time to transition was achieved by the partially recrystallised material (pRX) after around 260 days of exposure. At this stage, the acceleration of corrosion rate was however only very modest. Pre- to post-1st transition was observed after 200 days of exposure in low tin ZIRLO SR material with again only a modest increase in corrosion kinetics. In contrast, low tin ZIRLO in the recrystallised condition displayed a far more dramatic acceleration of the corrosion rate around 200 days of exposure. However, indications of transition were detectable from the change of surface oxide appearance from around 140 days of exposure. The corrosion data also suggest (Figure 5) that the recrystallised material undergoes a long transition regime of approximately 100 days. Figure 6 sheds more light onto this behaviour by presenting the corrosion data from two different sets. The 4 individual samples within each set were installed at different heights of the autoclave basket (Figure 2) but displayed almost no variation in corrosion kinetics. However, there is a distinguishable difference in terms of set 1 and 3 (i.e. sets that were put into the autoclave at a different time, see Figure 2). The root cause of such variation is

currently not clear and can only be speculated. It seems most likely that it is the result of processing heterogeneity during material fabrication.

Much earlier and clearer change of kinetics compared to the other two alloys were observed in tube ZIRLO^{TM} material, as presented in Figure 7. The 1st transition was reached after 120 days in SR material and 140 days in RX material. Similar early change of kinetics was also observed in sheet ZIRLO^{TM} materials where SR material reached 1st transition in 100 days and RX material reached 1st transition in 120 days (Figure 8). It was also noticed that one sheet ZIRLO^{TM} – RX sample displayed a consistently lower weight gain compared to the other ZIRLO^{TM} – RX samples. This might be related to an error when taking the initial pre-corrosion weight, since the corrosion kinetics were otherwise identical.

Sheet Zircaloy-4 showed a relatively similar corrosion performance in terms of time to transition and ranking order between recrystallised and stress relieved material, Figure 9. A slight different between RX materials of Zircaloy-4 (A) and (B) was noted. The recrystallised material, at least for alloy type (A), displayed relatively lower corrosion rates during pre-transition compared to the stress relieved condition.

As the data presented here demonstrate, many alloys displayed an earlier transition in corrosion rate for the SR condition compared to the RX condition. The exception is low tin ZIRLO. In the case of X2, no distinction between the two conditions can be made as the material did not undergo transition in the time frame of detailed corrosion studies. No significant difference of corrosion kinetics during autoclave testing was observed between ZIRLO^{TM} (sheet or tube) and Zircaloy-4 sheet. In contrast, a clear trend was found when comparing ZIRLO^{TM}, low tin ZIRLO and X2

with very significant delays of transition as the Sn content in the alloy is reduced. Other researchers have reported previously a similar effect of Sn [48-52] for Zircaloys (not containing Nb), an experimental Zr-Sn-0.19Fe-0.10Cr alloy (not containing Nb) and Zr-Nb binary alloys with 0.1 - 1.0 wt.% Nb content. Usually, the differences in corrosion performance have been associated with Sn affecting the thickness of a tetragonal phase layer at the metal oxide interface. Although some authors have suggested that increased Sn levels in Zircaloys destabilises tetragonal zirconia [52], there is sufficient evidence that Sn is in fact a tetragonal phase stabilising element [48, 49, 53, 54].

Corrosion kinetics of hydrided material

Corrosion weight gains of both non-hydrided reference and hydrided alloys are plotted in Figure 11 to 17 against exposure time. Photos of each hydrided alloy after 40 days of exposure are inserted demonstrating the surface appearance of the oxide at this stage. After 80 days of autoclave exposure, all hydrided alloys showed evidence of faster corrosion kinetics than their non-hydrided reference samples apart from recrystallised X2 and partially recrystallised low tin ZIRLO. The weight gain values after 80 days are compared to those recorded for non-hydrided samples in Table 3. Apart from the two conditions that did not show any accelerated corrosion at 80 days, material with a hydride rim showed 30-60% increased weight gain compared to their reference non-hydrided conditions. It was also noticeable that samples that showed accelerated corrosion displayed generally a whitish oxide colour with small regions of black oxide while alloys that showed no accelerated weight gain displayed a more uniform blackish oxide similar to their reference

conditions. Low tin ZIRLO – RX experienced moderate degree of acceleration and showed a greyish oxide appearance. The exception is hydrided ZIRLO^{TM} – SR, which displayed the highest weight gain and greatest acceleration while the oxide surface was generally patched with equal amount of black and white oxide. It was also noticed that some hydrided alloy conditions showed relatively slow oxide growth during the first 5-10 days compared to the reference samples without a hydride rim.

The fitted corrosion kinetics exponents n, rate constants K_p and R^2 are presented in Table 3. In contrast to the non-hydrided reference material, the corrosion rates of most hydrided alloys follow a parabolic law. No correlations were established between n or K_p and alloy chemistry or heat treatment conditions. Previous researches have explained that parabolic rate law is expected for a corrosion process controlled by either the bulk diffusion of oxygen through a perfect barrier layer [7] or by the grain boundary diffusion through the barrier layer, which is more rapid than bulk diffusion and expected to take predominant role [55, 56]. It has been argued that the near cubic kinetics of reference material arise from the reduction of grain boundary area as oxide thickens, i.e. preferential growth of oxide grains [5]. This argument is supported by many studies on the evolution of oxide grain structure where columnar oxide grain is widely observed [57-62]. As mentioned earlier, it was found that in most cases material with a hydride rim showed relatively slow early oxide growth. Figure 18 plots the rate constant K_p as a function of the kinetic exponent n. It is interesting to note that there is a clear relationship between the two and that in fact the oxide seems to become most protective (n is smallest) when the diffusion rate of ionic species seems to be

fastest (largest K_p). This is true when comparing between reference and hydrided material but also when comparing within each class of material. It might suggest that ionic species transport through the oxide is not the rate limiting step when the oxide has grown to a certain thickness.

The observed corrosion acceleration and the general tendency of parabolic towards linear law oxide growth in hydrided material are difficult to explain in view that not all alloys show the same behaviour. The three possible explanations below would be best understood if the same acceleration of oxide growth was observed in all alloys:

- A lower compressive stress state is expected for oxide grown on hydrided samples [44], making inward diffusion of oxygen easier [63] as pores on grain oxide grain boundaries [64] might form a network for fast diffusion.
- The oxide grains maintain certain size and morphology as oxide thickens, providing a relatively constant grain boundary area, i.e. more equiaxed grains (higher tetragonal fraction), fewer and smaller columnar grains (higher monoclinic fraction) when corrosion is faster [61].
- Transformation from tetragonal to monoclinic oxide happens earlier due to potentially lower compressive stress state compared to material without a hydride rim. The subsequent formation of cracks [28, 29] might enhance the transport of corrosion species to the metal-hydride/oxide interface, which would be expected to reduce the protective nature of the oxide with potential parabolic or even linear rate of corrosion.

Further investigations such as electron microscopy are required before the last two explanations can be confirmed or rejected. It is possible that more that one routes will be active in any given case.

The in-pile corrosion performance of zirconium clad is depended on the type of reactor, burnup, coolant chemistry and in-pile location etc and should generally be treated on a case by case base. The progression of corrosion in such case is generally evaluated as a function of burnup rather than exposure time. Earlier studies concentrating on Zircaloys showed that the high burnup corrosion acceleration could occur over the range of 35-93 GWd/tU, corresponds to an acceleration factor of 2.00-3.88 in BWRs and 1.45-2.85 in PWRs [14, 65-76]. Similar acceleration was also observed in Nb containing alloys such as M5^{TM} [14, 66], ZIRLO^{TM} [67], Zr-1.2Bi-0.5Nb and modified Zircaloy-2 with 0.2%Nb [73] where accelerating factors between 1.00-2.27 were recorded. This demonstrates that the corrosion acceleration observed in current study is in agreement with data available in open literature suggesting that the hydride rim is indeed largely responsible for in-pile breakaway corrosion. Further extrapolating from [14, 67], the acceleration factor decreases with decreasing Sn content (1.75 for ZIRLO^{TM} and no acceleration for M5^{TM}), which also seems to be in agreement with the present study.

The comparison of hydrided and non-hydrided material has demonstrated that in most cases the hydride rich rim has a detrimental effect on corrosion performance. However, the factor, by which the corrosion kinetics accelerates in the presence of a hydride rich rim, is different for each alloy. Most explanation to date for the accelerated rate of corrosion in the presence of a hydride rich would suggest that

acceleration should be independent of the alloy. This is clearly not the case from the data presented here. Further detailed characterisation of the oxide and metal/oxide interface is necessary to identify the mechanisms by which the hydride rich rim affects the corrosion rates.

Summary

Autoclave experiments were performed on X2, low tin ZIRLO, ZIRLO^{TM} and Zircaloy-4 materials of different heat treatment conditions. The corrosion weight gain was recorded as a function of the autoclave exposure time. In order to study the effect of a hydride rich rim, X2, low tin ZIRLO and ZIRLO^{TM} tubes had also been cathodically charged with hydrogen. The main findings can be summarised as follows:

- Non-hydrogen charged materials exhibited the typical corrosion kinetics with different time required to go from pre- to post-1st transition. The most significant difference in time to transition was found between ZIRLO^{TM}, low tin ZIRLO and X2, showing a dramatic increase of time to transition with decreasing Sn content. Sheet Zircaloy-4 exhibited similar 1st transition time as sheet ZIRLO^{TM}. Materials in SR condition generally experienced 1st transition slightly earlier than materials in RX condition.
- Pre-1st transition corrosion kinetics are similar for different materials, hence the factor dominating the corrosion performance of one material is the exposure time before 1st transition.

- Cathodic hydriding facilitated the formation of a hydride rich rim at the outer surface of cladding tubes, simulating end-of-life conditions of actual reactor claddings. The accumulation of hydrides near the hydride/oxide interface and local hydrogen concentration is in good agreement with the reported conditions of actual samples from nuclear reactors [46].
- Most materials with a hydride rich rim exhibited accelerated corrosion. The observed acceleration due to the presence of a hydride rich rim is depended on the type of alloy, in agreement with data collected on high burnup zirconium clads. Alloy with higher Sn content suffers more from the detrimental affect of hydride rich rim than low Sn alloys. SR materials are more sensitive to the accelerating effect than pRX and RX materials. Most hydrided material showed oxide growth slower than their reference non-hydrogen charged material during the initial stage of corrosion, and a clear relationship between the rate constant K_p and kinetic exponent n is observed in both hydrided and reference materials, regardless of the alloy chemistry and heat treatment.
- Further investigations are required before mechanistic explanation can be given. Current results suggest future studies should further investigate the effect of tin and the hydride rich rim on the corrosion kinetics of zirconium alloys.

Acknowledgement

The authors would like to thank the Engineering and Physical Science Research Council (EPSRC) and MoD in the UK for funding the research as part of the Materials for Energy call (research code: EP/E036171/1). The project would not have been possible without the strong support of our industrial project partners (in alphabetical order) EDF, National Nuclear Laboratory, Rolls-Royce, Serco and Westinghouse, who have provided substantial in-kind and financial support and our academic project partners from the University of Oxford and the Open University.

Figures and Tables

Table 1: Measured chemical compositions of the materials involved in this study.

Alloy	Heat treatment	Geometry	Alloying Elements				Hydrogen [wt.ppm]
			Fe[wt%]	Sn[wt%]	Nb[wt%]	Cr[wt%]	
X2	SRA[a], RX[b]	tube	0.08	0.14	0.90	< 0.01	17±8
Low tin ZIRLO	SR, pRX[c] & RX	tube	0.09	0.66	0.91	< 0.01	4±1
ZIRLO™	SR, RX	tube	0.09	0.92	0.91	< 0.01	10±4
ZIRLO™	SR, RX	sheet	0.09	0.94	0.92	< 0.01	27±8
Zircaloy 4 A	SR, RX	sheet	0.17	1.24	< 0.01	0.10	12±3
Zircaloy 4 B	RX	sheet	0.19	1.37	< 0.01	0.09	6±3

a: SR = Stress Relieved.
b: pRX = partially Recrystallised.
c: RX = Recrystallised.

Table 2: Autoclave corrosion weight gain results of non-hydrided reference materials.

Alloy	pre – Trans Kinetics			1st Trans		Max. t (days)	Max. ΔW (mg/dm^2)
	K_P	n	R^2	t (days)	ΔW (mg/dm^2)		
X2 - SR	5.381	0.365	0.993	> 360	> 45[a]	540	72.8 ± 0.9
X2 - RX	4.693	0.383	0.989	> 360	> 46[a]	540	78.7 ± 0.8
Low tin ZIRLO - SR	6.570	0.319	0.979	220	36.5 ± 2.4	260	47.5 ± 3.2
Low tin ZIRLO - pRX	6.595	0.311	0.977	260	38.2 ± 2.5	320	43.6 ± 2.9
Low tin ZIRLO - RX	5.935	0.344	0.985	140 - 240	32.9 ± 2.2	260	56.2 ± 3.7
ZIRLO™ - SR	6.262	0.339	0.938	120	32.8 ± 2.2	140	41.7 ± 2.8
ZIRLO™ - RX	5.848	0.339	0.968	140	31.2 ± 2.1	160	43.2 ± 2.9
sheet ZIRLO™ - SR	6.934	0.317	0.965	100	32.3 ± 2.2	160	56.0 ± 3.7
sheet ZIRLO™ - RX	5.247	0.364	0.923	120	31.1 ± 2.1	140	41.7 ± 2.8
Zircaloy 4 A - SR	8.179	0.275	0.974	120	31.4 ± 2.1	160	49.7 ± 3.3
Zircaloy 4 A - RX	4.099	0.368	0.941	160	28.1 ± 1.9	220	50.1 ± 3.3
Zircaloy 4 B - RX	5.728	0.331	0.959	140	30.4 ± 2.0	160	39.9 ± 2.7

a: measured on X2 alloys exposed to a total 360 days with no sign of 1st transition.

Table 3: Autoclave corrosion weight gain results of hydrided materials.

Alloy	80 days ΔW (mg/dm^2)			Corrosion Kinetics		
	reference	hydrided	hydrided/reference ratio	K_P	n	R^2
X2 - SR	26.1 ± 1.7	34.8 ± 2.0	1.333	7.018	0.364	0.928
X2 - RX	24.4 ± 1.6	26.7 ± 0.9	1.093	2.774	0.530	0.930
Low tin ZIRLO - SR	26.9 ± 1.8	35.0 ± 1.2	1.301	4.331	0.474	0.981
Low tin ZIRLO - pRX	25.5 ± 1.7	27.5 ± 2.3	1.080	2.798	0.520	0.923
Low tin ZIRLO - RX	26.8 ± 1.8	38.6 ± 0.7	1.441	3.790	0.539	0.949
ZIRLO™ - SR	27.4 ± 1.8	45.2 ± 1.9	1.647	2.223	0.685	0.952
ZIRLO™ - RX	25.9 ± 1.7	38.2 ± 1.7	1.479	3.073	0.588	0.801

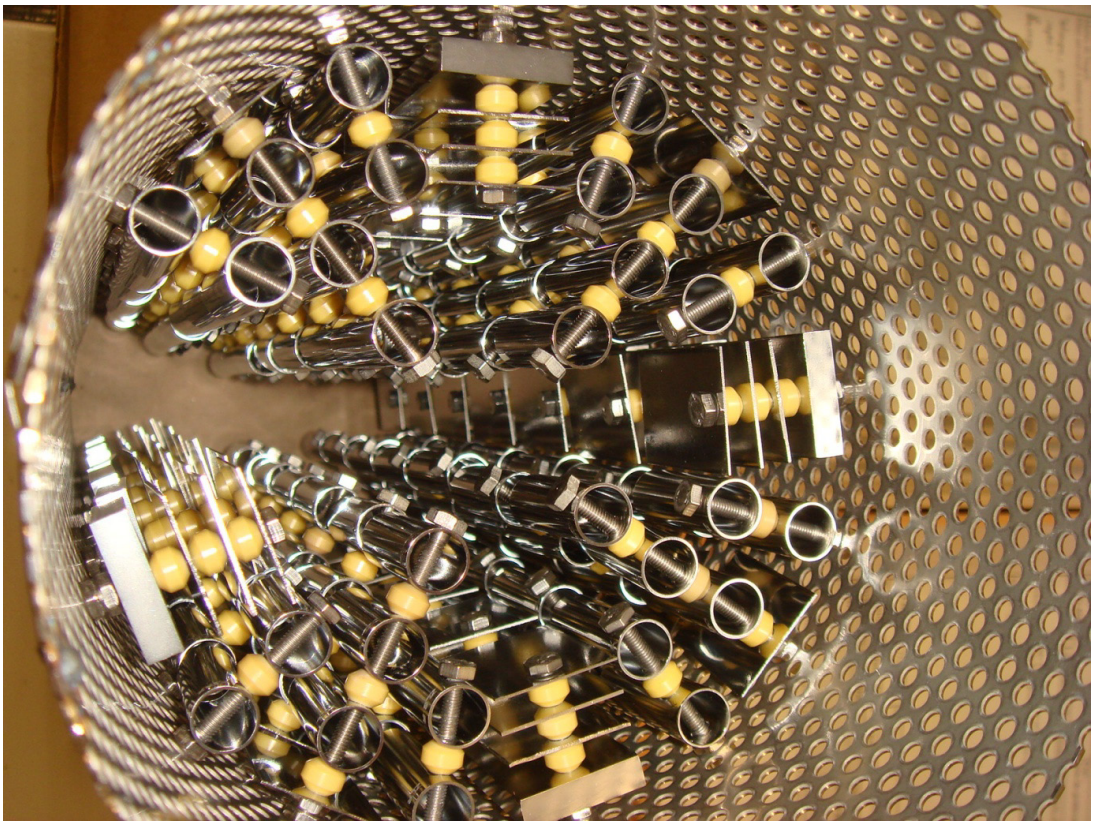

Figure 1: Autoclave basket showing all samples installed before autoclave exposure. The location of individual samples is kept unchanged.

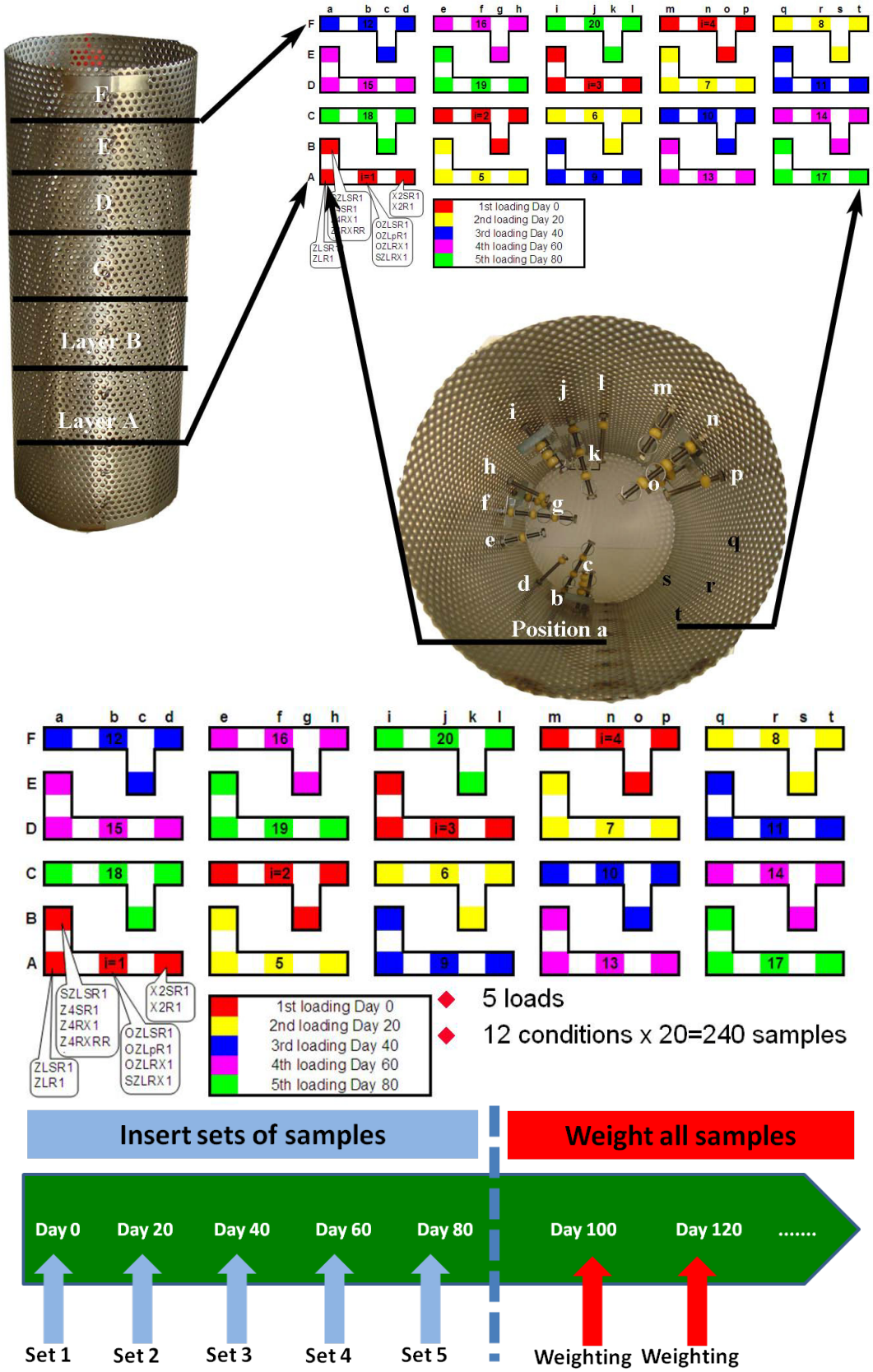

Figure 2: sample allocations inside the autoclave basket and autoclave test scheme.

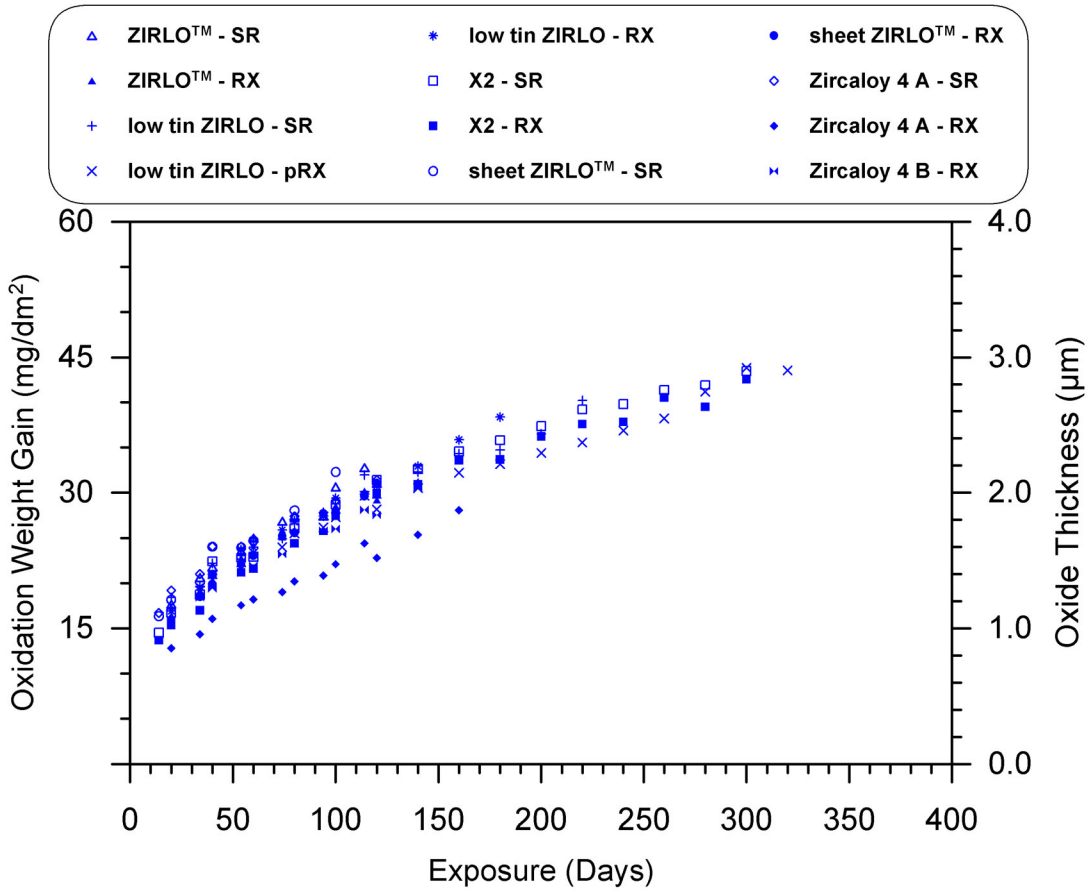

Figure 3: Summary of the Autoclave corrosion weight gain profiles showing the averaged pre-1st transition weight gain values for all 12 non-hydrided materials.

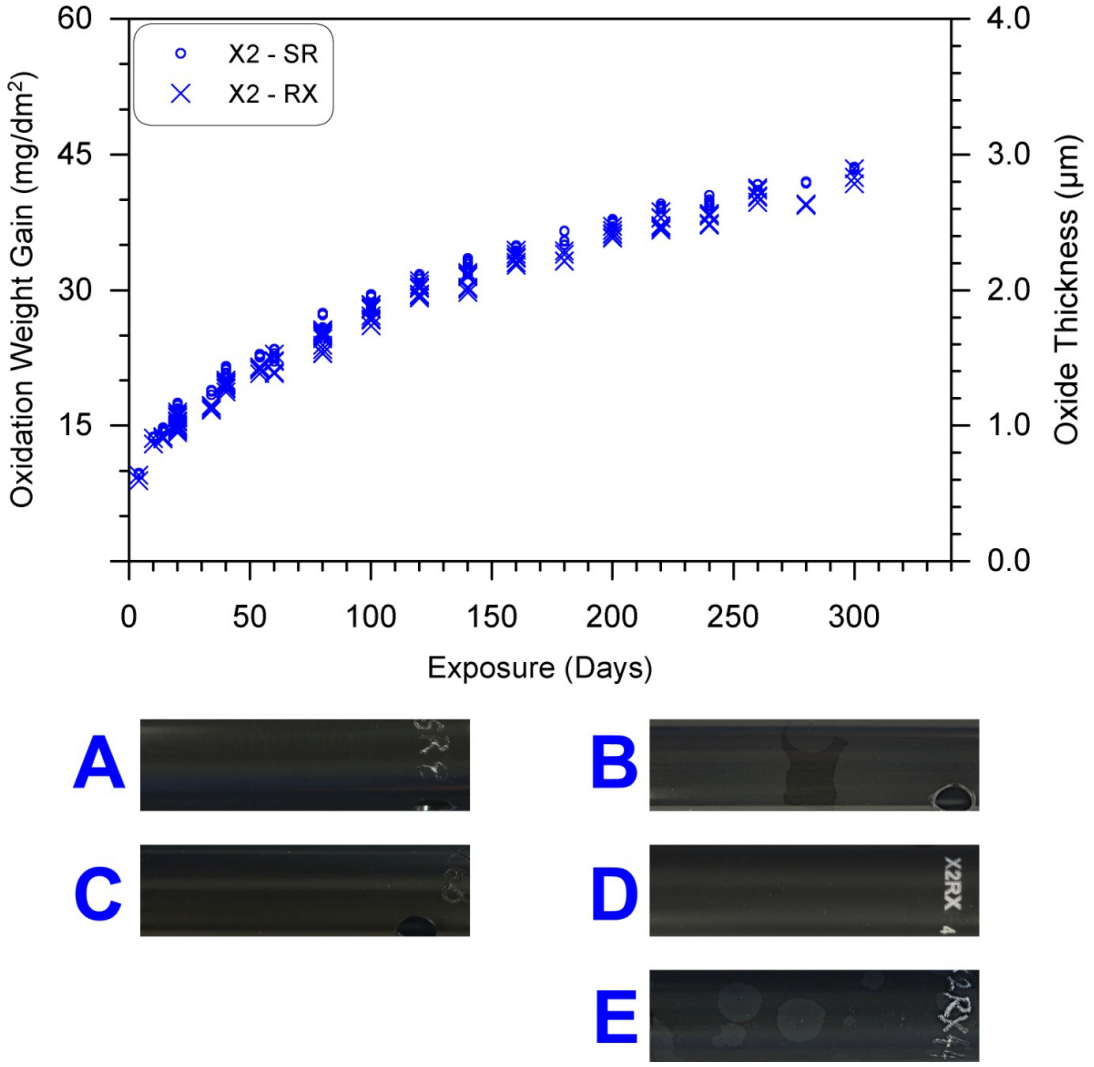

Figure 4: Autoclave corrosion weight gain profile of non-hydrided X2 SR and RX materials. Photographs of actual corrosion specimens included: (A) non-hydrided X2 – SR after 280 days of autoclave exposure, (B) non-hydrided X2 – SR after 540 days, (C) non-hydrided X2 – RX after 20 days, (D) non-hydrided X2 – RX after 300 days and (E) non-hydrided X2 – RX after 540 days of autoclave exposure.

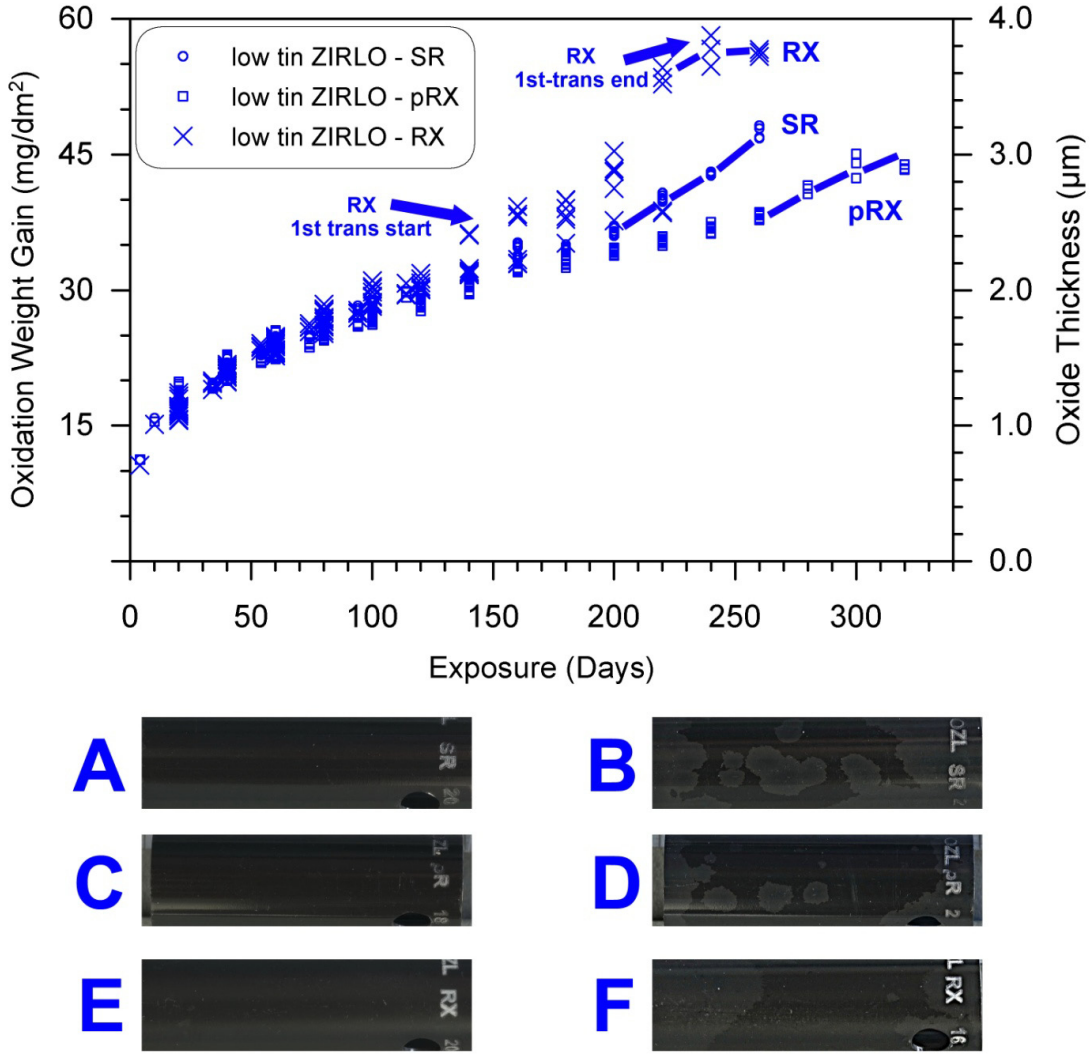

Figure 5: Autoclave corrosion weight gain profile of non-hydrided low tin ZIRLO SR, pRX and RX materials. Photographs of actual corrosion specimens included: (A) non-hydrided low tin ZIRLO – SR after 180 days of autoclave exposure, (B) non-hydrided low tin ZIRLO – SR after 260 days, (C) non-hydrided low tin ZIRLO – pRX after 240 days, (D) non-hydrided low tin ZIRLO – pRX after 320 days, (E) non-hydrided low tin ZIRLO – RX after 180 days and (F) non-hydrided low tin ZIRLO – RX after 200 days of autoclave exposure.

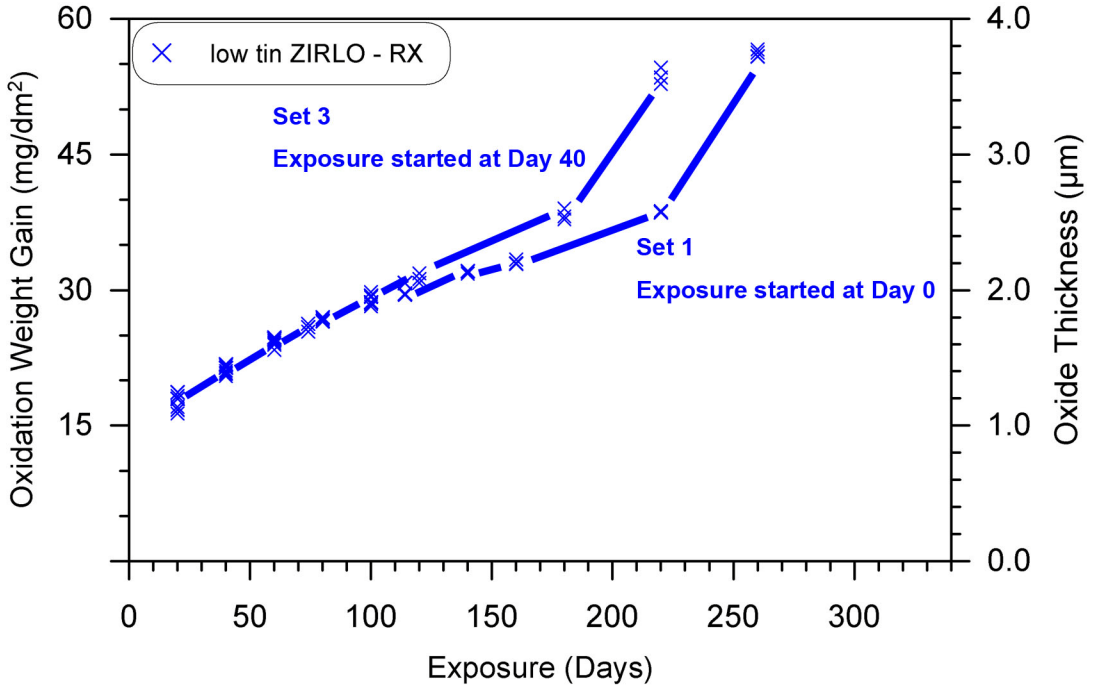

Figure 6: Autoclave corrosion weight gain profile of non-hydrided low tin ZIRLO RX material. Highlighting the differences between different sets of samples, only data from set 1 and 3 is plotted here.

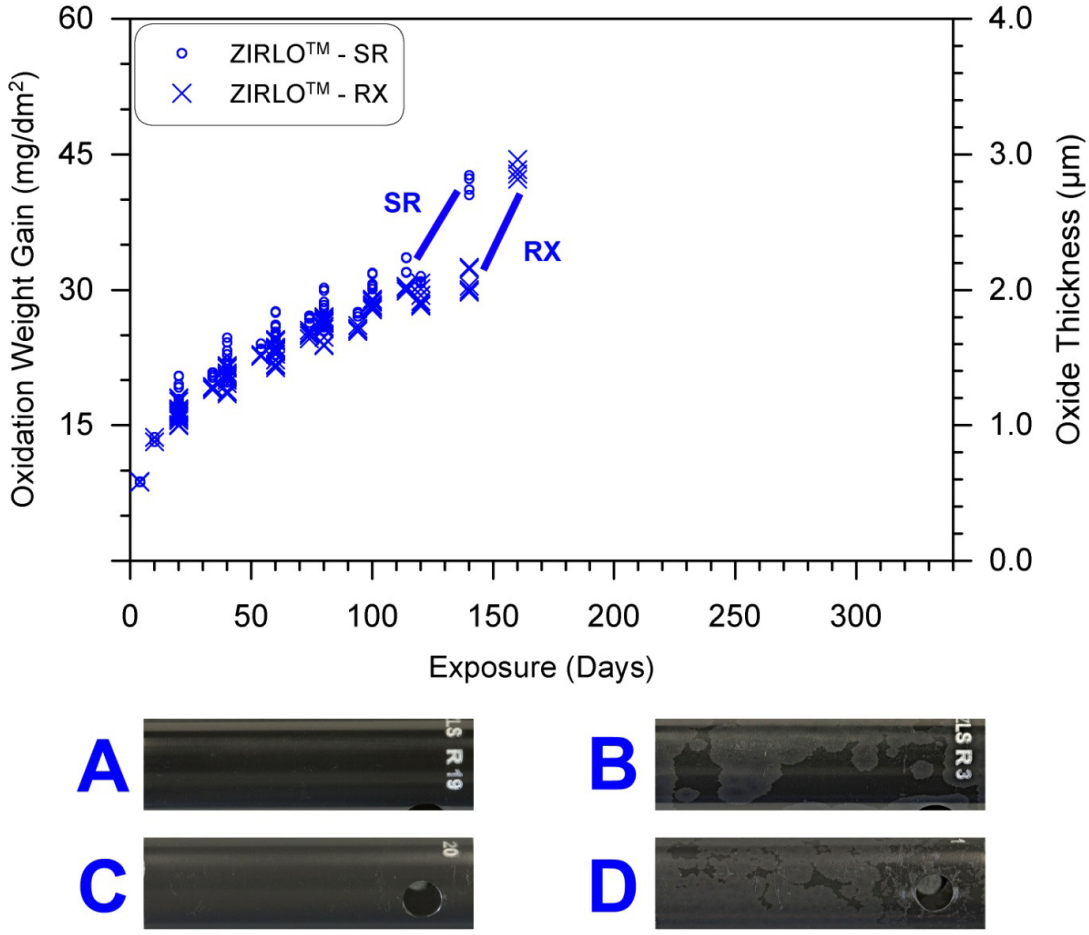

Figure 7: Autoclave corrosion weight gain profile of non-hydrided ZIRLO™ SR and RX materials. Photographs of actual corrosion specimens included: (A) non-hydrided ZIRLO™ – SR after 60 days of autoclave exposure, (B) non-hydrided ZIRLO™ – SR after 140 days, (C) non-hydrided ZIRLO™ – RX after 80 days and (D) non-hydrided ZIRLO™ – RX after 160 days.

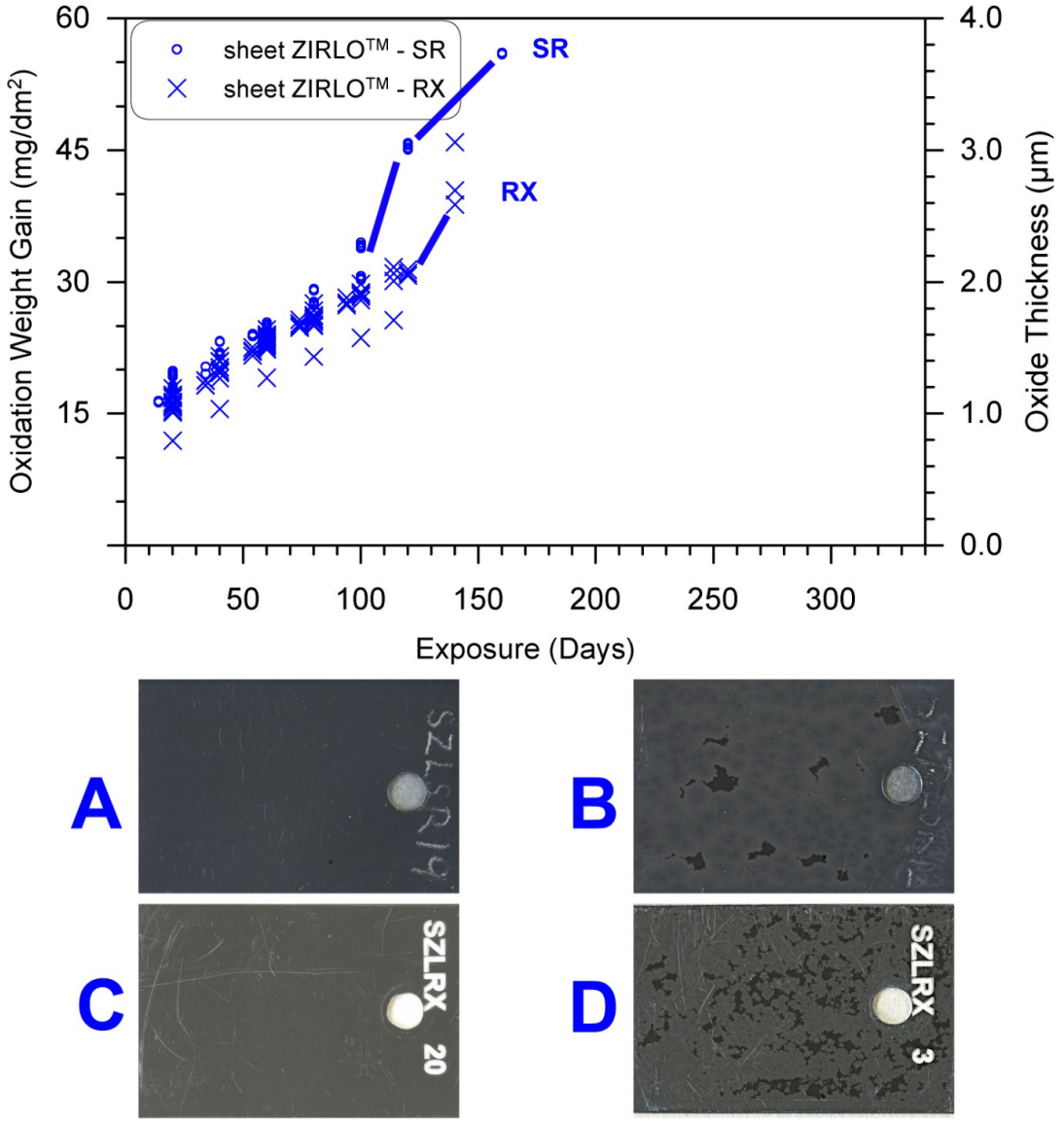

Figure 8: Autoclave corrosion weight gain profile of non-hydrided sheet ZIRLO™ SR and RX materials. Photographs of actual corrosion specimens included: (A) non-hydrided sheet ZIRLO™ – SR after 80 days of autoclave exposure, (B) non-hydrided sheet ZIRLO™ – SR after 120 days, (C) non-hydrided sheet ZIRLO™ – RX after 60 days and (D) non-hydrided sheet ZIRLO™ – RX after 140 days.

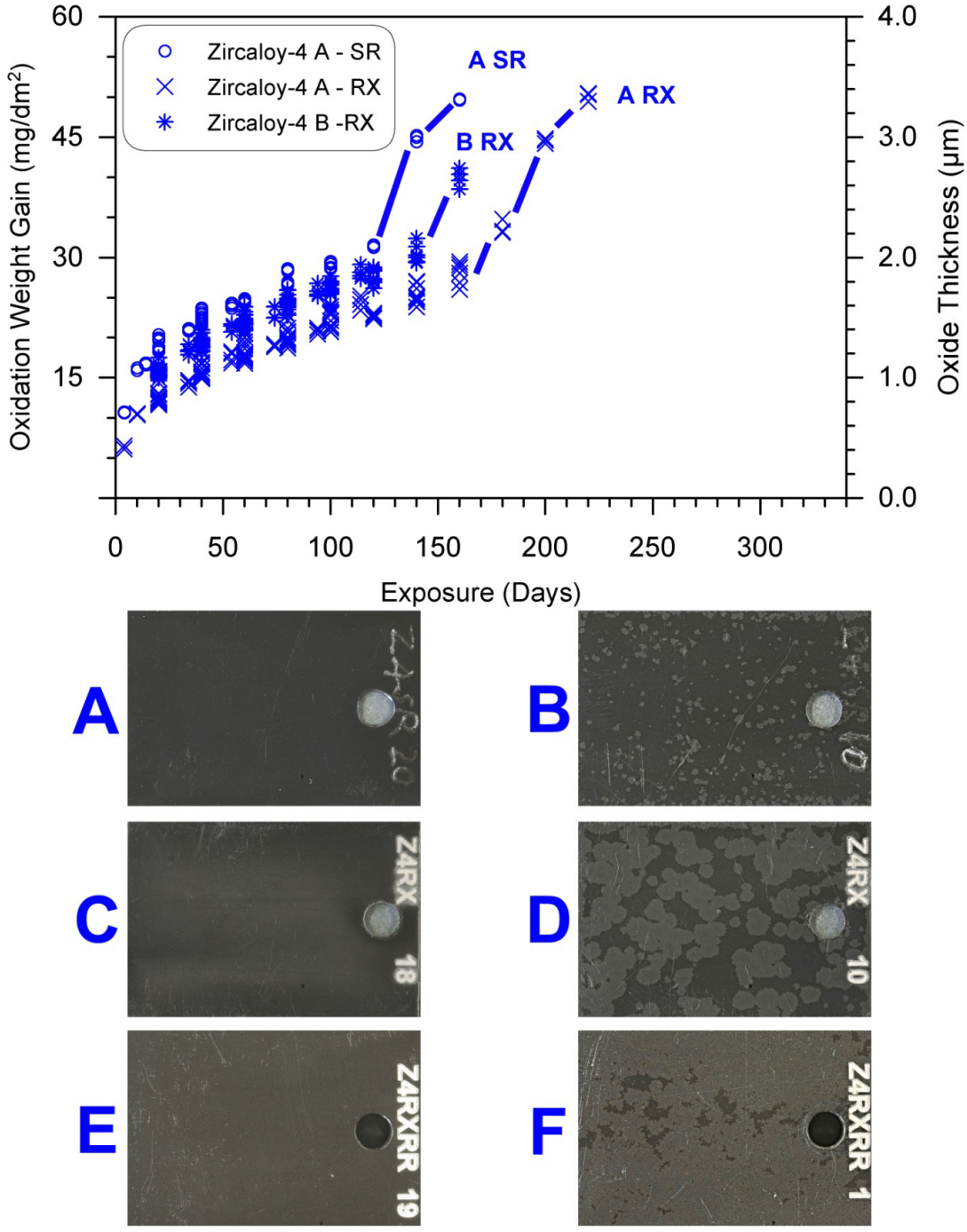

Figure 9: Autoclave corrosion weight gain profile of non-hydrided Zircaloy-4 A SR, RX and Zircaloy-4 B - RX materials. Photographs of actual corrosion specimens included: (A) non-hydrided Zircaloy-4 A – SR after 80 days of autoclave exposure, (B) non-hydrided Zircaloy-4 A – SR after 120 days, (C) non-hydrided Zircaloy-4 A – RX after 140 days, (D) non-hydrided Zircaloy-4 A – RX after 180 days, (E) non-hydrided Zircaloy-4 B – RX after 80 days and (E) non-hydrided Zircaloy-4 B – RX after 160 days of autoclave exposure.

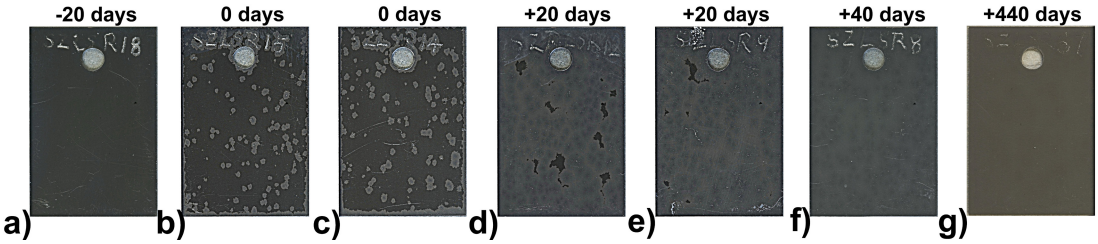

Figure 10: Photographs of sheet ZIRLO™ - SR corroded specimens demonstrating the progression of 1st transition, the number of days above the photos indicate the time to or after 1st transition, 1st transition occurred after 100 days of exposure: (a) 1st transition -20 days, (b) and (c) onset of 1st transition, (d) and (e) 1st transition +20 days, (f) 1st transition + 40 days and (g) 1st transition +440 days of autoclave exposure.

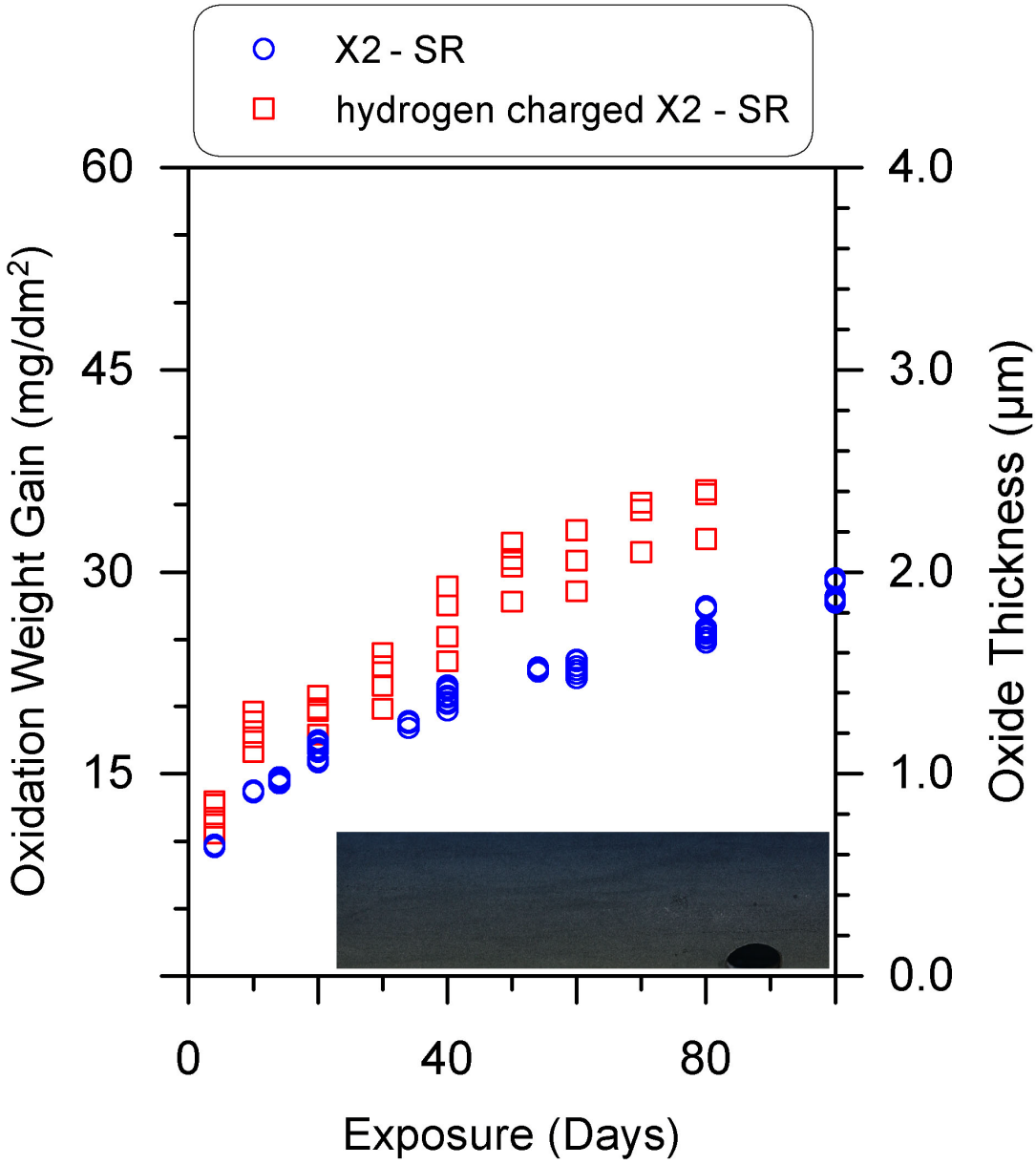

Figure 11: Autoclave corrosion weight gain profiles of hydrided X2 – SR, over all [H] around 700 wt.ppm and non-hydrided X2 – SR samples. Photographs of actual corrosion specimens inserted: hydrided X2 – SR after 40 days of autoclave exposure.

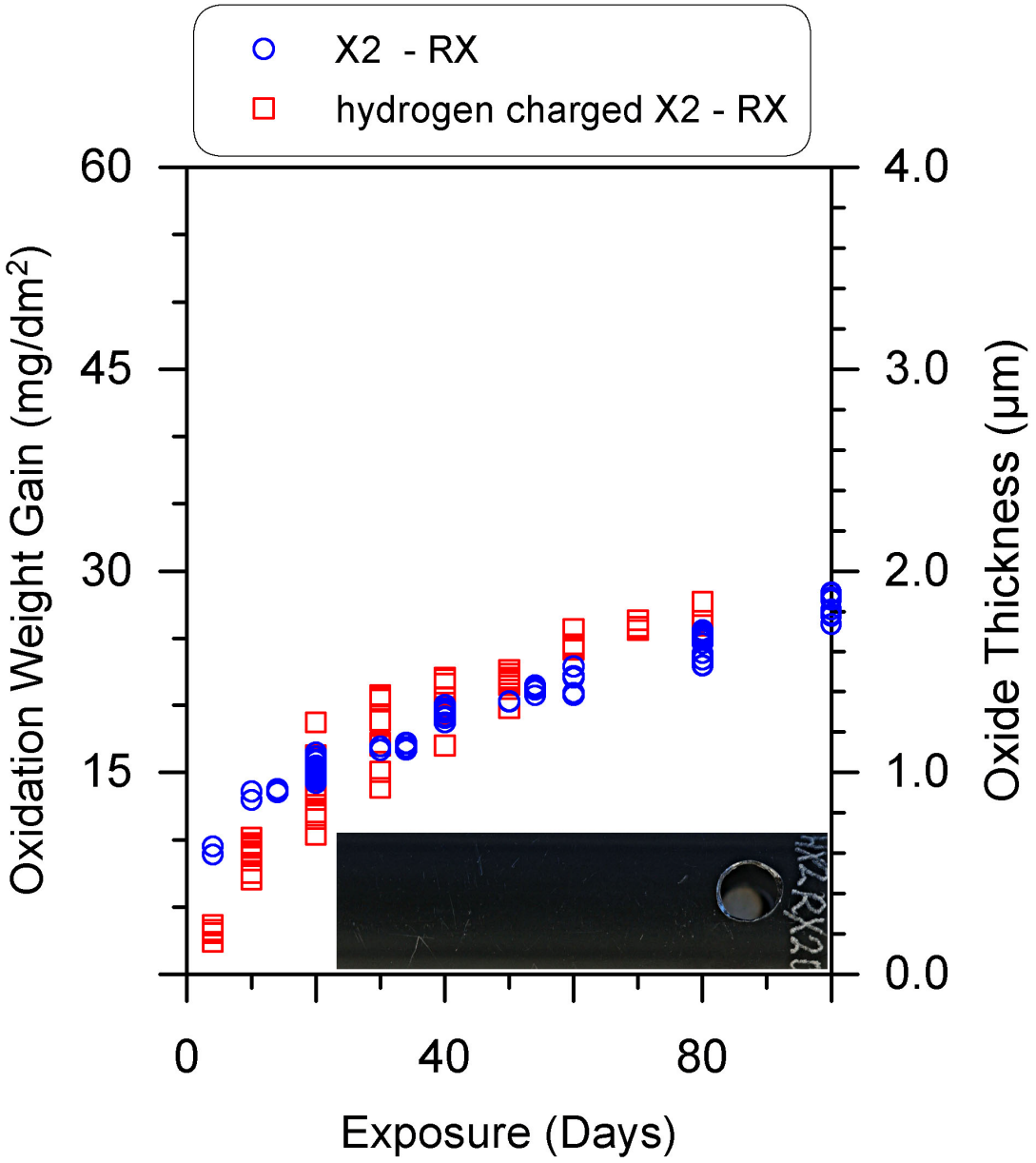

Figure 12: Autoclave corrosion weight gain profiles of hydrided X2 – RX, over all [H] around 600 wt.ppm and non-hydrided X2 – RX samples. Photographs of actual corrosion specimens inserted: hydrided X2 – RX after 40 days of autoclave exposure.

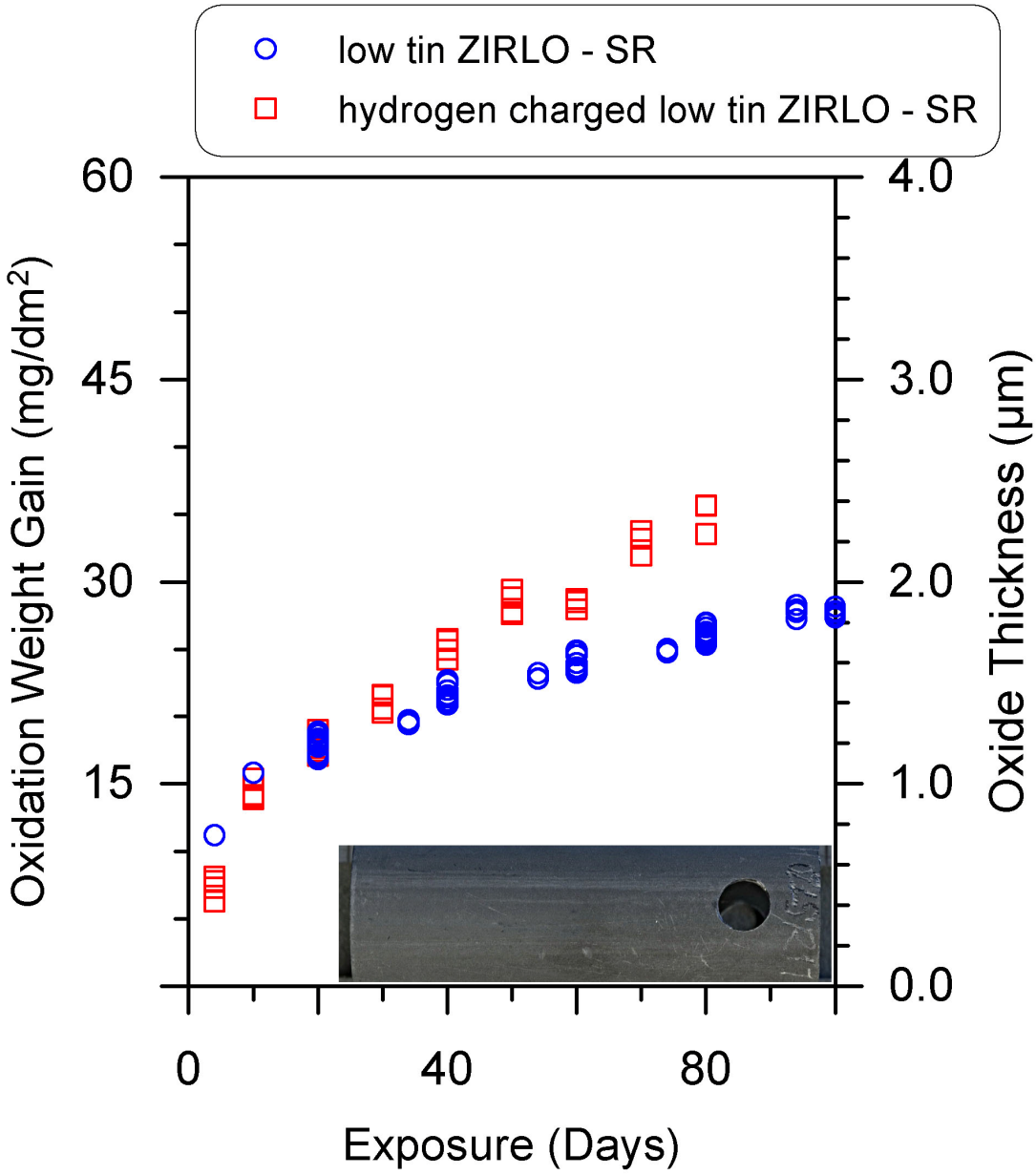

Figure 13: Autoclave corrosion weight gain profiles of hydrided low tin ZIRLO – SR, over all [H] around 700 wt.ppm and non-hydrided low tin ZIRLO – SR samples. Photographs of actual corrosion specimens inserted: hydrided low tin ZIRLO – SR after 40 days of autoclave exposure.

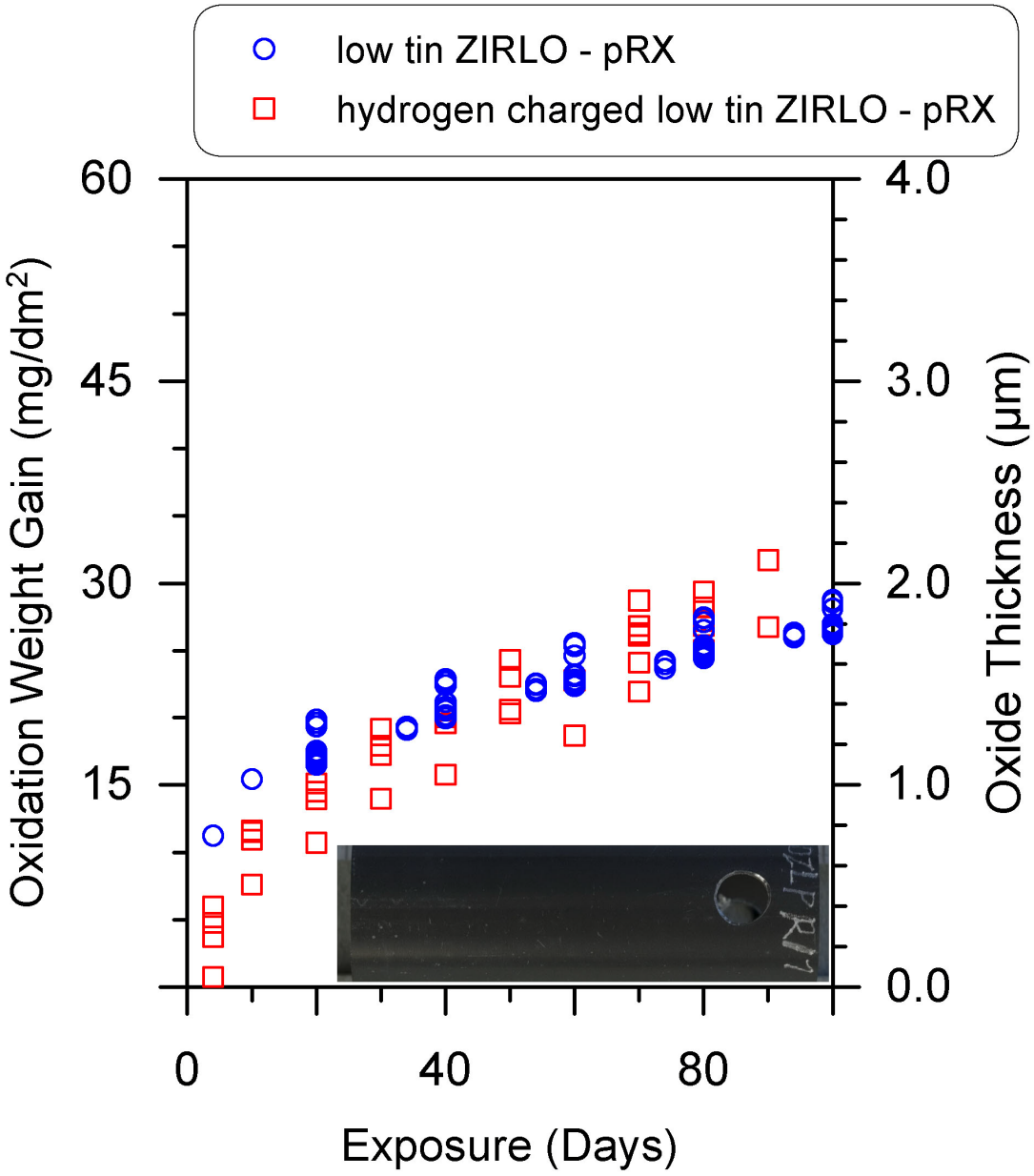

Figure 14: Autoclave corrosion weight gain profiles of hydrided low tin ZIRLO – pRX, over all [H] around 700 wt.ppm and non-hydrided low tin ZIRLO – pRX samples. Photographs of actual corrosion specimens inserted: hydrided low tin ZIRLO – pRX after 40 days of autoclave exposure.

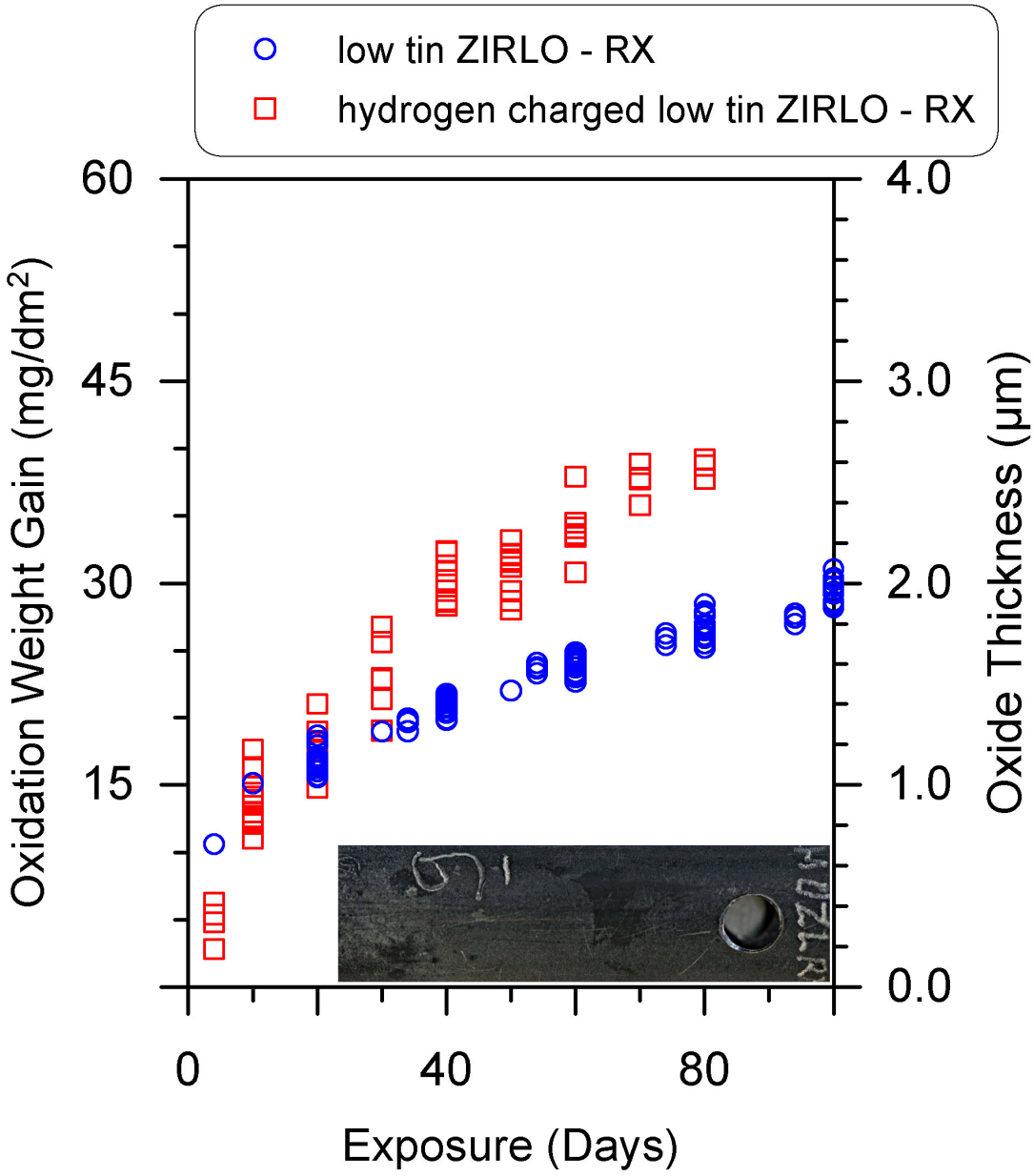

Figure 15: Autoclave corrosion weight gain profiles of hydrided low tin ZIRLO – RX, over all [H] around 650 wt.ppm and non-hydrided low tin ZIRLO – RX samples. Photographs of actual corrosion specimens inserted: hydrided low tin ZIRLO – RX after 40 days of autoclave exposure.

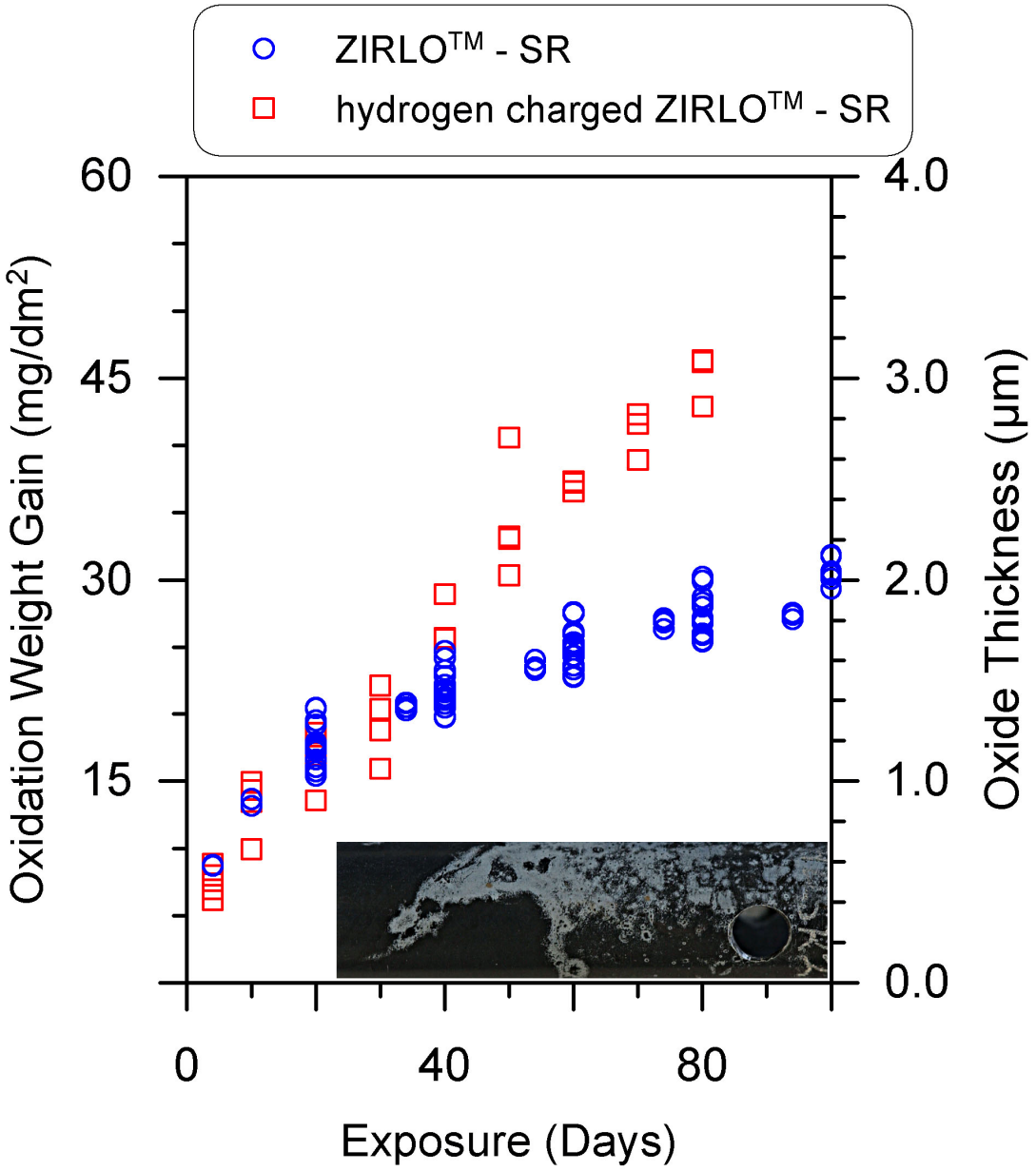

Figure 16: Autoclave corrosion weight gain profiles of hydrided ZIRLO™ – SR, over all [H] around 700 wt.ppm and non-hydrided ZIRLO™ – SR samples. Photographs of actual corrosion specimens inserted: hydrided ZIRLO™ – SR after 40 days of autoclave exposure.

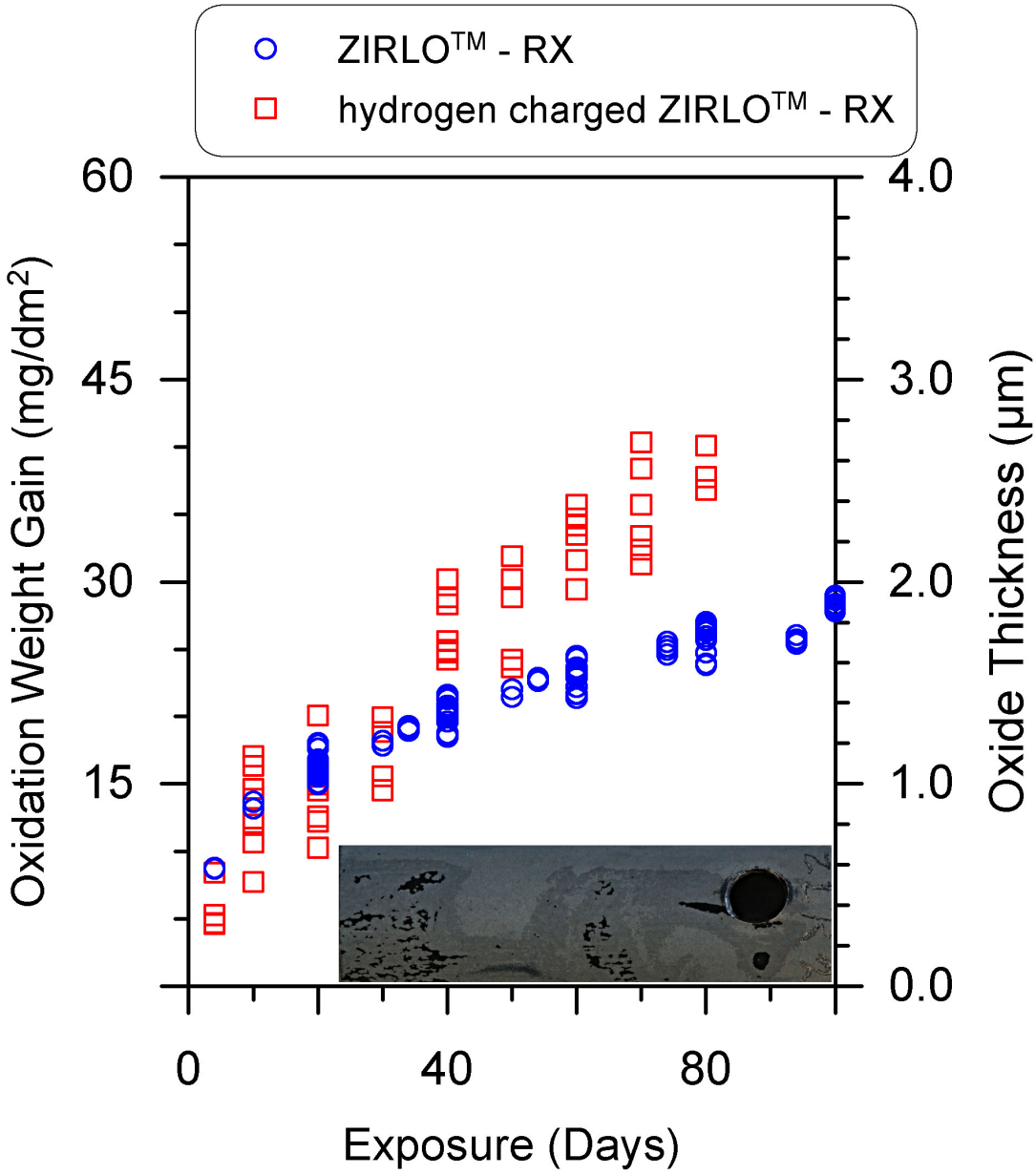

Figure 17: Autoclave corrosion weight gain profiles of hydrided ZIRLO™ – RX, over all [H] around 700 wt.ppm and non-hydrided ZIRLO™ – RX samples. Photographs of actual corrosion specimens inserted: hydrided ZIRLO™ – RX after 40 days of autoclave exposure.

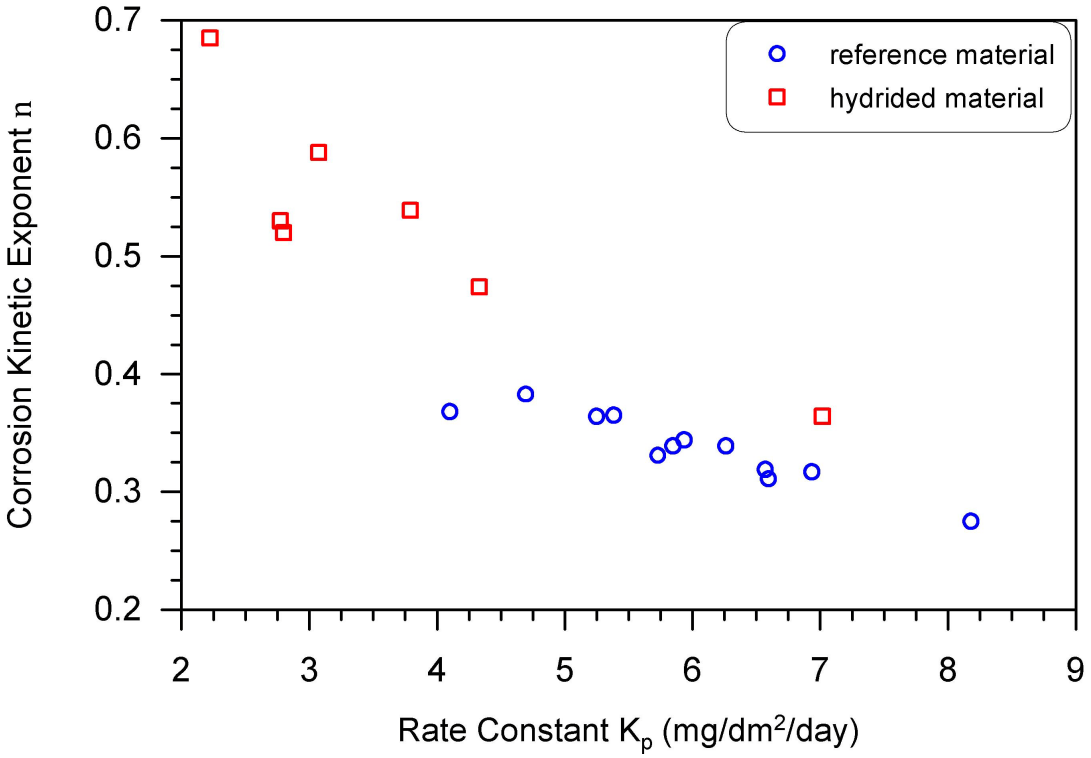

Figure 18: Corrosion kinetic exponent n plotted as a function of the rate constant K_p. Data involves all alloys and heat treatment conditions as well as their hydrogen charged counter parts.

References

1. Arima, T., et al., *Oxidation properties of Zr-Nb alloys at 500-600 °C under low oxygen potentials.* Corrosion Science, 2005. **47**(2): p. 435-446.
2. Arima, T., et al., *Oxidation kinetics of Zircaloy-2 between 450°C and 600°C in oxidizing atmosphere.* Journal of Nuclear Materials, 1998. **257**(1): p. 67-77.
3. Bryner, J.S., *The cyclic nature of corrosion of zircaloy-4 in 633 K water.* Journal of Nuclear Materials, 1979. **82**(1): p. 84-101.
4. Cox, B., *Comments on "aqueous corrosion of the Zircaloys at low temperatures".* Journal of Nuclear Materials, 1969. **30**(3): p. 351-352.
5. Cox, B., *Some thoughts on the mechanisms of in-reactor corrosion of zirconium alloys.* Journal of Nuclear Materials, 2005. **336**(2-3): p. 331-368.
6. Griggs, B., H.P. Maffei, and D.W. Shannon, *Multiple Rate Transitions in the Aqueous Corrosion of Zircaloy.* Journal of The Electrochemical Society, 1962. **109**(8): p. 665-668.
7. Hauffe, K., *Oxidation of metals*. 1965, New York: Plenum Press, Inc.
8. Kass, S. *The Development of the Zircaloys*. in *Corrosion of Zirconium Alloys*. 1964. ANS Winter meeting: ASTM International.
9. Kass, S., *Aqueous corrosion of the zircaloys at low temperatures.* Journal of Nuclear Materials, 1969. **29**(3): p. 315-321.
10. Kiselev, A.A., et al., *Corrosion of Reactor Materials*. Vol. 2. 1962, Vienna IAEA.
11. Lustman, B. and F.K. Jr, *The Metallurgy of zirconium*. 1st ed. National Nuclear Energy series, Div. 7, v. 4. 1955, New York: McGraw-Hill. 776.
12. Motta, A.T., et al., *Micostructural characterisation of oxides formed on model Zr alloys using synchrotron radiation*, in *15th International Symposium on Zirconium in the Nuclear Industry*, B. Kammenzind and M. Limback, Editors. 2009, ASTM International Sunriver Resort Oregon, USA. p. 486-506.
13. Sabol, G.P. and S.B. Dalgaard, *The Origin of the Cubic Rate Law in Zirconium Alloy Oxidation.* Journal of The Electrochemical Society, 1975. **122**(2): p. 316-317.
14. Bossis, P., et al., *Comparison of the High Burn-Up Corrosion on M5 and Low Tin Zircaloy-4*, in *14th International Symposium on Zirconium in the Nuclear Industry*, P. Rudling and B. Kammenzind, Editors. 2005, ASTM International: Stockholm, Sweden. p. 494-525.
15. Bouvier, P., J. Godlewski, and G. Lucazeau, *A Raman study of the nanocrystallite size effect on the pressure-temperature phase diagram of zirconia grown by zirconium-based alloys oxidation.* Journal of Nuclear Materials, 2002. **300**(2-3): p. 118-126.
16. Garde, A.M., *Enhancement of Aqueous Corrosion of Zircaloy-4 Due to Hydride Precipitation at the Metal-Oxide Interface*, in *9th International Symposium on Zirconium in the Nuclear Industry*, C.M. Eucken and A.M. Garde, Editors. 1991, ASTM International: Kobe, Japan. p. 566-592.
17. Godlewski, J., *How the tetragonal zirconia is stabilized in the oxide scale that is formed on a zirconium alloy corroded at 400°c in steam*, in *10th International Symposium on Zirconium in the Nuclear Industry:* , A.M. Garde and E.R. Bradley, Editors. 1994, ASTM International: Baltimore, MD. p. 663-683.
18. Peters, H.R., *Improved Characterization of Aqueous Corrosion Kinetics of Zircaloy-4*, in *6th International Symposium on Zirconium in the Nuclear Industry*, D.G. Franklin and R.B. Adamson, Editors. 1984, ASTM International: Vancouver, British Columbia, Canada. p. 507-519.

19. Yilmazbayhan, A., et al., *Structure of zirconium alloy oxides formed in pure water studied with synchrotron radiation and optical microscopy: relation to corrosion rate.* Journal of Nuclear Materials, 2004. **324**(1): p. 6-22.
20. Preuss, M., et al., *Towards a mechanistic understanding of corrosion mechanisms in zirconium alloys*, in *16th International Symposium on Zirconium in the Nuclear Industry*. 2010, ASTM International ChengDu, P.R.China.
21. Blat-Yrieix, M., et al., *Toward a Better Understanding of Dimensional Changes in Zircaloy-4: What is the Impact Induced by Hydrides and Oxide Layer?* Journal of ASTM International (JAI), 2008. **5**(9): p. 16.
22. Busser, V., et al., *Modelling of Corrosion Induced Stresses during Zircaloy-4 Oxidation in Air.* Materials Science Forum, 2008. **595-598**: p. 419-427.
23. Roy, C. and B. Burgess, *A study of the stresses generated in zirconia films during the oxidation of zirconium alloys.* Oxidation of Metals, 1970. **2**(3): p. 235-261.
24. Cox, B., *Are Zirconium Corrosion Films a Form of Partially Stablized Zirconia?* 1987, Atomic Energy of Canada Ltd.
25. Godlewski, J., et al., *Stress Distribution Measured by Raman Spectroscopy in Zirconia Films Formed by Oxidation of Zr-Based Alloys*, in *12th International Symposium on Zirconium in the Nuclear Industry*, G.P. Sabol and G.D. Moan, Editors. 2000, ASTM International: Toronto, Canada. p. 877-899.
26. Schwartz, C.M., D.A. Vaughan, and G.G. Cocks, *Report BMI-793 December 17, 1952.* , in *The Metallurgy of Zirconium*, B. Lustman and F. Kerze, Editors. 1955, McGraw-Hill: New York. p. 562.
27. Heuer, A.H. and M. Rühle, *Overview no. 45: On the nucleation of the martensitic transformation in zirconia (ZrO2).* Acta Metallurgica, 1985. **33**(12): p. 2101-2112.
28. Ploc, R.A. and S.B. Newcomb. *Microscopy of Oxidation 3*. in *Third International Conference on the Microscopy of Oxidation*. 1996. Trinity Hall, Cambridge: Institute of Materials, Minerals and Mining.
29. Cox, B., et al., *Waterside Corrosion of Zirconium Alloys in Nuclear Power Plants*. 1998, IAEA: Vienna.
30. Clayton, J.C., *Out-of-Pile Nickel Alloy-Induced Accelerated Hydriding of Zircaloy Fasteners*, in *6th International Symposium on Zirconium in the Nuclear Industry*, D.G. Franklin and R.B. Adamson, Editors. 1982, ASTM International: Vancouver, British Columbia, Canada. p. 572-591.
31. Garde, A.M., G.P. Smith, and R.C. Pirek, *In-PWR Irradiation Performance of Dilute Tin-Zirconium Advanced Alloys*, in *13th International Symposium on Zirconium in the Nuclear Industry*, G.D. Moan and P. Rudling, Editors. 2002, ASTM International: Annecy, France. p. 490-506.
32. Kammenzind, B.F., et al., *Hydrogen pickup and redistribution in alpha-annealed Zircaloy-4*, in *11th International Symposium on Zirconium in the Nuclear Industry*, E.R. Bradley and G.P. Sabol, Editors. 1996, ASTM International: Garmisch-Partenkirchen, Germany. p. 338-370.
33. Kearns, J.J., *Terminal solubility and partitioning of hydrogen in the alpha phase of zirconium, Zircaloy-2 and Zircaloy-4.* Journal of Nuclear Materials, 1967. **22**(3): p. 292-303.
34. Mcminn, A., E.C. Darby, and J.S. Schofield, *The Terminal Solid Solubility of Hydrogen in Zirconium Alloys*, in *12th International Symposium on Zirconium in the Nuclear Industry*, G.P. Sabol and G.D. Moan, Editors. 2000, ASTM International: Toronto, Canada. p. 173-196.
35. Kammenzind, B.F., et al., *The Long Range Migration Of Hydrogen Through Zircaloy In Response To Tensile And Compressive Stress Gradients*, in *12th International*

Symposium on Zirconium in the Nuclear Industry, G.P. Sabol and G.D. Moan, Editors. 2000, ASTM International: Toronto, Canada. p. 196-233.
36. Blat, M. and D. Noel, *Detrimental Role of Hydrogen on the Corrosion Rate of Zirconium Alloys*, in *11th International Symposium on Zirconium in the Nuclear Industry*, E.R. Bradley and G.P. Sabol, Editors. 1996, ASTM International: Garmisch-Partenkirchen, Germany. p. 319-337.
37. Cox, B. and T. Johnson, *Observation of a Second Transition Point During the Oxidation of Zirconium Alloys*, in *Corrosion*. 1962. p. 33.
38. Khatamian, D., *Role of hydrides on the oxidation and deuterium pickup of Zr-2.5Nb in D2O at 573 K.* Journal of Alloys and Compounds, 2005. **404-406**: p. 297-302.
39. Kido, T., *A Study on Enhanced Uniform Corrosion of Zircaloy-4 cladding during High Burnup Operation in PWRs*, in *6th Internanional Symposium on Environmental Degradation of Materials in Nuclear Power Systems - Water Reactors*, R.E. Gold and E.P. Simonen, Editors. 1993, The minerals, Metals & Materials Society: San Diego, California, USA. p. 449-456.
40. Blat, M., et al., *Contribution to a Better Understanding of the Detrimental Role of Hydrogen on the Corrosion Rate of Zircaloy-4 Cladding Materials*, in *12th International Symposium on Zirconium in the Nuclear Industry*, G.P. Sabol and G.D. Moan, Editors. 2000, ASTM International: Toronto, Canada. p. 563-592.
41. Carpenter, G.J.C., *The dilatational misfit of zirconium hydrides precipitated in zirconium.* Journal of Nuclear Materials, 1973. **48**(3): p. 264-266.
42. Daum, R.S., Y.S. Chu, and A.T. Motta, *Identification and quantification of hydride phases in Zircaloy-4 cladding using synchrotron X-ray diffraction.* Journal of Nuclear Materials, 2009. **392**(3): p. 453-463.
43. Santisteban, J.R., et al., *Hydride precipitation and stresses in zircaloy-4 observed by synchrotron X-ray diffraction.* Acta Materialia, 2010. **58**(20): p. 6609-6618.
44. Kim, Y.S., et al., *The Cause for Enhanced Corrosion of Zirconium Alloys by Hydrides*, in *13th International Symposium on Zirconium in the Nuclear Industry*, G.D. Moan and P. Rudling, Editors. 2002, ASTM International: Annecy, France. p. 274-295.
45. Seibold, A. and F. Garzarolli, *Influence of Composition and Condition on In-PWR Behavior of Zr-Sn-Nb-FeCrV alloys*, in *13th International Symposium on Zirconium in the Nuclear Industry*, G.D. Moan and P. Rudling, Editors. 2002, ASTM International: Annecy, France. p. 743-757.
46. Wei, J., et al., *Synthesis of a Hydride Rich Rim on Zirconium Alloys: A Cathodic Hydrogen Charging Method.* Corrosion Science, 2011. **To be Submitted**.
47. Cheng, B., P.M. Gilmore, and H.H. Klepfer, *PWR Zircaloy Fuel Cladding Corrosion Performance, Mechanisms, and Modeling*, in *11th International Symposium on Zirconium in the Nuclear Industry*, E.R. Bradley and G.P. Sabol, Editors. 1996, ASTM International: Garmisch-Partenkirchen, Germany. p. 137-160.
48. Barberis, P., *Zirconia powders and Zircaloy oxide films: tetragonal phase evolution during 400°C autoclave tests.* Journal of Nuclear Materials, 1995. **226**(1-2): p. 34-43.
49. Beie, H.-J., et al., *Examinations of the Corrosion Mechanism of Zirconium Alloys*, in *10th International Symposium on Zirconium in the Nuclear Industry:* , A.M. Garde and E.R. Bradley, Editors. 1994, ASTM International: Baltimore, MD. p. 615-643.
50. Harada, M., M. Kimpara, and K. Abe, *Effect of Alloying Elements on Uniform Corrosion Resistance of Zirconium-Based Alloy in 360°C Water and 400°C Steam*, in *9th International Symposium on Zirconium in the Nuclear Industry*, C.M. Eucken and A.M. Garde, Editors. 1991, ASTM International: Kobe, Japan. p. 368-390.
51. Mardon, J.P., D. Charquet, and J. Senevat, *Optimization of PWR Behavior of Stress-Relieved Zircaloy-4 Cladding Tubes by Improving the Manufacturing and Inspection Process*, in *10th International Symposium on Zirconium in the Nuclear Industry:* ,

A.M. Garde and E.R. Bradley, Editors. 1994, ASTM International: Baltimore, MD. p. 328-347.
52. Takeda, K. and H. Anada, *Mechanism of Corrosion Rate Degradation Due to Tin*, in *12th International Symposium on Zirconium in the Nuclear Industry*, G.P. Sabol and G.D. Moan, Editors. 2000, ASTM International: Toronto, Canada. p. 592-608.
53. Li, P., I.W. Chen, and J.E. Penner-Hahn, *Effect of Dopants on Zirconia Stabilization—An X-ray Absorption Study: II, Tetravalent Dopants.* Journal of the American Ceramic Society, 1994. **77**(5): p. 1281-1288.
54. Kim, D.-J., J.-W. Jang, and H.-L. Lee, *Effect of Tetravalent Dopants on Raman Spectra of Tetragonal Zirconia.* Journal of the American Ceramic Society, 1997. **80**(6): p. 1453-1461.
55. Cox, B. and J.P. Pemsler, *Diffusion of oxygen in growing zirconia films.* Journal of Nuclear Materials, 1968. **28**(1): p. 73-78.
56. Cox, B. and C. Roy, Electrochemistry Technology, 1966. **4**: p. 121.
57. Ploc, R.A., *Transmission electron microscopy of thin (<2000 å) thermally formed ZrO2 films.* Journal of Nuclear Materials, 1968. **28**(1): p. 48-60.
58. Ploc, R.A., *A transmission electron diffraction study of ZrO2 on α-Zr (0001).* Journal of Nuclear Materials, 1982. **110**(1): p. 59-64.
59. Ploc, R.A., *Electron diffraction from ZrO2 on αZr(101̄0).* Journal of Nuclear Materials, 1983. **115**(1): p. 110-117.
60. Ploc, R.A., *Electron diffraction analysis of ZrO2 on αZr(112̄0).* Journal of Nuclear Materials, 1983. **113**(1): p. 75-80.
61. Yilmazbayhan, A., et al., *Transmission electron microscopy examination of oxide layers formed on Zr alloys.* Journal of Nuclear Materials, 2006. **349**(3): p. 265-281.
62. Cox, B., in *Advances in Corrosion Science and Technology*, M.G. Fontana and R.W. Staehle, Editors. 1976, Plenum: New York. p. 173.
63. Donaldson, A.T. and H.E. Evans, *Oxidation-induced Creep in Zircaloy-2, Parts I-III*. 1980, Central Electricity Generating Board, Berkeley Nuclear LabsUK Reports, RD/T/N4855, 4952 and 4976: Berkeley, UK.
64. Ni, N., et al., *Porosity in oxides on zirconium fuel cladding alloys, and its importance in controlling oxidation rates.* Scripta Materialia, 2010. **62**(8): p. 564-567.
65. Park, J.-Y., et al., *Corrosion and Oxide Properties of HANA alloys*, in *15th International Symposium on Zirconium in the Nuclear Industry*, B. Kammenzind and M. Limback, Editors. 2009, ASTM International Sunriver Resort Oregon, USA. p. 471-485.
66. Bossis, P., et al., *In PWR Comprehensive Study of High Burn-Up Corrosion and Growth Behavior of M5 and Recrystallized Low-Tin Zircaloy-4*, in *15th International Symposium on Zirconium in the Nuclear Industry*, B. Kammenzind and M. Limback, Editors. 2009, ASTM International Sunriver Resort Oregon, USA. p. 430-456.
67. Yueh, H.K., et al., *Improved ZIRLO™ Cladding Performance through Chemistry and Process Modifications*, in *14th International Symposium on Zirconium in the Nuclear Industry*, P. Rudling and B. Kammenzind, Editors. 2005, ASTM International: Stockholm, Sweden. p. 330-348.
68. Takagawa, Y., et al., *The Correlation Between Microstructures and in-BWR Corrosion Behavior of Highly Irradiated Zr-based Alloys*, in *14th International Symposium on Zirconium in the Nuclear Industry*, P. Rudling and B. Kammenzind, Editors. 2005, ASTM International: Stockholm, Sweden. p. 386-403.
69. Sell, H.-J., S. Trapp-Pritsching, and F. Garzarolli, *Effect of Alloying Elements and Impurities on in-BWR Corrosion of Zirconium Alloys*, in *14th International Symposium on Zirconium in the Nuclear Industry*, P. Rudling and B. Kammenzind, Editors. 2005, ASTM International: Stockholm, Sweden. p. 404-417.

70. Dahlbäck, M., et al., *The Effect of Beta-Quenching in Final Dimension on the Irradiation Growth of Tubes and Channels*, in *14th International Symposium on Zirconium in the Nuclear Industry*, P. Rudling and B. Kammenzind, Editors. 2005, ASTM International: Stockholm, Sweden. p. 276-304.
71. Arborelius, J., et al., *The Effect of Duplex Cladding Outer Component Tin Content on Corrosion, Hydrogen Pick-up, and Hydride Distribution at Very High Burnup*, in *14th International Symposium on Zirconium in the Nuclear Industry*, P. Rudling and B. Kammenzind, Editors. 2005, ASTM International: Stockholm, Sweden. p. 526-546.
72. Garzarolli, F., H. Ruhmann, and L.V. Swam, *Alternative Zr Alloys with Irradiation Resistant Precipitates for High Burnup BWR Application*, in *13th International Symposium on Zirconium in the Nuclear Industry*, G.D. Moan and P. Rudling, Editors. 2002, ASTM International: Annecy, France. p. 119-134.
73. Etoh, Y., et al., *Development of New Zirconium Alloys for a BWR*, in *11th International Symposium on Zirconium in the Nuclear Industry*, E.R. Bradley and G.P. Sabol, Editors. 1996, ASTM International: Garmisch-Partenkirchen, Germany. p. 825-849.
74. Young S. Kim, K.S. Rheem, and D.K. Min, *Phenomenological Study of In-Reactor Corrosion of Zircaloy-4 in Pressurized Water Reactors*, in *10th International Symposium on Zirconium in the Nuclear Industry:* , A.M. Garde and E.R. Bradley, Editors. 1994, ASTM International: Baltimore, MD. p. 745-759.
75. Garzarolli, F., R. Schumann, and E. Steinberg, *Corrosion Optimized Zircaloy for Boiling Water Reactor (BWR) Fuel Elements*, in *10th International Symposium on Zirconium in the Nuclear Industry:* , A.M. Garde and E.R. Bradley, Editors. 1994, ASTM International: Baltimore, MD. p. 709-723.
76. Garde, A.M., et al., *Corrosion Behavior of Zircaloy-4 Cladding with Varying Tin Content in High-Temperature Pressurized Water Reactors*, in *10th International Symposium on Zirconium in the Nuclear Industry:* , A.M. Garde and E.R. Bradley, Editors. 1994, ASTM International: Baltimore, MD. p. 760-778.

End of Publication 2

Publication Number 3

The effect of Sn on autoclave corrosion performance and corrosion mechanisms in Zr-Sn-Nb alloys

The effect of Sn on autoclave corrosion performance and corrosion mechanisms in Zr-Sn-Nb alloys

J. Wei[1], P. Frankel[1], E. Polatidis[1], M. Blat[2], A. Ambard[2], R. J. Comstock[3], Lars Hallstadius[4] and Michael Preuss[1]

1: Materials Performance Centre, School of Materials, The University of Manchester, UK

2: EDF - R&D, Moret sur Loing, France

3: Westinghouse Electric Co., Pittsburgh, USA

4: Westinghouse Electric Co., Sweden

Abstract

Three Zr-Sn-Nb alloys with tin concentration ranging from 0.14 to 0.92 wt.% were autoclave tested using a simulating primary water environment at 360°C. It was found that the corrosion performance was strongly affected by the Sn content. The alloy with the lowest tin content, X2, exhibited the best corrosion performance while ZIRLO™, with the highest tin content, experienced the earliest 1st transition. The microstructure of the oxide grown on tube samples was investigated via cross-sectional Scanning Electron Microscope (SEM). Energy dispersed synchrotron X-ray diffraction measurements were conducted to reveal the residual stress state in the tetragonal and monoclinic phase as well as tetragonal phase fraction information. It was found that both oxide phases display high in-plane compressive stresses but of

different levels depending on the phase and alloy. The amount of tetragonal phase and most importantly, the frequency of tetragonal to monoclinic phase transformation decreases with decreasing Sn levels. Therefore a relationship could be established between level of phase transformation and time to transition. It is proposed that in low Sn alloys any tetragonal grains formed during corrosion are mainly very small sized stabilised grains that remain stable throughout the corrosion process. In contrast, it is proposed that alloys with higher Sn levels can in addition grow larger stress stabilised grains that become unstable as the corrosion front continues to grow further inwards and stresses in the existing oxide relax.

Introduction

The importance of zirconium alloys in Pressurised Water Reactors (PWRs) is attributed to their low neutron cross-section, high corrosion resistance and sufficient mechanical performance during reactor service. During the initial stage of corrosion in high temperature pressurised water, zirconium alloys deviate from the expected parabolic rate law with a tendency towards cubic growth kinetics [1-5]. In general, once the oxide has grown to a few microns (pre-transition), a brief acceleration of corrosion kinetics is observed (post-transition), followed by a second cycle of parabolic/cubic growth rates. These cycles are repeated until accelerated linear corrosion occurs (breakaway) [3, 6-16]. Knowledge of such corrosion kinetics, and especially a more mechanistic understanding of transition and breakaway, is of great importance for undertaking more accurate, physically based lifetime predictions of cladding tubes. During the gradual oxidation, a highly compressive stress is expected to build up inside the oxide due to a Pilling-

Bedworth ratio of 1.56 from zirconium to zirconia [1, 17], stabilising the metastable tetragonal ZrO_2 [7, 18-20] which has been reported to form and accumulate near the oxide/metal interface [16, 19, 21, 22]. The compressive stress in the oxide has to be balanced by tensile stress in the metal substrate and it has been argued that this will result in creep of the metal substrate with prolonged corrosion [19, 23]. It has been suggested that this will relax the compressive stresses in the oxide that formed earlier and generate a stress gradient with the highest stresses near the metal/oxide interface [19]. As a result of the stress relaxation away from the interface, the tetragonal ZrO_2 phase becomes destabilised, resulting in a martensitic phase transformation to monoclinic ZrO_2 associated with a 5% volume expansion [24]. It is generally believed that this phase transformation results in the formation of cracks [25], which will eventually lead to the break down of the inner oxide acting as a barrier. However, experimental evidence of a direct link between tetragonal to monoclinic phase transformation and crack formation remains elusive. Other proposed factors stabilising the tetragonal phase include the effect of small oxide grain size (smaller than 25-30nm) [26-29] and defects induced by dopants however the concentration of dopants in the oxide is generally considered to be too low to play any significant role.

Sn was originally introduced to zirconium alloys as an alloying element countering the poor corrosion resistance caused by nitrogen [30]. However, it has been found that Sn actually deteriorates the corrosion performance of Zr alloys. Since the nitrogen content of modern alloys is very low now, it has allowed developing alloys with reduced Sn content [26, 31-34]. The relationship between Sn content and

tetragonal phase in the oxide is considered to be key in terms of understanding its effect on corrosion. It was reported that decreasing Sn levels lead to the formation of a thicker tetragonal barrier layer at the oxide/metal interface improving corrosion performance [34]. However, other researchers have found that the decrease of Sn actually reduces the tetragonal phase fraction in the oxide grown on Zr alloys [26, 32]. The latter findings are further supported by studies on stabilisation of tetragonal phase in structural tetragonal zirconia by Sn although in this case the required Sn levels are comparatively high due to the larger oxide grain size [35, 36]. To date, mechanistic studies on the effect of Sn on corrosion performance has only been carried out in more traditional Zr alloys that do not contain any Nb. However, Nb containing alloys such as ZIRLO^{TM} and M5 have now widely replaced traditional Zircaloys in fuel assemblies for PWRs. It is also still not clear by which mechanism a change of tetragonal phase fraction, due to a different alloy chemistry, will affect the time it takes for an alloy to reach the point of transition during corrosion.

In the present study, three Zr-Nb-Sn alloys with different Sn content (ZIRLO^{TM}, low tin ZIRLO and the experimental alloy X2) were corrosion tested in an autoclave operating in “simulated” primary water condition. Autoclave tested materials were examined after different exposure times by means of high energy synchrotron X-ray diffraction to study the stress state and tetragonal/monoclinic ZrO_2 ratio in the oxide. In addition, the oxide was investigated by scanning electron microscopy (SEM) to identify possible cracks in the oxide.

Experimental

Materials Preparation

The alloys investigated in this study were recrystallized ZIRLO^{TM} and two low tin versions of it. Corrosion samples of 30 mm in length (9 mm diameter) were cut from tubes provided by Westinghouse. Chemical compositions of the alloys were determined at the EDF Research and Development facility in Moret-Sur-Loing, France and can be found in Table 1. Westinghouse commercially distributes one of the low tin versions of ZIRLO^{TM} alloy in a partially recrystallized condition known as Optimised-ZIRLO^{TM}. However, since all material studied in the present work was in a recrystallized condition (RX), this alloy is here referred to as 'low tin ZIRLO'. The other alloy X2 with even lower tin content is an experimental alloy. All samples were pickled at 60°C in a solution of 10 vol.% hydrofluoric acid, 45 vol.% nitric acid and 45 vol.% distilled water for 3 minutes to remove inorganic contamination from the fabrication process prior corrosion testing.

Autoclave Corrosion

In order to record detailed weight gain curves, sets of 4 samples were introduced into the autoclaves every 20 days 5 times. This allowed the corrosion weight gain to be tracked of as a function of exposure time, and provided a maximum of 20 weight gain readings for every given exposure length. The corrosion tests were carried out in static autoclaves operating at 360°C and 18 MPa, using a starting water chemistry similar to primary water ([LiOH] = 2 wt.ppm and [H_3BO_4] = 1000 wt.ppm). The corrosion experiments aimed to provide samples and weight gain data from the

early stage of corrosion until after the first transition. Oxide morphology was later studied via cross-sectional SEM examinations.

Oxide Microstructure Characterisation

For imaging of the oxide after corrosion testing, cross-sectional samples were prepared. For corrosion tested samples a Ni coating was applied before cutting the sample in order to protect the oxide. Samples were ground and polished carefully following standard metallographic procedures followed by etching in a solution of 5 vol.% hydrofluoric acid, 45 vol.% nitric acid and 50 vol.% distilled water at room temperature. Then a carbon layer around 5 nm thick was deposited on freshly etched sample surface using a Gatan Model 682 PECS^{TM} precision etching & coating system for SEM. The carbon layer improves the surface conductivity, prevents the accumulation of electrostatic charge which would otherwise result in image artefacts. Imaging of the cross sectional samples was performed using a Philips XL30 FEG-SEM.

Pole Figure Measurement with lab X-ray

Partial pole figures were measured on oxidised samples using a BRUKER D8 Discover diffractometer operating at 35kV (Co-tube) in coupled θ/2θ mode. Measurements were conducted on the as oxidised surface of the tube samples without mechanical polishing. Due to the surface curvature of the tube sample, a spot size of d≈0.5mm was selected. The estimated maximum penetration depth for the above X-ray setup is 8 μm, greater than the oxide thickness of all involved materials.

Synchrotron X-ray Diffraction

The advantage of using synchrotron X-rays over laboratory X-rays is the high flux and high peak position accuracy, which enables one to include the characterisation of minor phases such as the tetragonal phase in the present case. Experiments to characterise the residual stresses in the oxide layer (monoclinic and tetragonal ZrO_2) and metal substrate together with the tetragonal/monoclinic phase fraction ratio were carried out on the EDDI beam line at BESSY, Berlin, which is an energy dispersive instrument dedicated to material science. A detailed description of the EDDI beam line has been given by Ch. Genzel et al. [37], the general layout is shown in Figure 1. The residual stress measurements were undertaken using the classical $sin^2\psi$ approach [38] assuming a biaxial stress state in a Cartesian coordinate system. The elastic properties used for each phase are shown in Table 2 [39-41]. Based on single crystal values of the monoclinic zirconia phase, E. Polatidis et al. [41] calculated polycrystalline diffraction elastic constants using an Elasto-Plastic Self-Consistent (EPSC) model [42]. EPSC modelling simulates deformation of polycrystalline aggregates by predicating the response of each grain within an infinite medium to predict the overall response of a given diffraction plane within the polycrystalline material. The current study applied these same elastic constants to calculations regarding the tetragonal phase, due to the lack of reliable data for tetragonal phase at room temperature (yttrium stabilised zirconia data was considered in appropriate).

Since all measured samples had layers of oxide that were only a few microns thick, it is reasonable to assume that the out of plane stress in the oxide is zero. This

assumption in combination with the $sin^2\psi$ technique eliminates the need for a stress free lattice parameter. Measurements were carried out with an incident beam and the EDX detector placed at 3° (i.e. 2θ=6°) to the surface when the sample was at ψ = 0°. Twenty one individual ψ angles ranging from 22° to 66° were selected based on the intensity of the spectrum at each angle. This range corresponds to a $sin^2\psi$ range of 0.14 to 0.84. All stress data presented here are representative of the hoop direction of the cladding tube. Early measurements in the axial and hoop direction showed no significant differences between the two stress directions. A BESSY II in-house analysis program written in MATHEMATICA™ was used for processing the instruments' output files. It applies pseudo-voigt peak fitting for a selected energy range and produces plots of $sin^2\psi$, peak intensity, peak position and widths at half maximum of each peak (FWHM). In general, accurate peak analysis of the diffraction signal from a thin monoclinic/tetragonal oxide layer is inherently difficult due to many overlapping peaks, and the nano-sized grain structure resulting in low intensity and broad peaks. In the present case, the reflections from the oxide that could be fitted with the highest certainty were the $(\bar{1}11)$ reflection of the monoclinic phase and the (101) of the tetragonal phase. In addition, the $(10\bar{1}1)$ reflection of the α-zirconium phase and (111) reflection of the monoclinic phase were also analysed. A typical diffraction spectrum of autoclave tested material can be seen in Figure 2, highlighting the limited quality of the tetragonal ZrO_2 reflection. Note that hydrogen generated during corrosion led to the formation of hydrides after prolonged autoclave corrosion when the material was cooled to room temperature. This resulted in the observation of a weak (111) reflection of the δ Zr-hydride phase. In order to minimise texture effects in the

oxide when determining the integrated intensity (I) of each phase the data were averaged along the range of ψ angles. A more detailed description of the data analysis carried during such studies can be found in [41].

Results

Autoclave Corrosion

The corrosion kinetics of autoclave tested ZIRLO^{TM}, low tin ZIRLO and X2 samples are presented in Figure 3 as corrosion weight gain against autoclave exposure time. Please note that instead of presenting averaged set values, data of each individual sample are plotted in Figure 3, illustrating the level of scatter observed during the experiment.

Tested materials exhibited typical corrosion kinetics with an indication of change from pre- to post-1st transition at around 140 days in the case of ZIRLO^{TM} and 140-240 days in the case of low tin ZIRLO. Before transition, the oxide appeared black in all samples. During transition specimens exhibited patches where the oxide had become grey in colour. Note that in the case of low tin ZIRLO, a very long transition phase of about 100 days was detected. Corrosion tests carried out on the commercial version of this alloy (partially recrystallized), did not show such behaviour around transition.

With up to 260 days of autoclave exposure, X2 showed no sign of 1st transition. A universally black oxide was observed on pre-1st transition samples as early as after 20 days and as late as after 260 days of corrosion testing. A second series of autoclave exposures aimed at recording long term corrosion kinetics also confirmed

that X2 showed no sign of 1st transition despite after 360 days of exposure and ~45 mg/dm^2 weight gain, but clearly dark and light patchy surfaces after 540 days of exposure and ~80 mg/dm^2 weight gain.

Oxide Microstructure

At the early stage of corrosion (10 days of exposure), a continuous oxide layer (≈1μm) with almost no visible cracks and a smooth oxide/metal interface was observed for all three alloys, Figure 4 (a), (c) and (e). The oxide thickness, measured by using the FEG-SEM images, was consistent with that calculated from oxidation weight gain (15 mg/dm^2 = 1 μm [43, 44]).

Figure 4 (b), (d) and (f) show cross-sectional FEG-SEM images taken on the 3 different alloys after they had gained about 30 mg/dm^3 weight. This corresponded to an exposure time in the autoclave exceeding 120 days in the case of ZIRLO™ samples, 160 days in the case of low tin ZIRLO and 180 days in the case of X2. In the case of ZIRLO™ and low tin ZIRLO, the examined samples were near to the exposure time where transition occurred. It can be seen that at this stage the oxide had developed some short and medium sized cracks. In X2 alloy where the examined sample was still more than 180 days prior to the 1st transition, the oxide displayed only very few and small cracks.

Residual Stress and Phase Fraction Analysis

A number of autoclave tested specimens were investigated using synchrotron X-ray diffraction as described above. Generally, all samples were measured within one week of being taken out of the autoclave. Specimens were selected from relatively early stage of corrosion, i.e. before 1st transition and early after 1st transition. Since

transition samples display a patchy surface of grey (post transition) and black (pre transition) oxide, measurements were carried out in both areas. Measurements of the residual stresses in the metal substrate consistently showed tensile stresses of up to +150 MPa. In Figure 5 (a), (b) and (c), the measured oxide stresses (monoclinic and tetragonal phase) are plotted as a function of corrosion weight gain for ZIRLO^{TM}, low tin ZIRLO and X2. In both ZIRLO^{TM} and low tin ZIRLO the oxide stresses in the monoclinic phase were about -700 MPa to -1000 MPa regardless of the corrosion weight gain, while Stresses in X2 samples were slightly lower (-500 to -900 MPa) and accompanied by greater scatter. Note that in post-transition low tin ZIRLO and X2 samples, lower compressive monoclinic stresses were observed (hollow markers) compared to pre-transition samples (Solid markers).

The stresses measured in the tetragonal oxide phase had considerably higher uncertainty than the stresses measured in the monoclinic phase due to a very weak tetragonal (101) reflection, see Figure 2. The stresses determined in the tetragonal phase were generally between -1300 to -2100 MPa for ZIRLO^{TM} and low tin ZIRLO materials. It can be seen from Figure 5 (f) that X2 displayed very large stress variations in the tetragonal phase with compressive stresses as low as -500 MPa and as high as -2400 MPa.

It should be noted that no room temperature elastic properties are available for purely tetragonal zirconia, as this phase is not generally stable at room temperature. Therefore, the stresses have been calculated using the same elastic properties used for monoclinic zirconia. This may introduce further uncertainty for the absolute

value of the residual stresses in the tetragonal phase, but will not affect the trends observed.

Figure 6 shows the calculated tetragonal phase fraction and the equivalent layer thickness of the tetragonal phase as a function of weight gain. The calculation is based on the Garvie-Nicholson equation [45]:

$$Tetragonal\ Fraction = I_{tet\ (101)}/[I_{tet\ (101)} + I_{mono\ (111)} + I_{mono\ (\bar{1}11)}].$$

The Garvie-Nicholson equation was modified to include integration over Ψ angles where I is the integrated intensity averaged over ψ angles. The equivalent layer thickness of the tetragonal phase was calculated by multiplying the calculated tetragonal phase fraction with the actual corrosion weight gain. The calculated tetragonal fraction is an index for the fraction of tetragonal phase present in the oxide while the theoretical equivalent tetragonal phase thickness aims at also taking the oxide thickness into consideration. Figure 7 shows schematically, in a simplified manner, the expected distribution of tetragonal and monoclinic ZrO_2 based on observations such as [16, 19]. It highlights that with continuous growth of the oxide the ratio of tetragonal/monoclinic phase is expected to decrease, although the absolute amount of tetragonal oxide might remain unchanged. Such trend is indeed observed particularly for ZIRLO™ and to a slightly lesser degree for low tin ZIRLO, Figure 6 (a) and (b). Note that during the early stage of corrosion, the tetragonal phase fraction is significantly lower in low tin ZIRLO compared to ZIRLO™. In contrast, X2 shows hardly any change of the tetragonal/monoclinic ratio with increasing weight gain and a very low tetragonal phase fraction from the first measurement point, which is 10 days into corrosion only. The present results,

based on a large number of samples, clearly show that Sn increases the tetragonal phase fraction, which is in agreement with observations by [26, 32], but contradicts the observation by K. Takeda [34]. Finally, a decrease of the tetragonal phase fraction from pre- to post- transition conditions was observed in low tin ZIRLO and X2.

In order to ensure that the differences of calculated tetragonal phase fractions between the three alloys are not based on significant differences in the texture of the oxide, pole figures of the monoclinic $(\bar{1}11)$ reflection were measured on pre-1st transition samples, Figure 8. Attempts to measure tetragonal pole figures failed due to a very weak tetragonal reflection when using a lab based diffractometer. Figure 8 demonstrates that the monoclinic oxide textures are indeed practically identical when comparing the three alloys. Following the reasonable assumption that this is then also true for the tetragonal phase, it can be verified that the data presented in Figure 6 are not affected by oxide texture differences between the alloys.

Discussion

Relationship between tin content and corrosion

Current corrosion kinetics recorded during autoclave experiments clearly indicate the improvement introduced by the decrease of tin content in Zr-Nb-Sn alloys. The onset of 1st transition (defined by the re-acceleration of corrosion kinetics and the appearance of grey patch on the oxide surface) was delayed from as early as 140 days in ZIRLO^{TM} material to as late as more than 360 days in X2 material. It must be noted that apart from the exposure time required to reach 1st transition, the actual

corrosion kinetics in pre-1st transition stage were practically identical. This suggests that the transport mechanisms and rate determining diffusion species is the same for the three alloys. The oxidation kinetics exponent of the three alloys is 0.34 for ZIRLOTM, 0.34 for low tin ZIRLO and 0.38 for X2.

Evaluating the tetragonal phase fraction measurement

The pre-1st transition stage of the zirconium oxidation have been widely accepted as a process controlled by the inward diffusion of oxygen ions across the oxide film [12], although it has been argued whether bulk diffusion of oxygen through a perfect oxide or crystallite boundary diffusion plays the predominant role [46]. Therefore the structure of the oxide is considered to be of importance in determining the corrosion resistance. The tetragonal phase has been reported to accumulate near the oxidation progression front, the oxide/metal interface. Consequently, it has been argued that it is the tetragonal phase that acts as a barrier layer for oxygen diffusion [10, 16, 19, 21, 22, 47]. Following this line of thought, the thickness (indirectly represented by the tetragonal phase fraction) and the integrity of this tetragonal rich layer is the dominating contributor to corrosion resistance. K. Takeda and H. Anada [34] studied a range of Zircaloy-4 type alloys with different Sn content and found that the reduction of tin improved corrosion resistant. Their lab based X-ray measurements suggested that the tetragonal phase fraction increases as tin is reduced. They further proposed a degradation model of the tetragonal phase, which suggested that the oxidation of the segregated tin in the oxide accelerates the tetragonal to monoclinic phase transformation and created porosity in the monoclinic. However, the tetragonal phase fraction was only

determined for a single sample in each alloy, and considering the high uncertainty when measuring this phase by laboratory diffraction together with the general observation that tin does in fact stabilise the tetragonal phase, it seems unlikely that this model is correct. As demonstrated in Figure 6, the tetragonal/monoclinic ratio is strongly depending on the thickness of the oxide when measurements were conducted. Therefore comparison between tetragonal phase fractions of different alloys is only meaningful when multiple measurements were conducted as a function of corrosion weight gain.

Relationship between tin content and tetragonal to monoclinic phase transformation

The highest early tetragonal phase fraction and the steepest decline of it with weight gain was recorded in ZIRLO^{TM} (Figure 6 a), which has the highest tin content of the three alloys. The exponent for this trend is fitted to be -0.712 ± 0.087, where as an exponent of -1 is expected for a theoretical tetragonal rich layer with constant thickness. This is further confirmed by the near horizontal trend measured in Figure 6 d. This assumption requires that all tetragonal phase transforms once the compressive stresses have declined. However, there is sufficient experimental evidence that in regions of low stresses some tetragonal phase is still present [19]. Comparing Figure 6 a-c demonstrates unambiguously that the early tetragonal/monoclinic ratio goes down with the amount of Sn in the alloy and at the same time decline of the ratio with weight gain also decreases. As indicated in Figure 6 d-f, taking the oxide growth into consideration, the amount of tetragonal phase is clearly not constant but increases with weight gain. This is not to say that the tetragonal rich layer near the metal/oxide interface thickens but that there is

less phase transformation from tetragonal to monoclinic as the tin content is reduced. In order to further understand this observation it is important to consider the different aspects that will stabilise the tetragonal phase. The two main aspects that can stabilise the tetragonal phase are stress and grain size. Therefore, there will be a grain size below which the tetragonal phase will be stable without the requirement of stress. In the case of a Nb free Zr alloy it has been suggested that this critical grain size is about 30 nm [26].

In the case of ZIRLO^{TM} and low tin ZIRLO stresses measured in the tetragonal phase were generally between -1500 MPa and -2000 MPa, Figure 5d and e. Stress measurements of the tetragonal phase of X2 showed significantly more scatter but generally the observed stresses were similar to the stresses in the monoclinic phase. This suggests clearly that the majority of tetragonal phase in X2 is not stabilised by stress but by grain size. These observations suggest that in the presence of Sn tetragonal grains can be stress stabilised while when Sn is below a critical level, the stresses alone are not sufficient to stabilise grains that exceed a certain critical grain size.

Following these observations and discussions we propose the following new model that describes one factor that contributes to transition from pre- to post-transition, Figure 9.

When ZrO_2 first nucleates at the metal/oxide interface either monoclinic or tetragonal grains will be formed, which will be affected by local stress and chemistry variations and interface morphology. Most of those grains will be able to grow epitaxially as corrosion proceeds. For geometrical reason, some grains will not

grow and stay below a critical grain size that enables them to remain tetragonal if they started out as such. Tetragonal grains will only be able to grow and retain their crystal structure if they are under compressive stress beyond a critical level (-2 GPa) and contain small levels of tetragonal stabilisers such as tin. Stress alone is not sufficient. As the oxide/metal interface continues to drive away from those epitaxial grains, local compressive stress will decrease. As a result, stress stabilised tetragonal grains adjacent to the interface can maintain their crystal structure, corresponding to the tetragonal rich layer in Figure 7. Other stress stabilised tetragonal grains will transform as the stress reduces, while the size stabilised tetragonal grains will remain in the oxide. The link between martensitic phase transformation and crack formation then follows the shear model previously described by a number of researchers [3, 25, 48]. Subsequently, cracks initiate the kinetics transition by break down of the oxide layer's integrity.

A critical aspect of this model is the distinction between grain size and stress stabilised tetragonal grains and that Zr alloy chemistry affects the volume fraction of tetragonal grains that can be stress stabilised and can transform once the stress has decreased. The epitaxial growth of tetragonal is rare in material with lower tin content since the majority of the grains are monoclinic to start with. When the interface continues to drive away from the previously formed oxide, stress stabilised tetragonal grains still transform into monoclinic, only on a much smaller scale compared with material with higher tin content. The reduced amount of transformation brings about much slower and fewer formations of cracks (Figure 4 f), and subsequently longer pre-transition period (Figure 3 c).

For the three alloys invested in the present work, i.e. Nb containg Zr alloys, the proposed model seems to be responsible for the different time it takes for the three alloys to undergo transition. However, it remains to be confirmed that this model is also valid for different alloy systems.

Summary

Three recrystallized Zr-Sn-Nb alloys with different Sn content (ZIRLO^{TM}, low tin ZIRLO and X2) have been investigated in terms of their aqueous corrosion performance at 360°C and 18 bar in simulated primary water in order shed new light on the mechanism that leads to transition of the corrosion rate. The following observations have been made:

1. Corrosion resistance improves significantly with decreasing tin content.
2. Compressive stresses in the monoclinic oxide phase were within the range of -700 to -1000 MPa in the case of ZIRLO^{TM}, low tin ZIRLO materials and -500 to -900 MPa in the case of X2 material. Compressive stresses in tetragonal phase were between -1500 to -2000 MPa in both ZIRLO^{TM} and low tin ZIRLO. X2 displayed stresses in the tetragonal phase similar to the stresses in the monoclinic phase.
3. Tetragonal phase fractions and equivalent layer thickness of the tetragonal phase were calculated. It was possible to demonstrate that tin contributes to the stabilisation of the tetragonal phase. It was also found that the frequency of tetragonal to monoclinic phase transformation goes down with decreasing tin content.

4. A model explaining the corrosion rate transition phenomenon has been proposed highlighting the distinction between grain size stabilised and stress stabilised tetragonal phase. It assumes that stress stabilisation of tetragonal oxide phase is only possible in combination with some chemical stabilisation, which in the present case is tin.
5. The model identifies the stress stabilised tetragonal phase as detrimental to the corrosion performance due to stress relaxation in the oxide enabling tetragonal to monoclinic phase transformation with an associated shear strain and volume expansion.

Acknowledgement

The authors would like to thank the Engineering and Physical Science Research Council (EPSRC) and MoD in the UK for funding the research as part of the Materials for Energy call (research code: EP/E036171/1). The project would not have been possible without the strong support of our industrial project partners (in alphabetical order) EDF, National Nuclear Laboratory, Rolls-Royce, Serco and Westinghouse, who have provided substantial in-kind and financial support and our academic project partners from the University of Oxford and the Open University.

Figures and Tables

Table 1: Measured chemical composition of the materials.

Alloy	Alloying Elements				
	Zr	Fe[wt%]	Sn[wt%]	Nb[wt%]	Hydrogen [wt.ppm]
Recrystallised ZIRLO™	balance	0.09	0.92	0.91	10
Recrystallised low tin ZIRLO	balance	0.09	0.66	0.91	4
Recrystallised X2	balance	0.08	0.14	0.90	17

Table 2: Elastic constants used for stress calculation.

Phase		Poisson's ratio	Young's Modulus (GPa)
ZrO_2	[39, 41]	0.282	253
α-Zr	[40]	0.34	96

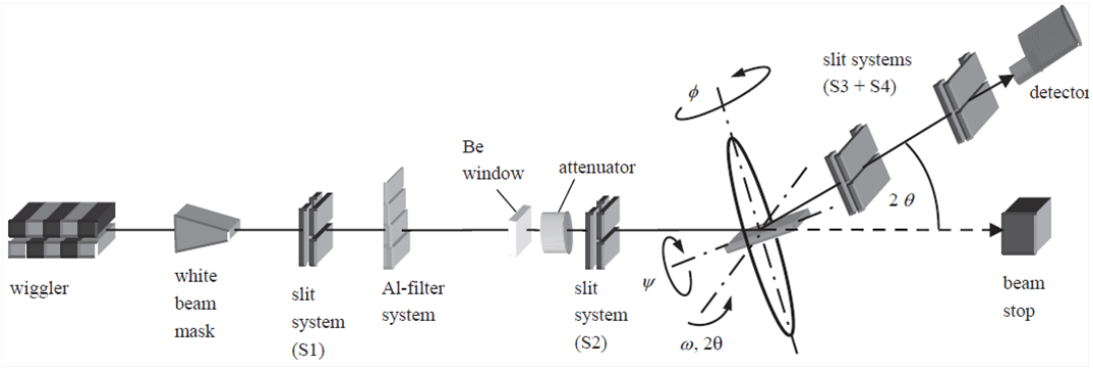

Figure 1: Schematic layout of the main beamline components at EDDI, BESSY II [37].

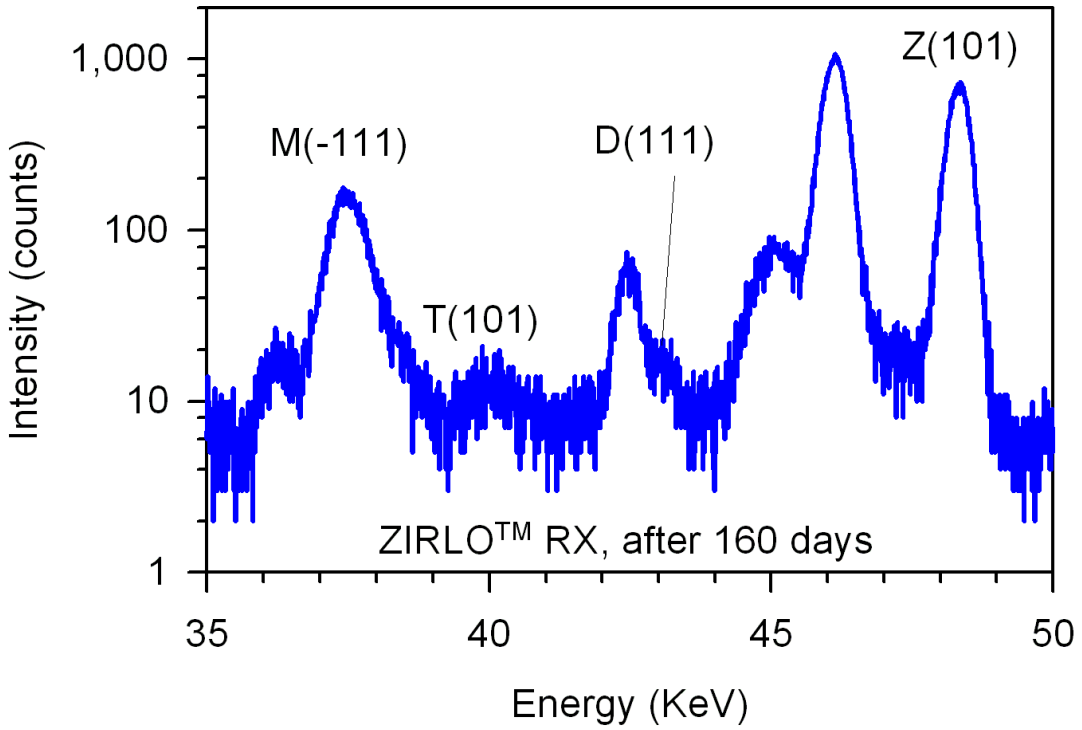

Figure 2: Partial diffraction spectrum recorded at Ψ = 0° on ZIRLO™ cladding tube sample after 160 days autoclave exposure on beam line EDDI. Labelled are the $(\bar{1}11)_m$ reflection of the monoclinic ZrO_2 phase, the $(101)_t$ reflection of the tetragonal ZrO_2 phase, the $(111)_\delta$ reflection of the δ Zr-hydride phase and the $(10\bar{1}1)_{\alpha\text{-}Zr}$ reflection of the α-Zr phase.

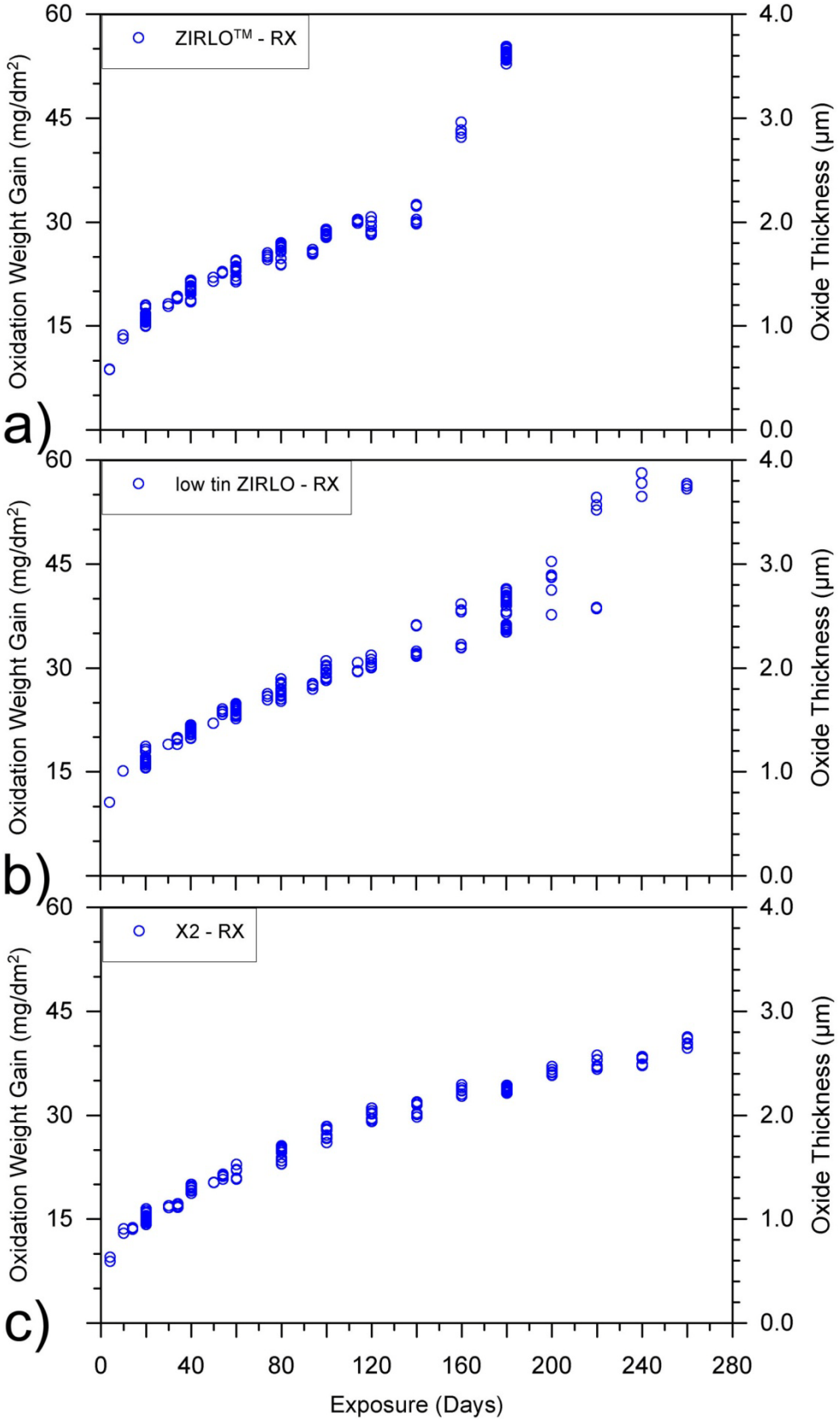

Figure 3: Autoclave corrosion weight gain profile of (a) recrystallized ZIRLO™ after 180 days of autoclave exposure, (b) recrystallized low tin ZIRLO after 260 days, (c) recrystallized X2 after 260 days of autoclave exposure.

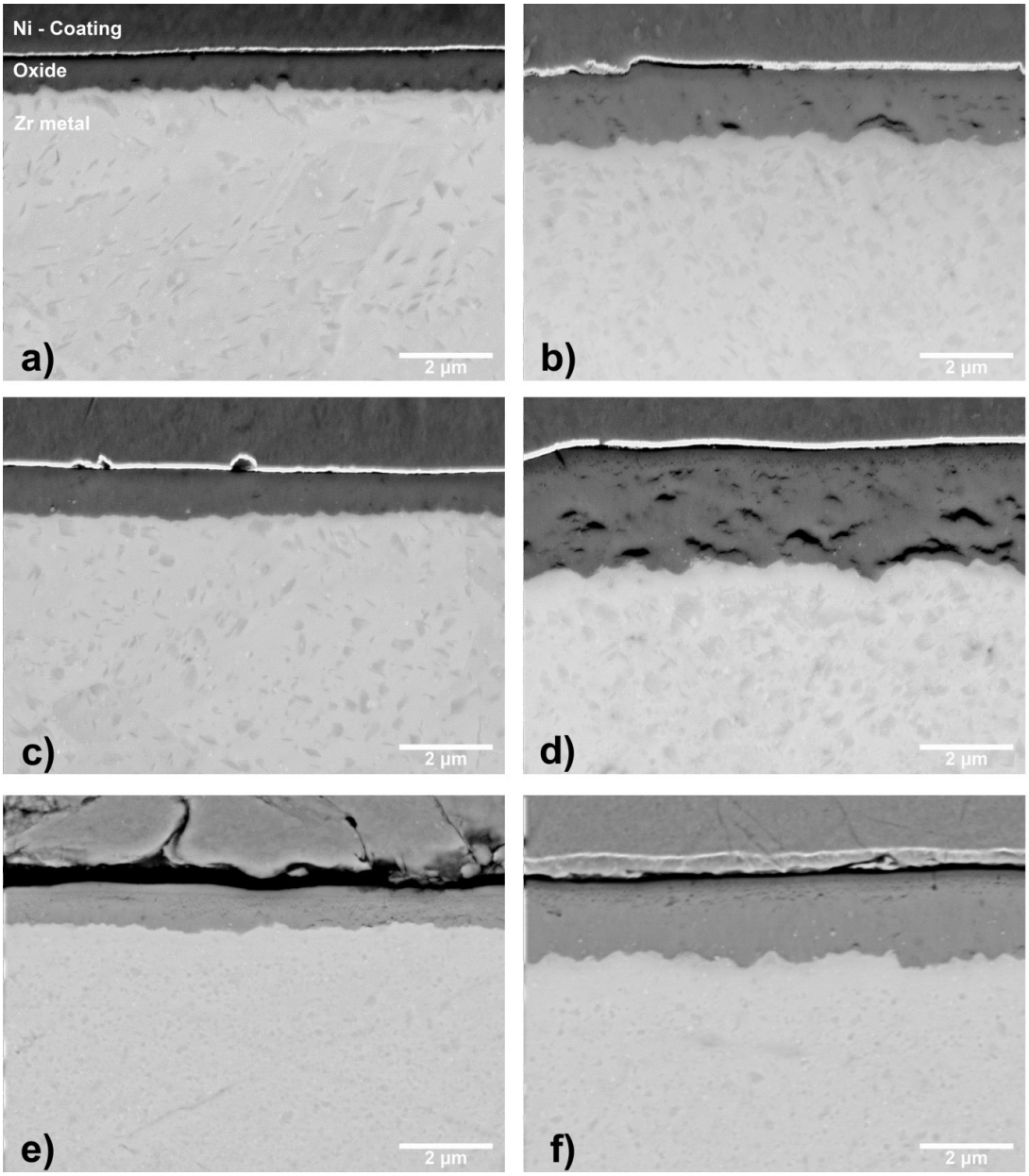

Figure 4: Back-scattered electron mode SEM images representative of the oxide (cross-section) (a) ZIRLO™ after 10 days of autoclave exposure, (b) ZIRLO™ (120 days exposure), (c) low tin ZIRLO (10 days exposure), (d) low tin ZIRLO (160 days exposure), (f) X2 (10 days exposure) and (g) X2 (180 days exposure). Note that an Au layer was deposited on top of the oxide prior to Ni-coating to improve the electrical conductivity of the surface for subsequent electroplating.

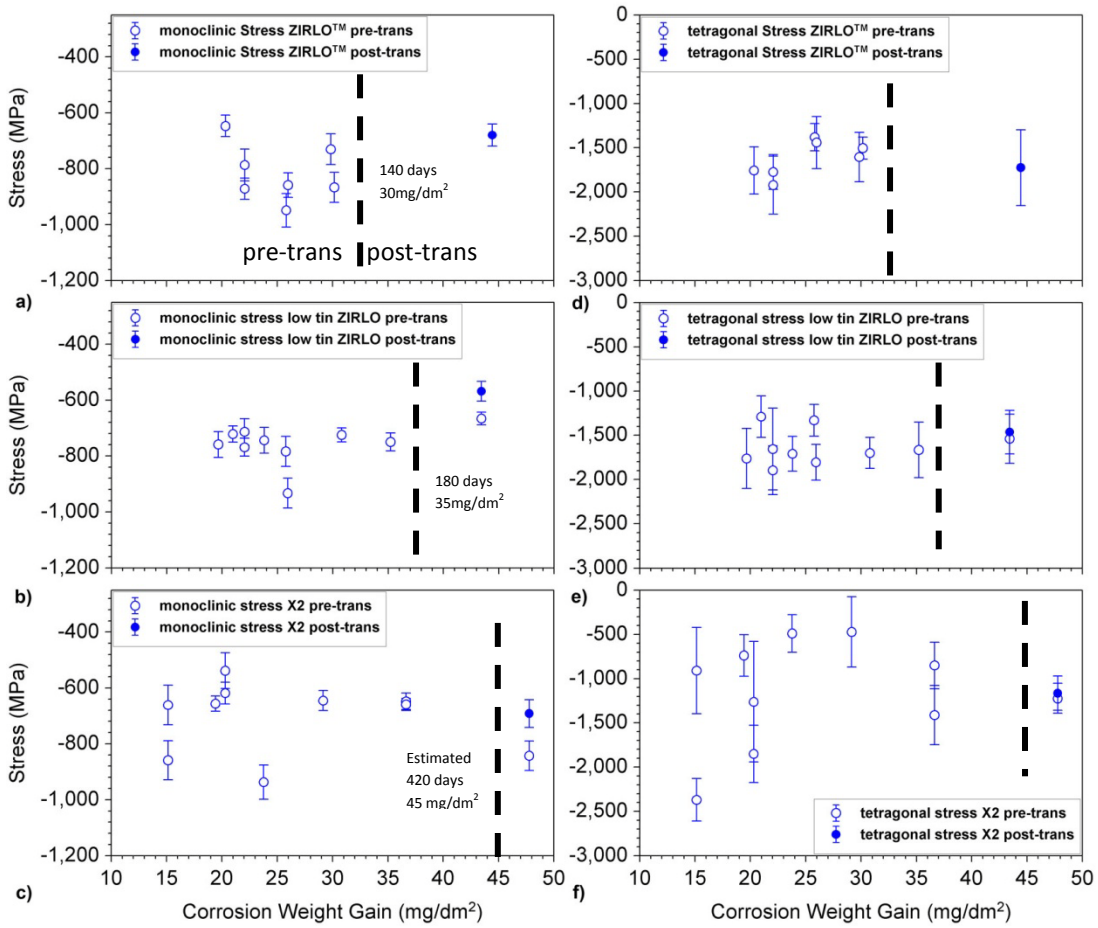

Figure 5: Axial stresses of the monoclinic oxide phase, stresses of the monoclinic phase measured (a) in ZIRLO™, (b) in low tin ZIRLO and (c) in X2 and of the tetragonal phase measured (d) in ZIRLO™, (e) in low tin ZIRLO and (f) in X2. The dashed line represents the estimated start of transition for each alloy.

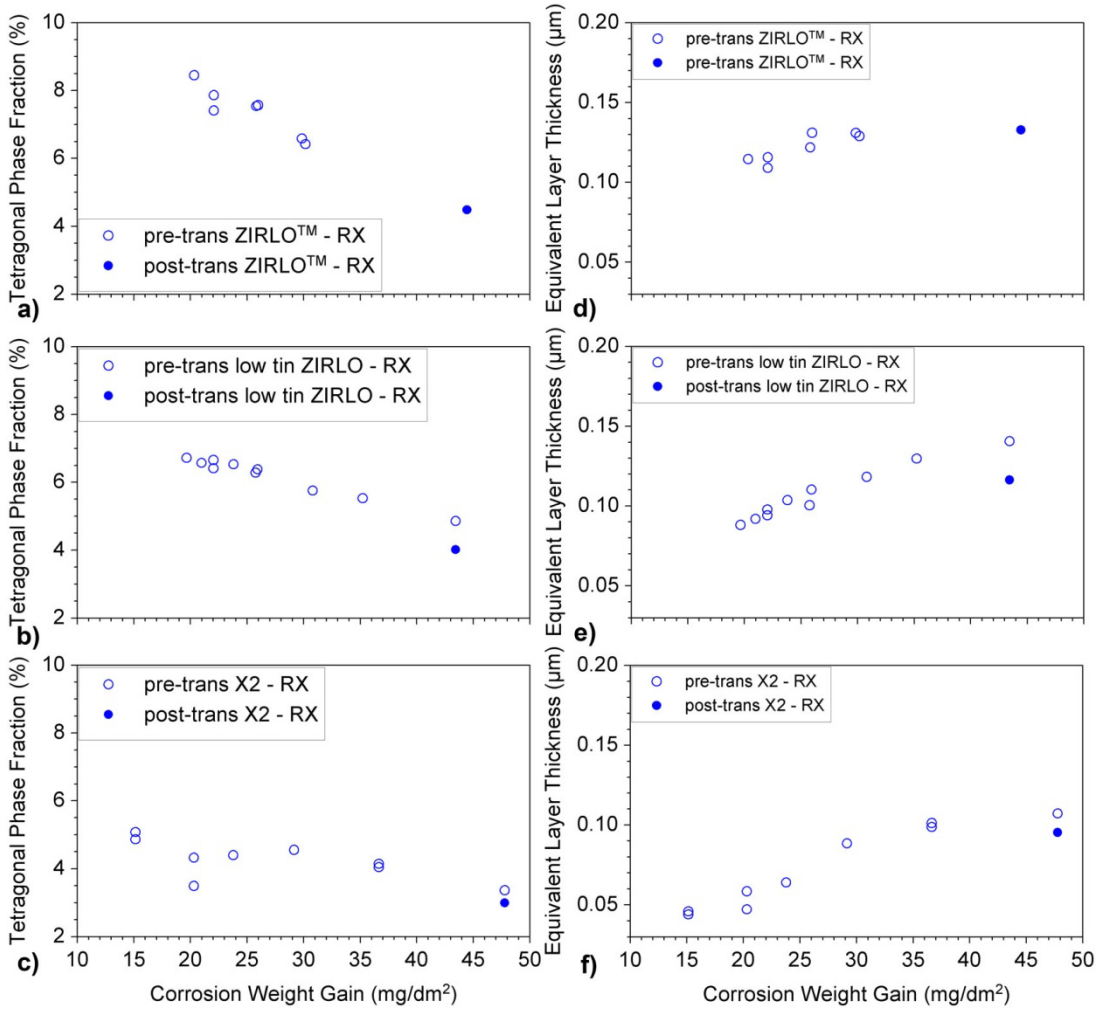

Figure 6: Calculated phase fraction and equivalent layer thickness of tetragonal phase plotted as a function of weight gain measured on (a) ZIRLO™, (b) low tin ZIRLO and (c) X2 material.

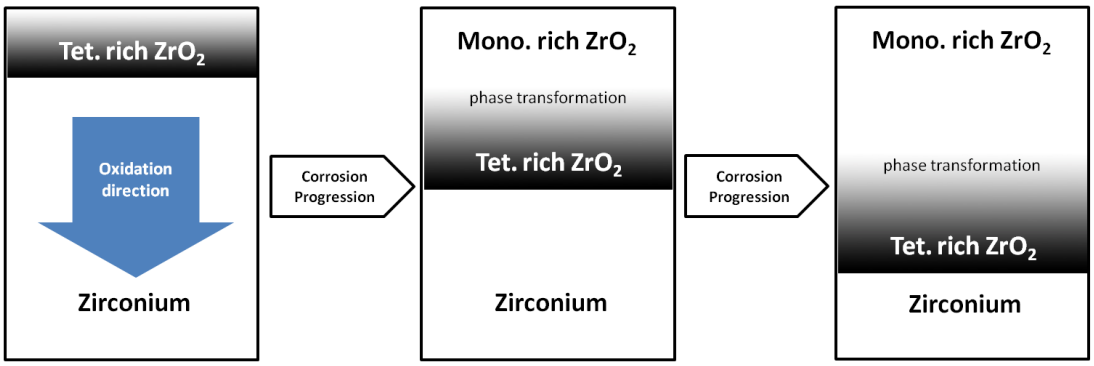

Figure 7: Schematic of the inward corrosion of Zr and the expected distribution of monoclinic and tetragonal ZrO_2 phase.

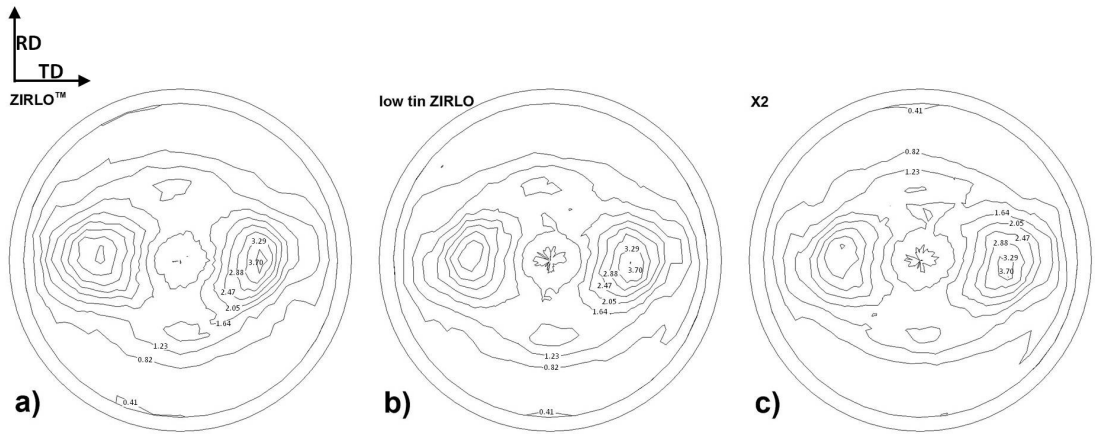

Figure 8: $(\bar{1}11)$ pole figure of the monoclinic oxide phase grown on (a) ZIRLO™, (b) low tin ZIRLO and (c) X2. Measurements were carried out on samples before 1st transition occurred. Measured by laboratory X-ray with maximum chi = 85°.

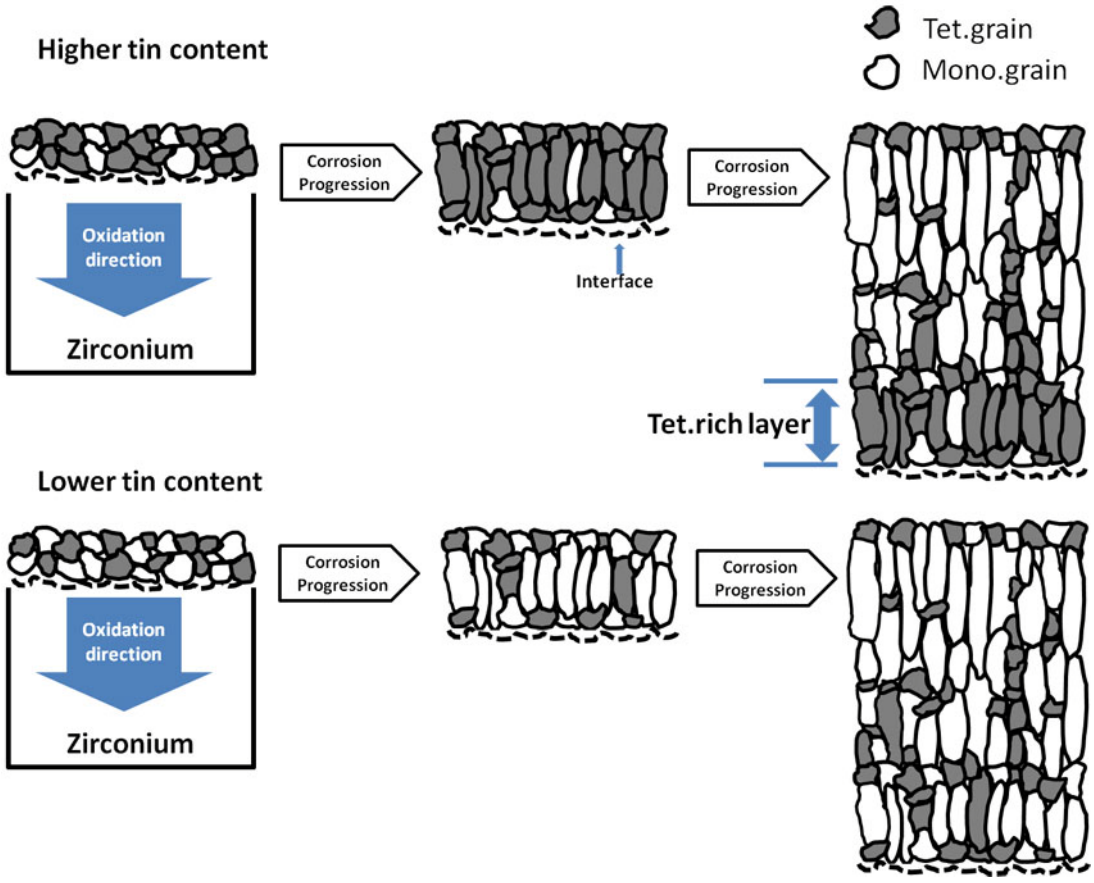

Figure 9: Schematic description of corrosion mechanisms in material with higher tin content and material with lower tin content. The proposed extreme cases are presented. The amount of tetragonal and monoclinic grains is only a schematic, not a quantitative representation.

References

1. Arima, T., et al., *Oxidation properties of Zr-Nb alloys at 500-600 °C under low oxygen potentials.* Corrosion Science, 2005. **47**(2): p. 435-446.
2. Cox, B., *Comments on "aqueous corrosion of the Zircaloys at low temperatures".* Journal of Nuclear Materials, 1969. **30**(3): p. 351-352.
3. Cox, B., *Some thoughts on the mechanisms of in-reactor corrosion of zirconium alloys.* Journal of Nuclear Materials, 2005. **336**(2-3): p. 331-368.
4. Motta, A.T., et al., *Micostructural characterisation of oxides formed on model Zr alloys using synchrotron radiation*, in *15th International Symposium on Zirconium in the Nuclear Industry*, B. Kammenzind and M. Limback, Editors. 2009, ASTM International Sunriver Resort Oregon, USA. p. 486-506.
5. Sabol, G.P. and S.B. Dalgaard, *The Origin of the Cubic Rate Law in Zirconium Alloy Oxidation.* Journal of The Electrochemical Society, 1975. **122**(2): p. 316-317.
6. Bossis, P., et al., *Comparison of the High Burn-Up Corrosion on M5 and Low Tin Zircaloy-4*, in *14th International Symposium on Zirconium in the Nuclear Industry*, P. Rudling and B. Kammenzind, Editors. 2005, ASTM International: Stockholm, Sweden. p. 494-525.
7. Bouvier, P., J. Godlewski, and G. Lucazeau, *A Raman study of the nanocrystallite size effect on the pressure-temperature phase diagram of zirconia grown by zirconium-based alloys oxidation.* Journal of Nuclear Materials, 2002. **300**(2-3): p. 118-126.
8. Bryner, J.S., *The cyclic nature of corrosion of zircaloy-4 in 633 K water.* Journal of Nuclear Materials, 1979. **82**(1): p. 84-101.
9. Garde, A.M., *Enhancement of Aqueous Corrosion of Zircaloy-4 Due to Hydride Precipitation at the Metal-Oxide Interface*, in *9th International Symposium on Zirconium in the Nuclear Industry*, C.M. Eucken and A.M. Garde, Editors. 1991, ASTM International: Kobe, Japan. p. 566-592.
10. Godlewski, J., *How the tetragonal zirconia is stabilized in the oxide scale that is formed on a zirconium alloy corroded at 400°c in steam*, in *10th International Symposium on Zirconium in the Nuclear Industry:* , A.M. Garde and E.R. Bradley, Editors. 1994, ASTM International: Baltimore, MD. p. 663-683.
11. Griggs, B., H.P. Maffei, and D.W. Shannon, *Multiple Rate Transitions in the Aqueous Corrosion of Zircaloy.* Journal of The Electrochemical Society, 1962. **109**(8): p. 665-668.
12. Hauffe, K., *Oxidation of metals*. 1965, New York: Plenum Press, Inc.
13. Kass, S. *The Development of the Zircaloys*. in *Corrosion of Zirconium Alloys*. 1964. ANS Winter meeting: ASTM International.
14. Lustman, B. and F.K. Jr, *The Metallurgy of zirconium*. 1st ed. National Nuclear Energy series, Div. 7, v. 4. 1955, New York: McGraw-Hill. 776.
15. Peters, H.R., *Improved Characterization of Aqueous Corrosion Kinetics of Zircaloy-4*, in *6th International Symposium on Zirconium in the Nuclear Industry*, D.G. Franklin and R.B. Adamson, Editors. 1984, ASTM International: Vancouver, British Columbia, Canada. p. 507-519.
16. Yilmazbayhan, A., et al., *Structure of zirconium alloy oxides formed in pure water studied with synchrotron radiation and optical microscopy: relation to corrosion rate.* Journal of Nuclear Materials, 2004. **324**(1): p. 6-22.
17. Roy, C. and B. Burgess, *A study of the stresses generated in zirconia films during the oxidation of zirconium alloys.* Oxidation of Metals, 1970. **2**(3): p. 235-261.

18. Block, S., J.A.H. Da Jornada, and G.J. Piermarini, *Pressure-Temperature Phase Diagram of Zirconia.* Journal of the American Ceramic Society, 1985. **68**(9): p. 497-499.
19. Preuss, M., et al., *Towards a mechanistic understanding of corrosion mechanisms in zirconium alloys*, in *16th International Symposium on Zirconium in the Nuclear Industry*. 2010, ASTM International ChengDu, P.R.China.
20. Zhilyaev, A.P. and J.A. Szpunar, *Influence of stress developed due to oxide layer formation on the oxidation kinetics of Zr-2.5%Nb alloy.* Journal of Nuclear Materials, 1999. **264**(3): p. 327-332.
21. Cox, B., *Are Zirconium Corrosion Films a Form of Partially Stablized Zirconia?* 1987, Atomic Energy of Canada Ltd.
22. Godlewski, J., et al., *Stress Distribution Measured by Raman Spectroscopy in Zirconia Films Formed by Oxidation of Zr-Based Alloys*, in *12th International Symposium on Zirconium in the Nuclear Industry*, G.P. Sabol and G.D. Moan, Editors. 2000, ASTM International: Toronto, Canada. p. 877-899.
23. Blat-Yrieix, M., et al., *Toward a Better Understanding of Dimensional Changes in Zircaloy-4: What is the Impact Induced by Hydrides and Oxide Layer?* Journal of ASTM International (JAI), 2008. **5**(9): p. 16.
24. Heuer, A.H. and M. Rühle, *Overview no. 45: On the nucleation of the martensitic transformation in zirconia (ZrO2).* Acta Metallurgica, 1985. **33**(12): p. 2101-2112.
25. Cox, B., et al., *Waterside Corrosion of Zirconium Alloys in Nuclear Power Plants*. 1998, IAEA: Vienna.
26. Barberis, P., *Zirconia powders and Zircaloy oxide films: tetragonal phase evolution during 400°C autoclave tests.* Journal of Nuclear Materials, 1995. **226**(1-2): p. 34-43.
27. Bouvier, P. and G. Lucazeau, *Raman spectra and vibrational analysis of nanometric tetragonal zirconia under high pressure.* Journal of Physics and Chemistry of Solids, 2000. **61**(4): p. 569-578.
28. Djurado, E., P. Bouvier, and G. Lucazeau, *Crystallite Size Effect on the Tetragonal-Monoclinic Transition of Undoped Nanocrystalline Zirconia Studied by XRD and Raman Spectrometry.* Journal of Solid State Chemistry, 2000. **149**(2): p. 399-407.
29. Garvie, R.C., *The Occurrence of Metastable Tetragonal Zirconia as a Crystallite Size Effect.* The Journal of Physical Chemistry, 1965. **69**(4): p. 1238-1243.
30. Garde, A.M., et al., *Corrosion Behavior of Zircaloy-4 Cladding with Varying Tin Content in High-Temperature Pressurized Water Reactors*, in *10th International Symposium on Zirconium in the Nuclear Industry:* , A.M. Garde and E.R. Bradley, Editors. 1994, ASTM International: Baltimore, MD. p. 760-778.
31. Harada, M., M. Kimpara, and K. Abe, *Effect of Alloying Elements on Uniform Corrosion Resistance of Zirconium-Based Alloy in 360°C Water and 400°C Steam*, in *9th International Symposium on Zirconium in the Nuclear Industry*, C.M. Eucken and A.M. Garde, Editors. 1991, ASTM International: Kobe, Japan. p. 368-390.
32. Beie, H.-J., et al., *Examinations of the Corrosion Mechanism of Zirconium Alloys*, in *10th International Symposium on Zirconium in the Nuclear Industry:* , A.M. Garde and E.R. Bradley, Editors. 1994, ASTM International: Baltimore, MD. p. 615-643.
33. Mardon, J.P., D. Charquet, and J. Senevat, *Optimization of PWR Behavior of Stress-Relieved Zircaloy-4 Cladding Tubes by Improving the Manufacturing and Inspection Process*, in *10th International Symposium on Zirconium in the Nuclear Industry:* , A.M. Garde and E.R. Bradley, Editors. 1994, ASTM International: Baltimore, MD. p. 328-347.
34. Takeda, K. and H. Anada, *Mechanism of Corrosion Rate Degradation Due to Tin*, in *12th International Symposium on Zirconium in the Nuclear Industry*, G.P. Sabol and G.D. Moan, Editors. 2000, ASTM International: Toronto, Canada. p. 592-608.

35. Kim, D.-J., J.-W. Jang, and H.-L. Lee, *Effect of Tetravalent Dopants on Raman Spectra of Tetragonal Zirconia.* Journal of the American Ceramic Society, 1997. **80**(6): p. 1453-1461.
36. Li, P., I.W. Chen, and J.E. Penner-Hahn, *Effect of Dopants on Zirconia Stabilization—An X-ray Absorption Study: II, Tetravalent Dopants.* Journal of the American Ceramic Society, 1994. **77**(5): p. 1281-1288.
37. Genzel, C., et al., *The materials science synchrotron beamline EDDI for energy-dispersive diffraction analysis.* Nuclear Instruments and Methods in Physics Research Section A: Accelerators, Spectrometers, Detectors and Associated Equipment, 2007. **578**(1): p. 23-33.
38. Withers, P.J., et al., *Methods for obtaining the strain-free lattice parameter when using diffraction to determine residual stress.* Journal Of Applied Crystallography, 2007. **40**(5): p. 891-904.
39. Frankel, P., et al., *Diffraction Elastic Constants of monoclinic ZrO2 and the effect of strong texture in ZrO2 films on residual stress measurements.* Journal Of Applied Crystallography 2011: p. SUBMITTED.
40. Northwood, D.O., I.M. London, and L.E. Bähen, *Elastic constants of zirconium alloys.* Journal of Nuclear Materials, 1975. **55**(3): p. 299-310.
41. Polatidis, E., et al., *Residual stress and phase characterization on Zircaloy-4 alloys using synchrotron X-ray diffraction.* Journal of Nuclear Materials, Submitted November 2011.
42. Tomé, C.N. and E.C. Oliver, *Computer Program: Elasto-Plastic Self-Consistent (EPSC) model* 2010, Los Alamos National laboratory, USA.
43. Hillner, E., D.G. Franklin, and J.D. Smee, *Long-term corrosion of Zircaloy before and after irradiation.* Journal of Nuclear Materials, 2000. **278**(2-3): p. 334-345.
44. Yilmazbayhan, A., et al., *Transmission electron microscopy examination of oxide layers formed on Zr alloys.* Journal of Nuclear Materials, 2006. **349**(3): p. 265-281.
45. Garvie, R.C. and P.S. Nicholson, *Phase Analysis in Zirconia Systems.* Journal of the American Ceramic Society, 1972. **55**(6): p. 303-305.
46. Cox, B. and J.P. Pemsler, *Diffusion of oxygen in growing zirconia films.* Journal of Nuclear Materials, 1968. **28**(1): p. 73-78.
47. Schwartz, C.M., D.A. Vaughan, and G.G. Cocks, *Report BMI-793 December 17, 1952.* , in *The Metallurgy of Zirconium*, B. Lustman and F. Kerze, Editors. 1955, McGraw-Hill: New York. p. 562.
48. Ploc, R.A. and S.B. Newcomb. *Microscopy of Oxidation 3*. in *Third International Conference on the Microscopy of Oxidation*. 1996. Trinity Hall, Cambridge: Institute of Materials, Minerals and Mining.

End of Publication 3

Publication Number 4

The effects of an artificially introduced hydride rim on corrosion performance of Zr-Nb-Sn alloys

The effects of an artificially introduced hydride rim on corrosion performance of Zr-Nb-Sn alloys

J. Wei[1], P. Frankel[1], E. Polatidis[1], M. Blat[2], A. Ambard[2], R. J. Comstock[3], Lars Hallstadius[4] and Michael Preuss[1]

1: Materials Performance Centre, School of Materials, The University of Manchester, UK

2: EDF - R&D, Moret sur Loing, France

3: Westinghouse Electric Co., Pittsburgh, USA

4: Westinghouse Electric Co., Sweden

Abstract

The corrosion performance of three Zr-Nb-Sn alloys: ZIRLO™, low tin ZIRLO and X2, with and without a hydride rich rim, were investigated in an attempt to study out-of-pile corrosion performance of cladding material that has reached end-of-life conditions. The main difference between the three alloys was the Sn content, which decreased from ZIRLO™ to X2. The hydride rich rim was created by cathodic charging. Its effect on corrosion performance was found to be dependent on the alloy chemistry. In the case of ZIRLO™, significant acceleration of oxide growth and a heavily cracked oxide layer were identified while the corrosion performance of X2 remained relatively unaffected. It was also noticed that the oxide grown on hydrogen charged ZIRLO™ had a mainly white/greyish appearance with a few black

oxide regions while the oxide of X2 remained black up to 80 days of testing. Microstructural investigations of the autoclaved material revealed localised hydride depletion in the rim region of hydrogen charged samples especially in the case of X2. Synchrotron and laboratory X-ray diffraction measurements were conducted to provide residual stress, phase fraction and texture information of the oxide. Significant differences of the monoclinic oxide phase's stress state, tetragonal phase fraction and crystallographic alignment of the monoclinic grains were found between white and black oxide regions. The results suggest that the hydride rich rim reduces the ability of the oxide grains to grow in a well aligned epitaxial fashion resulting in early crack formation. In addition, the hydride to oxide transformation seems to result in comparatively low oxide stresses promoting rapid tetragonal to monoclinic phase transformation. The observations also suggest that a low Sn content in these alloys promotes outwards hydrogen diffusion, which would explain the superior corrosion performance of hydrogen charged X2. The reason for the loss of hydrogen during corrosion testing, particularly in X2, is currently unclear but the observation is potentially of great importance when considering the effect of alloy chemistry on hydrogen pick up during aqueous corrosion.

Introduction

Zirconium alloys exhibit good mechanical properties, high corrosion resistance and low neutron cross-section in water cooled reactor and are therefore the choice of material to encapsulate nuclear fuel. Although the alloys used today provide good performance for current reactor applications, understanding the mechanisms of the transition and breakaway in corrosion kinetics is of great importance for both

further alloy developments as well as more accurate and physically meaningful lifetime predictions.

Initially, zirconium alloys oxidise following cubic rather than parabolic growth kinetics in high temperature pressurised water [1-13]. Once the oxide has thickened to a few microns (pre-transition, typically less than 3 μm), a brief re-acceleration of corrosion kinetics will occur, which is identified as 1st transition, followed by a second cycle of cubic growth. These cycles are repeated until breakaway corrosion occurs (growth accelerates to near linear rate) [4-6, 8, 11, 13-19]. The oxide is highly stressed in compression due to the volume expansion that takes place when zirconium transforms to zirconia (Pilling-Bedworth ratio = 1.56 [12, 20]). The compressive stress has two effects: first, it has the potential to stabilise the metastable tetragonal ZrO_2 phase [18, 21-23], which has been reported to form and accumulate near the oxide/metal interface [16, 19, 23-26]; secondly, the compressive stress in the oxide must be balanced by tensile stress in the zirconium metal beneath. Although the balancing tensile stresses are very small, researchers have shown that the metal substrate creeps after prolonged corrosion [16, 23, 27], which should reduce the compressive stress in the oxide that has formed. Combined with the continuous formation of new, highly stressed oxide at the metal/oxide interface, the above relaxation consequently generates a decreasing stress gradient leading away from the metal/oxide interface [23, 27, 28]. As a result, any stress stabilised tetragonal ZrO_2 is expected to undergo a martensitic phase transformation to monoclinic ZrO_2, which is associated wit a 3-5% volume

expansion [29]. This phase transformation has often been linked with crack formation in the oxide.

In a water-cooled reactor environment, hydrogen is generated from radiolysis of coolant water and zirconium corrosion [30-32]. Zirconium cladding tubes absorb some of the hydrogen created during the corrosion process and will precipitate hydrides when local hydrogen concentration reaches the solubility limit (120wt.ppm at reactor temperature [33, 34]). Diffusion of hydrogen is driven by concentration, temperature and stress gradients: hydrogen tends to migrate towards lower concentrations, lower temperatures and regions of higher tensile stresses. Because of the steep temperature gradient through the wall thickness of the cladding tubes (fuel inside – water outside), hydrogen diffuses towards the outer surface of the tube that eventually leads to the formation of a hydride rim, and even blisters if the oxide spalls off [35, 36]. The detrimental effects of such hydride accumulation on the corrosion performance of zirconium have since been reported, yet no clear mechanistic explanation has been suggested [6, 13-15, 27, 37-40].

In the present paper, the effects of a pre-existing hydride rich rim on the corrosion performance of three Zr-Nb-Sn alloys were investigated. A hydrogen rich rim was introduced into the materials by cathodic charging prior to autoclave corrosion in an attempt to simulate end-of-life condition of reactor fuel claddings. The morphology of the oxide layer formed during corrosion testing was investigated via cross-sectional SEM exanimations. Energy dispersive synchrotron X-ray diffraction was used to characterise the residual stress state and tetragonal/monoclinic phase

fraction ratio in the oxide. The potential relationship between oxide growth and level of alignment of the oxide grains was explored by texture analysis. It should also be emphasised that the present work only focused on out-of-pile investigations with in-reactor studies being outside the scope of this paper.

Experimental

Materials Preparation

Chemical compositions of the three alloys involved in this study, ZIRLO™, low tin ZIRLO and X2, were determined at the EDF Research and Development facility in Moret-Sur-Loing, France, as shown in Table 1. All alloys studied in the present paper were in a recrystallised condition (RX). ZIRLO™ is a commercially available alloy produced by Westinghouse. Low tin ZIRLO has the chemical composition of Optimised-ZIRLO™, a commercially distributed Westinghouse alloy in partially recrystallised state. X2 is an experimental alloy, which only differs from the two ZIRLO variants by having a lowest Sn content. Test samples, with the dimensions of 30 mm in length and 9 mm in diameter were prepared from tubes of each alloy. Pickling was performed subsequently at 60°C in a solution of 10 vol.% hydrofluoric acid, 45 vol.% nitric acid and 45 vol.% distilled water for 3 minutes to remove inorganic contamination from the fabrication process.

Pre-Hydriding

Pickled samples were cathodically hydrided for 10 days in 0.1 mole/L KOH solution using a fixed current density of 10 mA/cm^2, which created a hydride rich rim about 20-30 μm thick. After 10 days of hydrogen charging, a 24-hour homogenisation heat

treatment at 400 °C was performed under Ar atmosphere to create a more gradual transition between hydride rim and the bulk material. The overall hydrogen levels in the cathodically hydrided samples were determined via inert gas fusion analysis, using an H-MAT 2500 (Ströhlein) analyser. More details about the hydrogen charging process can be found in [41].

Characterization of the Hydrogen Charged Material and Oxide Morphology

Characterisation of local hydrogen concentration and hydride phase identification in the hydride rim region were performed by laboratory X-ray diffraction. Measurements were performed on a Philips X'Pert MPD operating at 45 kV (Cu-tube) in glancing-angle configuration, using an incident beam at θ = 6°. When undertaking surface measurements, this setup ensured that 90 % of the signal was collected from the top 3 µm of the specimen surface, which corresponds approximately to the depth of material that was consumed by the following short-term autoclave corrosion tests. Multiple diffraction peaks were recorded in the two-theta range from 25° to 85° and a Rietveld analysis was carried out using the commercial software package Topas^{TM}.

Cross-sectional metallographic samples were prepared for microstructural examinations. A protective Ni layer was coated on autoclave oxidised samples to prevent mechanical damage during sample preparation. Cross-sectional samples were ground and polished following standard metallographic procedures and etched subsequently in a solution of 5 vol.% hydrofluoric acid, 45 vol.% nitric acid and 50 vol.% distilled water at room temperature. Samples were examined both via electron and optical microscopy. In the case of scanning electron microscopy

investigations, a 5 nm thick carbon layer was deposited on the freshly etched sample surface using a Gatan Model 682 PECS^{TM} precision etching & coating system. The carbon layer improves the surface conductivity and prevents the accumulation of electrostatic charge, which would otherwise result in image artefacts. Imaging of the cross sectional samples was performed using a Philips XL30 FEG-SEM. The oxide morphology was investigated in the same way by studying cross-sectional samples in a FEG-SEM.

Autoclave Corrosion

The autoclave corrosion tests were carried out in static autoclaves operating at 360°C and 18 MPa, using a starting water chemistry similar to primary water ([LiOH] = 2 wt.ppm and [H_3BO_4] = 1000 wt.ppm). Two batches of samples were tested: one batch of cathodically hydrided samples aimed at providing samples and corrosion kinetics from the very early stage of corrosion and a second batch of reference non-hydrided samples aimed at recording corrosion data during early stages of corrosion up to 1st transition. Reference samples were inserted into autoclave 1 every 20 days while hydrided samples were inserted into autoclave 2 every 10 days. In all cases each sample condition was represented by a set of 4 samples. As five sets were inserted every 20/10 days, a maximum of 20 weight gain readings were recorded for a given exposure length. After the autoclave exposures, cross sectional SEM examinations were conducted to characterise the morphology of the oxide layers.

Residual Stress and Phase Fraction Analysis

For the present study, the energy dispersive (30 to 120 KeV) beamline EDDI at BESSY II, Berlin, Germany was selected. The set up of the beam line is shown in Figure 1 [42]. The aim of the measurements was to determine residual stresses in the two oxide phases as well as the volume fraction of tetragonal phase. Measurements were carried out in reflection mode using the so-called $sin^2\psi$ approach [43]. This approach assumes that a biaxial stress state exists with any out-of-plane stresses being zero. Although locally this might not always be true, due to slight undulations of the metal oxide interface, on a macroscopic scale it seems reasonable to assume such a stress state in an oxide layer only a few microns thick. The elastic properties were selected from literatures (Table 2 [44-47]). Due to the lack of available data, the same elastic properties were assumed for monoclinic and tetragonal zirconia. One of the benefits of using synchrotron X-ray diffraction for the characterisation of the oxide is its non-destructive nature. Samples can be taken out of autoclave, measured by synchrotron X-ray diffraction and reinserted subsequently into the autoclave for further exposure. Measuring the oxide in a fully stressed condition, i.e. no stress relief by cutting the sample and creating a free surface, is also important from the point of view that at least some of the tetragonal oxide phase is likely to be stress stabilised.

The measurements were set up with 2θ fixed at 6° while ψ was tilted from 22° to 66° ($sin^2\psi$ range from 0.14 to 0.84). The spot size used during the experiment was 30×500 µm. Preliminary experiments revealed no significant differences between the oxide stresses in the hoop and axial direction of the tube samples. Hence, all

measurements were carried out in order to determine stresses in hoop direction of the cladding tube.

Note that there are numerous factors contributing to the uncertainty of analysing the diffraction signal recorded from a thin monoclinic/tetragonal phase layer, including overlapping reflections from multiple phases (zirconium oxide, zirconium hydride and zirconium metal), low peak intensity and peak broadening due to small volume fraction and nano-sized oxide grain structure. In general, the $(\bar{1}11)$ reflection of the monoclinic phase, (101) of the tetragonal phase, $(10\bar{1}1)$ reflection of the α-zirconium phase and the (111) reflection of the δ-hydride phase were chosen for further analysis as these reflection could be clearly distinguished and showed adequate intensities throughout the range of measured ψ angles. In addition, the (111) reflection of the monoclinic phase was also used when calculating the tetragonal oxide phase volume fraction. Diffraction peaks were fitted using a Pseudo-Voigt function implemented in a Mathematica™ routine developed in-house at BESSY II. Peak information such as peak intensity, peak position and full width half maximum was calculated for every selected energy range. In order to determine the volume fraction of the tetragonal oxide phase, peak intensity and full width half maximum values were averaged over the range of ψ angles to minimise the effect of texture before employing the Garvie-Nicholson equation [48]:

$$Vol.\%(tetragonal) = I_{tet\,(101)}/[I_{tet\,(101)} + I_{mono\,(111)} + I_{mono\,(\bar{1}11)}], \qquad (1)$$

where I is the integrated intensity averaged over ψ angles. Typical diffraction spectra of oxide grown on autoclave corroded materials with and without a hydride

rim can be seen in Figure 2, highlighting the limited strength of the tetragonal ZrO_2 reflection. Please note the weak $(111)_{\delta\text{-hydride}}$ reflection of the hydride phase measured in the reference sample after prolonged autoclave exposure. A more detailed description of the data analysis has been provided by E. Polatidis et al. [47].

Oxide Texture Analysis

Texture measurements of the oxide were carried out on a BRUKER D8 Discover diffractometer operating at 35kV (Co-tube) in coupled θ/2θ mode. Measurements were conducted on the surface of corrosion tested tube samples without any prior mechanical polishing. Due to the surface curvature of the tube samples a small spot size of 0.5 mm was selected. The spot size also enabled to identify particular measurement regions such as differently coloured oxide patches. Due to the increased difficulties of measuring oxide reflections accurately when using laboratory based X-ray diffraction, only the $(\bar{1}11)$ reflection of the monoclinic phase was scanned. The estimated penetration depth of the X-rays in the present set up is 8 µm, exceeding the oxide thickness of any involved samples.

Results

Pre-Corrosion Examination

The overall hydrogen concentrations in cathodically hydrogen charged samples were determined by inert gas fusion analysis, to be 600 to 700 wt.ppm. A continuous hydride rich rim of approximately 20 µm was observed below the outer surface of the cladding tubes, while circumferentially oriented hydride strings, several hundreds of microns long, were observed in the bulk of the sample, as

shown in Figure 4 (a) and (b). High magnification SEM images revealed that the hydride strings are in fact chains of small hydrides, which are 5 to 10 μm long and several hundred nanometres wide, Figure 4 (c) and (d). Further laboratory X-ray diffraction study identified that the hydride rich rim consists predominantly of δ-hydrides with a local hydrogen concentration of 11,000 wt.ppm. The hydride rich rim created by cathodic charging seems in terms of morphology, density and hydrogen concentration similar to what has been reported for hydride rims of in-pile end-of-life cladding tubes [14, 15, 49, 50]. A more detailed description of the hydride rim can be found in [41].

Autoclave Corrosion

Figure 5 provides a direct comparison between the corrosion data of the three autoclave tested alloys: ZIRLO^{TM}, low tin ZIRLO and X2 by plotting weight gain data as a function of autoclave exposure time. Weight gain data of individual measurements are presented instead of averaged values in order to show the level of scatter. Photographs of actual specimens are also included in order to demonstrate the variation in oxide surface appearance between the different samples.

Figure 5 demonstrates that the three alloys in the non-hydrided condition displayed different times to transition of growth kinetics with ZIRLO^{TM} taking about 140 days, low tin ZIRLO about 200 days and X2 showing no indication of transition up to 260 days. While pre-transition oxide is black, samples going through transition developed light grey oxide patches (Figure5 (A) and (D)), which gradually developed into an entire grey appearance of the oxide during post transition. In the case of X2

a patchy oxide surface was detected in an additional autoclave experiment after about 360 days. The weight gain and oxide thickness at transition was about 25 mg/dm^2 - 1.7 μm (15 mg/dm^2≈1 μm of oxide [51, 52]) for ZIRLO^{TM}, 30 mg/dm^2 - 2.0 μm for low tin ZIRLO and 45 mg/dm^2 - 3.0 μm for X2. The pre-1st transition corrosion kinetics can be described by

$$\Delta W = K_p t^n \quad (2)$$

where ΔW is the sample weight gain in unit of mg/dm^2, t is the autoclave exposure time in unit of days, n is the corrosion kinetics exponent and K_p is the rate constant that is directly proportional to diffusivity of ionic species, which changes with temperature (360°C in this study) and alloys chemistry. It was found that the reference material displayed corrosion kinetic exponents close to cubic while the rate constants were in the range of 4.7 to 5.9, Table 3.

The hydrided materials displayed somewhat different oxide growth. When fitting the entire data set, the corrosion kinetic exponents tended to be close to parabolic while the rate constants were between 2.8 and 3.8, Table 3. However, the corrosion data recorded for ZIRLO^{TM} and low tin ZIRLO might also suggest linear oxide growth after about 30 days. Interestingly, while the diffusion related transport through the oxide seems faster in the reference material compared to the hydrided material, it develops a more protective oxide than the material displaying a hydride rich rim. After 80 days, this difference did result in about 50 % higher oxidation weight gain compared to the reference material in ZIRLO^{TM}, 40 % in low tin ZIRLO and only 10 % in X2, Table 3. Oxide grown on hydrided ZIRLO^{TM} material has a distinct whitish appearance with small regions of black colour even after only 10 days of exposure

(Figure 5 (C)). In the case of hydrided low tin ZIRLO the oxide displayed a more uniform greyish appearance, Figure 5 (F). Oxide grown on hydrided X2 retained a uniformly black colour even after 80 days, Figure 5 (I). In contrast, all reference samples displayed the expected black oxide during pre-transition corrosion.

Oxide Microstructure

Figure 6 shows cross sectional microstructure SEM images of the oxide and metal substrate/hydride rich rim after 10 days of autoclave exposure recorded in backscattered electron mode. At this stage, the reference samples show very few defects in the continuous oxide layer and a smooth oxide/metal interface, Figure 6 (a), (c) and (f)).

After 10 days of exposure, the thickness of the oxide layer grown on hydrided ZIRLO^{TM} sample is more than 2 μm, although the recorded corrosion weight gain is less than 20 mg/dm^2. As shown in Figure 6 (b), a jagged oxide/hydride rim interface is clearly visible, with significant levels of cracks parallel to the interface. It is clear that the formation of cracks initiated early. Cracks, as long as 12 μm, were observed in certain regions. The outer oxide surface of such a region appeared nearly white. Hydrided low tin ZIRLO showed fewer cracks in most regions at this stage, Figure 6 (d), except some localised regions that displayed thicker oxide (3~4 μm) and very significant cracking, Figure 6 (e). In contrast, hydrided X2 displays an oxide layer very similar to the reference material, Figure 6 (g).

Microstructural examinations of the hydrided samples were repeated after 50 or 80 days autoclave exposure and compared with reference material close to 1st

transition of oxide growth, Figure 7. Although the actual exposure varied greatly between alloys of the reference material presented in Figure 7, the oxide morphology appears similar when close to transition. At this stage, the oxide had reached around 2 to 3 μm, displaying numerous short cracks, particularly near the oxide/metal interface.

The oxide of the hydrided material exhibits a similar trend compared to the observations after 10 days. The hydrided ZIRLO^{TM} showed very widespread cracks in the oxide, Figure 7(b), while hydrided low tin ZIRLO still displayed a heterogeneous appearance of oxide growth and cracking, Figure 7(d) and (e). The frequency of local regions showing significant oxide growth and cracking had however increased in hydrided low tin ZIRLO.

The SEM images of the hydrided material also revealed some contrast within the hydride rich rim close to the oxide interface at this stage. As the images were recorded in backscatter mode, hydride regions should appear darker than metal regions. Therefore the images suggest that the hydride rich rim has been partially depleted of hydrogen, particularly near the interface with the oxide, Figure 7(b), (d), (e) and (g), and also most noticeably within the rim for X2, Figure 7(g).

Residual Stress Analysis of the Oxide

Both reference and hydrided samples were investigated using synchrotron X-ray diffraction. Since some hydrided samples exhibited regions of white/grey and black oxide, individual measurements were conducted on each region.

The stresses in the monoclinic and tetragonal oxide phases are plotted against corrosion weight gain in Figure 8. The reference samples displayed generally axial stresses of about -600 to -900 MPa in the monoclinic phase regardless of corrosion weight gain, though stresses in X2 samples were slightly lower in average, Figure 8 (a), (b) and (c). Black oxide regions of the hydrogen charged material displayed similar or slightly higher compressive stresses while white/grey oxide regions showed a clear trend towards lower compressive stresses of around -400 to -600 MPa. Stresses in the tetragonal phase of ZIRLO^{TM} and low tin ZIRLO were between -1200 MPa to -2200 MPa in the reference and hydrogen charged samples without any distinction between black or white/grey oxide, Figure 8 (d) and (e). In contrast, reference samples of X2 displayed a tendency of significantly lower compressive stresses in the tetragonal phase assuming similar stress values as seen for the monoclinic phase. A similar trend was seen in the black oxide of the hydrogen charged X2 samples, Figure 8(f). The stress data measured for the tetragonal phase in X2 showed large scatter as the peak intensity of the $(101)_{tet}$ reflection was significantly weaker compared to measurements in the other two alloys [53].

Phase Fraction Analysis of the Oxide

Plotted as a function of corrosion weight gain in Figure 9 (a), (b) and (c) is the calculated tetragonal phase fraction in the oxide for ZIRLO^{TM}, low tin ZIRLO and X2. In addition, Figure 9(d), (e) and (f) plots the equivalent tetragonal phase layer thickness as a function of weight gain for all three alloys. The equivalent tetragonal phase layer thickness takes into account the growth of the oxide layer by multiplying the tetragonal phase fraction value with the actual weight gain of

individual samples. In this way, it provides a value of the potential layer thickness of the tetragonal phase if one assumed that all tetragonal phase was placed in one layer [47].

In the case of reference ZIRLO^{TM}, the absolute amount of tetragonal oxide remains relatively uncharged, while the tetragonal phase fraction decreases with the continuous growth of the oxide. Reference low tin ZIRLO display a slight increase of the absolute amount of tetragonal oxide with weight gain. Reference X2 material displays very low levels of tetragonal phase at the beginning but the absolute value increases slightly with weight gain. The data sets measured on hydrogen charged ZIRLO^{TM} and low tin ZIRLO suffer greater scatter than their reference counterpart. This arises potentially from the scatter of weight gain data and the difficulty when distinguishing white from black regions of oxide. In general, black regions of ZIRLO^{TM} and low tin ZIRLO display tetragonal phase fractions similar to their reference, while white regions have much fewer tetragonal phases from the earliest measurements. All hydrogen charged X2 samples only developed black oxide over the duration of their autoclave exposures and consequently, the evolution of tetragonal phase in such oxide is similar to that in oxide grown on reference X2.

Texture Analysis of the Oxide

As described earlier, texture analysis of the monoclinic oxide phase was carried out on the $(\bar{1}11)$ reflection using laboratory X-ray diffraction. Figure 10 displays incomplete $(\bar{1}11)_{mono}$ pole figures showing a preferred orientation of $(\bar{1}11)$ reflections approximately 45° away from the oxide surface normal towards the tangential direction, which is in good agreement with [52]. The observations also

suggests that the (200) poles of the monoclinic phase are closely aligned with the oxide growth direction as previously reported by both M. Preuss et al. [23] and A. Yilmazbayhan et al. [52].

In order to obtain an indication of oxide texture strength variations between hydrogen charged and reference material, the evolution of the maximum monoclinic ($\bar{1}11$) intensity values recorded for each pole figure analysis is plotted against overall corrosion weight gain and residual stresses of the monoclinic phase in Figure 11. Reference samples generally exhibited intensity values of 3.5 to 3.7 regardless of the overall weight gain and the stresses recorded in the oxide (see also Figure 10a). Measurements carried out on white/grey oxide grown on the hydride rich rim of ZIRLO^{TM} and low tin ZIRLO displayed significantly lower intensity values of 2.3 to 3.1 (see also Figure 10b). Again, no obvious trend was seen between intensity values and weight gain or stress in the monoclinic phase of the white/grey oxide. In contrast, measurements carried out on black oxide grown on hydrogen charged ZIRLO^{TM} and low tin ZIRLO displayed increasing texture strength with increasing oxide stresses. When the stress was of similar value as measured in the grey oxide, the texture strength was also comparatively low. In the case the stress was as high as measured in the oxide of the reference material, the texture strength was comparable to the observation made in the reference material (see also Figure 10c). In X2, no difference in texture strength of the oxide was observed between the hydrided and reference samples.

Discussion

Since the differences in corrosion behaviour between ZIRLO^{TM}, low tin ZIRLO and X2 have been presented and discussed previously [53], the present paper only focuses on discussing the differences observed between reference and hydrogen charged material. The work presented here clearly demonstrates that the hydride rich rim produced by cathodic charging can have a significant effect on the corrosion behaviour of the material although the degree to which the hydride rich rim deteriorates the corrosion performance seems to depend strongly on the alloy chemistry. In this context, it is interesting to note that despite the differences between the three alloys, all hydrogen charged alloys showed comparatively slow oxide growth during the very early stage of oxidation, which manifested itself in low K_p values. Considering that in the case of zirconium hydrides two ionic species are potentially oxidised, Zr^{4+} and H^+, requiring more oxygen ions compared to oxidising Zr metal, the low oxide growth rate might not be entirely surprising. Particularly in the case of ZIRLO^{TM}, and to a lesser degree for low tin ZIRLO, the oxide developed a high porosity from a very early stage, which should result in linear rather than parabolic oxide growth if no protective layer is formed. Considering the relatively short autoclave tests for the hydrogen charged material, it is difficult to provide a definite answer, but the recorded corrosion data does indicate that the oxide has started to grow almost linearly after 30 days in the case of the two ZIRLO variants. As both alloys still show regions of black oxide after 80 days that seem to be similarly protective as the pre-transition oxide grown on the reference material, it is not surprising that the oxide growth rates are not exactly linear.

The relatively low residual stress data of the monoclinic phase as well as small fractions of tetragonal phase recorded in the white/grey oxide further confirm the substantial difference of such oxide compared to the pre-transition oxide grown on the reference material but also the black oxide grown on hydrided samples. The data also supports that there is very little difference between the black oxide grown on the reference and the hydrided material, which is particularly the case for X2. The 17% volume expansion involved in hydride formation reduces the effective Pilling-Bedworth ratio from 1.56 to 1.29 [12, 20, 54-56], causing a lowered compressive stress state in the oxide grown. This not only reduces the stability of the stress stabilised tetragonal oxide [18, 21-23, 53] which subsequently enhances tetragonal to monoclinic phase transformation and generates porosities and nano-scaled cracks via volume expansion [29, 57] and shear [13, 58, 59], but also results in a higher degree of oxide grain misorientation since the strong texture developed in the oxide is largely driven by the high level of compressive stresses [23, 60]. The oxide texture data provide a strong indication that the porous oxide has less crystallographically well aligned grains. Since one would expect that well aligned oxide grains promote epitaxial grain growth, which has been linked previously to the cubic growth law [13, 52], i.e. very protective oxide, the texture measurements suggest that in ZIRLO^{TM} and low tin ZIRLO, the oxidation of the zirconium hydrides reduces the ability of the oxide grains to grow in such a way. The exact reason for this is currently unclear but one might speculate that the nucleation of ZrO_2 is affected by the protons generated during the zirconium hydride to oxide transformation resulting in enhanced nucleation of oxide grains that have

crystallographic variants that are different from the preferred texture displayed in Figure 10.

The observation that might be most surprising is that hydrogen charged X2 shows hardly any accelerated corrosion after 80 days. The detailed characterisation of the oxide confirms that there is indeed no detectable difference of the oxide grown on reference and hydrogen charged X2. At the same time, Figure 7(g) suggests that the hydride rich rim of X2 has changed quite dramatically during corrosion. In order to shed more light on this, further analysis of the synchrotron X-ray diffraction experiment recorded for the hydrogen charged samples was carried out. Due to the oxide layer being very thin, it was possible to follow the evolution of the $(111)_{\delta\text{-hydride}}$ reflection measured near the surface in the oxidised samples. In order to eliminate any effect from flux variations of the beam during the experiment, the peak intensity of the hydride reflection was normalised by the peak intensity of the $(10\bar{1}1)_{\alpha\text{-zirconium}}$ reflection. In order to improve statistics, the intensities I of both reflections were averaged over ψ angels. Figure 12 plots the normalised intensity of the hydride reflection as a function of weight gain and distinguishes between measurements carried out on black and white/grey oxide. It can be clearly seen that most measurements carried out on the black oxide regions display far lower $(111)_{\delta\text{-hydride}}$ intensity values than measurements carried out on white/grey oxide regions. In the case of ZIRLO^{TM}, the intensity differences between these two regions are in the range of four times, Figure 12 (a). Measurements obtained from low tin ZIRLO are less clear, Figure 12 (b). This might be related to less distinguishable black and grey oxide regions as well as the significant heterogeneity in the oxide

morphology as demonstrated in Figure 6(d) and (e) and Figure 7(d) and (e). In the case of hydrogen charged X2, where only black oxide regions were observed within 80 days of autoclave testing, the δ-hydride peak intensity is the lowest compared to the other two alloys. Figure 12 (a-c) also indicate that the earliest measurements on black oxide regions often still display comparatively high levels of hydride peak intensity, suggesting that the loss of hydrogen in the hydride rich rim takes place over the first few days during autoclave testing. The mechanism for the observed hydrogen depletion process remains elusive at this stage. Although no unambiguous evidence can be provided in terms of hydrogen diffusion direction, the SEM images seem to suggest that hydrogen diffuses outwards. Experiments are planned in the near future to further investigate this phenomenon. If the indications from the SEM images are correct, this could have significant consequences for the current understanding of hydrogen pick up as hydrogen loss through the oxide might reduce the effective hydrogen pick up during corrosion. Further work is also needed to explain the effect of Sn on the ability of hydrogen to diffuse away from a hydride rich rim. However, the observations seem to explain the very different corrosion performance of hydrogen charged ZIRLO^{TM}, low tin ZIRLO and X2.

Conclusion

Three Zr-Nb-Sn alloys ZIRLO^{TM}, low-tin ZIRLO and X2 have been investigated with and without an artificially generated hydride rich rim adjacent to the sample surface. The aqueous corrosion performance were evaluated by autoclave corrosion experiments at 360°C and 18 bar in “simulated” primary water and the

material was investigated using SEM, high energy synchrotron and laboratory X-ray diffraction. The main findings are summarised as follows:

- The hydride rich rim significantly affects the corrosion behaviour of zirconium alloys although the degree to which it deteriorates the corrosion performance depends strongly on the alloy chemistry. An alloy with low tin content appears to suffer less deterioration than an alloy with high tin content. Hydrided ZIRLO^{TM} and low-tin ZIRLO developed grey surface appearance of oxide as well as patches of typical pre-transition black oxide. Hydrided X2 retained a black oxide appearance. In the case of the two ZIRLO variants, corrosion accelerates to almost linear rate after 30 days with high density of cracks in the oxide observed from a very early stage.
- All hydrogen charged alloys show very slow oxide growth during the very early stage of oxidation, which arises potentially from the requirement of additional oxygen ions to oxidise H^+.
- Compressive stresses of -600 to -900 MPa were recorded in monoclinic phase oxide regardless of the weight gain on reference samples of all three alloys. Similar stress levels were measured in the black oxide regions of hydrogen charged samples while lower compressive stresses were measured in grey/whitish oxide regions (-400 to -600 MPa). Compressive stresses of -1200 to -2200 MPa were measured in the tetragonal phase oxide for the two ZIRLO variants of both hydrided and reference conditions. Significantly lower tetragonal stresses similar to monoclinic stresses were measured in hydrided and reference X2.

- White/grey oxide grown on hydrided sample generally contains small fractions of tetragonal phase, which potentially arises from the enhanced transformation from tetragonal to monoclinic phase. It is speculated that less aligned oxide grains are less likely to grow epitaxially into protective columnar grains while the reduced residual stress, potentially related to a smaller volume expansion when oxidising hydrides compared to oxidising metal, weakens the ability of those grains to grow and maintain tetragonal structure if they started out as such. Both mechanisms have the potential to result in less protective oxide.
- The limited effect of a hydride rim in the case of a low Sn alloy has been related to an actual loss of hydrogen during the early stage of corrosion testing. SEM images suggest that hydrogen has been lost by outwards diffusion. The reason for this remains elusive at the moment but it is clear that such potential outwards corrosion of hydrogen in the case of low tin Zr alloys might be of importance when considering hydrogen pick up during aqueous corrosion.

Acknowledgement

The authors would like to thank the Engineering and Physical Science Research Council (EPSRC) and MoD in the UK for funding the research as part of the Materials for Energy call (research code: EP/E036171/1). The project would not have been possible without the strong support of our industrial project partners (in alphabetical order) EDF, National Nuclear Laboratory, Rolls-Royce, Serco and Westinghouse, who have provided substantial in-kind and financial support and our academic project partners from the University of Oxford and the Open University.

Tables and Figures

Table 1: Measured chemical composition of the materials.

Alloy	Alloying Elements				
	Zr	Fe[wt%]	Sn[wt%]	Nb[wt%]	Hydrogen [wt.ppm]
Recrystallised ZIRLO™	balance	0.09	0.92	0.91	10
Recrystallised low tin ZIRLO	balance	0.09	0.66	0.91	4
Recrystallised X2	balance	0.08	0.14	0.90	17

Table 2: Elastic constants used for stress calculation [44-47].

Phase		Poisson's ratio	Young's Modulus (GPa)
ZrO_2	[44, 47]	0.282	253
δ-$ZrH_{1.6}$	[45]	0.322	132
α-Zr	[46]	0.34	96

Table 3: Summary of the autoclave corrosion weight gain results.

Alloy	80 days ΔW (mg/dm^2)			Corrosion Kinetics					
				reference			hydrided		
	reference	hydrided	hydrided/ reference ratio	K_P	n	R^2	K_P	n	R^2
X2	24.4 ± 1.6	26.7 ± 0.9	1.093	4.693	0.383	0.989	2.774	0.530	0.930
Low Sn ZIRLO	26.8 ± 1.8	38.6 ± 0.7	1.441	5.935	0.344	0.985	3.790	0.539	0.949
ZIRLO™	25.9 ± 1.7	38.2 ± 1.7	1.479	5.848	0.339	0.968	3.073	0.588	0.801

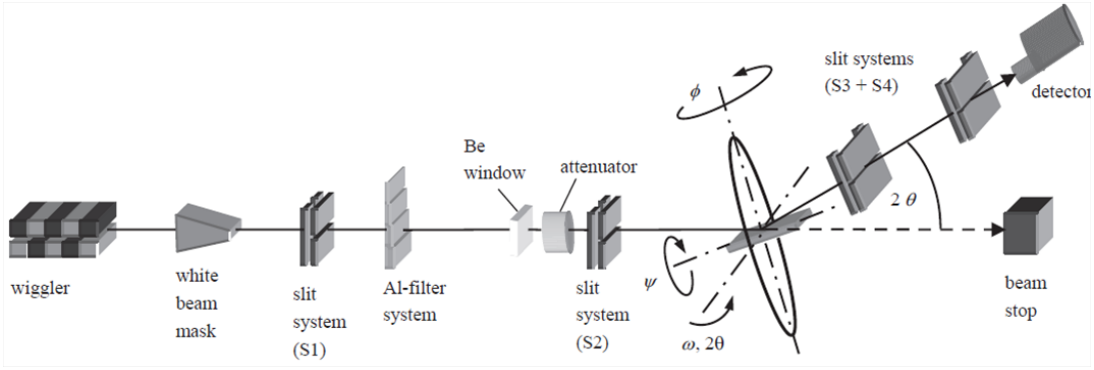

Figure 1: Schematic layout of the main beamline components at EDDI, BESSY [42].

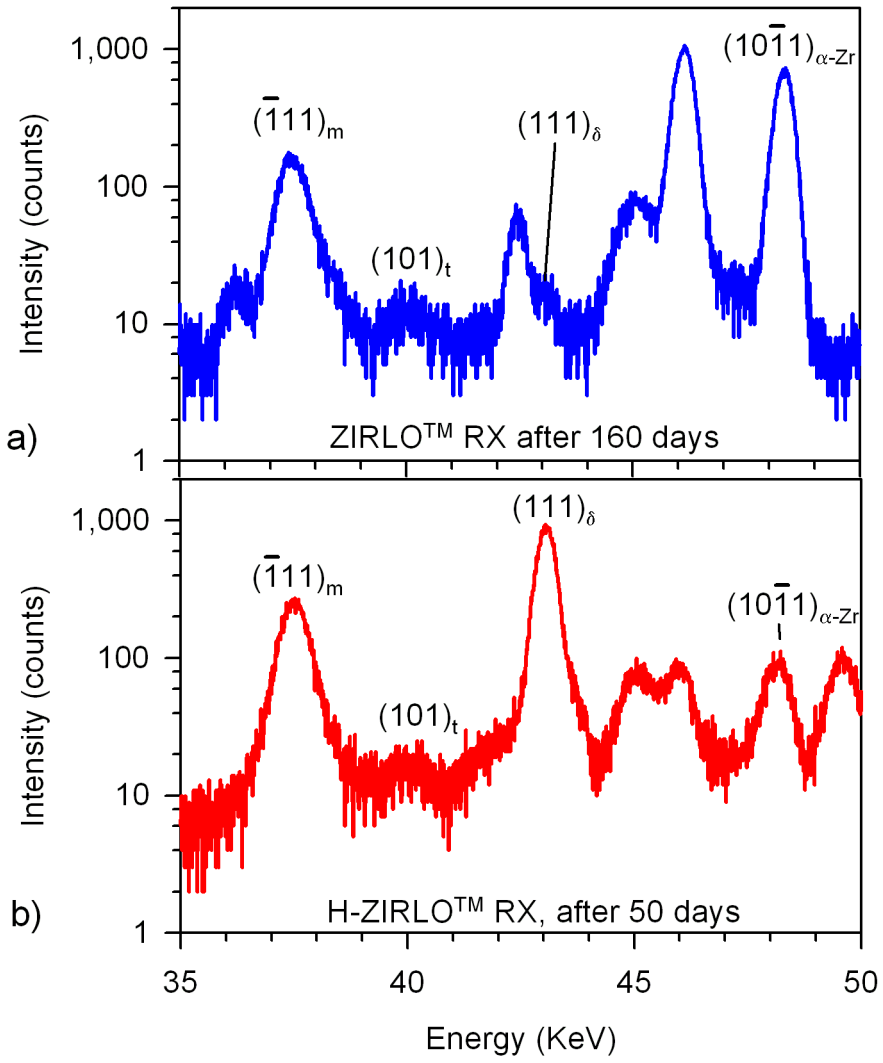

Figure 2: Partial diffraction spectrum recorded at Ψ = 0° on (a) reference non-hydrided ZIRLO™ cladding tube sample after 160 days autoclave exposure, (b) hydrided ZIRLO™ tube sample after 50 days autoclave exposure on beam line EDDI. Labelled are the $(\bar{1}11)_m$ reflection of the monoclinic ZrO2 phase, the $(101)_t$ reflection of the tetragonal ZrO2 phase, the $(111)_\delta$ reflection of the δ Zr-hydride phase and the $(10\bar{1}1)_{\alpha\text{-Zr}}$ reflection of the α-Zr phase.

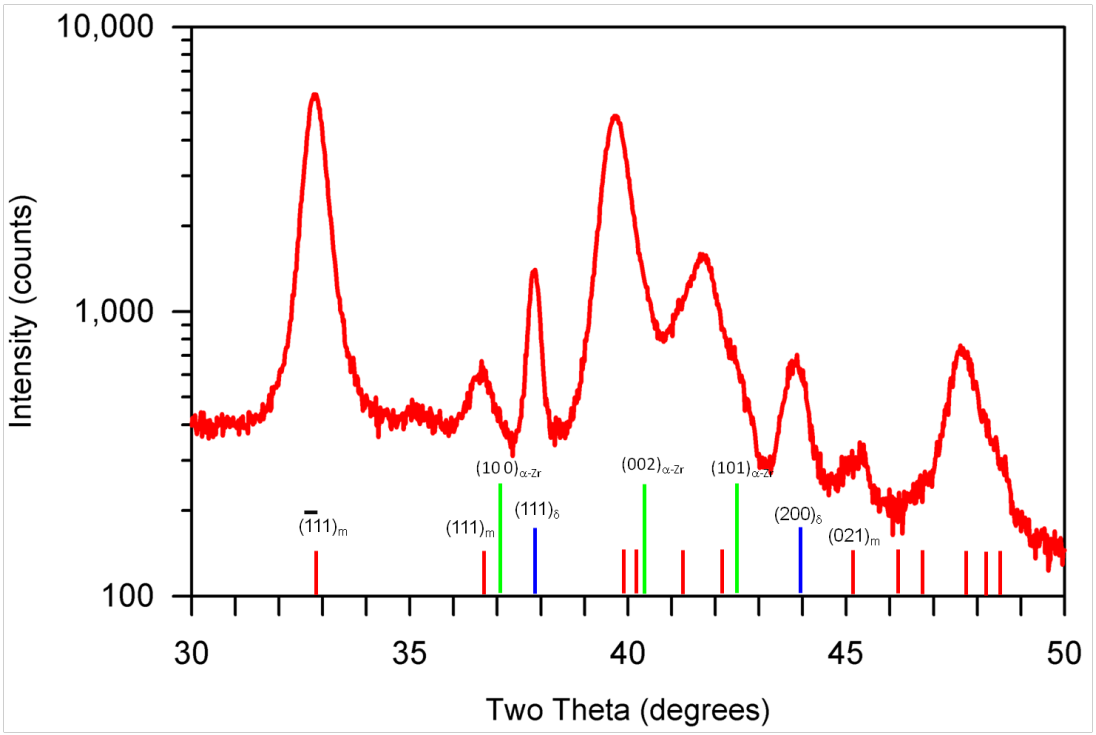

Figure 3: Partial laboratory X-ray diffraction spectrum recorded at Ψ = 0° on hydrided ZIRLO™ tube after 50 days autoclave exposure. Labelled are the $(\bar{1}11)_m$, $(111)_m$ and $(021)_m$ reflections of the monoclinic ZrO2 phase, the $(111)_\delta$ and $(200)_\delta$ reflections of the δ Zr-hydride phase and the $(100)_{\alpha\text{-}Zr}$,$(002)_{\alpha\text{-}Zr}$ and $(10\bar{1}1)_{\alpha\text{-}Zr}$ reflections of the α-Zr phase.

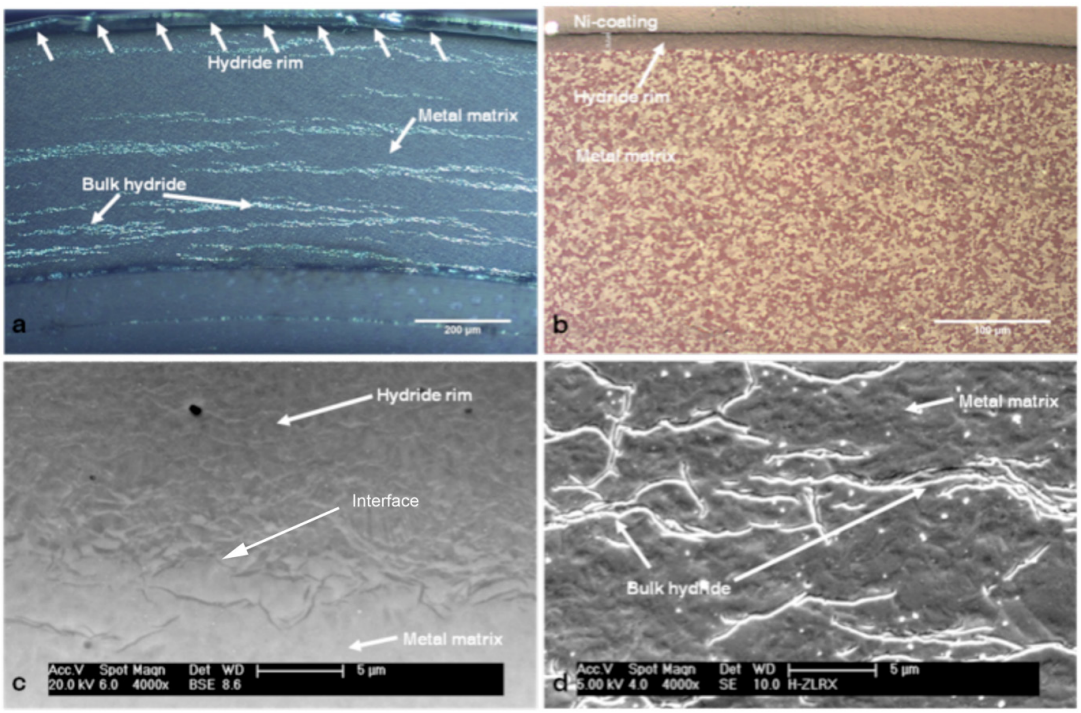

Figure 4: Hydride distribution in a recrystallised ZIRLO^{TM} tube after 10 days cathodic hydriding followed by 24 h at 400°C; overall [H] = 680 wt.ppm. Polarized light optical micrographs show a dense hydride rim at the outer surface of the clad (a) and (b), back-scattered electron mode SEM image showing the interface between hydride rim and bulk Zr metal (c) and secondary electron SEM image, showing hydrides in bulk Zr metal (d).

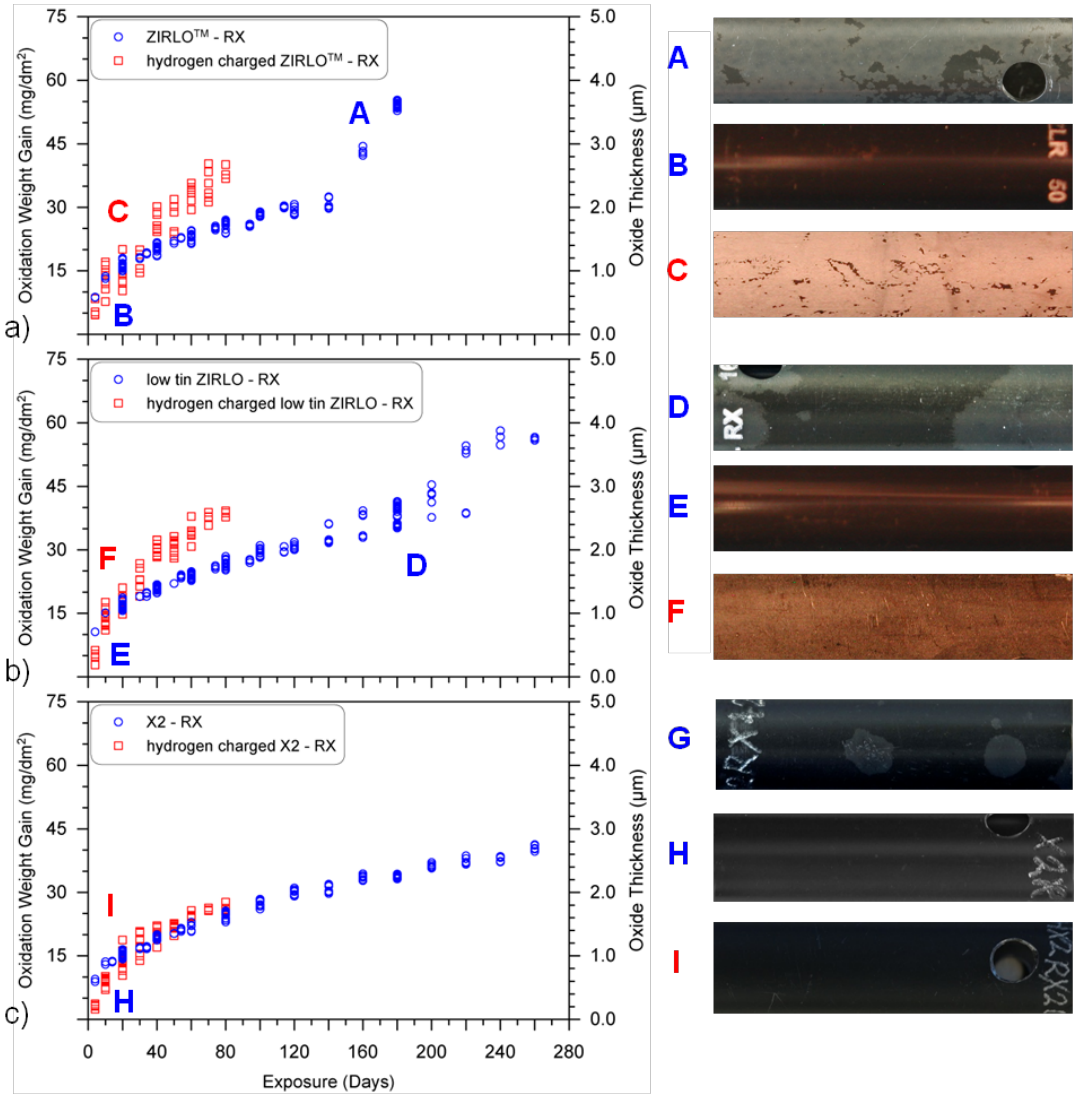

Figure 5: Autoclave corrosion weight gain profile of (a) hydrided ZIRLO™, overall [H] = 700 wt.ppm, and reference non-hydrided ZIRLO™ samples, (b) hydrided low tin ZIRLO, overall [H] = 650 wt.ppm and reference non-hydrided low tin ZIRLO, (c) hydrided X2, overall [H] = 600 wt.ppm, and reference non-hydrided X2. Photographs of actual corrosion specimens included: (A) reference ZIRLO™ after 160 days, (B) reference ZIRLO™ after 10 days, (C) hydrided ZIRLO™ after 10 days of autoclave exposure, (D) reference low tin ZIRLO after 180 days, (E) reference low tin ZIRLO after 10 days, (F) hydrided low tin ZIRLO after 10 days, (G) reference X2 after 360 days (H) reference X2 after 10 days and (I) hydrided X2 after 80 days of autoclave exposure.

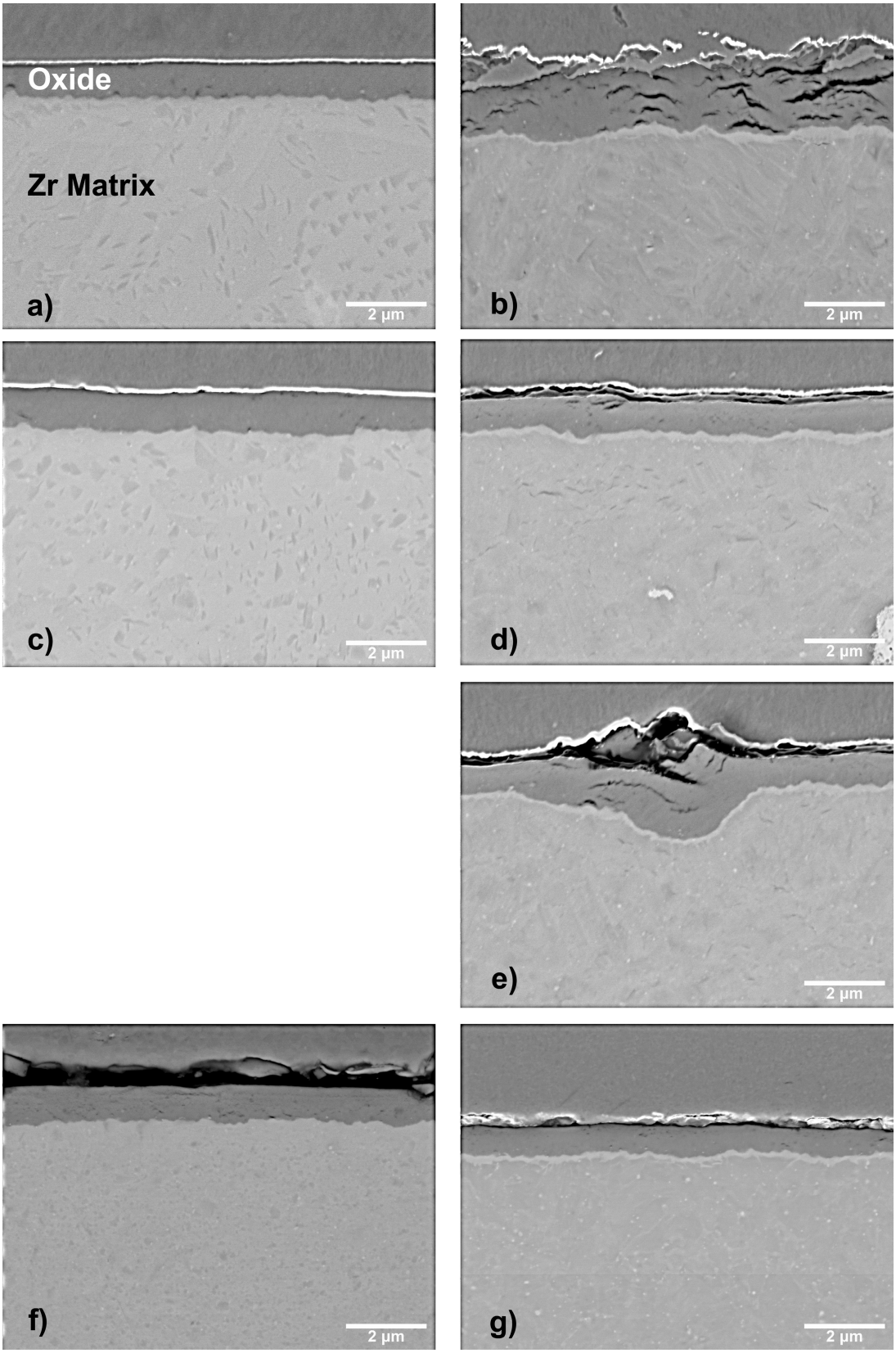

Figure 6: BSE mode SEM images representative of the oxide (cross-section) after 10 days of autoclave exposure for (a) non-hydrided ZIRLO^{TM}, (b) hydrided ZIRLO^{TM}, overall [H]=700wt.ppm, (c) non-hydrided low tin ZIRLO, (d, e) hydrided low tin ZIRLO, overall [H]=650wt.ppm, (f) non-hydrided X2 and (g) hydrided X2, overall [H]=600wt.ppm.

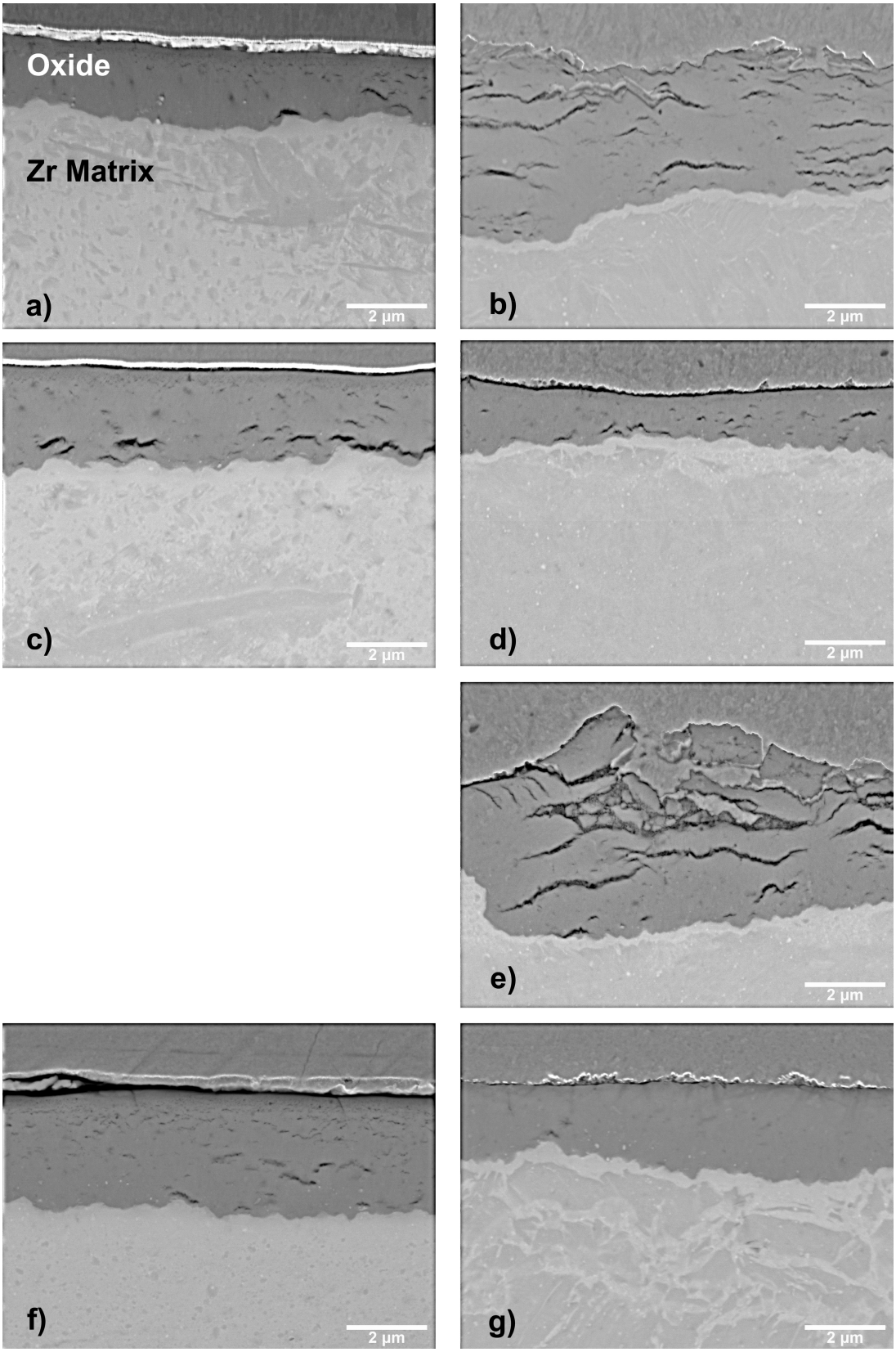

Figure 7: BSE mode SEM images of the oxide after non-hydrided samples had reached 1st transition. (a) ZIRLO™ (120 days exposure), (b) hydrided ZIRLO™ (50 days exposure), [H]=700wt.ppm, (c) low tin ZIRLO (160 days exposure), (d, e) hydrided low tin ZIRLO (50 days exposure), [H]=650wt.ppm, (f) X2 (360 days exposure) and (g) hydrided X2 (80 days exposure), [H]=600wt.ppm.

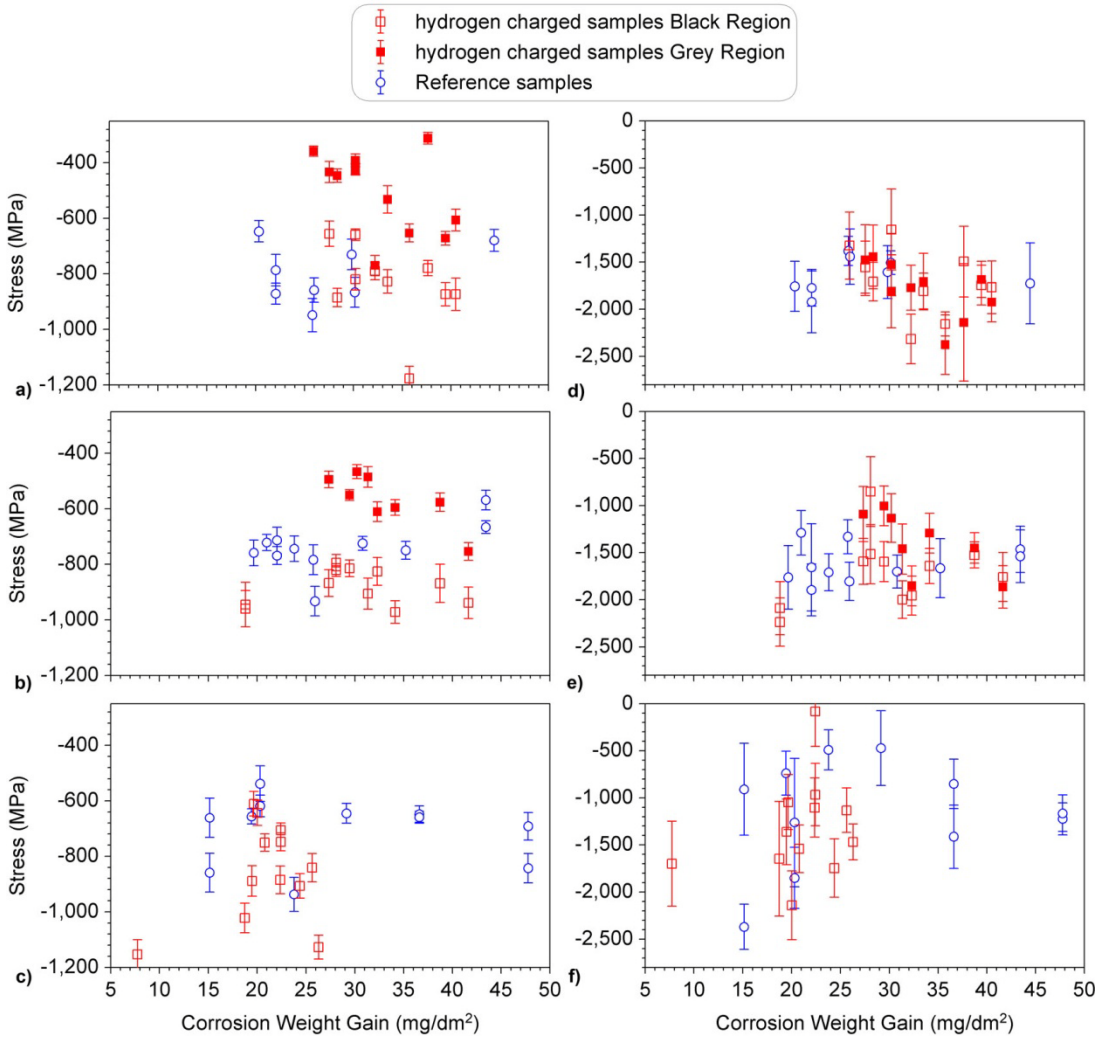

Figure 8: Oxide stresses of the monoclinic phase measured (a) in ZIRLO™, (b) in low tin ZIRLO and (c) in X2 and of the tetragonal phase measured (d) in ZIRLO™, (e) in low tin ZIRLO and (f) in X2.

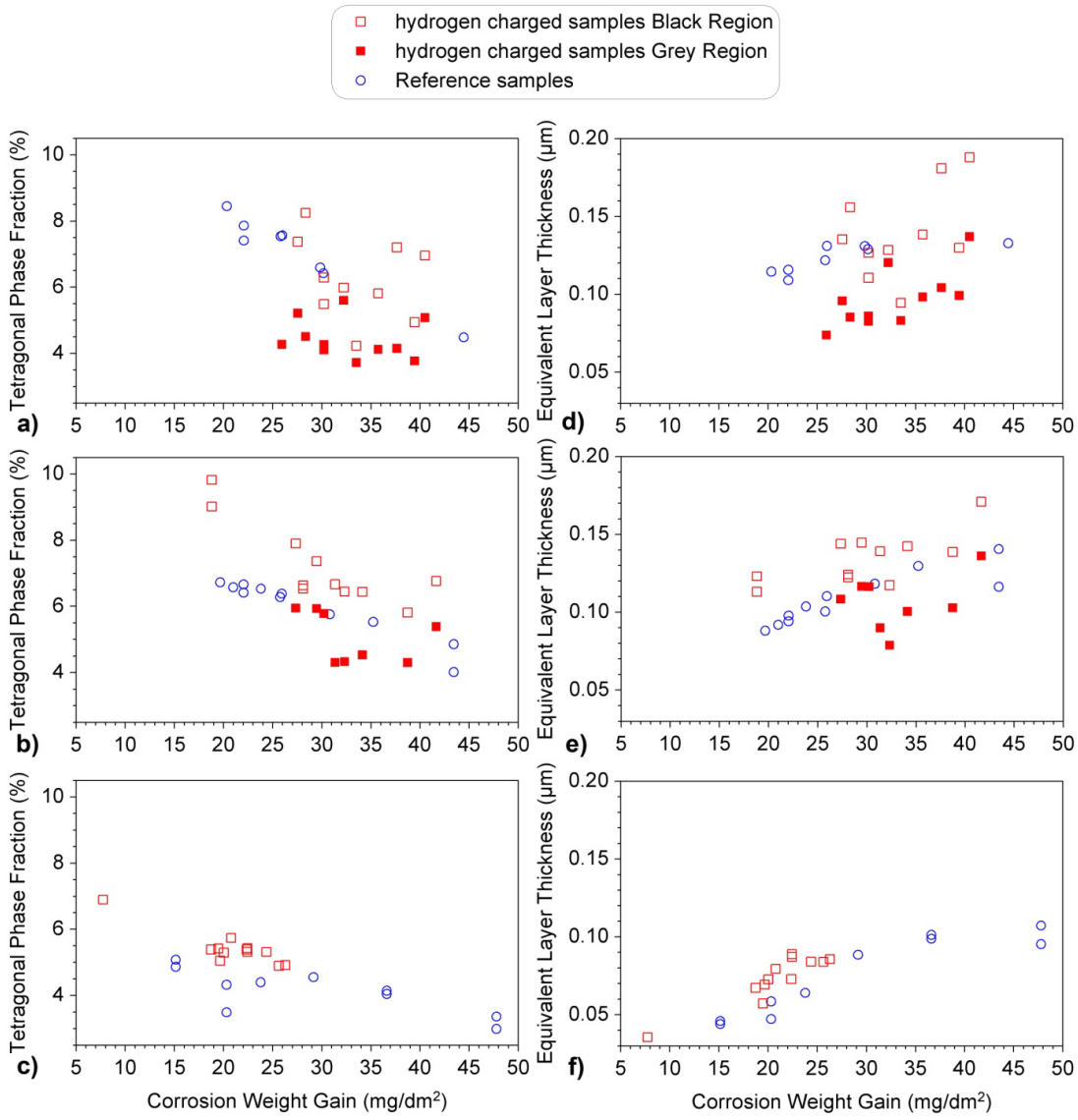

Figure 9: Calculated phase fraction and equivalent layer thickness of tetragonal phase plotted as a function of weight gain measured on (a), (d) ZIRLO™, (b), (e) low tin ZIRLO and (c) (f) X2 reference and hydrogen charged materials.

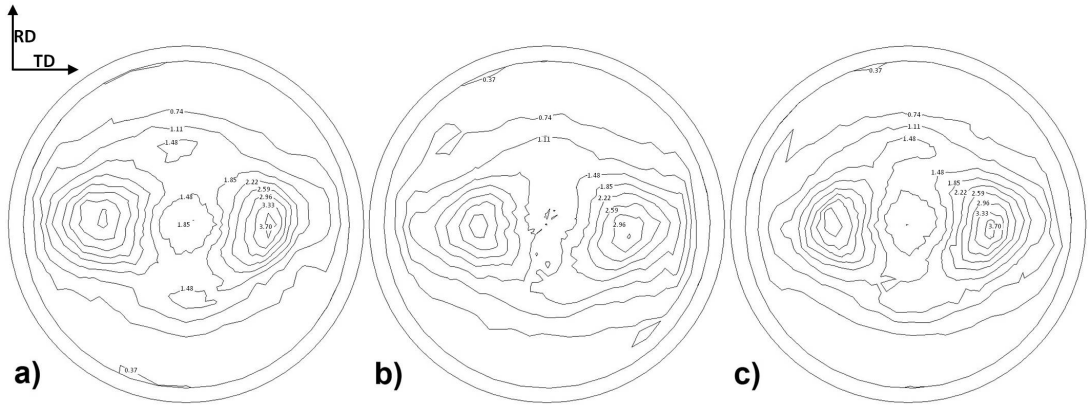

Figure 10: $(\bar{1}11)$-$_{monoclinic}$ pole figures measured on (a) reference ZIRLO^{TM} sample with maximum value of normalised intensity = 3.69, (b) white region of the oxide grown on hydrogen charged ZIRLO^{TM}, normalised intensity = 3.00 and (c) black region of hydrogen charged ZIRLO^{TM}, normalised intensity = 3.70.

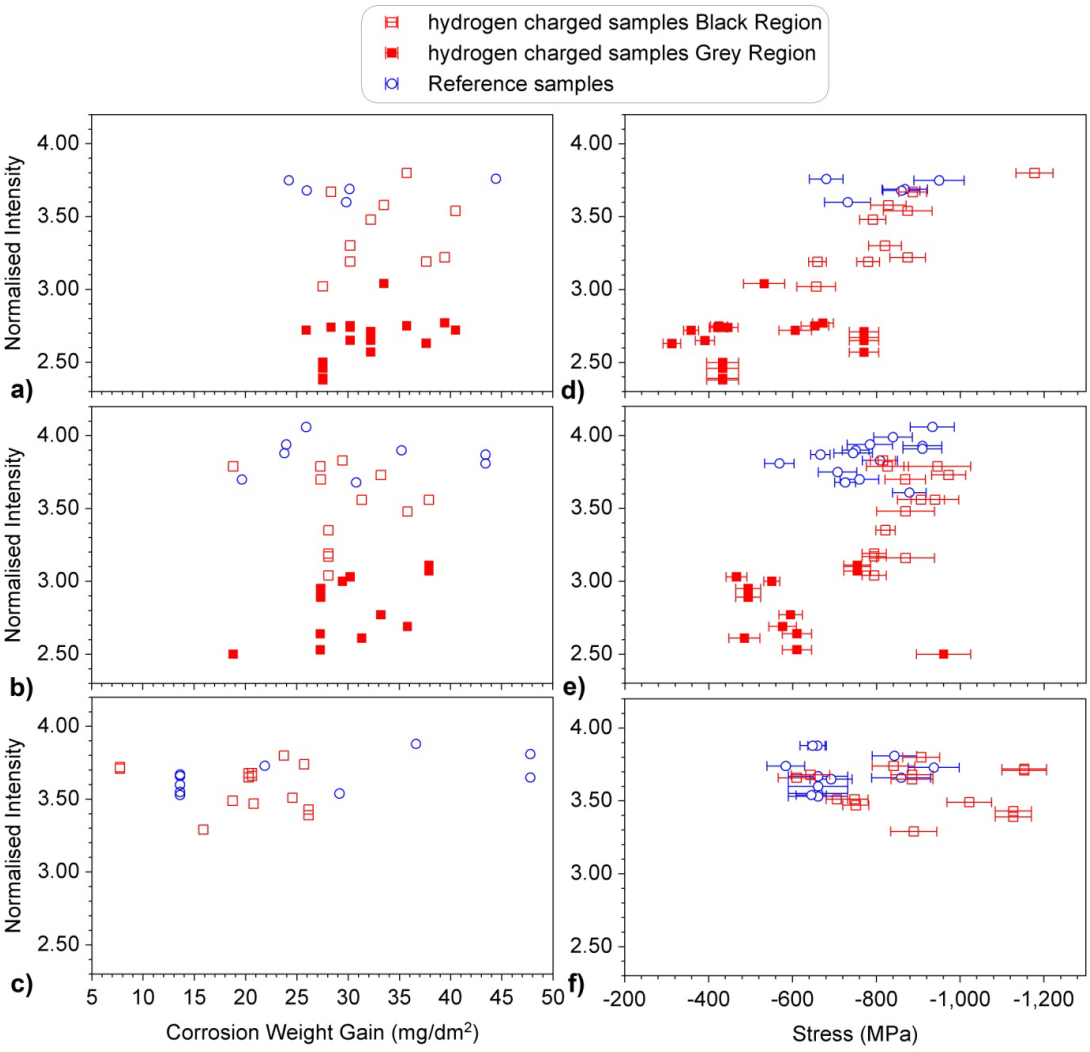

Figure 11: Maximum value of the normalised intensity of $(\bar{1}11)$ pole figure of the monoclinic ZrO_2 plotted as a function of corrosion weight gain and as a function of stress measured in monoclinic ZrO_2 of (a), (d) ZIRLO^{TM}, (b), (e) low tin ZIRLO and (c), (f) X2 materials.

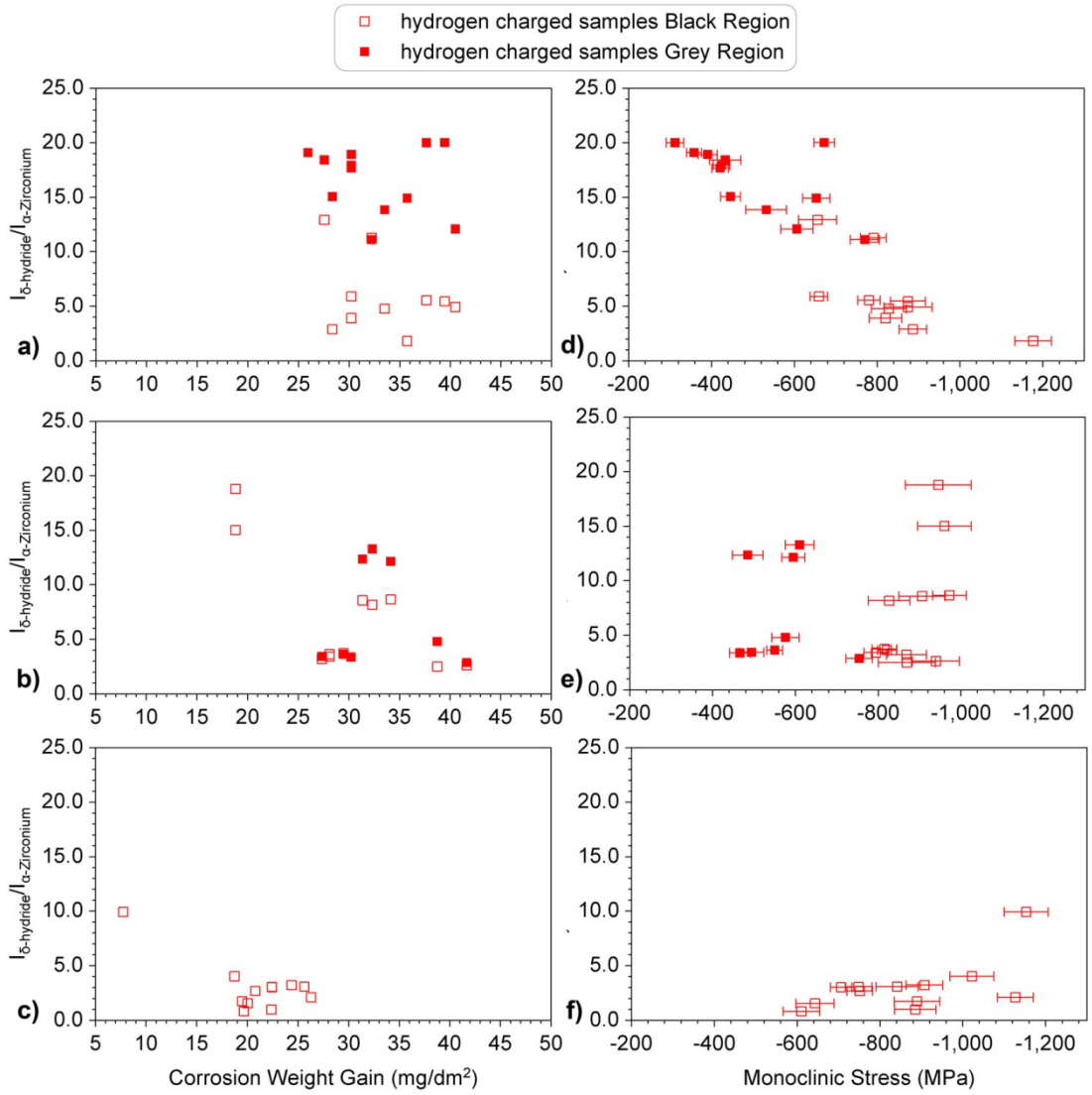

Figure 12: Peak intensity ratio between (111) reflection of the δ-hydride phase and $(10\bar{1}1)$ reflection of the α-Zirconium phase plotted as a function of corrosion weight gain and as a function of stress measured in monoclinic ZrO_2 of (a) and (d) ZIRLO™, (b) and (e) low tin ZIRLO and (c) and (f) X2 materials.

References

1. Kass, S., *Aqueous corrosion of the zircaloys at low temperatures.* Journal of Nuclear Materials, 1969. **29**(3): p. 315-321.
2. Cox, B., *Comments on "aqueous corrosion of the Zircaloys at low temperatures".* Journal of Nuclear Materials, 1969. **30**(3): p. 351-352.
3. Kiselev, A.A., et al., *Corrosion of Reactor Materials*. Vol. 2. 1962, Vienna IAEA.
4. Bryner, J.S., *The cyclic nature of corrosion of zircaloy-4 in 633 K water.* Journal of Nuclear Materials, 1979. **82**(1): p. 84-101.
5. Kass, S. *The Development of the Zircaloys*. in *Corrosion of Zirconium Alloys*. 1964. ANS Winter meeting: ASTM International.
6. Lustman, B. and F.K. Jr, *The Metallurgy of zirconium*. 1st ed. National Nuclear Energy series, Div. 7, v. 41955, New York: McGraw-Hill. 776.
7. Motta, A.T., et al., *Micostructural characterisation of oxides formed on model Zr alloys using synchrotron radiation*, in *15th International Symposium on Zirconium in the Nuclear Industry*, B. Kammenzind and M. Limback, Editors. 2009, ASTM International Sunriver Resort Oregon, USA. p. 486-506.
8. Griggs, B., H.P. Maffei, and D.W. Shannon, *Multiple Rate Transitions in the Aqueous Corrosion of Zircaloy.* Journal of The Electrochemical Society, 1962. **109**(8): p. 665-668.
9. Sabol, G.P. and S.B. Dalgaard, *The Origin of the Cubic Rate Law in Zirconium Alloy Oxidation.* Journal of The Electrochemical Society, 1975. **122**(2): p. 316-317.
10. Arima, T., et al., *Oxidation kinetics of Zircaloy-2 between 450°C and 600°C in oxidizing atmosphere.* Journal of Nuclear Materials, 1998. **257**(1): p. 67-77.
11. Hauffe, K., *Oxidation of metals*1965, New York: Plenum Press, Inc.
12. Arima, T., et al., *Oxidation properties of Zr-Nb alloys at 500-600 °C under low oxygen potentials.* Corrosion Science, 2005. **47**(2): p. 435-446.
13. Cox, B., *Some thoughts on the mechanisms of in-reactor corrosion of zirconium alloys.* Journal of Nuclear Materials, 2005. **336**(2-3): p. 331-368.
14. Bossis, P., et al., *Comparison of the High Burn-Up Corrosion on M5 and Low Tin Zircaloy-4*, in *14th International Symposium on Zirconium in the Nuclear Industry*, P. Rudling and B. Kammenzind, Editors. 2005, ASTM International: Stockholm, Sweden. p. 494-525.
15. Garde, A.M., *Enhancement of Aqueous Corrosion of Zircaloy-4 Due to Hydride Precipitation at the Metal-Oxide Interface*, in *9th International Symposium on Zirconium in the Nuclear Industry*, C.M. Eucken and A.M. Garde, Editors. 1991, ASTM International: Kobe, Japan. p. 566-592.
16. Godlewski, J., *How the tetragonal zirconia is stabilized in the oxide scale that is formed on a zirconium alloy corroded at 400°c in steam*, in *10th International Symposium on Zirconium in the Nuclear Industry:* , A.M. Garde and E.R. Bradley, Editors. 1994, ASTM International: Baltimore, MD. p. 663-683.
17. Peters, H.R., *Improved Characterization of Aqueous Corrosion Kinetics of Zircaloy-4*, in *6th International Symposium on Zirconium in the Nuclear Industry*, D.G. Franklin and R.B. Adamson, Editors. 1984, ASTM International: Vancouver, British Columbia, Canada. p. 507-519.
18. Bouvier, P., J. Godlewski, and G. Lucazeau, *A Raman study of the nanocrystallite size effect on the pressure-temperature phase diagram of zirconia grown by zirconium-based alloys oxidation.* Journal of Nuclear Materials, 2002. **300**(2-3): p. 118-126.

19. Yilmazbayhan, A., et al., *Structure of zirconium alloy oxides formed in pure water studied with synchrotron radiation and optical microscopy: relation to corrosion rate.* Journal of Nuclear Materials, 2004. **324**(1): p. 6-22.
20. Roy, C. and B. Burgess, *A study of the stresses generated in zirconia films during the oxidation of zirconium alloys.* Oxidation of Metals, 1970. **2**(3): p. 235-261.
21. Zhilyaev, A.P. and J.A. Szpunar, *Influence of stress developed due to oxide layer formation on the oxidation kinetics of Zr-2.5%Nb alloy.* Journal of Nuclear Materials, 1999. **264**(3): p. 327-332.
22. Block, S., J.A.H. Da Jornada, and G.J. Piermarini, *Pressure-Temperature Phase Diagram of Zirconia.* Journal of the American Ceramic Society, 1985. **68**(9): p. 497-499.
23. Preuss, M., et al., *Towards a mechanistic understanding of corrosion mechanisms in zirconium alloys*, in *16th International Symposium on Zirconium in the Nuclear Industry*2010, ASTM International ChengDu, P.R.China.
24. Cox, B., *Are Zirconium Corrosion Films a Form of Partially Stablized Zirconia?*, 1987, Atomic Energy of Canada Ltd.
25. Schwartz, C.M., D.A. Vaughan, and G.G. Cocks, *Report BMI-793 December 17, 1952.* , in *The Metallurgy of Zirconium*, B. Lustman and F. Kerze, Editors. 1955, McGraw-Hill: New York. p. 562.
26. Godlewski, J., et al., *Stress Distribution Measured by Raman Spectroscopy in Zirconia Films Formed by Oxidation of Zr-Based Alloys*, in *12th International Symposium on Zirconium in the Nuclear Industry*, G.P. Sabol and G.D. Moan, Editors. 2000, ASTM International: Toronto, Canada. p. 877-899.
27. Blat-Yrieix, M., et al., *Toward a Better Understanding of Dimensional Changes in Zircaloy-4: What is the Impact Induced by Hydrides and Oxide Layer?* Journal of ASTM International (JAI), 2008. **5**(9): p. 16.
28. Busser, V., et al., *Modelling of Corrosion Induced Stresses during Zircaloy-4 Oxidation in Air.* Materials Science Forum, 2008. **595-598**: p. 419-427.
29. Heuer, A.H. and M. Rühle, *Overview no. 45: On the nucleation of the martensitic transformation in zirconia (ZrO2).* Acta Metallurgica, 1985. **33**(12): p. 2101-2112.
30. Kammenzind, B.F., et al., *Hydrogen pickup and redistribution in alpha-annealed Zircaloy-4*, in *11th International Symposium on Zirconium in the Nuclear Industry*, E.R. Bradley and G.P. Sabol, Editors. 1996, ASTM International: Garmisch-Partenkirchen, Germany. p. 338-370.
31. Garde, A.M., G.P. Smith, and R.C. Pirek, *In-PWR Irradiation Performance of Dilute Tin-Zirconium Advanced Alloys*, in *13th International Symposium on Zirconium in the Nuclear Industry*, G.D. Moan and P. Rudling, Editors. 2002, ASTM International: Annecy, France. p. 490-506.
32. Clayton, J.C., *Out-of-Pile Nickel Alloy-Induced Accelerated Hydriding of Zircaloy Fasteners*, in *6th International Symposium on Zirconium in the Nuclear Industry*, D.G. Franklin and R.B. Adamson, Editors. 1982, ASTM International: Vancouver, British Columbia, Canada. p. 572-591.
33. Mcminn, A., E.C. Darby, and J.S. Schofield, *The Terminal Solid Solubility of Hydrogen in Zirconium Alloys*, in *12th International Symposium on Zirconium in the Nuclear Industry*, G.P. Sabol and G.D. Moan, Editors. 2000, ASTM International: Toronto, Canada. p. 173-196.
34. Kearns, J.J., *Terminal solubility and partitioning of hydrogen in the alpha phase of zirconium, Zircaloy-2 and Zircaloy-4.* Journal of Nuclear Materials, 1967. **22**(3): p. 292-303.
35. Santisteban, J.R., et al., *Determination of residual stresses around blisters in Zr-2.5%Nb pressure tubes.* Power Diffraction, 2009. **24 No.2-Sep**: p. 577-584.

36. Kammenzind, B.F., et al., *The Long Range Migration Of Hydrogen Through Zircaloy In Response To Tensile And Compressive Stress Gradients*, in *12th International Symposium on Zirconium in the Nuclear Industry*, G.P. Sabol and G.D. Moan, Editors. 2000, ASTM International: Toronto, Canada. p. 196-233.
37. Blat, M. and D. Noel, *Detrimental Role of Hydrogen on the Corrosion Rate of Zirconium Alloys*, in *11th International Symposium on Zirconium in the Nuclear Industry*, E.R. Bradley and G.P. Sabol, Editors. 1996, ASTM International: Garmisch-Partenkirchen, Germany. p. 319-337.
38. Cox, B. and T. Johnson, *Observation of a Second Transition Point During the Oxidation of Zirconium Alloys*, in *Corrosion*1962. p. 33.
39. Khatamian, D., *Role of hydrides on the oxidation and deuterium pickup of Zr-2.5Nb in D2O at 573 K.* Journal of Alloys and Compounds, 2005. **404-406**: p. 297-302.
40. Kido, T., *A Study on Enhanced Uniform Corrosion of Zircaloy-4 cladding during High Burnup Operation in PWRs*, in *6th Internanional Symposium on Environmental Degradation of Materials in Nuclear Power Systems - Water Reactors*, R.E. Gold and E.P. Simonen, Editors. 1993, The minerals, Metals & Materials Society: San Diego, California, USA. p. 449-456.
41. Wei, J., et al., *Synthesis of a Hydride Rich Rim on Zirconium Alloys: A Cathodic Hydrogen Charging Method.* To be Submitted to Corrosion Science.
42. Genzel, C., et al., *The materials science synchrotron beamline EDDI for energy-dispersive diffraction analysis.* Nuclear Instruments and Methods in Physics Research Section A: Accelerators, Spectrometers, Detectors and Associated Equipment, 2007. **578**(1): p. 23-33.
43. Cohen, J.B. and I.C. Noyan, *Residual stress : measurement by diffraction and interpretation*1987, New York: Springer-Verlag.
44. Frankel, P., et al., *Diffraction Elastic Constants of monoclinic ZrO2 and the effect of strong texture in ZrO2 films on residual stress measurements.* Journal Of Applied Crystallography 2011: p. SUBMITTED.
45. Yamanaka, S., et al., *Characteristics of zirconium hydride and deuteride.* Journal of Alloys and Compounds, 2002. **330-332**: p. 99-104.
46. Northwood, D.O., I.M. London, and L.E. Bähen, *Elastic constants of zirconium alloys.* Journal of Nuclear Materials, 1975. **55**(3): p. 299-310.
47. Polatidis, E., et al., *Residual stress and phase characterization on Zircaloy-4 alloys using synchrotron X-ray diffraction.* Journal of Nuclear Materials, Submitted November 2011.
48. Garvie, R.C. and P.S. Nicholson, *Phase Analysis in Zirconia Systems.* Journal of the American Ceramic Society, 1972. **55**(6): p. 303-305.
49. Bourgoin, J., et al., *Corrosion Behavior Analysis of Cladding Alloy in EDF's PWR. Evaluation of the Hydriding Effect*, in *EUROCORR'96*1996: Nice, France.
50. Holston, A.-M.A., et al., *A Combined Approach to Predict the Sensitivity of Fuel Cladding to Hydrogen-Induced Failures during Power Ramps*, in *2010 LWR Fuel Performance/TopFuel/WRFPM*2010: Hyatt Regency Grand Cypress, Orlando, Florida, USA. p. 167-183.
51. Hillner, E., D.G. Franklin, and J.D. Smee, *Long-term corrosion of Zircaloy before and after irradiation.* Journal of Nuclear Materials, 2000. **278**(2-3): p. 334-345.
52. Yilmazbayhan, A., et al., *Transmission electron microscopy examination of oxide layers formed on Zr alloys.* Journal of Nuclear Materials, 2006. **349**(3): p. 265-281.
53. Wei, J., et al., *The Effect of Sn on Autoclave Corrosion Performance and Corrosion Mechanisms in Zr-Sn-Nb Alloys.* To be Submitted to Acta Materialia.
54. Carpenter, G.J.C., *The dilatational misfit of zirconium hydrides precipitated in zirconium.* Journal of Nuclear Materials, 1973. **48**(3): p. 264-266.

55. Daum, R.S., Y.S. Chu, and A.T. Motta, *Identification and quantification of hydride phases in Zircaloy-4 cladding using synchrotron X-ray diffraction.* Journal of Nuclear Materials, 2009. **392**(3): p. 453-463.
56. Santisteban, J.R., et al., *Hydride precipitation and stresses in zircaloy-4 observed by synchrotron X-ray diffraction.* Acta Materialia, 2010. **58**(20): p. 6609-6618.
57. Skovgaard, M., et al., *Effect of microscale shear stresses on the martensitic phase transformation of nanocrystalline tetragonal zirconia powders.* Journal of the European Ceramic Society, 2010. **30**(13): p. 2749-2755.
58. Cox, B., et al., *Waterside Corrosion of Zirconium Alloys in Nuclear Power Plants*, 1998, IAEA: Vienna.
59. Ploc, R.A. and S.B. Newcomb. *Microscopy of Oxidation 3*. in *Third International Conference on the Microscopy of Oxidation*. 1996. Trinity Hall, Cambridge: Institute of Materials, Minerals and Mining.
60. Li, H., M.G. Glavicic, and J.A. Szpunar, *A model of texture formation in ZrO2 films.* Materials Science and Engineering A, 2004. **366**(1): p. 164-174.

End of Publication 4

5 A Model for the Corrosion Mechanism of Zirconium Alloys

A model is proposed in an attempt to establish the relationship between tetragonal to monoclinic phase transformation of zirconium dioxide and the rate transition of corrosion kinetics. This model considers the transition(s) as stress driven. The successive cycles of near cubic oxide growth are linked to the periodic breakdown and reconstruction of the barrier layer at the metal/oxide interface, which is then associated with tetragonal to monoclinic phase transformation.

The cyclic nature and breakaway of post-transition corrosion kinetics are schematically displayed in Figure 39. The corrosion of zirconium alloys has five different stages: A initial stage, B pre-1st transition growth, C 1st transition, D post-1st transition growth and E breakaway. The observations by [3, 48] have indicated that the duration between transitions decreases with each successive cycle.

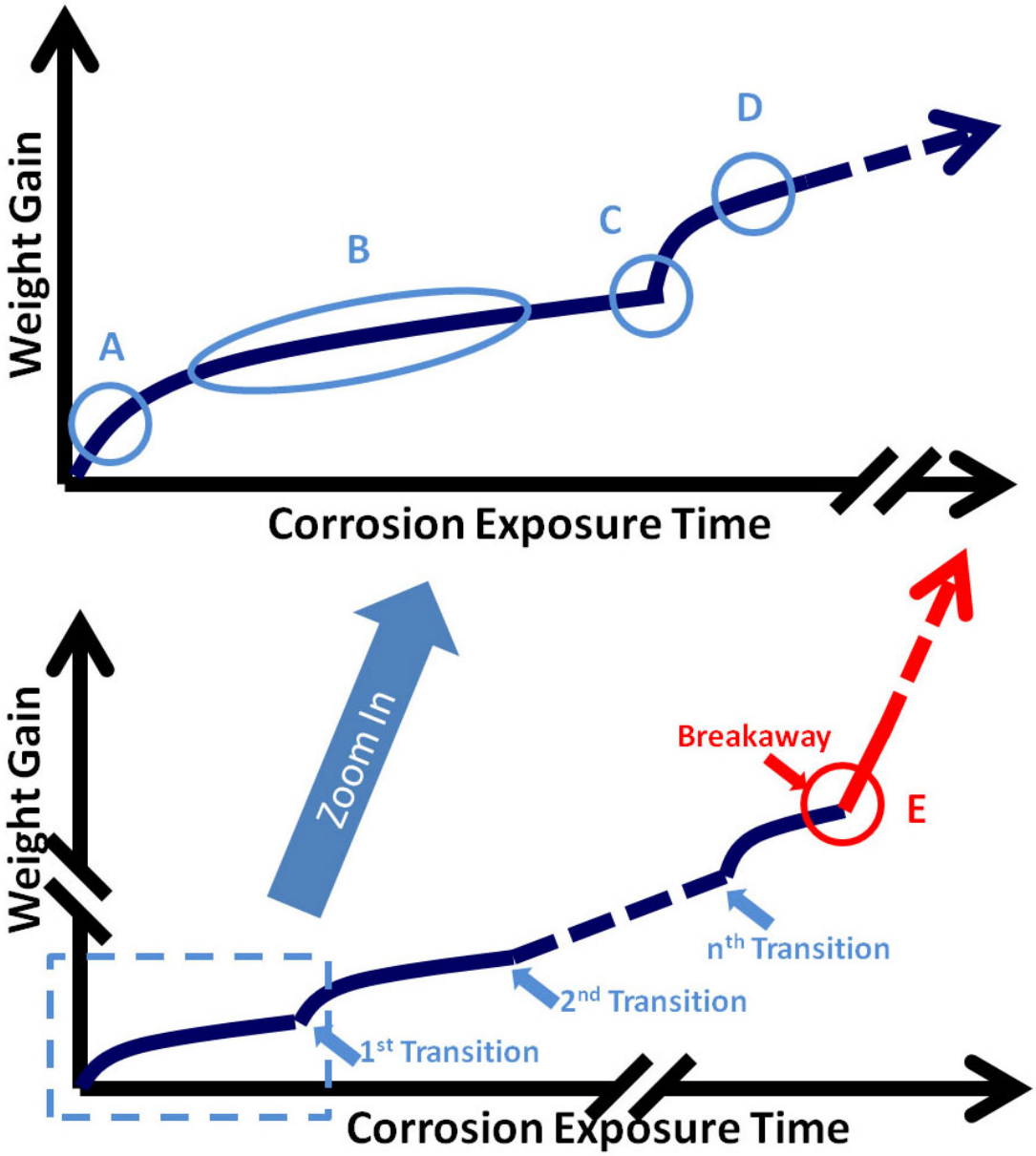

Figure 39: Schematics drawing of zirconium corrosion kinetics.

The proposed mechanism behind initial stage A and pre-1st transition growth stage B of Figure 39 is described in Figure 40. When zirconium oxide grains form at the metal/oxide interface (Figure 40 A), both monoclinic and tetragonal grains nucleate. This corrosion progression front is a mixture of equiaxed tetragonal and monoclinic grains. To date, reliable phase quantification of the interface has yet to be achieved, as discussed in previous chapters. Note that the schematics of Figure 40 to Figure 42 are not quantitative representations but extreme case scenarios.

The exact crystal structure of interfacial oxide grains is affected by local stress variation, change of local concentration of tetragonal stabiliser such as tin and interface morphology [83, 84]. Oxidation progresses firstly in terms of nucleation, then mainly in terms of epitaxial grain growth. At this stage, the transportation of corrosion species follows the diffusion mechanism where grain boundary diffusion takes the predominant role. This would bring about a parabolic oxide growth. The epitaxial growth of monoclinic and tetragonal oxide grains results in the formation of columnar oxide grains. The subsequent reduction in grain boundary area leads to near cubic growth rate. A highly compressive stress field is generated due to a Pilling-Bedworth ratio of 1.56 from zirconium to zirconia [35, 77]. The compressive stresses in the oxide are balanced by tensile stresses in the metal substrate, which eventually creeps upon prolonged exposure at 360°C. The current synchrotron X-ray diffraction experiments consistently measured up to 150 MPa of tensile stresses, which is higher than that required for stress balance. This possibly arises from a stress gradient in the metal, which is potentially the result of oxygen diffusion into the metal. The repetitive relaxations due to creep and formation of fresh oxide under compression will generate a stress gradient inside the oxide [54, 55, 80]. Note that delamination of the oxide could also contribute to the stress gradient. Not all oxide grains are capable of epitaxial growth. The strong texture in the oxide means some oxide grains (monoclinic and tetragonal) might not be in the correct orientation to grow and would stay equiaxed [25, 55, 171]. Combining grain orientations with geometrical restrictions, a fraction of the oxide grains will stay below a critical grain size and remain tetragonal if they started out as such. The monoclinic and tetragonal oxide grains can now be divided into two populations:

one population of grains below the critical grain size where tetragonal phase depends on the stabilisation of nano grain size; and the other one still relatively small but above certain critical grain size, where tetragonal phase depends on the combined stabilisation provided by compression beyond -2000 MPa [50, 55, 78, 79] and local concentration of tetragonal stabilisers such as tin [83, 84]. Stress alone is not sufficient. The critical grain size for tetragonal stabilisation is suggested to be 30 nm [15, 172-174].

During the pre-1st transition growth stage B, oxide/metal interface gradually moves inwards and the stress in the previously formed oxide decreases. Consequently stress stabilised tetragonal grains transform when local stress falls beneath the threshold. This process repeats with the progression of corrosion and forms a tetragonal rich layer at the interface, whose thickness is determined by the stress gradient inside the oxide. At this stage, the thickness of tetragonal rich layer remains relatively the same (i.e. Tet. rich layer 1 = Tet. rich layer 2, Figure 40). Note that the tetragonal rich layer is a mixture of monoclinic and tetragonal grains, as shown in Figure 40 to Figure 42. It is also suggested that epitaxial growth of tetragonal grains will be interrupted as soon as tetragonal to monoclinic phase transformation occurs. Current study has been unable to provide experimental evidence to either confirm or reject this.

Tetragonal to monoclinic phase transformation starts early during corrosion and continues over the duration of the corrosion exposure. The martensitic phase transformation causes tiny pores and cracks near the ends of columnar grains following the shear model previously described in [3, 105, 115]. These pores and

cracks currently have little influence upon the transportation of corrosion species since they are generally few, small and most importantly not inter-connected. Corrosion kinetics still follows the cubic rate law. During stage A and B, the absorbed hydrogen stays in solid solution. No hydrides are precipitated. Note that the compressive stress is also responsible for restraining the oxide and preventing crack propagation. The current mixture of tetragonal and monoclinic grains has good integrity and is considered as the barrier layer against corrosion. The barrier layer is not equal to the Tet. rich layer (i.e. Barrier layer 1 > Tet. rich layer 2, Figure 40 B).

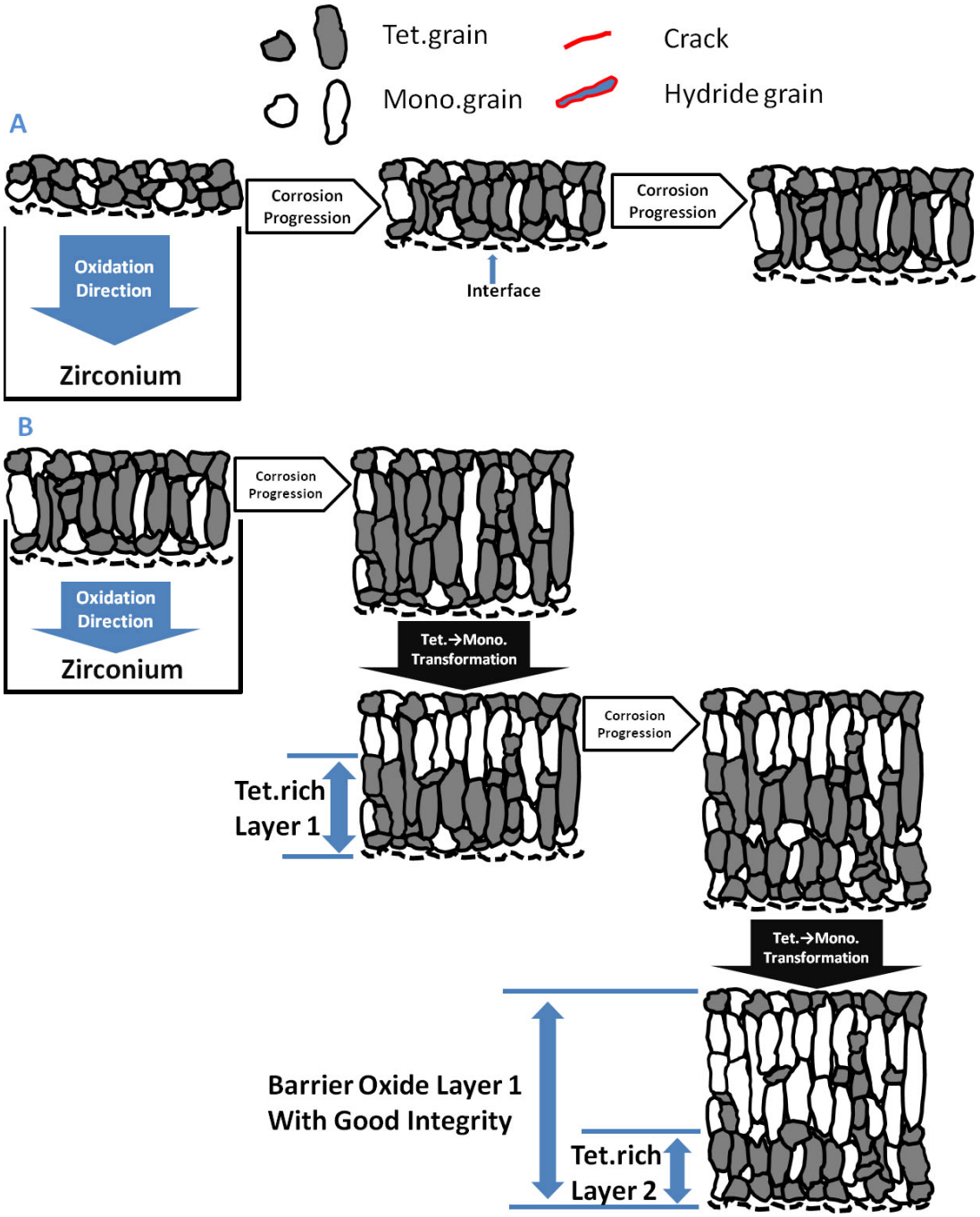

Figure 40: Schematic description of stages A initial and B pre-1st transition growth of oxide. The amount of tetragonal and monoclinic grains is only a schematic, not a quantitative representation.

The 1st transition stages C and D are shown schematically in Figure 41. With the progression of pre-1st transition growth, the cumulated effects of continued tetragonal to monoclinic phase transformations eventually introduce enough damage to the barrier layer, causing the break down of barrier layer 1 (Figure 41 C). The pores and small cracks become an inter-connected 3-dimensional network, enabling the transportation of corrosion medium, effectively making the majority of the barrier layer 1 transparent. This reduction of effective barrier layer thickness is responsible for the rate transition from pre- to post-1st transition. After 1st transition, any oxide beyond barrier layer 2 is considered as mere history, providing no protection. The growth of oxide then repeats the pre-1st transition kinetics.

With the progression of corrosion, more hydrogen is picked up by the metal until solid solution limit is exceeded, initiating the precipitation of hydrides near the metal/oxide interface. Although room temperature SEM images reveal precipitated hydrides in reference samples as early as just past 1st transition (publication No.3 and 4), hydrogen solid solution limit is higher at 360°C and the precipitation of hydride only occurs at a later stage. Note that the amount of hydrides in Figure 41 is not a quantitative representation. Observations in publication No.4 also suggest that the oxidation of zirconium hydride reduces the ability of the oxide grains to grow epitaxially into columnar structure, which leads to more parabolic rather than cubic growth rate. The formation of hydride also involves 17% of volume expansion [137, 140, 141], lowering the effective Pilling-Bedworth ratio from 1.56 to 1.29. This subsequently generates lowered residual stress which is required to stabilise the stress stabilised tetragonal grains and maintain the integrity of the barrier layer.

During each cycle, the above two factors together contribute to earlier phase transformation of tetragonal grains and thinner barrier layer than during the previous cycle. The barrier layer still has good integrity at this stage. Subsequently shorter and shorter duration between kinetics transitions is expected after each cycle. Although not directly stated, observations on corrosion behaviour by [3, 34] support this. The lowered residual stress state has been measured in grey oxide grown on hydrided samples, as shown in publication No.4.

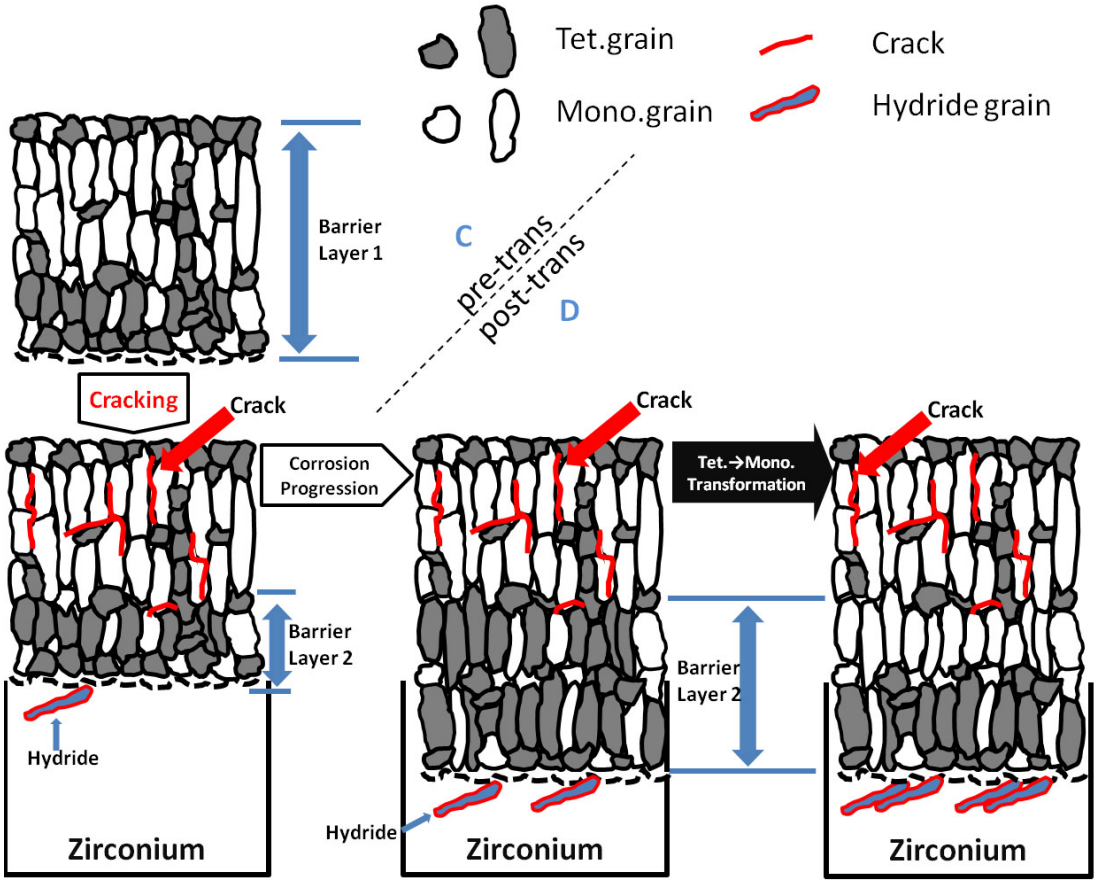

Figure 41: Schematic description of stages C during 1st transition and D post-1st transition growth of oxide. The amount of tetragonal, monoclinic, hydrides and cracks are only schematic, not quantitative representation.

In Figure 42, after n-1 transitions, the preferential precipitation of hydrides adjacent to the interface brings about the formation of a hydride rich rim. The lowered compressive stress eventually reaches a threshold where the tetragonal rich layer

becomes the last barrier layer. Further tetragonal to monoclinic phase transformation breaks down the last barrier layer and enables direct transportation of corrosion medium to the interface via the inter-connected crack network. The oxide no longer provides any protection and the corrosion is expected to progress following linear rate law.

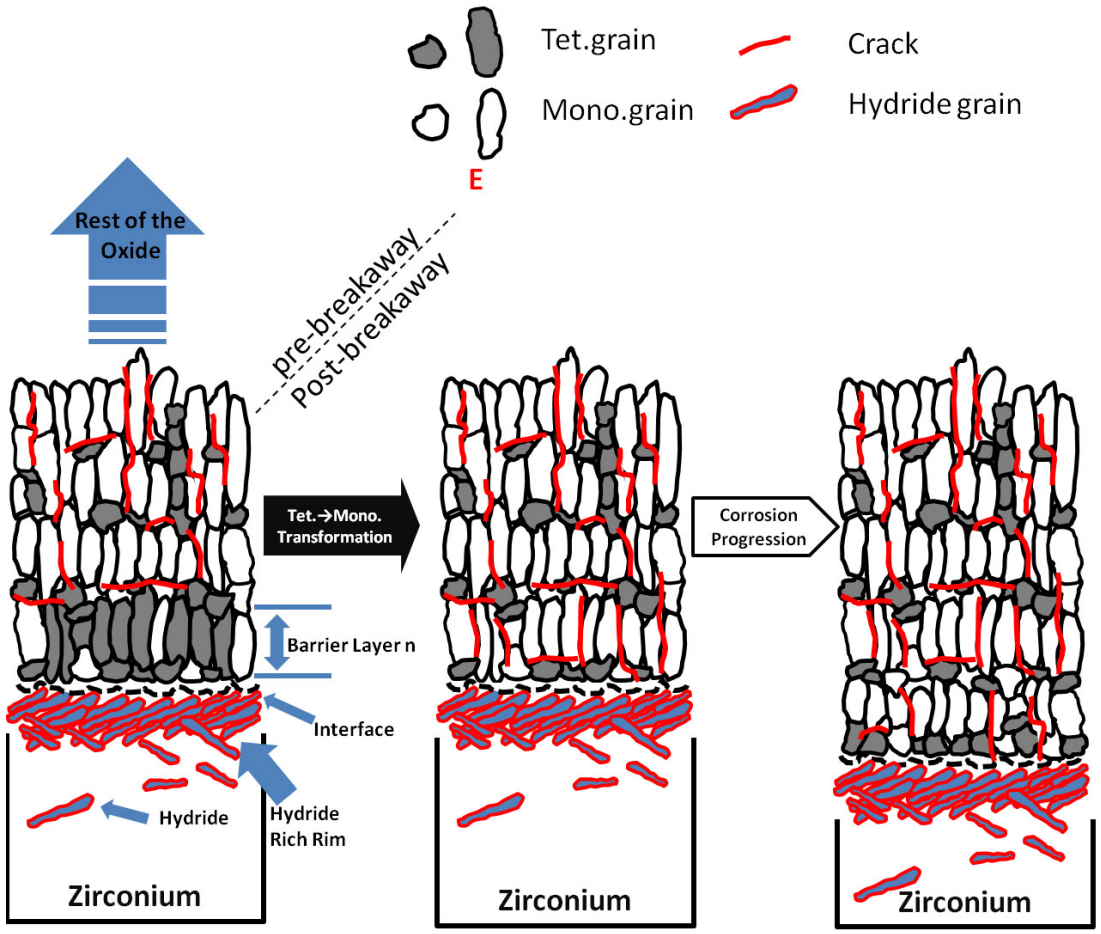

Figure 42: Schematic description of stage E breakaway. The amount of tetragonal, monoclinic, hydrides and cracks are only schematic, not quantitative representation.

The critical aspects of this model are:

- The distinction between barrier layer and the tetragonal rich layer.
- There are two populations of tetragonal grains depending on different stabilisation mechanisms.

It is predicated that corrosion performance can be improved by eliminating the tetragonal grains, which depend on the combined stabilisation of compressive stress and tetragonal stabilisers such as tin. The predication is supported by observations from both publication No.3 and publication No.4 where better corrosion performance and fewer tetragonal phases are associated with low tin alloys. Direct microstructural evidence is currently lacking. Combined with Focused Ion Beam (FIB) sample lift-out and Fresnel Contrasting method, TEM is considered as a feasible technique capable of the required resolution and magnification. The real difficulty is how to validate the observations after the presence of such proposed microstructure has been confirmed or rejected: sample preparation always introduces direct damage to the oxide; the creation of a free surface also relaxes the residual stress, causing phase transformation which generates porosities and cracks and damages the integrity of the oxide. It should be emphasized that microstructural characterisation via electron microscopy always requires the creation of a free surface. Hence, it seems impossible to use such technique to observe stress stabilised tetragonal oxide grains. The only tetragonal oxide grains observed by electron microscopy should be the ones stabilised by grain size.

6 Conclusion

The main goals of this research project were:

- Facilitate a data base with information regarding the corrosion performance of a number of engineering and experimental zirconium alloys.
- Provide ready to use corroded specimens for future research projects on the aqueous corrosion of zirconium alloys.
- Develop techniques capable of characterising the oxide regarding microstructure, residual stress state and phase information.
- Provide a mechanistic explanation for the detrimental effect of hydrides upon the corrosion performance of zirconium alloys.

The following are the outputs:

- Cathodic hydrogen charging technique has been explored to provide prior corrosion samples simulating end-of-life conditions of in-pile zirconium claddings. Cathodic hydrogen charging is sensitive to the chemistry of the charging solution. The layout and geometry of the charging cell also strongly influence the hydriding process by altering the distribution of potential field surrounding the sample. To date, sheet samples are considered undesirable as raw material for hydriding. Tube samples were hydrided successfully to form a dense hydride rim at the outer surface. In the present study, the hydride rim is predominately δ-hydride with local hydrogen concentration around 11,000 wt.ppm, in good agreement with hydrogen concentration measured in the rim region of actual end-of-life claddings from nuclear

reactor. Hydride phase in the rim region is slightly under compression while the neighbouring metal phase is slightly under tension. The stresses are considered to be the combination of remaining residual stresses from hydride formation and thermal stresses due to difference in thermal expansion coefficient.

- A series of autoclave loading plans were designed to accommodate up to 336 specimens in each autoclave chamber. The loading plans take into consideration the even distribution of specimens and potential temperature variation during prolonged exposure. A data base for autoclave corrosion performance of a series of reference and hydrided zirconium alloys was established. The data base covers 6 alloys from 2 different suppliers, 3 heat treatment conditions and 2 test piece geometries. Autoclave corrosion history of individual samples was recorded. Data includes the exposure duration before 1st transition, oxidation weight gain profile and photograph of individual samples. Reference samples exhibit the typical corrosion kinetics. Since Pre-1st transition corrosion kinetics is similar for different alloys, exposure time before 1st transition becomes the factor dominating the corrosion performance. The rate exponents n were measured around 1/3, suggesting a near cubic growth rate. In tubes, ZIRLO^{TM}, low tin ZIRLO and X2 exhibit dramatic delay of transition with decreasing tin content. In sheets, Zircaloy-4 commences 1st transition after an exposure similar to that of ZIRLO^{TM}. In both sheets and tubes, materials in SR condition generally experience 1st transition earlier than materials in RX condition. Pre-1st transition samples have black oxide appearance. Post-1st transition samples

have grey oxide appearance. During-transition samples have both grey and black patches on surface.

- Although nearly all hydrided materials exhibited slower oxidation rates than their reference during very early stage of corrosion, hydrided materials generally exhibited accelerated corrosion rates. The extent to which the material is susceptible to corrosion acceleration depends on the alloys' chemistry and heat treatment conditions. Alloys with higher tin content are more susceptible to corrosion acceleration by hydrogen charging than low tin alloys. Alloys in SR conditions are more sensitive to this deterioration than those in pRX and RX conditions. In both hydrided and reference materials, a clear relationship is established between the rate constant K_p and kinetic exponent n, regardless of the alloys' chemistry and heat treatment condition. Hydrided materials with higher rate exponent n tend to have a more greyish oxide appearance.
- Oxide grown on hydrided ZIRLO^{TM} has extensive cracks connected to the outer surface. Oxide grown on hydrided low-tin ZIRLO has thin regions of oxide with small internal cracks and localised thick regions with extensive opening cracks. Oxide grown on hydrided X2 has practically no cracks even after extended corrosion.
- Synchrotron experiments revealed that the oxide is generally under biaxial compression. In the case of the two ZIRLO variants: ZIRLO^{TM} and low tin ZIRLO, -700 to -1000 MPa compressive stresses are measured in monoclinic phase of reference samples while tetragonal stresses are between -1500 to -2000 MPa. Monoclinic stresses measured in grey/white regions of hydrided

samples are generally lower. Tetragonal stresses in hydrided and reference ZIRLO™ and low-tin ZIRLO samples are similar to the required -2000 MPa for tetragonal ZrO_2 stabilization regardless of oxide colour and weight gain. In the case of X2, stresses of -500 to -900 MPa were measured in the monoclinic oxide of reference and hydrided samples. Tetragonal stresses measured in both hydrided and reference X2 materials are similar to monoclinic stresses.

- It is assumed that stress stabilisation of tetragonal oxide phase is only possible in combination with some chemical stabilisation, which in the present study is tin. When compared with black oxide grown on either reference or hydrided samples, grey/white oxide grown on hydrided samples generally contains smaller fractions of tetragonal phase as well as less crystallographically-aligned grains. It is also speculated that in hydrided material with high tin content, less aligned oxide grains are less likely to grow epitaxially into protective columnar shape. The reduced residual stress level also reduces the ability of those do grow to maintain tetragonal structure if they started out as such. The above mechanisms together contribute to the formation of less protective oxide.
- The dramatic difference between corrosion performance of hydrogen charged ZIRLO™, low tin ZIRLO and X2 potentially arises from the local depletion of hydrides in the rim. At the moment, the mechanism behind this depletion and the effect of tin on the ability of hydrogen to diffuse away from the rim remains elusive.

7 Future Works

The author would like to suggest the following areas for future study:

1. Continuation of autoclave corrosion experiments on reference samples. The model has predicated that alloy with low tin content is less susceptible to tetragonal to monoclinic phase transformation. This potentially leads to much later or even no breakaway. Corrosion experiments exceeding the onset of breakaway corrosion are required to validate or disprove this claim.
2. Continuation of autoclave corrosion experiments on hydrided samples. The model considers the detrimental effect of hydride rim as the result of lowered compressive stress and nucleation of less crystallographically-aligned grains. A deceleration of corrosion rate is expected when the artificially introduced hydride rim has been completely consumed. The increase of compressive stress in the oxide and enhancement of oxide texture are also expected. Corrosion experiments exceeding 400 mg/dm^2 of weigh gain are suggested.
3. Integrity of the oxide layer especially in the case of hydrided ZIRLO^{TM} has been questioned. It is necessary to check for potential oxide fallen off by filtering the simulated primary water from autoclaves.
4. Characterization of oxide crystallite structure, pores and tiny cracks. The investigation should be conducted on pre- and post-transition reference samples as well as black and grey patches of hydrided samples. ZIRLO^{TM} and X2 are of special interest. Combined with Focused Ion Beam (FIB) sample lift-out and Fresnel Contrasting method, HR-TEM is potentially the most feasible technique with the required resolution and magnification. Care must be taken

during sample preparation since the fabrication of TEM thin films can potentially facilitate the exact features being looked for.

5. The proposed inter-connected crack network after transition needs to be validated. The author proposes FIB sectioning of the oxide followed by SEM imaging and 3D computer reconstruction. FIB tends to remove material preferentially around edges, i.e. cracks and porosities, while the creation of a free surface is accompanied by residual stress relaxation. It can potentially boost the SEM contrast in pores and small cracks. HR-TEM and FIB sectioning can act as sensitivity measures for each other. Cracks and pores are more likely to be artifacts if they can only be observed with one technique. It is also suggested that TEM sample lift-out should be conducted at the end of each FIB sectioning session, thus investigating the same region.
6. Laboratory and synchrotron X-ray tomography of the oxide. It is understood that nanometre sized pores and cracks are only visible under the magnification and resolution range of TEM, but tomography provides the potential of characterising relatively bigger cracks in a less destructive way. The high magnification still involves sample preparation and subsequent relaxation to certain degree. Samples of difference sizes (hence different magnifications) should be used as sensitivity measure.

8 References

[1] F.W. Boulger, The Properties of Zirconium, Report AECD-2726, 1949, U.S.A.E.C.
[2] D.O. Pickman, Zirconium Alloy Performance in Light Wateer Reactors: A Review of UK and Scandanavian Experience, in: A.M. Garde, E.R. Bradley (Eds.) 10th International Symposium on Zirconium in the Nuclear Industry, 1994, ASTM International, Baltimore, MD, pp.19-32.
[3] B. Cox, Some Thoughts on the Mechanisms of In-Reactor Corrosion of Zirconium Alloys, Journal of Nuclear Materials, (336), 2005: pp.331-368.
[4] B. Cox, Y.M. Wong, A Hydrogen Uptake Micro-Mechanism for Zr Alloys, Journal of Nuclear Materials, (270), 1999: pp.134-146.
[5] A.T. Motta, et al., Synchrotron Radiation Study of Second-Phase Particles and Alloying Elements In Zirconium Alloys, in: G.D. Moan, P. Rudling (Eds.) 13th International Symposium on Zirconium in the Nuclear Industry, 2002, ASTM International, Annecy, France, pp.59-79.
[6] F.E. Bowman, D.D. Cubicciotti, Use of Zirconium in Liquid-Sodium Systems, American Institute of Chemical Engineers Journal, (2), 1956: pp.173-176.
[7] G.P. Sabol, ZIRLO^{TM} - An Alloy Development Success, in: P. Rudling, K. B (Eds.) 14th International Symposium on Zirconium in the Nuclear Industry, 2005, ASTM International, Stockholm, Sweden, pp.2-24.
[8] E.C. Miller, Zirconium: A Structural Material for Nuclear Reactors, Nucleonics (U.S.), (11), 1953: pp.27-31.
[9] B. Lustman, F. Kerze, The Metallurgy of zirconium, 1st ed., National Nuclear Energy series, Div. 7, v. 4, 1955, McGraw-Hill, New York.
[10] A.D. Schwope, A General Comparison of the Metallurgy of Zirconium with that of Better Known Commercial Metals, in: Zirconium and Zirconium alloys, American Society for Metals, Cleverland, 1953, pp.162-180.
[11] D.G. Franklin, P.M. Lang, Zirconium-Alloy Corrosion: A Review Based on an International Atomic Energy Agency (IAEA) Meeting, in: 9th International Symposium on Zirconium in the Nuclear Industry, 1990, ASTM International, pp.3-29.
[12] H.G. Rickover, et al., History of the Development of Zirconium Alloys for use in Nuclear Reactors, 1975, Division of Naval Reactors, Washington DC.
[13] B. Cox, The Effects of Some Alloying Additions on the Oxidation of Zirconium in Steam, Report AERE-R4458, 1963, U.A.E. Authority.
[14] B. Cox, The Oxidation and Corrosion of Zirconium and Its Alloys, Journal of Electrochemical Society, 1961: pp.24-30.
[15] P. Barberis, Zirconia Powders and Zircaloy Oxide Films: Tetragonal Phase Evolution During 400°C Autoclave Tests, Journal of Nuclear Materials, (226), 1995: pp.34-43.
[16] H.-J. Beie, et al., Examinations of the Corrosion Mechanism of Zirconium Alloys, in: A.M. Garde, E.R. Bradley (Eds.) 10th International Symposium on Zirconium in the Nuclear Industry, 1994, ASTM International, Baltimore, MD, pp.615-643.

[17] M. Harada, et al., Effect of Alloying Elements on Uniform Corrosion Resistance of Zirconium-Based Alloy in 360°C Water and 400°C Steam, in: C.M. Eucken, A.M. Garde (Eds.) 9th International Symposium on Zirconium in the Nuclear Industry, 1991, ASTM International, Kobe, Japan, pp.368-390.
[18] J.P. Mardon, et al., Optimization of PWR Behavior of Stress-Relieved Zircaloy-4 Cladding Tubes by Improving the Manufacturing and Inspection Process, in: A.M. Garde, E.R. Bradley (Eds.) 10th International Symposium on Zirconium in the Nuclear Industry, 1994, ASTM International, Baltimore, MD, pp.328-347.
[19] K. Takeda, H. Anada, Mechanism of Corrosion Rate Degradation Due to Tin, in: G.P. Sabol, G.D. Moan (Eds.) 12th International Symposium on Zirconium in the Nuclear Industry, 2000, ASTM International, Toronto, Canada, pp.592-608.
[20] M. Tupin, et al., Oxidation Kinetics of ZrNbO in Steam: Differences Between the Preand Post-Transition Stages, Journal of Nuclear Materials, (342), 2005: pp.108-118.
[21] W. Liu, et al., Effect of Heat Treatment on the Microstructure and Corrosion Resistance of a Zr-Sn-Nb-Fe-Cr Alloy, Journal of Nuclear Materials, (341), 2005: pp.97-102.
[22] H.G. Kim, et al., Corrosion and Microstructural Characteristics of Zr–Nb Alloys with Different Nb Contents, Journal of Nuclear Materials, (373), 2008: pp.429-432.
[23] A.T. Motta, et al., Microstructure and Growth Mechanism of Oxide Layers Formed on Zr Alloys Studied with Micro-Beam Synchrotron Radiation, in: P. Rudling, B. Kammenzind (Eds.) 14th International Symposium on Zirconium in the Nuclear Industry, 2004, ASTM International, Stockholm, Sweden, pp.205-232.
[24] A. Yilmazbayhan, et al., Structure of Zirconium Alloy Oxides Formed in Pure Water Studied with Synchrotron Radiation and Optical Microscopy: Relation to Corrosion Rate, Journal of Nuclear Materials, (324), 2004: pp.6-22.
[25] A. Yilmazbayhan, et al., Transmission Electron Microscopy Examination of Oxide Layers Formed on Zr Alloys, Journal of Nuclear Materials, (349), 2006: pp.265-281.
[26] M.M.R. Howlader, et al., The Electrical Conductivity of Zircaloy Oxide Films, Journal of Nuclear Materials, (253), 1998: pp.149-155.
[27] J.H. Schemel, ASTM Manual on Zirconium and Hafnium, Vol.ASTM STP 639, 1st ed., 1977, American Society for Materials Testing, West Conshohocken.
[28] H.-J. Sell, et al., Effects of Alloying Elements and Impurities on in-BWR Corrosion of Zirconium Alloys, in: P. Rudling, B. Kammenzind (Eds.) 14th International Symposium on Zirconium in the Nuclear Industry, 2004, ASTM International, pp.404-417.
[29] M. Steinbrück, Hydrogen Absorption by Zirconium Alloys at High Temperatures, Journal of Nuclear Materials, (334), 2004: pp.58-64.
[30] J.P. Mardon, et al., Influence of Composition and Fabrication Process on Out-of-Pile and In-Pile Properties of M5 Alloy, in: G.P. Sabol, G.D. Moan (Eds.) 12th International Symposium on Zirconium in the Nuclear Industry, 2000, ASTM International, pp.505-524.
[31] R.J. Comstock, et al., Influence of Processing Variables and Alloy Chemistry on the Corrosion Behavior of ZIRLO Nuclear Fuel Cladding, in: E.R. Bradley, G.P. Sabol (Eds.) 11th International Symposium on Zirconium in the Nuclear Industry, 1996, ASTM International, pp.710-725.

[32] S.V. Ivanova, Effect of Hydrogen on Serviceability of Zirconium Items in VVER and RBMK-Type Reactors Fuel Assemblies, International Journal of Hydrogen Energy, (27), 2002: pp.819-824.
[33] G.L. Miller, Zirconium, Metallurgy Of The Rarer Metals, 1954, Butterworths Scientific Publications, London.
[34] E. Hillner, et al., Long-Term Corrosion of Zircaloy Before and After Irradiation, Journal of Nuclear Materials, (278), 2000: pp.334-345.
[35] T. Arima, et al., Oxidation Properties of Zr-Nb Alloys at 500-600 °C under Low Oxygen Potentials, Corrosion Science, (47), 2005: pp.435-446.
[36] T. Arima, et al., Oxidation Kinetics of Zircaloy-2 Between 450°C and 600°C in Oxidizing Atmosphere, Journal of Nuclear Materials, (257), 1998: pp.67-77.
[37] J.S. Bryner, The Cyclic Nature of Corrosion of Zircaloy-4 in 633 K Water, Journal of Nuclear Materials, (82), 1979: pp.84-101.
[38] B. Cox, Comments on "Aqueous Corrosion of the Zircaloys at Low Temperatures", Journal of Nuclear Materials, (30), 1969: pp.351-352.
[39] B. Griggs, et al., Multiple Rate Transitions in the Aqueous Corrosion of Zircaloy, Journal of The Electrochemical Society, (109), 1962: pp.665-668.
[40] K. Hauffe, Oxidation of Metals, 2nd ed., 1965, Plenum Press, Inc., New York.
[41] S. Kass, The Development of the Zircaloys, in: Corrosion of Zirconium Alloys at ANS Winter meeting, 1964, ASTM International, San Francisco, U.S.A, pp.3-27.
[42] S. Kass, Aqueous Corrosion of the Zircaloys at Low Temperatures, Journal of Nuclear Materials, (29), 1969: pp.315-321.
[43] A.A. Kiselev, et al., Corrosion of Reactor Materials, Vol.2, 1962, International Atomic Energy Agency, Vienna
[44] A.T. Motta, et al., Micostructural Characterisation of Oxides Formed on Model Zr Alloys Using Synchrotron Radiation, in: B. Kammenzind, M. Limback (Eds.) 15th International Symposium on Zirconium in the Nuclear Industry, 2009, ASTM International, Sunriver Resort Oregon, USA, pp.486-506.
[45] G.P. Sabol, S.B. Dalgaard, The Origin of the Cubic Rate Law in Zirconium Alloy Oxidation, Journal of The Electrochemical Society, (122), 1975: pp.316-317.
[46] B. Cox, C. Roy, Transport of Oxygen in Oxide Films on Zirconium Determined by the Nuclear Reaction O^{17} (He^{3}, α) O^{16}, Electrochemistry Technology, (4), 1966: pp.121-127.
[47] B. Cox, J.P. Pemsler, Diffusion of Oxygen in Growing Zirconia Films, Journal of Nuclear Materials, (28), 1968: pp.73-78.
[48] B. Cox, in: M.G. Fontana, R.W. Staehle (Eds.) Advances in Corrosion Science and Technology, Plenum, New York, 1976, pp.173.
[49] P. Bossis, et al., Comparison of the High Burn-Up Corrosion on M5 and Low Tin Zircaloy-4, in: P. Rudling, B. Kammenzind (Eds.) 14th International Symposium on Zirconium in the Nuclear Industry, 2005, ASTM International, Stockholm, Sweden, pp.494-525.
[50] P. Bouvier, et al., A Raman Study of the Nanocrystallite Size Effect on the Pressure-Temperature Phase Diagram of Zirconia Grown by Zirconium-Based Alloys Oxidation, Journal of Nuclear Materials, (300), 2002: pp.118-126.
[51] A.M. Garde, Enhancement of Aqueous Corrosion of Zircaloy-4 Due to Hydride Precipitation at the Metal-Oxide Interface, in: C.M. Eucken, A.M. Garde (Eds.) 9th

International Symposium on Zirconium in the Nuclear Industry, 1991, ASTM International, Kobe, Japan, pp.566-592.
[52] J. Godlewski, How the Tetragonal Zirconia is Stabilized in the Oxide Scale that is Formed on a Zirconium Alloy Corroded at 400°c in Steam, in: A.M. Garde, E.R. Bradley (Eds.) 10th International Symposium on Zirconium in the Nuclear Industry, 1994, ASTM International, Baltimore, MD, pp.663-683.
[53] H.R. Peters, Improved Characterization of Aqueous Corrosion Kinetics of Zircaloy-4, in: D.G. Franklin, R.B. Adamson (Eds.) 6th International Symposium on Zirconium in the Nuclear Industry, 1984, ASTM International, Vancouver, British Columbia, Canada, pp.507-519.
[54] V. Busser, et al., Modelling of Corrosion Induced Stresses during Zircaloy-4 Oxidation in Air, Materials Science Forum, (595-598), 2008: pp.419-427.
[55] M. Preuss, et al., Towards a Mechanistic Understanding of Corrosion Mechanisms in Zirconium Alloys, in: 16th International Symposium on Zirconium in the Nuclear Industry, 2010, ASTM International ChengDu, P.R.China.
[56] J. Godlewski, et al., Raman Spectroscopy Study of the Tetragonal-to-Monoclinic Transition in Zirconium Oxide Scales and Determination of Overall Oxygen Diffusion by Nuclear Microanalysis of O^{18}, in: C.M. Eucken, A.M. Garde (Eds.) 9th International Symposium on Zirconium in the Nuclear Industry, 1991, ASTM International, Kobe, Japan, pp.416-436.
[57] D. Pecheur, et al., Microstructure of Oxide Films Formed during the Waterside Corrosion of the Zircaloy-4 Cladding in Lithiated Environment, in: E.R. Bradley, G.P. Sabol (Eds.) 11th International Symposium on Zirconium in the Nuclear Industry, 1996, ASTM International, Garmisch-Partenkirchen, Germany, pp.94-113.
[58] B. Cox, Pore Structure in Oxide Films on Irradiated and Unirradiated Zirconium Alloys, Journal of Nuclear Materials, (148), 1987: pp.332-343.
[59] N. Ni, et al., Porosity in Oxides on Zirconium Fuel Cladding Alloys, and Its Importance in Controlling Oxidation Rates, Scripta Materialia, (62), 2010: pp.564-567.
[60] H. Anada, et al., Effect of Annealing Temperature on Corrosion Behavior and ZrO_2 Microsturcture of Zircaloy-4 Cladding Tube, in: C.M. Eucken, A.M. Garde (Eds.) 11th International Symposium on Zirconium in the Nuclear Industry, 1996, ASTM International, Garmisch-Partenkirchen, Germany, pp.74-93.
[61] C. Lemaignan, Corrosion of Zirconium Alloy Components in Light Water, Vol.13C, ASM Handbook, 2006, ASM International, Ohio.
[62] A.J.G. Maroto, et al., Growth and Characterization of Oxide Layers on Zirconium Alloys, Journal of Nuclear Materials, (229), 1996: pp.79-92.
[63] B. Lustman, Effect of Nitrogen and Carbon on the Corrosion of Zirconium in 600°F water, Report WAPD-RM-17, 1950, W.E. Corp.
[64] D.S. Kneppel, T.T. Magel, Beneficial Effect of Alloy Additions to Zirconium on the Corrosion Resistance in 600°F water, in: Proc. AEC Metallurgy Conference, 1952.
[65] R.J. Comstock, Zr-1Nb-0.2Ti Weight Gain Data, 2009, W.E. Corp.
[66] R.J. Comstock, Zr-1Nb Weight Gain Data, 2009, W.E. Corp.
[67] E. Hillner, Corrosion of Zirconium-Base Alloys - An Overview, in: A.L. Lowe, G.W. Parry (Eds.) 3rd International Symposium on Zirconium in the Nuclear Industry, 1977, ASTM International, Quebec, Canada, pp.211-235.

[68] B. Cox, Effects of Irradiation on the Oxidation of Zirconium Alloys in High Temperature Aqueous Environments: A Review, Journal of Nuclear Materials, (28), 1968: pp.1-47.
[69] J.P. Abriata, et al., O - Zr Phase Diagram, in: T.B. Massalski, H. Okamoto, P.R. Subramanian, L. Kacprzak (Eds.) Binary Alloy Phase Diagrams, William W. Scott, Jr., 1990, pp.2940 - 2941.
[70] B. Cox, Are Zirconium Corrosion Films a Form of Partially Stablized Zirconia?, Report AECL-9382, 1987, C.R.N.L. Reactor Materials Division, Chalk River, Ontario.
[71] J. Godlewski, et al., Stress Distribution Measured by Raman Spectroscopy in Zirconia Films Formed by Oxidation of Zr-Based Alloys, in: G.P. Sabol, G.D. Moan (Eds.) 12th International Symposium on Zirconium in the Nuclear Industry, 2000, ASTM International, Toronto, Canada, pp.877-899.
[72] C.M. Schwartz, et al., Identification and Growth of Oxide Films on Zirconium in High-Temperature Water, Report BMI-793, 1955, C. Battelle Memorial Inst., Ohio.
[73] A.H. Heuer, M. Rühle, Overview no. 45: On the Nucleation of the Martensitic Transformation in Zirconia (ZrO_2), Acta Metallurgica, (33), 1985: pp.2101-2112.
[74] H.S. Maiti, et al., Kinetics and Burst Phenomenon in ZrO_2 Transformation, Journal of the American Ceramic Society, (55), 1972: pp.317-322.
[75] G.M. Wolten, Diffusionless Phase Transformations in Zirconia and Hafnia, Journal of the American Ceramic Society, (46), 1963: pp.418-422.
[76] W. Wei-E, D.R. Olander, U-O and Zr-O Thermochemistry from the Pure Metal to the Dioxide and Application to Core-Concrete Interactions in Severe Fuel Damage Accident Analysis, Journal of Nuclear Materials, (201), 1993: pp.231-237.
[77] C. Roy, B. Burgess, A Study of the Stresses Generated in Zirconia Films During the Oxidation of Zirconium Alloys, Oxidation of Metals, (2), 1970: pp.235-261.
[78] S. Block, et al., Pressure-Temperature Phase Diagram of Zirconia, Journal of the American Ceramic Society, (68), 1985: pp.497-499.
[79] A.P. Zhilyaev, J.A. Szpunar, Influence of Stress Developed due to Oxide Layer Formation on the Oxidation Kinetics of Zr-2.5%Nb Alloy, Journal of Nuclear Materials, (264), 1999: pp.327-332.
[80] M. Blat-Yrieix, et al., Toward a Better Understanding of Dimensional Changes in Zircaloy-4: What is the Impact Induced by Hydrides and Oxide Layer?, Journal of ASTM International (JAI), (5), 2008: pp.1-16.
[81] M. Oskarsson, et al., Characterisation of Pre-Transition Oxides on Zircaloys, Journal of Nuclear Materials, (297), 2001: pp.77-88.
[82] P. Li, et al., Effect of Dopants on Zirconia Stabilization—An X-ray Absorption Study: I, Trivalent Dopants, Journal of the American Ceramic Society, (77), 1994: pp.118-128.
[83] D.-J. Kim, et al., Effect of Tetravalent Dopants on Raman Spectra of Tetragonal Zirconia, Journal of the American Ceramic Society, (80), 1997: pp.1453-1461.
[84] P. Li, et al., Effect of Dopants on Zirconia Stabilization—An X-ray Absorption Study: II, Tetravalent Dopants, Journal of the American Ceramic Society, (77), 1994: pp.1281-1288.
[85] R. Collongues, et al., Etude de la Zircone A Température Au-Dessus de 2000K, Colloque. Int. CNRS, (205), 1971: pp.241-246.

[86] J.B.M. Steinbrück, et al., Status of Studies on High-Temperature Oxidation and Quench Behaviour of Zircaloy-4 and E110 Cladding Alloys, in: The third European Review Meeting on Severe Accident Research, 2008, Nesseber, Bulgaria.
[87] F. Garzarolli, et al., Oxide Growth Mechanism on Zirconium Alloys, in: C.M. Eucken, A.M. Garde (Eds.) 9th International Symposium on Zirconium in the Nuclear Industry, 1990, ASTM International, Kobe, Japan, pp.395-415.
[88] G. Lelièvre, et al., Characterisation by Neutron Diffraction in High Temperature Pressurised Water of the Surface Corrosion and Hydrogen Embrittlement of Zircaloy-4, Journal of Alloys and Compounds, (347), 2002: pp.288-294.
[89] N. Pétigny, et al., In-situ XRD Analysis of the Oxide Layers Formed by Oxidation at 743 K on Zircaloy 4 and Zr–1NbO, Journal of Nuclear Materials, (280), 2000: pp.318-330.
[90] B. Wadman, et al., Microstructure of Oxide Layers Formed During Autoclave Testing of Zirconium Alloys, in: A.M. Garde, E.R. Bradley (Eds.) 10th International Symposium on Zirconium in the Nuclear Industry, 1993, ASTM International, Baltimore, MD, pp.579-598.
[91] A.H. Heuer, et al., Stability of Tetragonal ZrO2 Particles in Ceramic Matrices, Journal of the American Ceramic Society, (65), 1982: pp.642-650.
[92] B.C. Muddle, R.H.J. Hannink, Crystallography of the Tetragonal to Monoclinic Transformation in MgO-Partially-Stabilized Zirconia, Journal of the American Ceramic Society, (69), 1986: pp.547-555.
[93] J.-Y. Park, et al., Crystal Structure and Grain Size of Zr Oxide Characterized by Synchrotron Radiation Microdiffraction, Journal of Nuclear Materials, (335), 2004: pp.433-442.
[94] Y.H. Jeong, et al., Effect of β phase, Precipitate and Nb-Concentration in Matrix on Corrosion and Oxide Characteristics of Zr–xNb Alloys, Journal of Nuclear Materials, (317), 2003: pp.1-12.
[95] G. Wikmark, et al., The Importance of Oxide Morphology for the Oxidation Rate of Zirconium Alloys, in: E.R. Bradley, G.P. Sabol (Eds.) 11th International Symposium on Zirconium in the Nuclear Industry, 1996, ASTM International, Garmisch-Partenkirchen, Germany, pp.55-73.
[96] J. Chirigos, D.E. Thomas, The Mechanism of Oxidation and Corrosion of Zirconium, in: Proc.AEC Metallurgy Conf, 1952, pp.337.
[97] U.R. Evans, The Mechanism of Oxidation and Tarnishing, Transactions of The Electrochemical Society, (91), 1947: pp.547-572.
[98] K. Hauffe, The Mechanism of Oxidation of Metals and Alloys at High Temperature, in: B. Chalmers (Ed.) Progress in Metal Physics, Interscience, New York, 1953, pp.71.
[99] J.K. Dawson, et al., Observations on the Early Stages of Oxidation of Zirconium and Zircaloy-2, Electrochemical Technology, (4), 1966: pp.137-142.
[100] A.T. Donaldson, H.E. Evaaans, Oxidation-Induced Creep in Zircaloy-2: I. Basic Observations, Journal of Nuclear Materials, (99), 1981: pp.38-46.
[101] A.T. Donaldson, H.E. Evans, Oxidation-Induced Creep in Zircaloy-2: II. Stress Distribution in the Oxygen-Stabilised α-Phase Layer, Journal of Nuclear Materials, (99), 1981: pp.47-56.

[102] A.T. Donaldson, H.E. Evans, Oxidation-Iinduced Creep in Zircaloy-2: III. The Average Stress in the Oxide Layer, Journal of Nuclear Materials, (99), 1981: pp.57-65.
[103] J.K. Dawson, et al., The Kinetics and Mechanism of the Oxidation of Zircaloy-2 at 350–500 °C, Journal of Nuclear Materials, (25), 1968: pp.179-200.
[104] B. Cox, Some Effects of Pressure on the Oxidation of Zircaloy-2 in Steam and Oxygen, Journal of the Less Common Metals, (5), 1963: pp.325-336.
[105] B. Cox, et al., Waterside Corrosion of Zirconium Alloys in Nuclear Power Plants, Report TECDOC-996, 1998, IAEA.
[106] H.K. Yueh, B. Cox, Cathodoluminescence Imaging of Oxidised Zirconium Alloys, Journal of Nuclear Materials, (324), 2004: pp.203-214.
[107] A.G. Evans, J.W. Hutchinson, On the Mechanics of Delamination and Spalling in Compressed Films, International Journal of Solids and Structures, (20), 1984: pp.455-466.
[108] Y. Nishino, et al., Formation and Dissolution of Oxide Film on Zirconium Alloys in 288°C Pure Water under γ-ray Irradiation, Journal of Nuclear Materials, (248), 1997: pp.292-298.
[109] X. Guo, Hydrothermal Degradation Mechanism of Tetragonal Zirconia, Journal of Materials Science, (36), 2001: pp.3737-3744.
[110] M. Hirano, Inhibition of Low Temperature Degradation of Tetragonal Zirconia Ceramics. A Review, British Ceramic Transactions, (91), 1992: pp.139-147.
[111] M. Yoshimura, Phase Stability of Zirconia, American Ceramic Society Bulletin, (67), 1988: pp.1950-1955.
[112] H. Coriou, et al., Corrosion du Zircaloy Dans Divers Milieux Alcalins a Haute Temperature, Journal of Nuclear Materials, (7), 1962: pp.320-327.
[113] B. Cox, et al., Mechanisms of LiOH Degradation and H_3BO_3 Repair of ZrO_2 Film, in: E.R. Bradley, G.P. Sabol (Eds.) 11th International Symposium on Zirconium in the Nuclear Industry, 1996, ASTM International, Garmisch-Partenkirchen, Germany, pp.114 - 136.
[114] M. Oskarsson, et al., Phase Transformation of Stabilised Zirconia in Water and 1.0 M LiOH, Journal of Nuclear Materials, (295), 2001: pp.126-130.
[115] R.A. Ploc, S.B. Newcomb, Microscopy of Oxidation 3, in: S.B. Newcomb, J.A. Little (Eds.) Third International Conference on the Microscopy of Oxidation, 1996, Institute of Materials, Minerals and Mining, Trinity Hall, Cambridge, pp.475-487.
[116] M. Skovgaard, et al., Effect of Microscale Shear Stresses on the Martensitic Phase Transformation of Nanocrystalline Tetragonal Zirconia Powders, Journal of the European Ceramic Society, (30), 2010: pp.2749-2755.
[117] J.C. Clayton, Out-of-Pile Nickel Alloy-Induced Accelerated Hydriding of Zircaloy Fasteners, in: D.G. Franklin, R.B. Adamson (Eds.) 6th International Symposium on Zirconium in the Nuclear Industry, 1982, ASTM International, Vancouver, British Columbia, Canada, pp.572-591.
[118] A.M. Garde, et al., In-PWR Irradiation Performance of Dilute Tin-Zirconium Advanced Alloys, in: G.D. Moan, P. Rudling (Eds.) 13th International Symposium on Zirconium in the Nuclear Industry, 2002, ASTM International, Annecy, France, pp.490-506.
[119] B.F. Kammenzind, et al., Hydrogen Pickup and Redistribution in Alpha-Annealed Zircaloy-4, in: E.R. Bradley, G.P. Sabol (Eds.) 11th International

Symposium on Zirconium in the Nuclear Industry, 1996, ASTM International, Garmisch-Partenkirchen, Germany, pp.338-370.
[120] J.J. Kearns, Terminal Solubility and Partitioning of Hydrogen in the Alpha Phase of Zirconium, Zircaloy-2 and Zircaloy-4, Journal of Nuclear Materials, (22), 1967: pp.292-303.
[121] A. Mcminn, et al., The Terminal Solid Solubility of Hydrogen in Zirconium Alloys, in: G.P. Sabol, G.D. Moan (Eds.) 12th International Symposium on Zirconium in the Nuclear Industry, 2000, ASTM International, Toronto, Canada, pp.173-196.
[122] S. Yamanaka, et al., Study on the Hydrogen Solubility in Zirconium Alloys, Journal of Nuclear Materials, (247), 1997: pp.315-321.
[123] Y.S. Kim, et al., A Model of the Threshold Stress Intensity Factor, KIH, for Delayed Hydride Cracking of Zr–2.5Nb Alloy, Journal of Nuclear Materials, (278), 2000: pp.251-257.
[124] C. Anghel, Modified Oxygen and Hydrogen Transport in Zr-Based Oxides, in: KTH, School of Industrial Engineering and Management (ITM), Materials Science and Engineering, 2006, KTH, Stockholm, pp.48.
[125] B. Cox, A Mechanism for the Hydrogen Uptake Process in Zirconium Alloys, Journal of Nuclear Materials, (264), 1999: pp.283-294.
[126] E. Hillner, Hydrogen Absorption in Zircaloy during Aqueous Corrosion: Effect of Environment, Report WAPD-TM-411, 1964, U.S.A.E.C.
[127] K.M. Goldman, D.E. Thomas, Hydrogen Pickup during Corrosion on Testing of Zirconium, Report WAPD-MM-184, 1953, U.S.A.E.C.
[128] C. Andrieu, et al., Release of Fission Tritium Through Zircaloy-4 Fuel Cladding Tubes, Journal of Nuclear Materials, (347), 2005: pp.12-19.
[129] P. Rudling, G. Wikmark, A Unified Model of Zircaloy BWR Corrosion and Hydriding Mechanisms, Journal of Nuclear Materials, (265), 1999: pp.44-59.
[130] P. Bossis, et al., Multi-Scale Characterization of the Metal-Oxide Interface of Zirconium Alloys, in: G.P. Sabol, G.D. Moan (Eds.) 12th International Symposium on Zirconium in the Nuclear Industry, 2000, ASTM International, Toronto, Canada, pp.918-945.
[131] N. Ramasubramanian, et al., Hydrogen Transport in the Oxide and Hydrogen Pickup by the Metal During Out- and In-Reactor Corrosion of Zr-2.5Nb Pressure Tube Material, in: G.P. Sabol, G.D. Moan (Eds.) 12th International Symposium on Zirconium in the Nuclear Industry, 2000, ASTM International, Toronto, Canada, pp.853-876.
[132] D. Charquet, et al., Hydrogen Absorption Kinetics During Zircaloy Oxidation in Steam, in: A.M. Garde, E.R. Bradley (Eds.) 10th International Symposium on Zirconium in the Nuclear Industry, 1994, ASTM International, Baltimore, MD, pp.80-96.
[133] P. Rudling, et al., Impact of Second Phase Particles on BWR Zry-2 Corrosion and Hydriding Performance, in: G.P. Sabol, G.D. Moan (Eds.) 12th International Symposium on Zirconium in the Nuclear Industry, 2000, ASTM International, Toronto, Canada, pp.678-706.
[134] B. Cox, Corrosion and Hydriding of Zircaloy Fuel Cladding, in: Proc. 6th Int. Conf. on CANDU Fuel, 1999, Canada Nuclear Society, Niagara Falls, pp.338-347.

[135] J.P. Abriata, et al., H - Zr Phase Diagram, in: T.B. Massalski, H. Okamoto, P.R. Subramanian, L. Kacprzak (Eds.) Binary Alloy Phase Diagrams, William W. Scott, Jr., 1990, pp.2078 - 2080.
[136] S. Yamanaka, et al., Characteristics of Zirconium Hydride and Deuteride, Journal of Alloys and Compounds, (330-332), 2002: pp.99-104.
[137] R.S. Daum, et al., Identification and Quantification of Hydride Phases in Zircaloy-4 Cladding Using Synchrotron X-ray Diffraction, Journal of Nuclear Materials, (392), 2009: pp.453-463.
[138] S. Yamanaka, et al., Thermal and Mechanical Properties of Zirconium Hydride, Journal of Alloys and Compounds, (293-295), 1999: pp.23-29.
[139] J.H. Root, et al., Kinetics of the δ to γ Zirconium Hydride Transformation in Zr-2.5Nb, Acta Materialia, (51), 2003: pp.2041-2053.
[140] G.J.C. Carpenter, The Dilatational Misfit of Zirconium Hydrides Precipitated in Zirconium, Journal of Nuclear Materials, (48), 1973: pp.264-266.
[141] J.R. Santisteban, et al., Hydride Precipitation and Stresses in Zircaloy-4 Observed by Synchrotron X-ray Diffraction, Acta Materialia, (58), 2010: pp.6609-6618.
[142] W.M. Small, et al., Observation of Kinetics of γ Zirconium Hydride Formation in Zr–2.5Nb by Neutron Diffraction, Journal of Nuclear Materials, (256), 1998: pp.102-107.
[143] D.O. Northwood, R.W. Gilbert, Hydrides in Zirconium-2.5 wt. % Niobium Alloy Pressure Tubing, Journal of Nuclear Materials, (78), 1978: pp.112-116.
[144] J.E. Bailey, Electron Microscope Observations on the Precipitation of Zirconium Hydride in Zirconium, Acta Metallurgica, (11), 1963: pp.267-280.
[145] Y. Liu, et al., Hydride Precipitation by Cathodic Hydrogen Charging Method in Zirconium Alloys, Materials Chemistry and Physics, (110), 2008: pp.56-60.
[146] S. Neogy, et al., Microstructural Study of Hydride Formation in Zr–1Nb Alloy, Journal of Nuclear Materials, (322), 2003: pp.195-203.
[147] C. Roy, J.G. Jacques, {10-17} Hydride Habit Planes in Single Crystal Zirconium, Journal of Nuclear Materials, (31), 1969: pp.233-237.
[148] B. Cox, Hydrogen Trapping by Oxygen and Dislocations in Zirconium Alloys, Journal of Alloys and Compounds, (256), 1997: pp.L4-L7.
[149] G.C. Weatherly, The Precipitation of γ-Hydride Plates in Zirconium, Acta Metallurgica, (29), 1981: pp.501-512.
[150] B. Cox, Some Factors Which Affect The Rate of Oxidation And Hydrogen Absorption of Zircaloy-2 In Steam, Report AERE-R-4348, 1963, H. Atomic Energy Research Establishment, Berks, England.
[151] B. Cox, T. Johnston, The Oxidation And Corrosion of Zirconium and Its Alloys. XIII. Some Observations Of Hydride In Zirconium And Zircaloy-2 And Its Subsequent Effect On Corrosion, Report AERE-R-3881, 1962, H. Atomic Energy Research Establishment, Berks, England.
[152] M. Blat, D. Noel, Detrimental Role of Hydrogen on the Corrosion Rate of Zirconium Alloys, in: E.R. Bradley, G.P. Sabol (Eds.) 11th International Symposium on Zirconium in the Nuclear Industry, 1996, ASTM International, Garmisch-Partenkirchen, Germany, pp.319-337.

[153] B. Cox, T. Johnson, Observation of a Second Transition Point During the Oxidation of Zirconium Alloys, in: Corrosion, Metals Park, Ohio, American Society for Metals, 1962, pp.33-39.
[154] D. Khatamian, Role of Hydrides on the Oxidation and Deuterium Pickup of Zr-2.5Nb in D_2O at 573 K, Journal of Alloys and Compounds, (404-406), 2005: pp.297-302.
[155] T. Kido, A Study on Enhanced Uniform Corrosion of Zircaloy-4 cladding during High Burnup Operation in PWRs, in: R.E. Gold, E.P. Simonen (Eds.) Proceedings of Sixth Symposium on Environmental Degradation of Materials in the Nuclear Power Systems-Water Reactors, 1993, National Association of Corrosion Engineers, Houston, TX, pp.449-456.
[156] M. Blat, et al., Contribution to a Better Understanding of the Detrimental Role of Hydrogen on the Corrosion Rate of Zircaloy-4 Cladding Materials, in: G.P. Sabol, G.D. Moan (Eds.) 12th International Symposium on Zirconium in the Nuclear Industry, 2000, ASTM International, Toronto, Canada, pp.563-592.
[157] J. Mayer, et al., TEM Sample Preparation and FIB-Induced Damage, MRS Bulletin, (32), 2007: pp.400-407.
[158] C. Genzel, et al., The Materials Science Synchrotron Beamline EDDI for Energy-Dispersive Diffraction Analysis, Nuclear Instruments and Methods in Physics Research Section A: Accelerators, Spectrometers, Detectors and Associated Equipment, (578), 2007: pp.23-33.
[159] G. Swislow, Spec, 1996, Certified Scientific Software, Cambridge, MA, USA.
[160] J.B. Cohen, I.C. Noyan, Residual Stress : Measurement by Diffraction and Interpretation, 1987, Springer-Verlag, New York.
[161] F. Garzarolli, et al., Oxide Growth Mechanism on Zirconium Alloys, in: C.M. Eucken, A.M. Garde (Eds.) 9th International Symposium on Zirconium in the Nuclear Industry, 1991, ASTM International, Kobe, Japan, pp.395-436.
[162] D.H. Bradhurst, P.M. Heuer, The Influence of Oxide Stress on the Breakaway Oxidation of Zircaloy-2, Journal of Nuclear Materials, (37), 1970: pp.35-47.
[163] Y.-S. Kim, et al., Stress Measurements During Thin Film Zirconium Oxide Growth, Journal of Nuclear Materials, (412), 2011: pp.217-220.
[164] S. Sprio, et al., Yttria-Stabilized Zirconia Films Grown by Radiofrequency Magnetron Sputtering: Structure, Properties and Residual Stresses, Surface and Coatings Technology, (200), 2006: pp.4579-4585.
[165] L. Gosmain, et al., Study of Stress Effects in the Oxidation of Zircaloy-4, Solid State Ionics, (141-142), 2001: pp.633-640.
[166] C. Roy, G. David, X-ray Diffraction Analyses of Zirconia Films on Zirconium and Zircaloy-2, Journal of Nuclear Materials, (37), 1970: pp.71-81.
[167] K. Une, et al., Effect of Proton Irradiation on Deuterium Diffusion in Zirconium Oxide Layer, Journal of Nuclear Materials, (420), 2012: pp.445-451.
[168] H.X. Zhang, et al., Crystal Structure, Corrosion Kinetics of New Zirconium Alloys and Residual Stress Analysis of Oxide Films, Journal of Nuclear Materials, (396), 2010: pp.65-70.
[169] J.L. Béchade, et al., Influence of Temperature on X-ray Diffraction Analysis of ZrO_2 Oxide Layers Formed on Zirconium Based Alloys Using A Synchrotron Radiation, Materials Science Forum, (404-407), 2002: pp.803-808.

[170] J.L. Béchade, et al., Studies of Zirconium ALloy Oxide Layer Using Synchrotron Radiation, Materials Science Forum, (347-349), 2000: pp.471-476.
[171] H. Li, et al., A Model of Texture Formation in ZrO_2 Films, Materials Science and Engineering A, (366), 2004: pp.164-174.
[172] P. Bouvier, G. Lucazeau, Raman Spectra and Vibrational Analysis of Nanometric Tetragonal Zirconia under High Pressure, Journal of Physics and Chemistry of Solids, (61), 2000: pp.569-578.
[173] E. Djurado, et al., Crystallite Size Effect on the Tetragonal-Monoclinic Transition of Undoped Nanocrystalline Zirconia Studied by XRD and Raman Spectrometry, Journal of Solid State Chemistry, (149), 2000: pp.399-407.
[174] R.C. Garvie, The Occurrence of Metastable Tetragonal Zirconia as a Crystallite Size Effect, The Journal of Physical Chemistry, (69), 1965: pp.1238-1243.